



HAL
open science

Study of the degradations induced by start-up/shut-down operations in PEMFC

Adrien Lamibrac

► **To cite this version:**

Adrien Lamibrac. Study of the degradations induced by start-up/shut-down operations in PEMFC. Other. Université de Lorraine, 2013. English. NNT : 2013LORR0117 . tel-01750103

HAL Id: tel-01750103

<https://hal.univ-lorraine.fr/tel-01750103v1>

Submitted on 29 Mar 2018

HAL is a multi-disciplinary open access archive for the deposit and dissemination of scientific research documents, whether they are published or not. The documents may come from teaching and research institutions in France or abroad, or from public or private research centers.

L'archive ouverte pluridisciplinaire **HAL**, est destinée au dépôt et à la diffusion de documents scientifiques de niveau recherche, publiés ou non, émanant des établissements d'enseignement et de recherche français ou étrangers, des laboratoires publics ou privés.



AVERTISSEMENT

Ce document est le fruit d'un long travail approuvé par le jury de soutenance et mis à disposition de l'ensemble de la communauté universitaire élargie.

Il est soumis à la propriété intellectuelle de l'auteur. Ceci implique une obligation de citation et de référencement lors de l'utilisation de ce document.

D'autre part, toute contrefaçon, plagiat, reproduction illicite encourt une poursuite pénale.

Contact : ddoc-theses-contact@univ-lorraine.fr

LIENS

Code de la Propriété Intellectuelle. articles L 122. 4

Code de la Propriété Intellectuelle. articles L 335.2- L 335.10

http://www.cfcopies.com/V2/leg/leg_droi.php

<http://www.culture.gouv.fr/culture/infos-pratiques/droits/protection.htm>

Université de Lorraine
Centre National de la Recherche Scientifique
Region Lorraine
Ecole doctorale EMMA « Energie, Mécanique, Matériaux »

THESE

Présentée pour l'obtention des titres de

Docteur de l'Université de Lorraine

Spécialité : Mécanique et Energétique

Par

Adrien LAMIBRAC

Ingénieur de l'Ecole Polytechnique de l'Université de Nantes

**Etude des dégradations dans les piles à combustible
PEMFC pendant les phases de démarrage/arrêt**

**Study of the degradations induced by start-up/shut-down
operations in PEMFC**

Soutenue publiquement le 28 juin 2013 devant le jury constitué de :

Rapporteurs :

Mme Elena R. SAVINOVA
M. Lionel FLANDIN

Professeur, ICPEES, Strasbourg
Professeur, LEPMI, Le Bourget du Lac

Examineurs :

M. Rangachary MUKUNDAN
M. Marian CHATENET
M. Bruno AUVITY
M. Olivier LOTTIN
M. Gaël MARANZANA
M. Jérôme DILLET

Ingénieur-Docteur, LANL, Los Alamos, USA
Professeur, Grenoble-INP - LEPMI, Grenoble
Maître de conférences, LTN, Nantes
Professeur, LEMTA, Nancy
Maître de conférences, LEMTA, Nancy
Ingénieur-Docteur, LEMTA, Nancy

Université de Lorraine
Centre National de la Recherche Scientifique
Region Lorraine
Ecole doctorale EMMA « Energie, Mécanique, Matériaux »

THESE

Présentée pour l'obtention des titres de

Docteur de l'Université de Lorraine

Spécialité : Mécanique et Energétique

Par

Adrien LAMIBRAC

Ingénieur de l'Ecole Polytechnique de l'Université de Nantes

**Etude des dégradations dans les piles à combustible
PEMFC pendant les phases de démarrage/arrêt**

**Study of the degradations induced by start-up/shut-down
operations in PEMFC**

Soutenue publiquement le 28 juin 2013 devant le jury constitué de :

Rapporteurs :

Mme Elena R. SAVINOVA
M. Lionel FLANDIN

Professeur, ICPEES, Strasbourg
Professeur, LEPMI, Le Bourget du Lac

Examineurs :

M. Rangachary MUKUNDAN
M. Marian CHATENET
M. Bruno AUVITY
M. Olivier LOTTIN
M. Gaël MARANZANA
M. Jérôme DILLET

Ingénieur-Docteur, LANL, Los Alamos, USA
Professeur, Grenoble-INP - LEPMI, Grenoble
Maître de conférences, LTN, Nantes
Professeur, LEMTA, Nancy
Maître de conférences, LEMTA, Nancy
Ingénieur-Docteur, LEMTA, Nancy

Remerciements

Au terme de ces trois années (et demi), je tiens à remercier tout particulièrement :

- Olivier Lottin, mon directeur de thèse, pour m'avoir fait confiance, pour son encadrement rigoureux et ses conseils toujours pertinents.
- Gaël Maranzana, mon co-directeur de thèse, pour sa grande disponibilité, pour sa patience et son enthousiasme contagieux.
- Jérôme Dillet, pour son aide précieuse à la mise au point des expériences et pour son soutien moral.

Mes remerciements les plus chaleureux vont également aux membres de l'équipe Pile à Combustible :

- Les anciens : Julia Mainka (pour les sorties VTT), Sylvain Chupin (pour la photo), Libeth Maldonado et Thibaut Colinart.
- Anthony Thomas, pour sa bonne humeur permanente et pour les bons moments passés ensemble.
- Nicolas Carême, pour son sérieux.
- Dung Le, membre de l'équipe pile par adoption.
- Jean-Christophe Perrin, pour avoir soigné mon hypermétropie.
- Vincent Coeuriot, pour les pauses détentes.
- Mathieu Klein, l'homme à la guitare.
- Sofyane Abbou, auquel je confie mon banc d'essai avec beaucoup d'espoir pour la suite.
- Sophie Didierjean, pour l'attention qu'elle a prêtée à mes travaux.
- Alain Chenu, parce qu'il ne m'est rien arrivé (ou presque) en trois ans.
- Feina Xu.

Je remercie aussi:

- Les personnes du LEPMI avec lesquelles j'ai pris beaucoup de plaisir à travailler notamment Julien Durst, Luis Castanheira, Marian Chatenet et Frédéric Maillard.
- Mes camarades de cantine qui n'ont pas déjà été cités et en particulier ceux qui ont perdu une plaquette de chocolat (Yves Jannot, Denis Maillet, Christian Moyne, André Mézin, Didier Stemmelen, Fabrice Lemoine, Johanna Goncalves, Eric Kremer et Fatmir Asslanaj).
- Mes collègues doctorants, pour avoir partagé de leur temps (Clément Baillard, Alexandre Jenft, Lionel Perrin, Pierre Dunand, Nicolas Lopez, Caroline Hanotin, Bamdad Salemi et Adrian-Marie Philippe).
- Les secrétaires : Irène Léonard, Edith Lang, Valérie Reichhart, Fatiha Boumendjel, Dalida Simonigh et Christine Sartori, pour m'avoir épaulé dans toutes les démarches administratives.
- Les ingénieurs et techniciens (Jean-Yves Morel, Pascal Thomann, Eric Blaise et Franck Demeurie), pour m'avoir bien dépanné même quand il ne s'agissait pas de ma manip.
- Les personnes avec qui j'ai effectué mon monitorat (Ophélie Caballina, Alexandre Labergue, Jean-François Schmitt, Rachid Rahouadj et Pascal Fontaine), pour leur aide dans la préparation des TP et TD.
- Les personnes avec qui j'ai effectué mon demi-ATER (Emmanuel Plaut, Mathieu Jenny et Vincent Schick), pour l'encadrement.

I would like also:

- To express my appreciation and my gratitude to the members of the fuel cell group of the LANL (Rodney Borup, Dusan Spornjak, Rangachary Mukundan and Joseph Fairweather), for their participation to this work.
- To thank the members of the Jury, who accepted to review this Ph.D thesis.

Je tiens à saluer mes amis, en particulier Franklin, Géraud, Ingrid et Wolfgang.

Enfin, je remercie mes parents, Pascal et Isabelle, pour m'avoir toujours soutenu et encouragé, mes grands-parents pour leur gentillesse et mes sœurs, Marie et Juliette dont je suis très fier (sans oublier Jérémy).

Schliesslich danke ich meiner Frau Tiina für ihre Unterstützung und Geduld.

Preamble

The exhaustion of natural resources is an always more burning issue, especially with the emergence of developing nations. In parallel, the scientific community has demonstrated the role of human beings in the global warming, which consequences can be dramatic in a near future. A transition is needed to find new resources of energy and to reduce our impact on the environment. Both can be done if a new energy policy is pursued with the objectives to develop more renewable and sustainable activities. Today, wind and solar energies are favoured: wind turbines and solar panels produce electricity but this energy is difficult to use, in particular for automotive applications since there is still no efficient way to store it. Moreover, the time when electricity is consumed does not always correspond to the time when wind and sun are available. A way to avoid such problems is to transform electricity into chemical energy which will be stored, transported and converted again into electricity when necessary.

Proton Exchange Membrane Fuel Cells (PEMFC) are one of the devices that can realize the conversion of the energy carriers - in this case hydrogen molecules - into electricity. Batteries as well as other types of fuel cells are also considered but they are out of the scope of this work. Each has its own advantages and disadvantages. However, PEMFC are one of the most promising for many reasons, among which:

- The ease of use. PEMFCs only need to be supplied with hydrogen and air to start providing electricity quickly.
- A high efficiency. About 50% of the hydrogen chemical energy is converted into electricity.
- A good flexibility. Customized fuel cell stacks can be designed for automotive as well as stationary applications.
- PEMFC can be considered as environmentally friendly since they do not produce any direct pollution.

In the short term, PEMFCs are suitable candidates to reinforce the present market of power supply devices. In the long term, it is even to expect that they replace combustion engines and batteries, first for specific applications such as forklifts or backup power systems, then for powering cars and trucks.

Nevertheless, further investigations are necessary to overcome some remaining technical barriers. They concern mainly:

- Hydrogen production. Today, about 95%¹ of hydrogen is produced worldwide using steam reforming, a technique where coal (18% of the hydrogen production), oil (30% of the hydrogen production) or natural gas (47% of the hydrogen production) react chemically with water. The reaction is enabled by the provision of heat and allows breaking the bonds between hydrogen and its neighbouring atoms. Steam reforming, which is already a widespread technique in the petrochemical and food industry, allows mass production at relatively low cost. However, this process is energy consuming and heat has to be provided. In addition, some pollution can result from the chemical reaction since components such as carbon monoxide or dioxide are emitted. Finally, it uses fossil fuels and alternatives have to be developed. A possible solution could be biogases, which are produced by anaerobic digestion of organic matter.

¹ <http://www.afh2.org/uploads/memento/Fiche%201.3%20revision%20fevrier%202008.pdf>

However, such process is incapable of satisfying the current needs of hydrogen, not to mention its increasing consumption in the future.

- Another way to produce hydrogen is water splitting or electrolysis (about 5% of the hydrogen production). If the electricity source is wind or sun for instance, this method can be considered as clean and renewable. Current researches aim to increase the efficiency of this technique to achieve mass production at reasonable costs.
- Hydrogen storage. For automotive applications, good storage capabilities are necessary to cover long distances with a vehicle. The hydrogen tanks have to respect severe criteria in term of security and space: the energy contained in 50 litres of gasoline (heat of combustion $\Delta H_f^0(\text{gasoline}) = 35 \text{ MJ/l}$) corresponds to approximately 215 litres of hydrogen (heat of combustion $\Delta H_f^0(H_2) = 12 \text{ kJ/l}$) compressed at 700 bar. High pressure hydrogen storage requires significant amount of energy during the phase of gas compression. In addition, the hydrogen tanks are about four times bigger than usual gasoline tanks and their ability to withstand high pressure makes them much heavier. Finally, they have to be resilient to shocks in the case of a car accident to prevent any gas leakage. To reduce the energy cost and the space necessary for storage, researches are focusing on materials able to retain and free high amount of hydrogen at ambient pressure and temperature.
- Fuel cell durability. The American Department of Energy (DOE) set the lifetime target to 5000 hours for automotive application by 2015. This target was extended to 40 000 hours for stationary applications [1]. However, depending on the operating conditions, the cell failure can still occur within a few hundred hours (start-up/shut-down, open circuit voltage hold, humidity cycling, fuel starvation).
- Fuel cell cost. Some components are expensive, like platinum used as catalyst in the electrode ($\sim 40 \text{ euros/g}$) and PFSA membranes used as electrolyte. Objectives are to reduce or replace these components by cheaper ones while maintaining or even increasing the performance and durability. The costs related to the fabrication process have also to decrease in particular those concerning the flow field plates.

As well as technical, these barriers are also economic and politic. Implementing a new industry requires both important political decisions and substantial investments. While efforts have been done and progress have been achieved, proton exchange membrane fuel cells are not yet mature enough to fully emerge.

In this context, this Ph.D thesis focuses on one of the main limitations of fuel cells: their low durability and reliability. A wide range of degradation mechanisms, described in the first chapter, were reported in the literature. They often result from specific or inappropriate operating conditions. Even if some of the situations which favour damages can be prevented, all cannot be avoided. For instance, start-ups and shut-downs are necessary, if only for security reasons: when not in use, a cell must not contain any hydrogen. However, start-ups and shut-downs were also held responsible for severe MEA damages. As a consequence, mitigation strategies have to be found, which requires first to identify and to analyze the degradation mechanisms involved. While some papers report about possible mechanisms, their results were mostly obtained ex-situ which does not completely reflect what happen in real conditions. Similarly, post-mortem analyses give information about the mechanisms involved but not about their kinetics. Recently, development of new measurement techniques enabled in-situ observation of the degradations in real conditions and at a local scale.

In this PhD thesis, start-ups and shut-downs were investigated in real conditions and with segmented cells which were designed on purpose. Combined with techniques such as impedance spectroscopy or cyclic voltammetry, segmented cells can provide a diagnosis at a local scale of the cell performance and therefore of the impact of the degradations. Moreover, it was evidenced that start-ups and shut-downs lead to the production of internal currents when the cell is not connected to a load. Segmented cells enable measuring these internal currents, part of which results from electrochemical reactions which participate to the degradation of the cell. Identification of these reactions is attempted in the second chapter. In particular, the carbon oxidation contribution was studied by measuring carbon dioxide emissions in the cathode gas exhaust. Influence of the nature of gas used to flush the anode compartment and of its injection flow rate was also investigated.

In a third chapter, long term aging experiments performed by repeating start-ups and shut-downs were implemented using Johnson Matthey MEAs. The objective was to reproduce, the everyday operation of a fuel cell powering a road vehicle. Several protocols were established to discriminate the impacts of the nature of the gas used to flush the anode compartment (air or nitrogen) and of the injection flow rate used to start or stop the cell on the durability. These impacts were evaluated regarding the evolution with time of the fuel cell voltage, local current densities and Electrochemical Surface Area. These in-situ observations were complemented by post-mortem analyses realised in the Laboratory of Electrochimie and of Physicochimie of Materials and Interfaces (LEPMI) in Grenoble (France). These analyses confirmed the observations made in-situ and helped identifying more accurately the degradation mechanisms.

In the fourth chapter, a model is presented, which aims at simulating numerically the internal currents. This model takes several phenomena into account such as the electrochemical reactions, the mass transport losses and the capacitive effects. While it cannot achieve a perfect correspondence with experiment, the numerical approach allows an easy decoupling of the different reactions (which is difficult to achieve with the experiments). Thus, the faradic and capacitive contributions to the internal currents can be separated and quantified. In addition, the numerical approach confirmed the evolution of the internal currents with the gas injection flow rate or with the nature of the gas used to flush the anode compartment during shut-down observed in the second chapter.

Some of the results presented in this thesis were used within the framework of the H₂E project, in partnership with the LEPMI. The objective of this project is to improve performance and lifetime of fuel cell stacks developed by Axane, a subsidiary of Air Liquide. Some of the experimental works presented in this manuscript were transposed on single cells from Axane, which geometry is more sophisticated (serpentine flow field plates) than the one we used.

Some experiments were implemented in the framework of a partnership with the LANL in Los Alamos: Ion Power MEAs were used to study the impact of their specifications (carbon support, platinum loading in the anode and cathode) on the internal currents and CO₂ emissions during single start-ups and shut-downs. Long-term aging experiments were also performed to assess the effects of specification changes on the durability.

Contents

PREAMBLE	I
CONTENTS.....	V
LIST OF SYMBOLS	XI
1 FUEL CELLS AND THEIR MAIN DEGRADATIONS MECHANISMS.....	1
1.1. Principle of operation	1
1.2. Proton Exchange Membrane Fuel Cell.....	3
1.2.1 Thermodynamics and Reference Parameters.....	4
1.2.2 Effective Fuel Cell Performances	8
1.2.3 Reactions mechanisms	10
<i>a. Hydrogen Oxidation Reaction.....</i>	<i>10</i>
<i>b. The Oxygen Evolution Reaction.....</i>	<i>10</i>
1.2.4 Reaction kinetics	11
1.3. Diagnosis Tools.....	13
1.3.1 Cyclic Voltammetry and Active Surface	14
<i>a. Principle.....</i>	<i>14</i>
<i>b. Reaction Mechanisms.....</i>	<i>15</i>
<i>c. Remark</i>	<i>19</i>
<i>d. Platinum Active Surface</i>	<i>20</i>
<i>e. Limitations of cyclic voltammetry</i>	<i>22</i>
1.3.2 Electrochemical Impedance Spectroscopy	23
<i>a. Principle.....</i>	<i>23</i>
<i>b. Experimental implementation</i>	<i>23</i>
<i>c. Theoretical approach</i>	<i>25</i>
<i>d. Limitations of EIS.....</i>	<i>26</i>
1.4. MEA main degradation mechanisms	27
1.4.1 Flow field plates.....	28
1.4.2 Gas Diffusion Layers and MPLs	29
1.4.3 Electrodes.....	29
<i>a. Carbon support oxidation</i>	<i>30</i>
<i>b. Catalyst poisoning.....</i>	<i>31</i>
<i>c. Catalyst degradation.....</i>	<i>33</i>
<i>d. Main issues concerning the electrodes.....</i>	<i>35</i>
1.4.4 Membrane	37
<i>a. Chemical degradations</i>	<i>37</i>
<i>b. Mechanical degradations.....</i>	<i>41</i>
<i>c. Main issues related to membrane durability.....</i>	<i>42</i>
1.5. Conclusion	43

2 ELECTROCHEMICAL DESCRIPTION OF START-UP AND SHUT-DOWN	47
2.1. Description of start-ups	47
2.1.1 Principle and internal currents	47
2.1.2 Description of potential evolution during start-ups	53
<i>a. First stage of a start-up</i>	56
<i>b. Cathode metal potential V_m^c and cathode potential ϕ^c during start-up</i>	58
<i>c. Second stage of a start-up</i>	60
2.2. 2D segmented cell and test bench	62
2.3. Charge balance.....	64
2.4. Start-up with the 2D segmented cell.....	66
2.4.1 Potentials distribution	66
2.4.2 Local current densities and charges during a start-up.....	72
<i>a. Internal currents</i>	72
<i>b. Definition and identification of the charges</i>	74
<i>c. Limitation concerning the charges measured</i>	76
<i>d. Charge exchanged vs. hydrogen injection flow rate</i>	79
2.5. Carbon dioxide in cathode exhaust gases	81
2.6. Shut-down with air	82
2.6.1 Principle	82
2.6.2 Potential evolution during shut-down	83
2.6.3 Local Current densities	85
2.6.4 Comparaision between start-up and shut-down	87
2.6.5 Carbon dioxide measurement in the cathode exhaust gas	88
2.7. Shut-down with nitrogen	91
2.8. Comparison of start-ups and shut-downs performed with different MEAs	92
2.8.1 General comparison (multiple MEAs).....	92
2.8.2 Specific comparison (Ion Power MEAs)	93
<i>a. Charge exchanged and CO₂ emissions during individual start-ups and shut-downs</i>	93
<i>b. Reproducibility</i>	96
2.9. Conclusion	97
3 FUEL CELL AGING	101
3.1. Impact of Cyclic voltammetry	101
3.2. Aging protocols.....	106
3.2.1 Start-up and shut-down aging protocols	106
3.2.2 Potential cycling protocol	106
3.2.3 Protocol structure	107
3.3. Potential cycling	108
3.4. Start-up aging.....	110

3.4.1 ECSA evolution	110
3.4.2 Charge exchanged evolution.....	112
3.4.3 Charge exchanged vs. ECSA	113
3.4.4 Performance evolution.....	115
3.4.5 Further investigations into start-up aging protocol by injection of hydrogen in nitrogen	117
3.4.6 Conclusion about start-up agings.....	119
3.5. Shut-down aging.....	120
3.6. Start-up and shut-down aging with different MEAs	124
3.6.1 Impact on the whole cell	124
3.6.2 Local impact along the gas channel	128
3.7. Post-mortem analyses of aged MEA	130
3.7.1 In-situ aging analysis	130
3.7.2 Post-aging analysis	131
<i>a. Inlet vs. outlet degradation heterogeneities</i>	<i>131</i>
<i>b. Channel vs. land degradation heterogeneities</i>	<i>131</i>
3.8. Conclusion	137
<u>4 NUMERICAL SIMULATION OF START-UP</u>	<u>141</u>
4.1. Previous numerical model	141
4.1.1 Presentation.....	141
4.1.2 Experimental and numerical results – main limitations of the first model.....	143
4.2. New numerical model	143
4.2.1 Generic electrode model	144
<i>a. Electrochemical and chemical reactions</i>	<i>144</i>
i Active part	144
ii Passive part.....	145
<i>b. Reactions kinetics.....</i>	<i>149</i>
<i>c. Mass transport.....</i>	<i>156</i>
<i>d. Mass balance.....</i>	<i>158</i>
4.2.2 Parameter setting.....	159
<i>a. Polarization curve</i>	<i>161</i>
<i>b. Cyclic voltammetry.....</i>	<i>161</i>
4.2.3 2D transient state modelling of a complete cell.....	166
<i>a. Start-up by injection of hydrogen in air</i>	<i>167</i>
i Internal currents	167
ii Potential evolution	180
iii Influence of hydrogen flow rate.....	182
<i>b. Simulation of a start-up by injection of hydrogen in nitrogen</i>	<i>183</i>
4.3. Conclusion	186
<u>5 CONCLUSIONS AND PERSPECTIVES</u>	<u>189</u>
<u>REFERENCES</u>	<u>193</u>

ANNEX..... 205

List of Symbols

Symbols

a	Coefficient in natural logarithm form of Tafel equation	
a_i	Chemical activity of substance i	
b	Tafel slope	V
C_{dl}	Double layer capacity	F
C_i	Concentration of the species i	mol/L
$C_i(0)$	Concentration of the species i at the electrode	mol/L
C_i^*	Reference concentration of the species i	mol/L
d_v	Mean volume-averaged diameter i	m
D_i^α	Diffusion coefficient of the species i in the component α	m ² /s
e_α	Thickness of the component α	m
E_{ref}	Reference Potential (fictive)	V
E^0	Standard electrode potential	V
E	Equilibrium potential (Nernst potential)	V
F	Faraday constant	96485 C/mol
ΔG^0	Standard Gibbs Free Energy of reaction	J/mol
ΔG	Gibbs Free Energy of reaction	J/mol
ΔG_i	Gibbs Free Energy change of the species i	J/mol
ΔH^0	Standard Enthalpy of reaction	J/mol
ΔH	Enthalpy of reaction	J/mol
ΔH_i	Enthalpy of formation of the species i	J/mol
I	Current	A
I_L	Lateral current	A
j	Current density	A/cm ²
j_f	Faradic current density	A/cm ²
j_c	Capacitive current density	A/cm ²
j_{Ox}	Current density of oxidation	A/cm ²
j_{perm}	Permeation current density	A/cm ²
j_{Red}	Current density of reduction	A/cm ²
j_0	Exchange current density	A/cm ²
L_{Pt}	Platinum loading	g _{Pt} /m ²
N_i	Amount of the species i	mol
P	Total pressure	Pa
P_i	Partial pressure of the species i	Pa
Q	Heat	J/mol
Q	Charge	C

Q_A	Charge measured in the active part during start-up/shut-down	C
Q_B	Balancing charge during start-up/shut-down	C
Q_P	Charge exchanged (measured in the passive part during start-up/shut-down)	C
Q_{HOR}	Charge deduced from the hydrogen desorption during cyclic voltammetry	C
R	Gas constant	8.31 J/mol/K
R_{ct}	Charge transfer resistance	Ω
R_{hf}	High frequency resistance	$\Omega.m^2$
RH	Relative Humidity	%
S	Surface of the cell	m^2
ΔS^0	Standard Entropy of reaction	J/K/mol
ΔS	Entropy of reaction	J/K/mol
ΔS_i	Entropy change of the species i	J/K/mol
t	Time	s
T	Temperature	K
U	Fuel cell voltage	V
V_m^α	Metal Potential at the electrode α	V
V_e	Potential of the electrolyte	V
W_{elec}^{rev}	Reversible Electrical Work	J/mol
Z	Impedance	Ω
α	Charge transfer coefficient	
ε	Porosity of the electrode	
φ	Phase angle	rad
θ_{PtO}^b	Platinum oxide (PtO) coverage in the bulk	
θ_{PtO}^s	Platinum oxide (PtO) coverage on the surface	
θ_{PtOH}^s	Platinum oxide (PtOH) coverage on the surface	
ϕ^α	Potential of the electrode α	V
γ	Roughness factor of the electrode	
η_{act}	Activation Overpotential	V
η_{ohm}	Ohmic Overpotential	V
v	Potential sweep rate	V/s
ω	Angular velocity	rad/s
χ	Fraction of the platinum oxide coverage on the platinum particle surface above which platinum starts oxidizing in the sublayers	

Indices and exponents

0	Standard conditions
a	Anode
ads	Adsorbed

<i>act</i>	Activation
<i>b</i>	Bulk
<i>c</i>	Cathode
<i>down</i>	Downstream part
<i>elec</i>	Electrical
<i>liq</i>	Liquid
<i>ox</i>	Oxidant
<i>red</i>	Reductant
<i>ref</i>	Reference
<i>rev</i>	Reversible
<i>s</i>	Surface
<i>sat</i>	Saturation
<i>up</i>	Upstream part
<i>v</i>	Volume
<i>vap</i>	Vapour

Abbreviations

AC	Alternative Current
CCM	Catalyst-coated membrane
CL	Catalyst Layer
CNT	Carbon Nanotube
CV	Cyclic Voltammetry
DC	Direct Current
DMFC	Direct Methanol Oxide Fuel Cell
ECSA	Electrochemical Surface Area
EIS	Electrochemical Impedance Spectroscopy
FIB	Focused Ion Beam
GDL	Gas Diffusion Layer
HER	Hydrogen Evolution Reaction
HOR	Hydrogen Oxidation Reaction
MEA	Membrane Electrode Assembly
MPL	Micro Porous Layer
MCFC	Molten Carbonate (electrolyte) Fuel Cell
NDIR	Non-Dispersive Infrared Spectroscopy
OCV	Open Circuit Voltage
OER	Oxygen Evolution Reaction
OPD	Over Potential Deposition
ORR	Oxidation Reduction Reaction
PAFC	Phosphoric Acid (electrolyte) Fuel Cell
PEMFC	Proton Exchange Membrane Fuel Cell
PFSA	Perfluorosulfonic Acid
PPM	Parts Per Million
PTFE	PolyTetraFluoroEthylene
RHE	Reference Hydrogen Electrode
SCCM	Standard Cubic Centimetre per Minute
SEM	Scanning Electron Microscope
SHE	Standard Hydrogen Electrode
SOFC	Solid Oxide Fuel Cell

SU
SD
TEM
UPD

Start-up
Shut-Down
Transmission Electron Microscope
Under Potential Deposition

1 Fuel Cells and Their Main Degradations Mechanisms

A Proton Exchange Membrane Fuel Cell is a complex system constituted by various components: flow field plates, gas diffusion layers, micro porous layers, electrodes and membrane. Each component plays a specific role and, in this purpose, must possess the corresponding properties such as good electrical or thermal conductivity, mechanical resistance or chemical stability. It must be noted that adjacent components can have completely different properties. For example, carbon electrodes are developed to conduct electrons and to repel water when the ionomer membrane needs to be well humidified to conduct protons. Even in a given component, antagonist properties can be in competition. The membrane for instance has to be thick enough to avoid the permeation of gases from one electrode to the other but it also has to be thin enough to limit ohmic losses resulting from protons transport.

To achieve the best performance and take the maximum benefit of the material properties, fuel cell management can be done by acting on external parameters such as the cooling water temperature, gases stoichiometry or humidification. This may not be enough to ensure optimal working conditions for each of the components but can provide a sufficient compromise so that they all work together. However, the achievement of this compromise appears to be sometimes difficult because of the large operation range of a PEMFC. For instance, at low current densities, high voltage is reached while the water production is low. On the contrary, at high current densities, voltage is low and water flow is increased. Depending on the current, certain components have therefore to withstand various environmental stresses. Despite the efforts to avoid tough conditions and to improve the quality of the materials, some damages can still occur. Then, since all the components are highly coupled, cell failure can arise rapidly.

After a short introduction to PEMFC, this chapter lists and describes the main degradations taking place in a cell. This description is done with regards to the triggering effects, the degradation rate and the main governing parameters.

1.1. Principle of operation

A fuel cell is an electrochemical device which converts the chemical energy of a fuel and combustive pair into electricity and heat. A value can be given to the heat if it is used in cogeneration systems, which is easier with fuel cells operating at high temperature.

Figure 1-1 summarizes the different types of fuel cell and Table 1-1 lists their main characteristics. Today, most of the research focuses on PEMFC, AFC (Alkaline Fuel Cell), SOFC (Solid Oxide Fuel Cell) and MCFC (Molten Carbonate Fuel Cell), which operating ranges are complementary: low temperatures fuel cells (PEMFCs, AFCs) are more adapted to low or medium power range and quick start-up while those operating at high temperatures (SOFC, MCFC) work better in steady state and can deliver high power. Fuel cells present therefore a good potential for large scale commercial deployment. They can, for example, be used in backup, auxiliary or portable power units, powertrains for cars, trucks and buses or as distributed generation units (Table 1-1).

1 – Fuel Cells and their Main Degradations Mechanisms

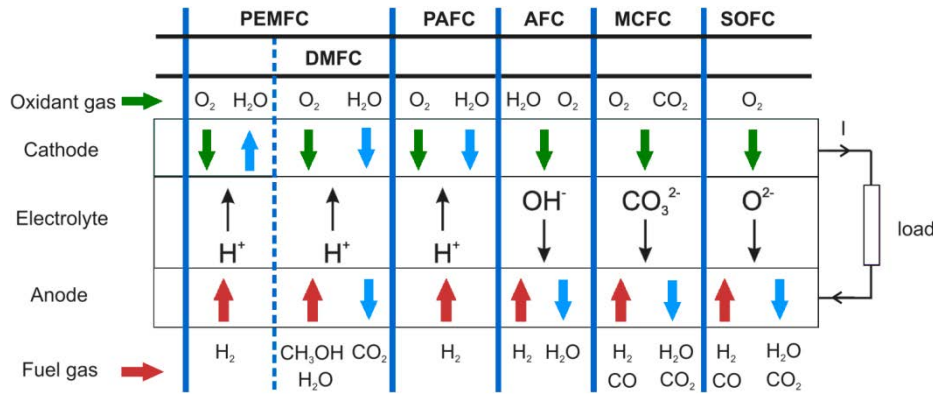


Figure 1-1. The different types of fuel cells.

Fuel Cell Type	Common Electrolyte	Operating Temperature	Typical Stack Size	Efficiency	Applications	Advantages	Disadvantages
Polymer Electrolyte Membrane (PEM)	Perfluoro sulfonic acid	50-100°C 122-212° typically 80°C	< 1kW-100kW	60% transportation 35% stationary	• Backup power • Portable power • Distributed generation • Transportation • Specialty vehicles	• Solid electrolyte reduces corrosion & electrolyte management problems • Low temperature • Quick start-up	• Expensive catalysts • Sensitive to fuel impurities • Low temperature waste heat
Alkaline (AFC)	Aqueous solution of potassium hydroxide soaked in a matrix	90-100°C 194-212°F	10-100 kW	60%	• Military • Space	• Cathode reaction faster in alkaline electrolyte, leads to high performance • Low cost components	• Sensitive to CO ₂ in fuel and air • Electrolyte management
Phosphoric Acid (PAFC)	Phosphoric acid soaked in a matrix	150-200°C 302-392°F	400 kW 100 kW module	40%	• Distributed generation	• Higher temperature enables CHP • Increased tolerance to fuel impurities	• Pt catalyst • Long start up time • Low current and power
Molten Carbonate (MCFC)	Solution of lithium, sodium, and/or potassium carbonates, soaked in a matrix	600-700°C 1112-1292°F	300 kW-3 MW 300 kW module	45-50%	• Electric utility • Distributed generation	• High efficiency • Fuel flexibility • Can use a variety of catalysts • Suitable for CHP	• High temperature corrosion and breakdown of cell components • Long start up time • Low power density
Solid Oxide (SOFC)	Yttria stabilized zirconia	700-1000°C 1202-1832°F	1 kW-2 MW	60%	• Auxiliary power • Electric utility • Distributed generation	• High efficiency • Fuel flexibility • Can use a variety of catalysts • Solid electrolyte • Suitable for CHP & CHHP • Hybrid/GT cycle	• High temperature corrosion and breakdown of cell components • High temperature operation requires long start up time and limits

Table 1-1. Main characteristic of each fuel cell.

The different types of fuel cells are generally made of a set of components having similar functions:

- Flow field plates. Their role consists of delivering the fuel and the combustive to the electrodes. They are also in charge of the electronic transfers from one electrode to the other. In addition, they can be used for the thermal regulation of the cell.
- Electrodes or Catalyst Layers (CL) where oxidation and reduction reactions take place.
- An electrolyte transporting ions from one electrode to the other. It also ensures the electronic insulation between the electrodes.

While having similar functions, these components are made of different materials depending on the operating conditions of each type of fuel cells. In PEMFCs, the electrolyte is an ionomer membrane which forms, together with the anode and cathode, the Membrane Electrodes Assembly (MEA, Figure 1-2). In addition, Gas Diffusion Layers (GDL) are inserted between the catalyst layers and the flow field plates. Their function is to homogenise the reactant flow in the catalyst layers and make easier the evacuation of water. They are also

used for the electronic conduction from the flow field plate to the catalyst layer. It must be noted that GDL are used in PEM fuel cells only.

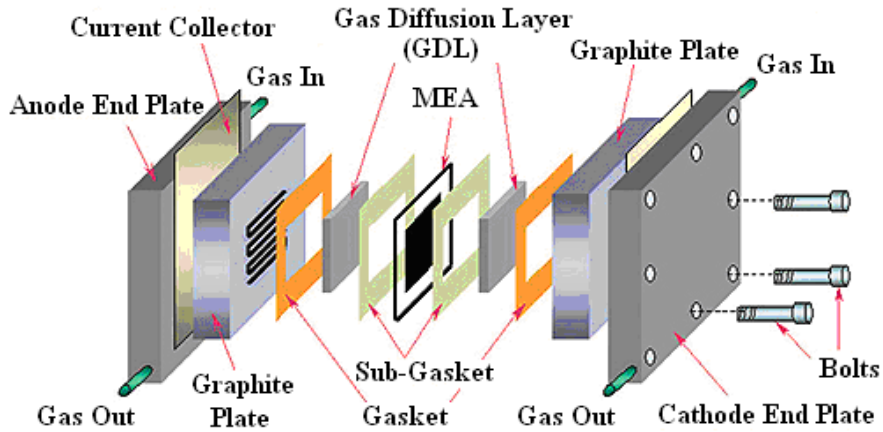


Figure 1-2. Components of a PEMFC.

1.2. Proton Exchange Membrane Fuel Cell

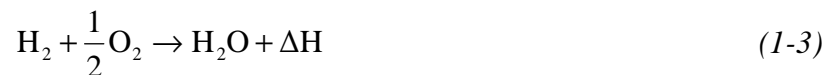
A PEMFC uses pure hydrogen as fuel and oxygen (either from air or pure oxygen) as oxidant. The half-reactions occurring at each electrode are very simple (Figure 1-4):
Hydrogen Oxidation Reaction (HOR) at the anode:



Oxygen Reduction Reaction (ORR) at the cathode:



The global reaction is consequently:



The reactions take place in the electrodes at the so-called triple phase boundary [2]. While the triple phase boundary remains a theoretical conception, it facilitates the understanding of the mechanisms involved in the electrochemical reactions. It corresponds to the interface formed by carbon, reactant gases and ionomer, each having a specific role and being indispensable for the half reactions to occur: carbon captures or provides electrons, the ionomer plays the same role with protons and gases are supplied and evacuated through various porous media: GDL, MPL and electrodes. An additional boundary can be formed with platinum which is deposited on carbon to catalyse the reaction. Manufacturing processes of the CL are still empirical and it is very difficult to obtain a controlled balance between each constituent. Moreover, the reactions sites are not frozen aggregates of different elements. With the change of ambient conditions and the aging of the cell, they evolve to form a more or less active surface.

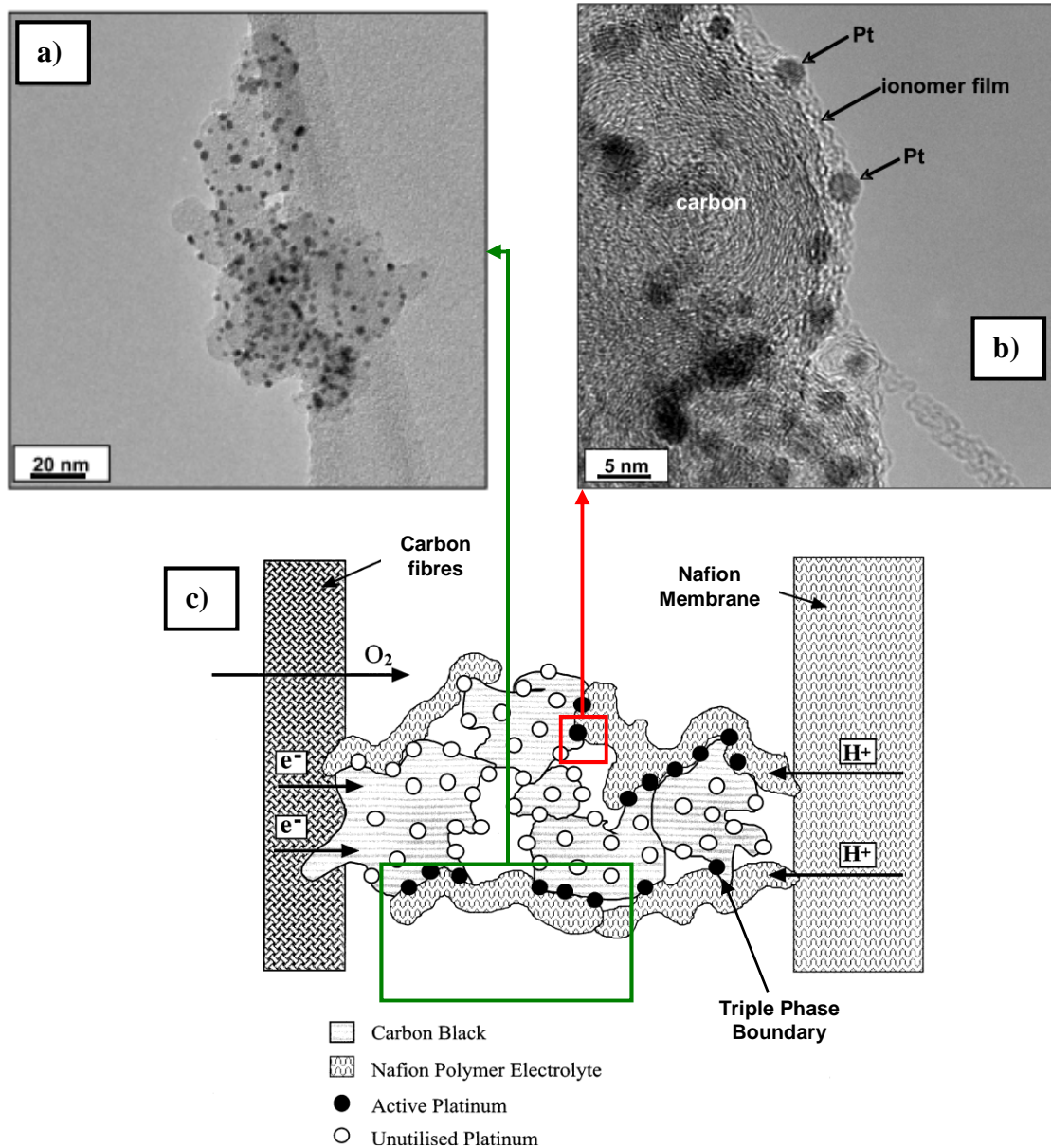


Figure 1-3. a) Large view of the carbon support with uniform Pt dispersion [3] – b) Close-up on individual Pt particles on the surface of a carbon sphere [3] – c) Overview of an electrode adapted [4].

1.2.1 Thermodynamics and Reference Parameters

The electrical power delivered by a cell is determined as well by the reactions rates as by their ability to convert efficiently chemical energy into electrical energy. A simple way to improve the reactions rates is to increase the surface on which they occur: individual cells can easily be stacked to produce more power. Nevertheless, compactness and weight remain critical issues, especially for automotive application. The real challenge consists in increasing the power density, which means either to increase the reactions rates per surface unit or to improve the conversion from chemical to electrical energy (while decreasing cost or at least by keeping it constant). In the following, the reactions are described from a thermodynamic point of view.

The total quantity of chemical energy associated with the global reaction of hydrogen combustion (1-3) corresponds to the reaction enthalpy:

$$\Delta H(T, P_i) = \Delta H_{H_2O} - \Delta H_{H_2} - \frac{1}{2} \Delta H_{O_2} \quad (1-4)$$

Where P_i stands for the partial pressure of each species i ($i = H_2O, H_2, O_2$).

The reaction enthalpy depends of the phase of water. In standard conditions ($T^0 = 298$ K and $P^0 = 10^5$ Pa) we have:

$$\Delta H_{liq}^0 = -285.8 \text{ kJ} / \text{mol}_{H_2} \quad (1-5)$$

$$\Delta H_{vap}^0 = -241.8 \text{ kJ} / \text{mol}_{H_2} \quad (1-6)$$

The global reaction enthalpy allows to define a (fictive) reference potential E_{ref} that the fuel cell would reach if the totality of the chemical energy was transformed into electrical energy, without any heat production. This reference potential is given by:

$$E_{ref}(T, P_i) = \frac{-\Delta H(T, P_i)}{2F} \quad (1-7)$$

Where F (96485 C/mol) is the Faraday constant standing for the electrical charge of one mole of electrons. Like enthalpy, the reference potential depends on temperature, pressure and on the phase of water. In standard conditions:

$$E_{ref,liq}^0 = 1.48 \text{ V} \quad (1-8)$$

$$E_{ref,vap}^0 = 1.25 \text{ V} \quad (1-9)$$

Of course, this reference potential remains fictive. According to the 2nd law of thermodynamics, even in ideal (reversible) conditions, a part of the chemical energy is necessarily converted into heat, which lowers the value of the electrical work produced during the reaction and thus the cell voltage. The parameter associated with this ideal heat production is the reaction entropy:

$$\Delta S = \Delta S_{H_2O} - \Delta S_{H_2} - \frac{1}{2} \Delta S_{O_2} \quad (1-10)$$

Like the reaction enthalpy, the entropy depends on the working conditions and on the state of water. In standard (for liquid water) and saturated (for vapour) conditions:

$$\Delta S_{liq}^0 = -163.3 \text{ J} \cdot \text{K}^{-1} \cdot \text{mol}_{H_2}^{-1} \quad (1-11)$$

$$\Delta S_{vap}(T^0, P_{sat}(T^0)) = -16 \text{ J} \cdot \text{K}^{-1} \cdot \text{mol}_{H_2}^{-1} \quad (1-12)$$

It can be worth recalling that for vapour production, it is necessary to use the saturated vapour pressure at T^0 , since below 100°C vapour cannot exist at standard pressure. The entropy variations ΔS_{vap} or ΔS_{liq} corresponds to a heat production that is given by:

$$Q = T\Delta S \quad (1-13)$$

As a consequence, the electrical energy available for the user in ideal conditions is given by the variation of the Gibbs free energy, defined by:

$$\Delta G(T, P_i) = \Delta H(T, P_i) - T\Delta S(T, P_i) \quad (1-14)$$

Which allows defining the reversible electrical work W_{elec}^{rev} (counted positively):

$$W_{elec}^{rev} = -\Delta G \quad (1-15)$$

In standard conditions:

$$\Delta G_{liq}^0 = -237.1 \text{ kJ} / \text{mol}_{H_2} \quad (1-16)$$

In saturated conditions, the value of the Gibbs free energy is independent of the phase of water, although $\Delta H_{liq}^{tot} > \Delta H_{vap}^{tot}$. The difference between these reaction enthalpies is only due to the latent heat of evaporation L_v . Since $L_v = T(\Delta S_{vap} - \Delta S_{liq})$, there is no variation in the Gibbs energy, whatever the phase of water.

The ideal cell voltage E_{eq} is thus given by:

$$E_{eq}(T, P_i) = \frac{\Delta G(T, P_i)}{2F} \quad (1-17)$$

E is also called the reversible open circuit voltage (OCV). In standard conditions, the reversible cell voltage is:

$$E^0 = E_{eq}(T^0, P^0) = \frac{-\Delta G_{liq}^0}{2F} = 1.23 \text{ V} \quad (1-18)$$

Assuming that hydrogen, oxygen and vapour behave like ideal gases, $\Delta G(T, P_i)$ can be obtained by:

$$\Delta G(T, P_i) = \Delta G^0 - \int_{298K}^T \Delta S(T, P^0) dT + RT \ln \left(\frac{a_{H_2O}}{a_{H_2} a_{O_2}^{1/2}} \right) \quad (1-19)$$

Where a_i stands for the activity of species i . For gases, the activity can be evaluated knowing the partial pressure P_i , by reference to the standard pressure P^0 :

$$a_i = \frac{P_i}{P^0} \quad (1-20)$$

The liquid water activity is considered equal to 1: $a_{H_2O,liq} = 1$. $\Delta S(T, P^0)$ stands for the reaction entropy at standard pressure. In the case of PEMFC, the temperature reached being close to T^0 , it is possible to neglect the variation of the reaction entropy with respect to T in (1-19) and to consider that $\Delta S(T, P^0) \approx \Delta S^0$. Combining (1-17) and (1-19) (with the

corresponding values of ΔG^0 (1-16) and ΔS^0 (1-11) and (1-12)) allows deriving some explicit expressions of the thermodynamic voltage as functions of the temperature and pressure (concentration/activity):

$$E_{eq}(T, P_i) = 1.229 - 23.10^{-5}(T - 298) + \frac{RT}{2F} \ln \left(a_{H_2} a_{O_2}^{\frac{1}{2}} \right) \quad (1-21)$$

$$E_{eq}(T, P_i) = 1.184 - 23.10^{-5}(T - 298) + \frac{RT}{2F} \ln \left(\frac{a_{H_2} a_{O_2}^{\frac{1}{2}}}{a_{H_2O}} \right) \quad (1-22)$$

Equation (1-22) must be used in the case of vapour production; equation (1-21) must be used when water is in liquid phase. For saturated vapour ($P_{H_2O} = P_{sat}$), equation (1-21) and (1-22) yield the same result. Of course, in standard conditions, equation (1-21) gives the same result than (1-18). Independently of the temperature deviation from standard conditions, equation (1-21) and (1-22) express the open cell voltage corrected by the loss induced by a limited gas concentration:

$$E_{eq}(T, P_i) = E^0 - \frac{RT}{2F} \ln \left(\frac{a_{H_2O}}{a_{H_2} a_{O_2}^{\frac{1}{2}}} \right) \quad (1-23)$$

This expression of the OCV is known as the Nernst equation and it is a fundamental equation in electrochemistry.

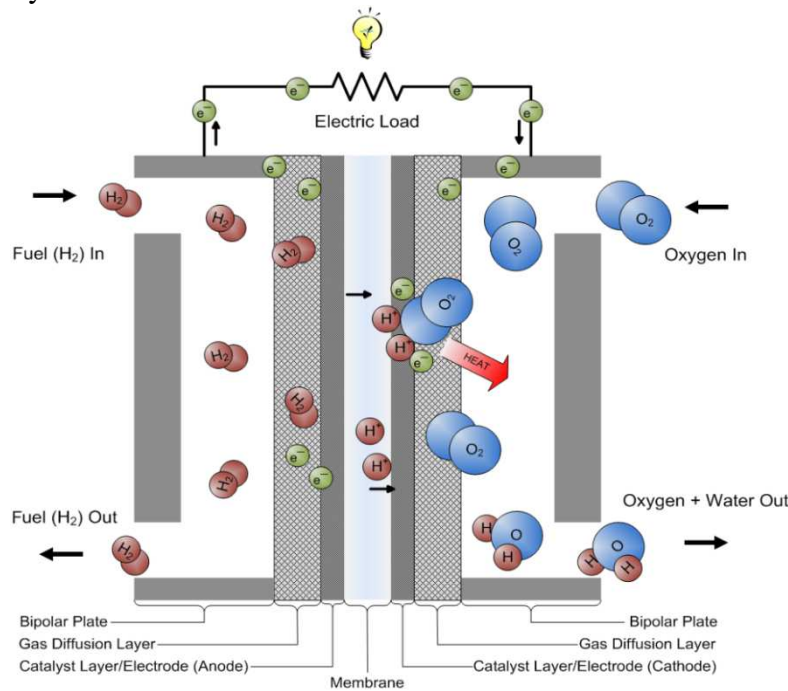


Figure 1-4. Detail of the operation inside a PEMFC.

1.2.2 Effective Fuel Cell Performances

In practice, the effective OCV is lower than $E_{eq}(T,P)$ due to gas permeation and platinum oxidation, which generates mixed potentials at both electrodes. For the sake of simplicity, $E(T,P)$ is assimilated to the effective OCV in the following. When the cell is in operation, several additional energy losses have to be deducted from the reversible cell voltage. They can be classified as follows:

- Activation losses: η_{act} ;
- Ohmic losses: η_{ohm} ;

The activation losses correspond to the energy needed to initiate the reactions and to overcome the activation barrier. They are specific to each half-reaction. For the HOR (1-1), the potential of the anode increases of $\eta_{act,A} \geq 0$ while for the ORR (1-2), the cathode potential decreases of $\eta_{act,C} \leq 0$. As the cell voltage is determined by the difference between the two electrodes potentials (1-17), the total activation loss is:

$$\eta_{act} = \eta_{act,A} - \eta_{act,C} \quad (1-24)$$

As the ORR activation barrier is high, a noble metal is commonly used as catalyst. The catalyst does not take part to the reaction but help the reactants to bind together and to form intermediate species. Platinum is usually chosen but its high price participates to the high cost of fuel cells. Significant research is conducted to reduce its utilization and even to replace it. Pt-based alloy or non Pt-based catalysts are currently under development (see §1.4.3 Main issues concerning the electrodes).

Activation losses are not only determined by reaction kinetic but also by mass transfer limitations, which result from two different phenomena:

- The right amounts of reactants are supplied to the cell but their diffusion to the reaction sites is impeded, which does not allow generating the required current density. Water for instance, if not removed, floods the cathode and limits the diffusion of air to the reaction sites. In standard conditions, the diffusion coefficient of oxygen in nitrogen ($D_{O_2 \rightarrow N_2} = 1.76 \cdot 10^{-1} \text{ cm}^2 / \text{ s}$) is about 8000 times higher than that of oxygen in liquid water ($D_{O_2 \rightarrow H_2O(liq)} = 2.1 \cdot 10^{-5} \text{ cm}^2 / \text{ s}$). Such situation is usually encountered at high current densities where a sudden drop of the fuel cell voltage can be observed. While often referred to concentration losses in the literature, mass transfer limitations are actually only one of the contributions to the activation losses.
- The reactants are not supplied in sufficient quantity regarding the required current density (substoichiometry). As the reactants are consumed along the gas channels, starvation phenomena can occur near the gas outlet. This problem can be encountered at every current density. To avoid it, more reactants than needed are usually sent to the cell. The stoichiometry is the ratio between the amount of reactant supplied and that needed to produce a given current density.

The transport of electrical charges from the anode to the cathode is at the origin of ohmic losses: electrons and protons are submitted to the resistance of the material they go through. This concerns more specifically protons flowing through the electrolyte membrane and to a lesser extent, the contact resistances between the different materials. These contact resistances

are mainly located at the membrane or GDL/catalyst layer interface. They are usually expressed by an ohmic law:

$$\eta_{ohm} = r \cdot j \quad (1-25)$$

where r stands for the materials and contact resistances. While these two contributions are difficult to distinguish, r is not a difficult parameter to measure thanks to the Electrochemical Impedance Spectroscopy (high frequency resistance, see §1.3.2). r results also from the proton resistance in the electrode. However, this contribution is assumed to be insignificant due to the good humidification of the ionomer in the electrode.

The actual cell voltage U corresponds to the open circuit voltage minus the overpotentials:

$$U = E_{eq} - \eta_{act} - \eta_{ohm} = \phi_c - \phi_a - \eta_{ohm} \quad (1-26)$$

Where ϕ_i represents the electrode potential that is to say the potential difference between metal and electrolyte (i standing for the anode or cathode):

$$\phi_i = E_{eq}^i + \eta_{act,i} \quad (1-27)$$

In practice, the difference between the metal potentials V_m of each electrode allows measuring the fuel cell voltage:

$$U = V_m^c - V_m^a \quad (1-28)$$

The fuel cell voltage is usually plotted versus the current density. The different types of losses described above appear on the polarization curve shown in Figure 1-5.

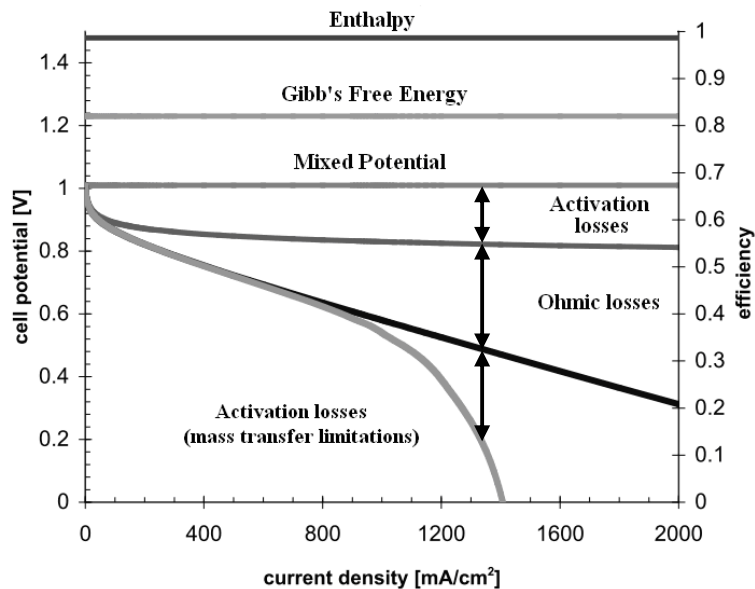


Figure 1-5. Polarization curve with the different overvoltages.

1.2.3 Reactions mechanisms

Kinetics are different for each half-reaction and the rate of charge exchange is governed by the slowest reaction.

a. Hydrogen Oxidation Reaction

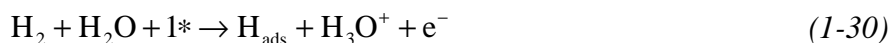
The HOR occurs in two steps [5]:

- The first step corresponds to H₂ adsorption on platinum: two different reactions are possible. The simplest one is the Tafel reaction (1-29) where the atoms of the hydrogen molecule are adsorbed simultaneously on catalyst sites. The other one is the Heyrovsky reaction (1-30) where the hydrogen molecule is split so that one hydrogen atom is adsorbed on a catalyst particle while the other reacts with water to form a hydronium ion.
- The adsorbed hydrogen atoms H_{ads} are then oxidized in a second step called the Volmer reaction (1-31).

Tafel reaction:



Heyrovsky reaction:



Volmer reaction:



The set of reactions (1-29) and (1-31) is known as the Tafel-Volmer mechanism while reactions (1-30) and (1-31) correspond to the Heyrovsky-Volmer mechanism. Several groups [5], [6], [7] report about the contribution of each of these mechanisms to the HOR and its inverse process, the Hydrogen Evolution Reaction (HER). The general trend emerging from these works is that the current is mainly produced through the Tafel-Volmer pathway at low overpotential and following the Heyrovsky-Volmer mechanism at high overpotential. The variation in coverage of free Pt sites seems to be at the origin of the transition between both because it leads to a modification of the bond strength between hydrogen and platinum particles. The platinum loading and the orientation of platinum faces play also a role in the hydrogen oxidation process. This is described with more details in §1.3.1. As most of the experiments were conducted on microelectrodes or rotating disc electrodes and with liquid electrolyte (H₂SO₄ solutions for example), the values encountered in the literature [5], [6], [7] cannot accurately describe the exact mechanisms taking place in the anode of a PEMFC, but they can be used as starting points for modelling [8], [9], [10], [11].

b. The Oxygen Reduction Reaction

Like the HOR, the Oxygen Reduction Reaction (ORR) is not a direct process. In addition, it can lead to the production of two species: water and hydrogen peroxide. The formation of water can either be achieved through a direct four electrons mechanism after the chemical adsorption of oxygen on platinum sites:



Or by a two electrons mechanism:



The formation of hydrogen peroxide is due to the desorption of the intermediate species $(\text{H}_2\text{O}_2)_{\text{ads}}$ during the two electrons transfer process of oxygen reduction to water. Antoine et al. [12] studied the oxygen reduction mechanisms on platinum and found that it is mainly a four electrons process. The production of hydrogen peroxide, even in negligible amount, has to be taken into account since it is involved in further reactions that tend to damage the ionomer (in the membrane or in the electrode).

The different pathways of oxygen reduction are summarized in Figure 1-6.

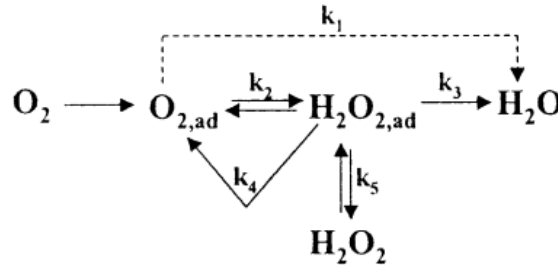


Figure 1-6: Oxygen reduction reaction mechanism on Pt [13].

The ORR was clearly identified as the rate determining step (RDS) among the whole reactions in PEMFC and this for two main reasons:

- The reaction itself is “slow” and requires high activation overpotentials of about 200mV-300mV in acidic media and on Pt surfaces. For comparison, the exchange current density $j_0^{\text{O}_2/\text{H}_2\text{O}}$ of oxygen reduction is of about $5 \cdot 10^{-3} \text{ A/m}^2$ while that of hydrogen oxidation is close to 100 A/m^2 .
- The oxygen effective diffusion coefficient in the GDL and in the active layer is limited, especially if air is employed instead of pure oxygen. Furthermore, as water is the main product of the ORR, high mass transport losses have to be expected if it is not removed efficiently from the reaction sites.

1.2.4 Reaction kinetics

Considering a single electrode, the general form of the electrochemical reactions involving an oxidant/reducer (Ox/Red) couple is:



The net faradic current is defined conventionally as the quantity of electrons produced by the oxidation reaction (the backward reaction in (1-34)) minus the quantity of electrons consumed by the reduction reaction (the forward reaction in (1-34)). In the equilibrium state, both reactions rates are identical and the faradic current density is zero:

$$j_{f,ref} = j_{ref}^{\text{Ox}} - j_{ref}^{\text{Red}} = 0 \quad (1-35)$$

That is to say:

$$j_{ref}^{Ox} = j_{ref}^{Red} = j_{ref} \quad (1-36)$$

Where j_{ref} is the exchange current density.

Producing a faradic current requires to activate the reaction, which has a cost in term of energy. This results in the apparition of an activation overpotential η_{act} (at low current density when ohmic losses can be neglected) defined by:

$$\eta_{act} = \phi - E_{ref} \quad (1-37)$$

With $E_{ref} = E_{eq}(Ox/Red) = E_{Ox/Red}$ the equilibrium potential of the redox reaction and ϕ the effective potential of the electrode. In the absence of mass transport limitation, the relation between faradic current and overpotential in a single electrode is given by a simplified form of the Butler-Volmer equation:

$$j_f = j_{ref} \left[\exp\left(\frac{\alpha_{Red} nF}{RT} \eta_{act}\right) - \exp\left(\frac{-\alpha_{Ox} nF}{RT} \eta_{act}\right) \right] \quad (1-38)$$

In equation (1-38), the first exponential concerns the oxidation process, predominating when the overpotential is positive, while the second concerns the reduction, predominating when the overpotential is negative. The charge transfer coefficient α characterises the reversibility of the reactions. If oxidation is favoured, it is at the expense of reduction and vice-versa. α ranges from 0 to 1. Often, $\alpha_{Ox} = (1 - \alpha_{Red})$ and if $\alpha_{Ox} = \alpha_{Red} = 0.5$, the reaction is perfectly symmetric. If $\alpha_{Ox} = 1$, the oxidation reaction only can take place and this whatever the overpotential.

For the reaction to occur, the electrode has to be supplied with enough reactant. In the Butler-Volmer equation, the reactions are considered as first-order reactions. In other words, the current density is proportional to the reactants concentration:

$$j_f = j_{ref} \left[\frac{c_{Red}}{c_{Red}^{ref}} \exp\left(\frac{\alpha_{Red} nF}{RT} \eta_{act}\right) - \frac{c_{Ox}}{c_{Ox}^{ref}} \exp\left(\frac{-\alpha_{Ox} nF}{RT} \eta_{act}\right) \right] \quad (1-39)$$

With c_{Ox} and c_{Red} the effective oxidant and reducer concentrations at the electrode. c_{Ox}^{ref} and c_{Red}^{ref} are the oxidant and reducer concentrations when the electrode potential is at equilibrium $E(c_{Ox}^{ref}, c_{Red}^{ref}) = E_{Ox/Red}$.

In standard conditions, the Butler-Volmer equation becomes:

$$j_f = j_0 \left[\frac{c_{Red}}{c_{Red}^0} \exp\left(\frac{\alpha_{Red} nF}{RT} \eta_{act}\right) - \frac{c_{Ox}}{c_{Ox}^0} \exp\left(\frac{-\alpha_{Ox} nF}{RT} \eta_{act}\right) \right] \quad (1-40)$$

With j_0 the exchange current density, c_{Ox}^0 and c_{Red}^0 the oxidant and reducer concentrations in standard conditions. In this case, $\eta_{act} = \phi - E_{Ox/Red}^0$.

At high values of $|\eta_{act}|$, one of the exponential can be neglected with respect to the other (the reduction of the proton H^+ in the anode and the oxidation of water in the cathode in a PEMFC). The Butler-volmer equations can thus be rewritten:

$$\text{In the anode: } j_{f,a} = j_0 \left[\frac{c_{H_2}}{c_{H_2}^0} \exp\left(\frac{\alpha_{H_2} nF}{RT} \eta_{act,a}\right) \right] \quad (1-41)$$

$$\text{In the cathode } j_{f,c} = -j_0 \left[\frac{c_{O_2}}{c_{O_2}^0} \exp\left(\frac{-\alpha_{O_2} nF}{RT} \eta_{act,c}\right) \right] \quad (1-42)$$

With $j_{f,a} = j_{f,c} = j_f$ since the two electrodes are connected.

Equations (1-41) and (1-42) can then be rewritten under the form:

$$\eta_{act,i} = a_i + b_i \cdot \ln(j_f) \quad (1-43)$$

Equation (1-43) is known as the Tafel law. a and b depend on the reaction kinetics through α and j_0 . b is called the Tafel slope.

For the hydrogen oxidation:

$$b_{H_2} = \frac{RT}{\alpha_{H_2} nF} \quad (1-44)$$

For the oxygen reduction:

$$b_{O_2} = \frac{RT}{\alpha_{O_2} nF} \quad (1-45)$$

And a is given by:

$$a_{H_2/O_2} = -b_{H_2/O_2} \cdot \ln\left(j_0 \frac{c_{H_2/O_2}}{c_{H_2/O_2}^0}\right) \quad (1-46)$$

a and b (or j_0 and α) can be determined either thanks to the polarization curve or using the Electrochemical Impedance Spectroscopy (EIS). However, due to the broad diversity of experimental conditions, their dispersion in the literature is important. Neyerlin et al. [14] lists some values of the exchange current density of the ORR. This parameter varies usually between 1.10^{-10} and 1.10^{-8} $A.cm_{Pt}^{-2}$. By comparison, the HOR exchange current density ranges from 0.235 to 0.600 $A.cm_{Pt}^{-2}$ [15]. The ORR is consequently the slowest reaction of both.

1.3. Diagnosis Tools

Fuel cells are submitted to different degradation processes. These degradations can be observed simply through the performance losses but different techniques also exist to help identify and quantify specific mechanisms. These techniques can be applied in-situ, in

complement to post mortem analysis. This allows monitoring the state of a cell, which can then be related with the evolution of the performances.

1.3.1 Cyclic Voltammetry and Active Surface

a. Principle

The evolution of the reaction active surface is a key indicator for the study of fuel cell durability. This parameter is indeed directly related to the electrode structure and more precisely to the presence of reaction sites. Its monitoring during aging protocols makes it possible to better understand how and why the electrode structure is modified with time.

The active surface depends, amongs other things, on the catalyst used. Two parameters, allow the characterisation of a catalyst:

- The strength of the bond between the catalyst atoms and the adsorbed species (the Gibbs energy of adsorption);
- The activity of the catalyst, i.e. its ability to adsorb and make react quickly a high quantity of species.

More generally, a good catalyst has a high activity and forms a weak bond with the hydrogen atom (a bond easy to break during the desorption process, which is energy consuming). The main reason for the choice of platinum is illustrated by the volcano curve which shows the activity of different catalysts in term of exchange current density vs. the strength of the bond with hydrogen (Figure 1-7). Platinum is one of the most active catalysts and the bond it forms with hydrogen is in the average.

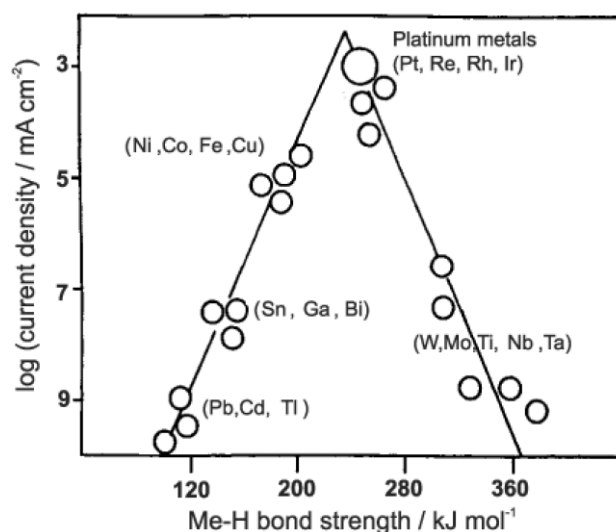


Figure 1-7. Volcano curve: activity of different catalysts vs. the bond strength with adsorbed hydrogen.

The active surface can be estimated thanks to cyclic voltammetry, which consists in applying a potential variation to one electrode (the working electrode) while recording the resulting currents. A counter electrode ensures the flow of the electrical charges (Figure 1-8). The metal potential of the working electrode V_m^w is controlled thanks to a reference electrode, which metal potential V_m^{ref} has to be stable. In the case of a PEMFC, the anode can be both the counter and the reference electrode since the hydrogen oxidation reactions occurring there

do not induce strong potential variations ($V_m^{ref} = V_m^a \approx E_{H^+/H_2}^0$ and $V_m^w = V_m^c$). Therefore, the potential of the cathode metal can be considered as equal to the cell voltage:

$$U = V_m^c - V_m^a \approx V_m^c \quad (1-47)$$

The active surface measurement has to be realised on a clean electrode, which means that no active gas should be injected in the cell during the voltammetry. This requirement is satisfied by flushing the working electrode with nitrogen. To avoid the physical desorption of the species needed for the active surface determination, the nitrogen flow is stopped during the potential variations of the working electrode [16].

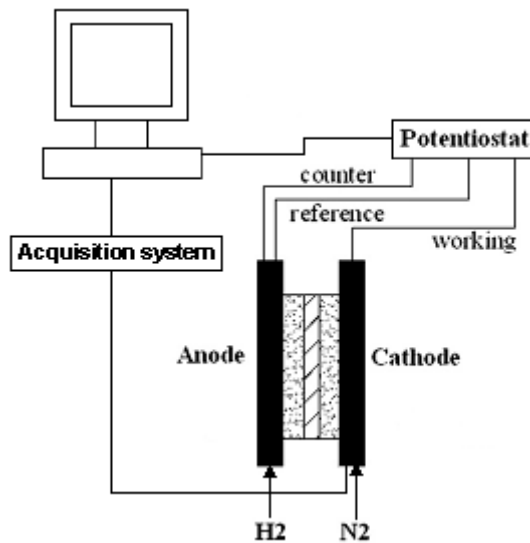


Figure 1-8. Experimental set-up for cyclic voltammetry tests.

The results obtained by this technique are usually represented in a voltammogram: a graph giving the current density vs. the metal potential of the working electrode (Figure 1-9).

b. Reaction Mechanisms

The working electrode being in contact with nitrogen, only species already present on the reaction sites or crossing the membrane can react: carbon, protons, hydrogen, water or platinum for example.

When the metal potential of the cathode V_m^c increases, the cathode potential ϕ_c exceeds several redox standard electrode potentials. Each time this happens, oxidation occurs and positive peaks of current appears in the neighbourhood of the corresponding standard potentials on the voltammogram. In a fuel cell electrode, hydrogen and platinum are the main species to react during a cyclic voltammetry: hydrogen at low potential and platinum at high potential. For hydrogen, the mechanism associated with the forward evolution of the potential is proton desorption. It is used to estimate the platinum active surface. Other species also react but their contribution is often very limited and therefore difficult to detect. For instance, carbon oxidation starts when the electrode potential exceeds 0.2V.

During the increasing metal electrode potential sweep, oxidants concentration increases in the cathode and the Nernst potentials are shifted to values higher than the standard electrode potentials. When the metal electrode potential decreases, it falls below the Nernst potentials:

the direction of the reactions changes and the reverse reactions, that is to say the reduction reactions, occur (above the standard potentials).

For instance and according to Figure 1-9, the Nernst potential E_{H^+/H_2} is shifted to about 0.4V during the forward metal electrode potential sweep. This value is obtained:

- By considering that the electrode potential can be approximated by the Nernst potential since activation overpotentials are low in the case of H^+/H_2 redox reactions (ohmic losses are also neglected since the currents involved are very low):

$$\phi_c = E_{H^+/H_2} - \eta_{act,c} \approx E_{H^+/H_2} \approx V_m^c$$

- By recording the electrode potential at which the production of current due to H^+ reduction begins.

Thus, when the electrode potential sweep decreases, reduction reactions start 0.4V higher than the H^+/H_2 standard electrode potential. For hydrogen, the backward evolution of the metal electrode potential leads to the adsorption of the protons previously desorbed. However, since the metal potential of the working electrode does not fall below the H^+/H_2 standard electrode potential (the minimum is 0.1V), the protons are not fully reduced but remain adsorbed on the platinum particles.

The increase of the reducers concentration during the decreasing metal potential sweep of the cathode induces a negative shift of the Nernst potentials. Thus, if a second potential scan is applied, oxidation reactions start when the metal electrode potential exceeds the Nernst potentials (and not necessarily as soon as the standard electrode potentials are reached).

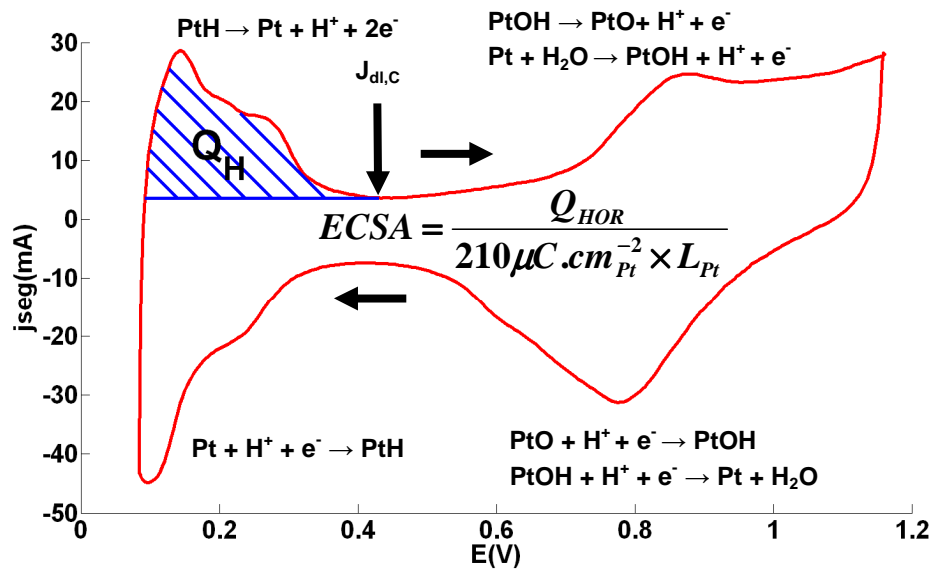


Figure 1-9. Voltammogram and estimation of the ECSA.

During protons adsorption/desorption, platinum intervenes as a catalyst. From a microscopic point of view, platinum is a crystal exhibiting a face-centered cubic (fcc) lattice (Figure 1-10).

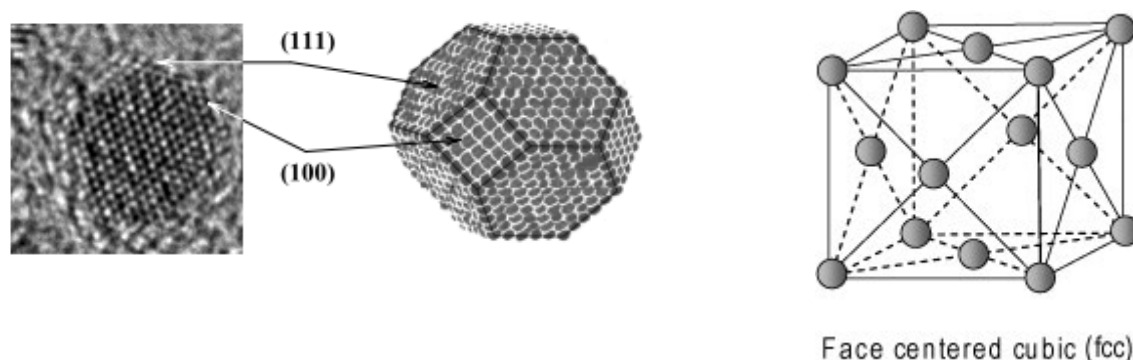


Figure 1-10. Left: High resolution TEM micrograph of a representative Pt particle and the proposed cubooctahedral shape (Middle) [13]. Right: face-centered cubic lattice.

The total active surface of platinum particles consists actually in a set of active surfaces, each being specific to a crystallographic plane. For instance, the hydrogen desorption domain in a voltammogram (between 0.1V and 0.5V during the forward potential sweep) can be deconvolved into three peaks, each one being associated with the active surface of a single plane. Several papers report about the different crystallographic planes of platinum implicated in the HOR [17], [18], [19] and point out that they are not equivalent in term of activity. Markovic et al. [18] classified them as follows: $\{111\}_{Pt} < \{100\}_{Pt} < \{110\}_{Pt}$ whereas according to Conway et al. [19]: $\{100\}_{Pt} < \{111\}_{Pt} < \{110\}_{Pt}$. This disagreement seems to originate from differences in the experimental procedures they used. Solla-Gullon et al. [20] have grown mono- and poly-oriented platinum particles. The mono-oriented particles developed were the $\{100\}_{Pt}$, the $\{111\}_{Pt}$ and the $\{110\}_{Pt}$ (**Figure 1-11**). By applying cyclic voltammetry to each of them, they could identify their respective contributions in the voltammogram of poly-oriented platinum particles (**Figure 1-12**).

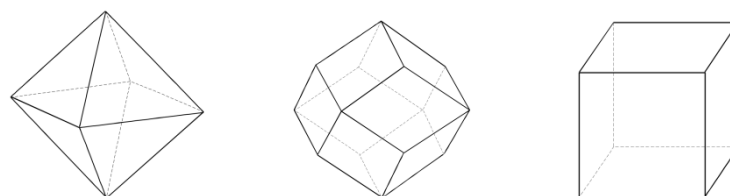


Figure 1-11. Mono-oriented platinum particle from left to right: $\{111\}_{Pt}$ (octahedral structure), $\{110\}_{Pt}$ (rhombic dodecahedral structure), $\{100\}_{Pt}$ (cubic structure).

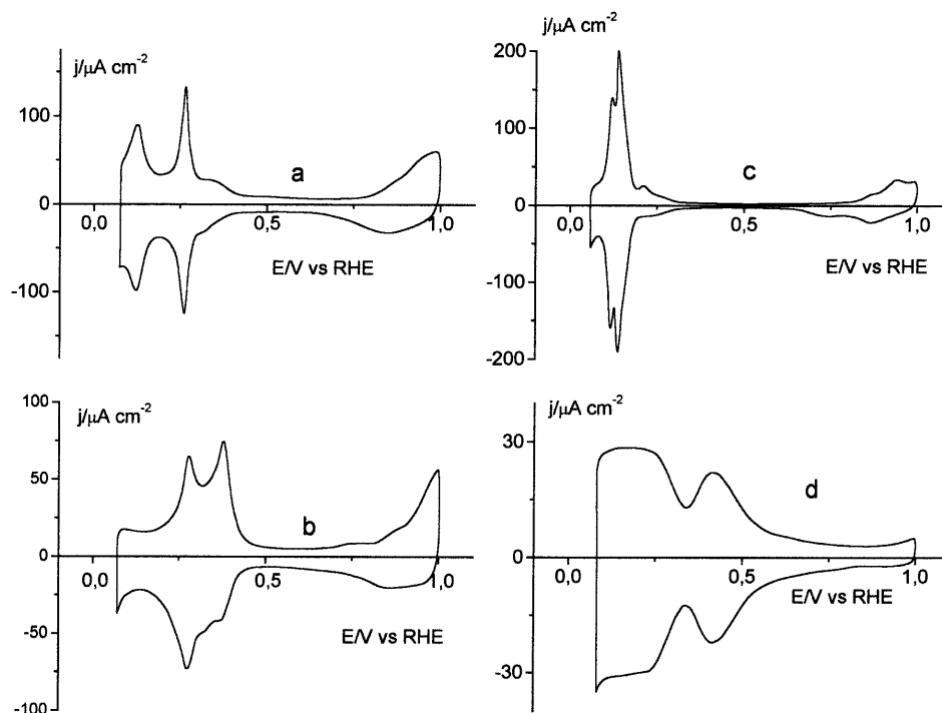


Figure 1-12. Voltammograms of (a) Planar polyoriented platinum; (b) $\{100\}_{Pt}$; (c) $\{110\}_{Pt}$ and (d) $\{111\}_{Pt}$ electrodes. Test solution: $0.5\text{ M H}_2\text{SO}_4$, sweep rate 50 mV/s [20].

According to their results, the first peak of a poly-oriented platinum particles is associated to the $\{110\}_{Pt}$ plane and the second one to the $\{100\}_{Pt}$ plane. The contribution of the $\{111\}_{Pt}$ plane is lower than that of two others but remains significant. However, its low activity over a large potential range makes it difficult to identify on the voltammogram of poly-oriented platinum. These results tend therefore to confirm those of Markovic et al: $\{111\}_{Pt} < \{100\}_{Pt} < \{110\}_{Pt}$.

In the literature ([7], [21]), references to the Under Potential Deposited Hydrogen (H_{UPD}) and to the Over Potential Deposited Hydrogen (H_{OPD}) are usually encountered. These species are adsorbed or desorbed at potentials respectively higher and lower than the standard electrode potential $E^0_{H^+/H_2}$. H_{UPD} is the only species involved in cyclic voltammetry. The distinction has to be made between H_{UPD} and H_{OPD} since they take place at different potential and have distinct Gibbs energies of adsorption. This is due to the fact that they adsorb on different reaction sites in a same plane: the H_{UPD} occupy the three or four-fold hollow sites on the $\{111\}_{Pt}$ and the $\{100\}_{Pt}$ faces respectively while the H_{OPD} is adsorbed on the top sites of platinum atoms (Figure 1-13).

Although HOR and ORR are reactions with very different mechanisms, Markovic et al. [22] showed that the platinum planes involved in the hydrogen oxidation are also those participating in the Oxygen reduction. Thus, it is generally considered that the platinum active surface is the same for both reactions.

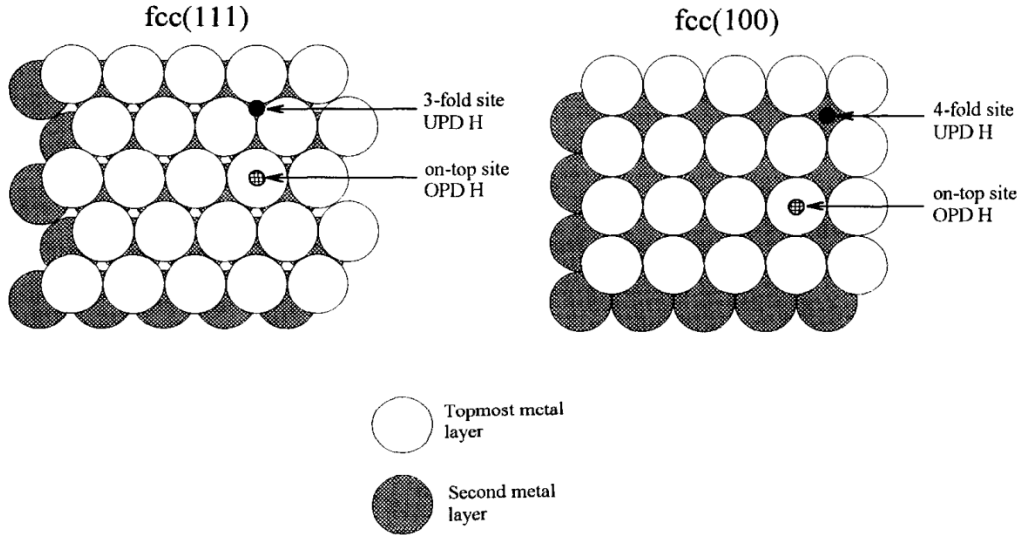


Figure 1-13. Reaction sites on different crystallographic planes. UPD H refers to the Under Potential Deposition of Hydrogen and OPD H to the Over Potential Deposition of Hydrogen [17].

c. Remark

In the following, we consider that the number of atoms adsorbed and desorbed are identical during a voltammetry. This means that the reactions are considered as reversible. The following equation should therefore always be fulfilled:

$$\int_{V_m^c(\min)}^{V_m^c(\max)} j_c dV_m^c + \int_{V_m^c(\max)}^{V_m^c(\min)} j_c dV_m^c = 0 \quad (1-48)$$

And as the metal potential sweep rate is constant:

$$v = \frac{dV_m^c}{dt} = \pm 50.10^{-3} V / s \quad (1-49)$$

The equation (1-48) can be rewritten:

$$\int_0^{\frac{V_m^c(\max)-V_m^c(\min)}{v}} j_c v dt + \int_{\frac{V_m^c(\max)-V_m^c(\min)}{v}}^0 j_c v dt = 0 \quad (1-50)$$

On the voltammograms, the oxidized charge has therefore to be equal to the reduced charge. In practice however, the oxidized charge is slightly higher than the reduced charge: this is due to hydrogen permeation through the membrane from the anode to the cathode during both the forward and backward evolution of the metal cathode potential:

$$\int_0^{\frac{V_m^c(\max)-V_m^c(\min)}{v}} j_c v dt + \int_{\frac{V_m^c(\max)-V_m^c(\min)}{v}}^0 j_c v dt = Q_{perm}^{H_2} > 0 \quad (1-51)$$

This permeation leads to a positive shift of the voltammogram due to the oxidation of hydrogen. The positive shift is assumed to be constant over the whole cathode potential range (Figure 1-14) and it is identified as hydrogen permeation current:

$$j_{perm}^{H_2} = \frac{vQ_{perm}^{H_2}}{2(V_m^c(\max) - V_m^c(\min))} \quad (1-52)$$

Permeation, even if it does not represent the main information extracted from the voltammogram, is an indication of the state of the membrane. A correction is applied on the voltammogram, as shown in Figure 1-14, to avoid the bias resulting from hydrogen permeation.

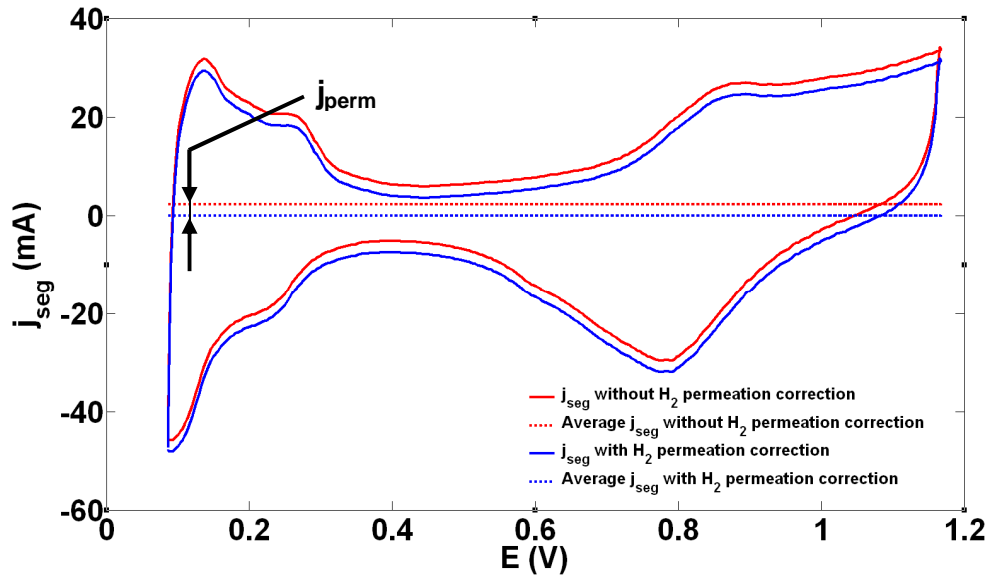


Figure 1-14. Voltammogram before and after correction accounting for the hydrogen permeation current.

d. Platinum Active Surface

The platinum surface participating to the reactions is called Electrochemical Surface Area (ECSA). Two steps are necessary for the ECSA estimation:

- First the capacitive current contribution has to be subtracted from the global current. The electrode of a fuel cell is indeed the place of charges separation (protons and electrons). The capacitive current is usually the result of a potential difference between carbon or platinum and the ionomer. Thus, the total current through the cathode is the sum of a faradic and a capacitive contribution:

$$j_c = j_{f,c} + j_{dl,c} \quad (1-53)$$

Where $j_{dl,c}$ is the capacitive contribution, function of the double layer capacity of the cathode and of the potential variation:

$$j_{dl,c}(t) = C_{dl,c} \frac{dE_c(t)}{dt} = j_{dl,c} \quad (1-54)$$

With $E_c(t)$ the potential difference applied to the cathode double layer capacity $C_{dl,c}$. During cyclic voltammetry, the potential sweep rate being constant (equation (1-49)), the capacitive contribution to the global current is also constant (assuming that the double layer capacity does not depend on the potential).

$$j_{dl,c}(t) = vC_{dl,c} = j_{dl,c} \quad (1-55)$$

The capacitive current is thus given by the lowest value of the current density recorded during the cycle, assuming that no faradic reactions occur. This lowest value is reached in the transitional region between hydrogen and platinum reactions, that is to say between 0.4V and 0.6V.

- The hydrogen desorption peak is used to estimate the ECSA once the capacitive contribution was deducted from the global current as shown by equation (1-56). The faradic current is then integrated over time which allows deducing the charge released during hydrogen oxidation (1-57).

$$j_{f,HOR} = j_{0.1V \rightarrow 0.5V} - j_{dl,c} \quad (1-56)$$

$$Q_{HOR} = \int j_{f,HOR} \cdot dt \quad (1-57)$$

Knowing the number of charges that can react on platinum surface ($210 \mu C \cdot cm_{Pt}^{-2}$ [23]), it is possible to deduce the electrode active surface area (Figure 1-9):

$$ECSA = \frac{Q_{HOR}}{210 \mu C \cdot cm_{Pt}^{-2} \times L_{Pt}} \quad (1-58)$$

where L_{Pt} is the platinum load, expressed usually in $mg \cdot cm^{-2}$. The ECSA is expressed in platinum surface per masse (m^2_{Pt}/g_{Pt}). The higher the ECSA, the higher the current the electrode can provide. Smaller particles tend to have higher ECSA because of their better surface per volume ratio [24] (Figure 1-15).

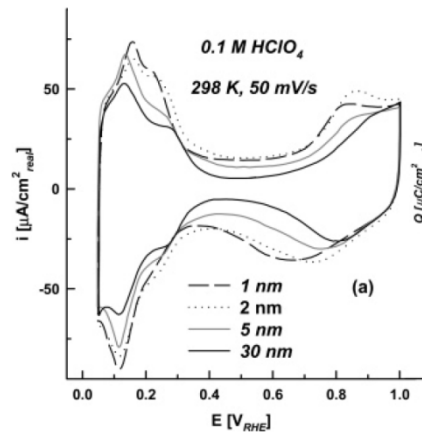


Figure 1-15. Voltammograms corresponding to different platinum particles sizes recorded in perchloric acid at room temperature. Potential sweep rate: 50 mV/s [24].

e. Limitations of cyclic voltammetry

While cyclic voltammetry allows estimating two interesting parameters for the study of degradations in a fuel cell (ECSA and hydrogen permeation), it presents some limitations:

- The platinum active surface estimated by cyclic voltammetry corresponds in practice to the sum of the active surfaces of each plane of the poly-oriented platinum crystals. However, ECSA does not provide information about the evolution of each of these local surfaces.
- The determination of the capacitive current is arguable. It can be easily observed experimentally that its value varies depending on the direction of the potential sweep of the working electrode: $|j_{dl,c (0.1V \rightarrow 1.2V)}| < |j_{dl,c (1.2V \rightarrow 0.1V)}|$. The hypothesis of a constant double layer capacity seems therefore to be strong. In addition, all the reactions occurring during a cyclic voltammetry are not reversible like carbon oxidation or water hydrolysis. Therefore, the correction applied to avoid the bias created by hydrogen permeation (which consists in centering the voltammogram to obtain as many reduction than oxidation reactions) is not very accurate. Usually, the capacitive current is estimated by averaging the forward and backward currents in the potential domain where no faradic reactions should occur.
- The number of charges reacting on a platinum surface unit is also questionable. In the literature, it is assumed to be $210 \mu\text{C}/\text{cm}^2$. However, the origin of this number is difficult to find. Its utilization in the equation (1-58) is only valid if one monolayer reacts on the platinum surface (no reactions in the platinum particle volume). This last condition is fulfilled if the potential sweep rate is high enough. Nevertheless, it has not to be too high so that the reactions with slow kinetics can be observed and so that the different implicated species have time to diffuse to the reaction sites. Compliance with this last condition implies that more than one monolayer reacts on the platinum.
- Cyclic voltammetry accounts also for platinum particles which cannot be accessed by oxygen during normal fuel cell operation. Therefore, ECSA estimated by this technique may overestimate the effective active platinum surface.
- The ECSA is sensitive to parameters such as temperature or hygrometry [25]. To ensure a rigorous monitoring of the catalyst evolution, the conditions in which cyclic voltammetry is implemented have to be kept constant.

For all these reasons, the values of platinum ECSA obtained with cyclic voltammetry remain qualitative data and must be interpreted with care.

On top of that, as a diagnostic tool of fuel cell degradations, cyclic voltammetry should not be intrusive. However, there are evidences of the contrary:

- Cyclic voltammetry requires shutting-down the cell by flushing the cathode compartment with nitrogen. Considering the results obtained in chapter 3, this procedure is likely to induce degradations and therefore to interfere with the degradation mechanisms which are investigated.
- Some of the reactions involved during CV are not reversible: the reduction of the oxidized platinum for instance may not be always complete. Platinum can also dissolve and migrate to redeposit in the membrane. In addition, carbon oxidation is known to occur [26]. While the currents associated with these reactions should be very low, CV cannot be considered as fully non intrusive. A more detailed study of the impact of CV on the electrode is presented in chapter 3.

The use of cyclic voltammetry must remain limited when one wishes to neglect the degradations it induces compared to those resulting from regular fuel cell operations.

1.3.2 Electrochemical Impedance Spectroscopy

a. Principle

The behaviour of a fuel cell can be described at different scales. Electrochemical reactions, protons and electrons separation and transport, reactant species diffusion, all of these phenomena can be described at a microscopic scale. However for a macroscopic understanding of fuel cell operations, it is necessary to integrate these microscopic mechanisms in a broader model which takes the dimension of each of the MEA components into account as well as the presence of interfaces between them.

The most common PEMFC impedance model is the Randles equivalent circuit, which accounts only for one electrode (the cathode) and the membrane:

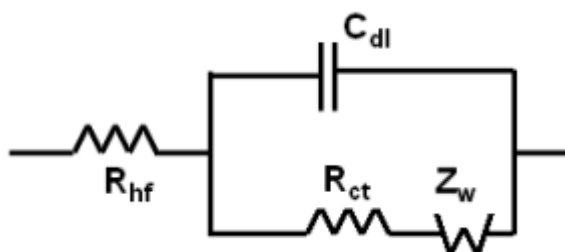


Figure 1-16. Randles equivalent circuit.

In this equivalent circuit, four different components appear:

- R_{hf} stands for the high frequency resistance, which results from the protonic resistance of the membrane (and electrodes) and contact resistances between the MEA components;
- C_{dl} is the double layer capacity associated with charges separation in the electrode: protons in the ionomer and electrons in carbon or platinum;
- R_{ct} corresponds to the charge transfer resistance. It characterizes the efficiency of the electrochemical reaction and its value can therefore be estimated from the Butler-Volmer law;
- Z_w is the finite Warburg impedance. This impedance represents the contribution of oxygen transport to the voltage losses.

These impedances depend on the properties of the different components in the cell and their monitoring during aging protocols can bring complementary information to those provided by the platinum ECSA and fuel cell voltage.

b. Experimental implementation

Electrochemical Impedance Spectroscopy (EIS) consists in analyzing the response of a cell to a perturbation controlled in amplitude and frequency. If the perturbation is applied to the current, then the potential response is measured and vice-versa. In this work, EIS is carried out in galvanostatic mode, which means that the controlled variable is the current while the

response corresponds to the voltage oscillation. The opposite case is the potentiostatic mode. The sinusoidal perturbation $\Delta I(t)$ adds to a DC signal $\langle I(t) \rangle$:

$$\Delta I(t) = I(t) - \langle I(t) \rangle = \Delta \bar{I} e^{i\omega t} \quad (1-59)$$

With ω the angular velocity ($\omega = 2\pi\nu$). i is the imaginary unit defined by $i^2 = -1$.

To keep the analyze of the response as simple as possible, the amplitude of the perturbation is chosen as small as possible. In this case, it can be considered that there exists a linear relationship between current and voltage (although Butler-Volmer law depicts a non linear relation between them, Figure 1-17).

Assuming that the system is linear, the voltage response $\Delta U(t)$ is necessary under the form:

$$\Delta U(t) = U(t) - \langle U(t) \rangle = \Delta \bar{U} e^{i(\omega t + \varphi)} \quad (1-60)$$

where φ represents the phase angle between current and voltage.

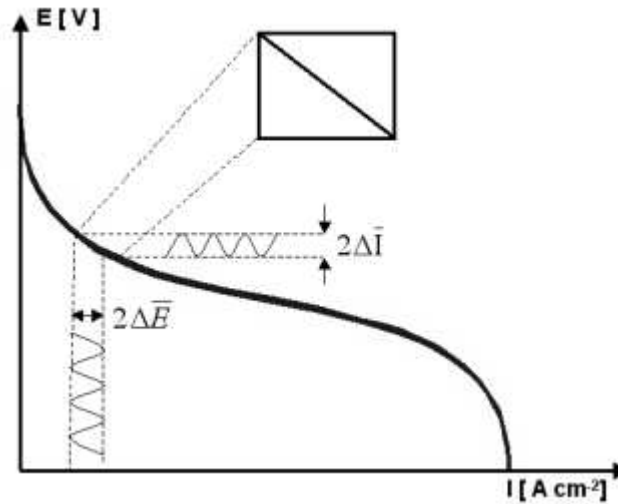


Figure 1-17. Polarization curve with a magnification on the application domain of the EIS. The amplitude of the signal is chosen small so that voltage and current are linear.

In these conditions, the ratio between the voltage and the current perturbation defines the impedance, which is constant in time but which depends on the applied frequency:

$$Z = \frac{\Delta U(t)}{\Delta I(t)} = \frac{\Delta \bar{U} e^{i(\omega t + \varphi)}}{\Delta \bar{I} e^{i(\omega t)}} = \bar{Z} e^{i\varphi} \quad (1-61)$$

As for the cyclic voltammetry, the perturbation (the current amplitude) has to be chosen with care:

- Low enough to remain in the linear domain;
- High enough to obtain a signal to noise ratio as high as possible.

An Amplitude of 5% to 10% of the nominal current corresponds to a good compromise between these two criteria.

The frequency range depends on the phenomena to observe. Since these phenomena have completely different kinetics in a fuel cell, the frequency range is therefore broad. The low frequencies are suitable for the characterisation of slow mechanisms, especially these implicating mass transports like oxygen diffusion to the reaction sites at the cathode for

instance. The high frequencies allow studying faster mechanisms such as the charge or discharge of the double layer capacities. Frequencies range usually from 5 mHz to 10 kHz (for fuel cells).

c. Theoretical approach

The potential response to a current variation can be expressed as a function of the components constituting the equivalent electrical circuit. In a first time, the response of each of the components can be described separately. For instance, the high frequency resistance involves no phase angle between the current and the voltage and thus no imaginary part:

$$Z_R = \frac{\Delta \bar{U} e^{i\omega t}}{\Delta \bar{I} e^{i\omega t}} = R_{hf} \quad (1-62)$$

On the contrary, the impedance of a capacitance is purely imaginative and according to equation (1-54), for a sinusoidal voltage perturbation $\Delta U(t) = \Delta \bar{U} e^{i\omega t}$:

$$\Delta I(t) = i\omega C_{dl} \Delta \bar{U} e^{i\omega t} = \omega C_{dl} \Delta \bar{U} e^{i(\omega t + \frac{\pi}{2})} \quad (1-63)$$

Therefore:

$$Z_C = \frac{\Delta \bar{U} e^{i\omega t}}{i\omega C_{dl} \Delta \bar{I} e^{i\omega t}} = \frac{1}{i\omega C_{dl}} \quad (1-64)$$

At high frequency, the impedance of a capacitance tends to 0.

In the following, the finite Warburg impedance is not taken into account. The main reason for this is that we did not perform EIS measurements at a working point where diffusion problem should occur (0.5A/cm²). In addition, the finite Warburg element does not describe accurately the diffusion losses in a cell since it does not consider [27]:

- Oxygen consumption along the channel.
- Oscillations of oxygen concentration due to the implementation of EIS in the channel [28].
- The diversity of materials through which gases flow (a unique and homogeneous material is considered).
- Convection of the gases perpendicular to the electrodes (only diffusion is taken into account).
- The voluminal character of the electrode which is considered as a plan.

By neglecting oxygen diffusion, the expression of the charge transfer resistance can be extracted from the Butler-Volmer law as presented in equation (1-38) where no concentration loss occurs. The faradic impedance R_{ct} characterizes the response of the overpotential to a faradic current variation:

$$R_{ct} = \frac{\Delta \eta_{act}(t)}{\Delta j_f(t)} \quad (1-65)$$

With equation (1-40) (without mass transport losses), the faradic impedance becomes:

$$R_{ct}^{-1} = j_0 \frac{nF}{RT} \left[\alpha_{Red} \exp\left(\frac{\alpha_{Red} nF}{RT} \eta_{act}\right) + \alpha_{Ox} \exp\left(\frac{-\alpha_{Ox} nF}{RT} \eta_{act}\right) \right] \quad (1-66)$$

and at low overvoltage, the equation (1-66) can be simplified:

$$R_{ct} = \frac{RT}{j_0 nF} \quad (1-67)$$

At high overpotential, the equation (1-66) becomes:

$$R_{ct} = \frac{b}{j_f} \quad (1-68)$$

And according to the Randles model, in the absence of diffusion limitation, the global impedance is:

$$Z(\omega) = R_{hf} + \frac{1}{\frac{1}{R_{ct}} + i\omega C_{dl}} \quad (1-69)$$

In practice, both the current and the fuel cell voltage are recorded during an EIS. The voltage to current ratio gives the experimental impedance as a function of the frequencies applied. The objective is then to estimate the different parameters in equation (1-69) by an inverse method starting from the experimental data and using the method of least squares. A usual way to visualize this resolution is obtained with the Nyquist plot which represents the imaginary part vs the real part of the impedance (Figure 1-18).

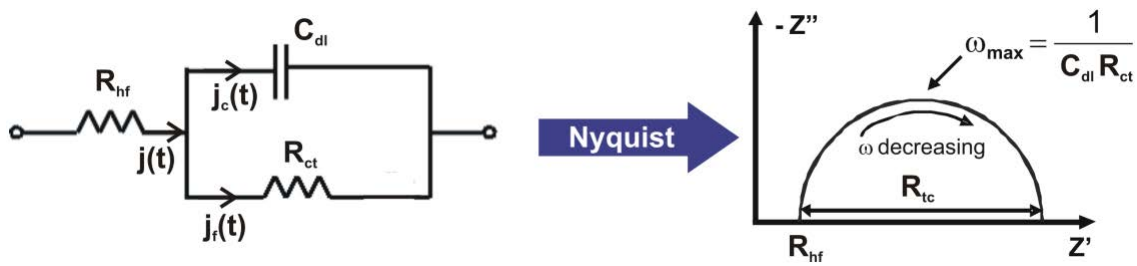


Figure 1-18. Simple electrical equivalent circuit of a cell (left) and its representation with a Nyquist plot (right).

d. Limitations of EIS

EIS is easier to implement than cyclic voltammetry because it can be realized during the normal fuel cell operation (without any gas change). Moreover, it is not an intrusive technique and it requires only a load controller able to induce the current/voltage oscillations. However, this tool is not without disadvantages. From an experimental point of view, an impedance spectrum is sensitive to many parameters, which have therefore to be kept constant.

For instance, the current density should be kept constant for an accurate estimation of the charge transfer resistance. However, it can be highly heterogeneous:

- Between the different segments due to a non uniform aging;
- Over time for a given segment.

An illustration of this phenomenon is given in Figure 1-19. The presented spectra were obtained during an aging test where a segmented cell was submitted to repetitive start-ups by injection of hydrogen in air in the anode at 2 slph (shut-down are realised by injecting air in hydrogen at 20 slph in the anode). While spectra can be initially easily fitted, those obtained at the end of the aging and especially the ones close to the segment 20 are too much distorted to be simulated. Moreover, local current densities are as higher close to the hydrogen inlet (segment 1), which impedes any charge transfer resistances comparison.

Consequently, the parameters estimated from EIS have to be considered with care and rather from a qualitative point of view. They can be used only to complete or confirm the observations made using other means (coulometry, cyclic voltammetry, post-mortem analysis).

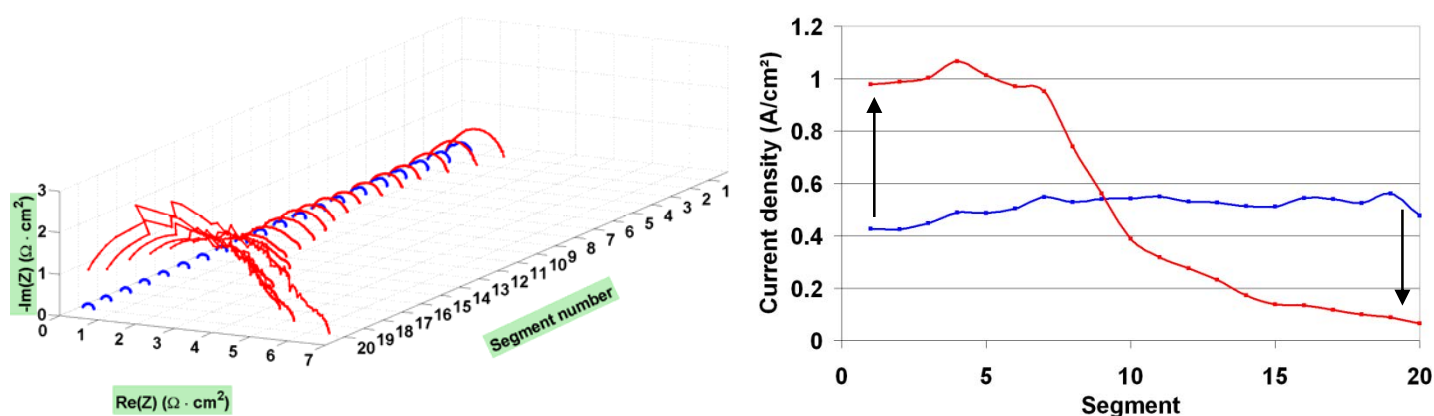


Figure 1-19. Left: Impedance spectra of the 20 segments of a segmented cell before (blue) and after 272 start-ups (red) performed by injecting hydrogen in air at 2 slph in the anode (shut-down realised by injecting air in hydrogen at 20 slph in the anode). Right: Local current densities of the 20 segments when 0.5A/cm² are required before (blue) and after 272 start-ups (red).

1.4. MEA main degradation mechanisms

Since fuel cells achieved the required performances (about 650 W/litre [29]), the attention of a significant part of the scientist community was transferred to durability issues. The American Department of Energy (DOE) set the 2015 lifetime targets to 5000 and 40 000 hours for automotive and stationary applications [1], [30]. While these values can be approached, strong damages can also appear quickly in some conditions that can be encountered frequently, reducing considerably the fuel cell lifetime: start-up/shut-down, OCV hold, fuel starvation, humidity cycling for instance. Several papers report about the mechanisms leading to the cell failure. They also provide a general overview of the main directions of research [31], [32], [33], [34], [35].

Several degradation mechanisms have been identified. Although, they can be classified in two groups: chemical or electrochemical and mechanical degradations, it must be kept in mind that mechanical failures can also be caused by chemical degradations.

Another way to classify the degradations consists in considering their location in the cell: flow field plate, electrode, and membrane for instance. Indeed, specific degradations take place in each component. Usually, the mechanisms they originate from appear at the same location. However, some are initiated in a different component than that where the degradation occur. The description done in this section respects the classification by component but it also mentions the origins of the degradations.

1.4.1 Flow field plates

Flow field plates collect electrical current, supply or evacuate reactions species and eventually, ensure the control of the cell temperature. Plate materials have therefore to be well adapted to these roles, which means that they have to present good thermal and electrical conductivities and good corrosion resistance. The main flow field plate materials are [36], [37]:

- Graphite, which satisfies well enough most of the requirements. More particularly, it appears to be stable under working conditions which are quite aggressive in term of oxidation capability. However, because of its brittleness, graphite is uneasy to machine and it must be thick to enable sufficient mechanical resistance. Therefore graphite flow field plates are expensive and heavy.
- Metals or alloys (titanium, stainless steel) are cheaper because they are easier to machine and can be made thinner. Ideally, flow field plate made of metal can be embossed and produced in high amounts. For this reason, metals are often preferred to graphite. While they often offer a higher thermal and electrical conductivity, they however present a much lower resistance to oxidation than graphite [37]. Oxidation is stronger on the cathode side due to the simultaneous presence of water, air and high potential. Two distinct mechanisms can then occur. The first one is the electrochemical oxidation (dissolution) of the metal giving cations [38] released from the surface. Then, they can migrate through the membrane and cause irreversible damages (see §1.4.4). The other mechanism consists in a passivation of the metal due to the adsorption of oxygen on its surface [39] with a subsequent increase of the electrical contact resistance [40]. To avoid such inconvenient, a solution consists in coating the plate with a protective layer (alloys such as Ni-Co-B for example [41]). The role of this layer is to maintain and even to improve the contact resistance between the flow field plate and the GDL. Good electrical and thermal conductivities are therefore required as well as mechanical and electrochemical stability to adhere to the plate. In addition, the thermal expansion coefficient of the protective layer has to be chosen close to that of the plate to avoid the formation of micro pores or cracks. Materials able to fulfil all these requirements are difficult to meet.
- Graphite composites such as polymer/graphite [42] are alternatives to graphite and metals. They present interesting characteristics: contrary to graphite, plates in graphite composites can be moulded, which enable to reduce the fabrication costs. The addition of polymer allows obtaining a plate which is also less brittle than pure graphite. The main difficulty consists in finding the best combination of polymer and graphite to attain acceptable mechanical resistance without sacrificing too much of the electrical conductivity.

1.4.2 Gas Diffusion Layers and MPLs

Gas Diffusion Layers are porous media constituted by carbon fibres made hydrophobic with a fluoropolymer coating (typically PolyTetraFluoroEthylene or PTFE is used). Their roles are:

- To distribute homogeneously the reactants coming from the flow field plates to the active layers;
- To evacuate water from the electrodes;
- To ensure electronic conductivity between the electrodes and the flow field plates.

No electrochemical reaction takes place in the GDL. However, at the GDL/cathode catalyst layer interface, electrochemical reactions involving carbon from the GDL (in contact with the electrolyte) and water can lead to carbon monoxide and dioxide emissions [43]. The oxidation of the GDL can result from chemical attacks, especially from hydrogen peroxide, according to the following mechanism:



This degradation process requires both the production of hydrogen peroxide and its diffusion through the GDL. These two requirements being a priori difficult to satisfy, the amount of H_2O_2 involved in chemical attacks of the GDLs should remain relatively limited.

Another degradation is the PTFE decomposition. However, further investigations are needed to explain this phenomenon and assess its impact on fuel cell operation and efficiency [44].

The consequence of carbon oxidation and PTFE decomposition is the loss of GDL hydrophobicity and therefore a modification of liquid water transport properties with time [45]: the electrodes become more prone to flooding since water is more difficult to evacuate.

Most of the time, a Micro Porous Layer (MPL) is added to the GDL. Consisting of a carbon black and PTFE mixture, its role is to avoid the possible backflow of liquid water condensing in the GDL toward the catalyst layer and to improve the electrical conductivity between these two components. The first function is ensured by the coated fluoropolymer (PTFE) and the small size of the MPL pores, which makes the MPL highly hydrophobic. The micrometer size of the MPL pores is also responsible for the better electrical contact between the GDL and the catalyst layer. However, this property worsens carbon oxidation. The currents involved are nevertheless very small and require a high potential to appear (less than $1 \cdot 10^{-6}$ A/cm² at 1.0V vs SHE [43]).

Compared to the membrane and catalyst layers, the degradations underwent by GDLs and MPLs remain most of the time limited. However, their association with other aging phenomena may participate to the cell failure. Moreover, GDLs and MPLs lifetime issues could become more significant with the improvement of the durability of catalyst layers and membrane.

1.4.3 Electrodes

Electrodes are complex environments where a lot of different species and materials interact and where multiple phenomena take place at the same time. The understanding of their degradation mechanisms can therefore be difficult, all the more so since they may be correlated. Some of them are presented hereafter but they may not be exhaustive.

a. Carbon support oxidation

Complete oxidation

In the electrodes, carbon is responsible for both conduction of the electrons and mechanical support of the catalyst. The standard electrode potential of the carbon/carbon dioxide couple (1-72) is equal to 0.2V vs RHE, a value which is always exceeded at the cathode in regular steady state operation.



However, the kinetic of this reaction being low, carbon oxidation is negligible. In the literature, a wide range of values for carbon oxidation exchange current density can be found: 2.5×10^{-9} A/cm² for Meyers et al. [46], 1.5×10^{-15} A/cm² for Takeuchi et al. [47] or 6.06×10^{-19} A/cm² for Kulikovsky [48] for instance. Despite these low exchange current densities, in certain transient conditions such as start/stop or potential cycles, the electrochemical oxidation of carbon can take place due to the high potentials reached. For example, Maass et al. [49] detected carbon dioxide in the exhaust gases of a 50% Pt/C electrode from Tanaka undergoing a cyclic voltammetry between 0.1V and 1.2V vs RHE with a potential sweep rate of 2 mV/s. They observed that the oxidation rate of carbon increased with the electrode potential (Figure 1-20). They also demonstrated that CO₂ emissions were higher when the cell temperature increased and when more water was present in the electrode, which is consistent with equation (1-72).

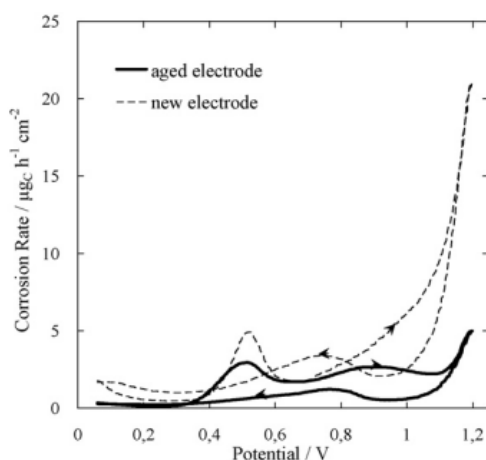


Figure 1-20. Carbon corrosion rate measured by Non-Dispersive InfraRed spectroscopy (NDIR) during a cyclic voltammetry realised on a Pt/C electrode [49] (potential sweep rate = 2mV/s).

The structure of carbon seems also to play a determining role in its oxidation process. Antonucci et al. [50] show for instance that the more carbon is graphitized, the more it is stable. The graphitization of carbon is usually obtained by applying a heat treatment, which can be expensive.

Partial oxidation

During the manufacturing process, the carbon of the electrode can chemically bind with oxygen and hydrogen atoms to form different oxygen surface groups (carboxylic, quinonic or phenolic groups) [51], [52] (Figure 1-21). These groups are known to influence the oxidation of the carbon support. Giordano et al. [53] noted for example that the carbon oxidation rate increased with the oxygen surface groups concentration (results obtained during potentiostatic corrosion tests in H_3PO_4 at 170°C). They also observed that oxidation was higher when the surface carbon area was lower, indicating that carbon with low surface area has a higher oxygen/carbon ratio. However, the role of oxygen surface groups in carbon oxidation is not well understood. According to Giordano et al., these groups act either as intermediate species or, once formed in a sufficient amount, they can protect the carbon from further oxidation acting like a passive layer. This last assumption is motivated by the fact that oxidation decreases with time during the corrosion tests. In this case and contrary to full carbon oxidation (1-72), reverse reactions can occur.

Logically, oxidation or reduction of these groups should intervene during the transient operation of the cell, like start-up or shut-down sequences for instance. It is shown in chapter 2, that an important fraction of the internal currents produced during a start-up is linked to reversible phenomena. The attribution of at least a fraction of these reversible currents to the formation of oxygen groups on the carbon surface is therefore a possibility to consider.

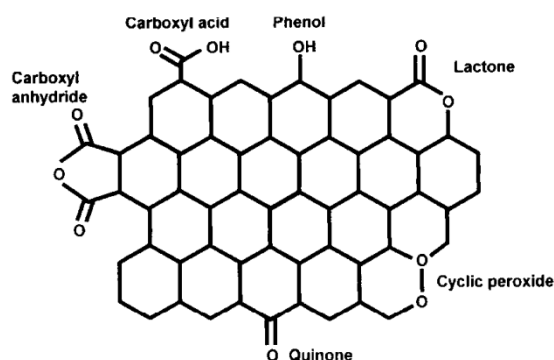


Figure 1-21. Example of oxygen groups formed on carbon [52].

b. Catalyst poisoning

Electrodes contain platinum particles that catalyse the electrochemical reactions. The catalysts are chosen for their ability to adsorb species which then react and are finally desorbed. As the fuel or the oxidant may contain impurities, there is a risk that these impurities are also adsorbed on platinum. In this case, they occupy a reaction site, which becomes inactive. Impurities or pollutants exhibit most of the time a lower activity and a stronger bond with platinum than usual reactants. That is the reason why their presence leads to a reduction of the reaction rate and an increase of the activation overpotentials.

One of the most frequent origin of catalyst poisoning results from the presence of carbon monoxide in hydrogen. This could be the consequence of steam reforming of natural gas (or other fossil fuels) which leads to the formation of a H_2 -CO mixture. Without thorough purification, traces of this contaminant can be found in hydrogen. The resulting decrease of the performance of the cell is correlated to the CO concentration [54] but also to the time during which the anode is exposed [55] (Figure 1-22).

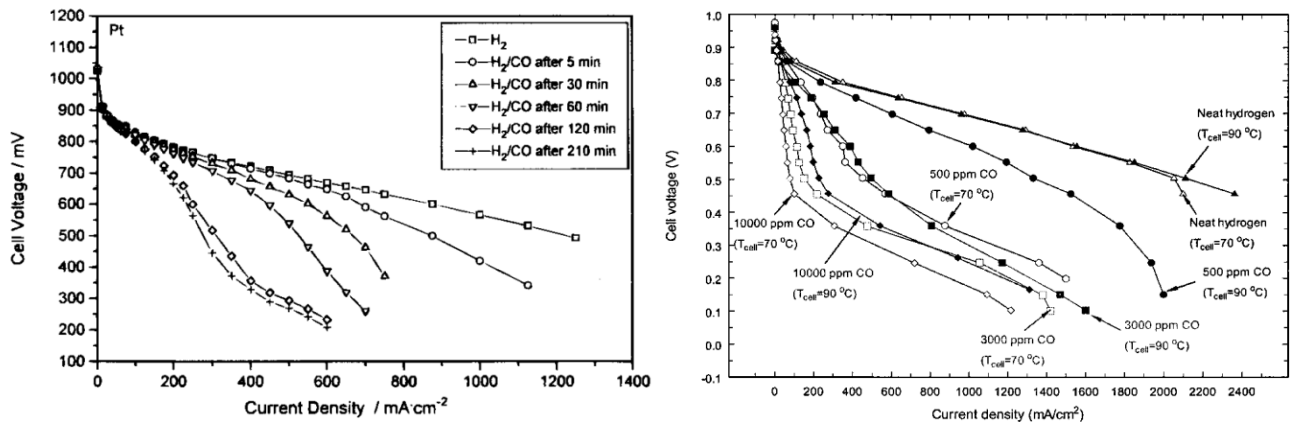
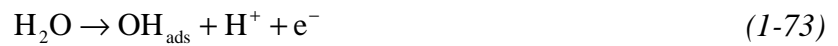


Figure 1-22. Left: polarization curves of a fuel cell fed with CO contaminated hydrogen vs time [55] – right: polarization curves of a fuel cell contaminated at different CO concentration and temperature [54].

CO adsorbed on platinum can be removed. However, this requires to increase the potential high enough so that it oxidizes into carbon dioxide, according to these reactions [56]:



CO oxidation can be observed during cyclic voltammetry, under the form of a current peak occurring around 0.75V vs RHE depending on the Pt surface morphology (Figure 1-23). This peak comes together with the disappearance of the one corresponding to hydrogen oxidation. Depending on the potential sweep rate, several potential scans of the electrode are sometime necessary to remove all adsorbed CO from platinum. The electrode is considered as clean when the CO oxidation peak does not occur anymore and when the hydrogen oxidation peak is back.

Like hydrogen oxidation, CO oxidation depends on the Pt active surfaces and on the size of platinum particles [57].

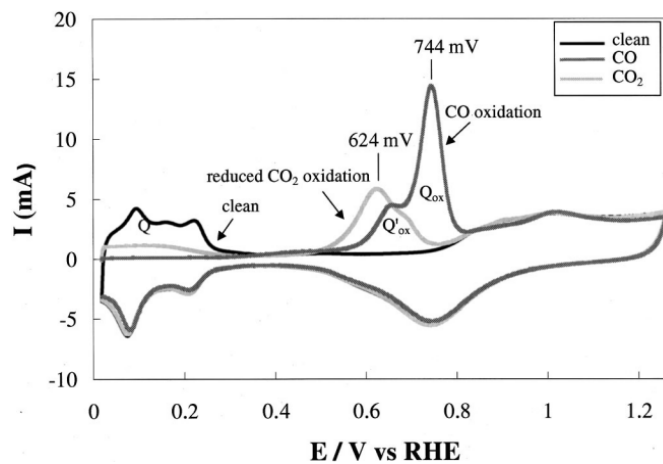


Figure 1-23. Cyclic voltammogram of clean, CO, and CO₂ saturated carbon supported Pt in 1 N H₂SO₄ [58].

Other contaminations can occur with different degree of reversibility. The most studied in the literature involve ammonia (NH₃), hydrogen sulphide (H₂S) or hydrocarbon contaminants (for hydrogen) and sulphur dioxide (SO₂), nitrogen dioxide (NO₂) and sodium chloride (NaCl) (for air).

c. Catalyst degradation

The catalyst has a strong influence on the cell performance and durability. When some platinum is lost, the reactions rate can decrease dramatically. In the literature, many mechanisms of platinum degradation have been identified. The monitoring of the time evolution of platinum active surface thanks to cyclic voltammetry allows investigating the parameters which have a direct impact on its degradation. In addition, ex-situ analyses of fresh and aged MEAs provide information concerning the evolution of the platinum particles structure. These data are used to identify the mechanisms involved in catalyst degradation.

The detachment of platinum particles from their support is a direct consequence of carbon oxidation. Once carbon is oxidized, the platinum particles are less anchored to their support and free to move. Then, these particles can relocate where there is neither carbon nor ionomer and thus no possibility to form again the triple phase boundary (or at least a region where catalyst support, catalyst and membrane are in close contact). In this case, platinum becomes useless and is not detected by cyclic voltammetry anymore.

The coalescence via crystal migration results from the tendency of platinum crystals to minimize their surface energies. The coalescence of two separate crystals leads to the formation of a single particle with a lower surface per volume ratio than that of the initial crystals. As a result, the global surface energy is reduced but atoms previously on the surface are now in the bulk, which implies a decrease of the platinum active surface. Since high temperatures are required to initiate the migration, coalescence is more prone to occur in Phosphoric Acid Fuel Cell than in PEMFC [59].

Dissolution and precipitation of platinum particles leads to two similar phenomena. The first one, called **short range Ostwald ripening**, consists in the dissolution and redeposition of platinum atoms of a small platinum particle onto a bigger one. The transport of platinum under the form of Pt^{Z+} occurs at the nanometer scale, which explains the term “short range”. Short range Ostwald ripening has been shown to be promoted when the potential is high [60]. It occurs therefore mainly in the cathode. Its consequence is a disappearance of the smallest particles in favour of the largest ones (Figure 1-24) and consequently, a reduction of the active surface.

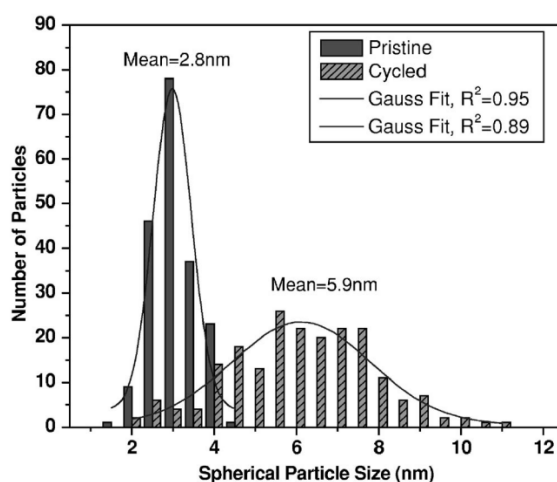
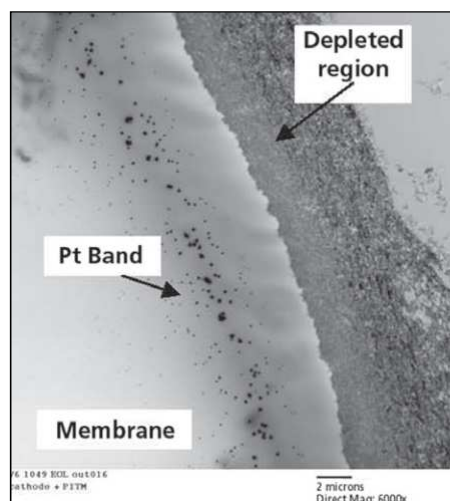


Figure 1-24. Size distributions of platinum nanoparticles in pristine Pt/Vulcan sample and powders scraped from cycled MEA cathode surface near the DM/cathode interface (potential cycles between 0.6V and 1.0V of a nitrogen filled cathode at 80°C)- Measurements of 200 randomly selected spherically shaped particles were made for each distribution [61].

The second phenomena is called **long range Ostwald ripening**. It corresponds also to a dissolution and redeposition of platinum particles. This time however, the transport of platinum (again under the form of Pt^{z+}) occurs at the micrometer scale and mostly from the cathode to the membrane. The depth platinum migrates is determined by the mixed potential inside the membrane [62], [63]. This potential depends on the presence of hydrogen and oxygen molecules crossing the membrane. Once platinum reaches a region where the mixed potential is low enough (that is to say a region in the membrane where the partial pressure of hydrogen is sufficiently high compared to that of oxygen), platinum cations are reduced and redeposit. This leads to the formation of a Pt-band inside the membrane, which position is consequently a function of hydrogen and oxygen partial pressures (Figure 1-25). When hydrogen and air are supplied at identical pressure to the cell, the Pt-band is close to the cathode. Indeed, the mixed potential drops rapidly, firstly because oxygen represents less than 20% of the air in the cell (accounting for O_2 depletion and air humidification) and secondly because the diffusivity of hydrogen inside the membrane is higher than that of oxygen ($4.10^{-9} \text{ m}^2/\text{s}$ and $1.10^{-9} \text{ m}^2/\text{s}$ respectively). It is shown in §1.4.4 that the redeposited platinum remains active and participates to the membrane degradation.

Figure 1-25. TEM image of the cross-section of degraded catalyst-coated membrane (CCM) with the presence of a Pt band in the membrane after potential cycling [64].



The above mechanisms are represented in Figure 1-26:

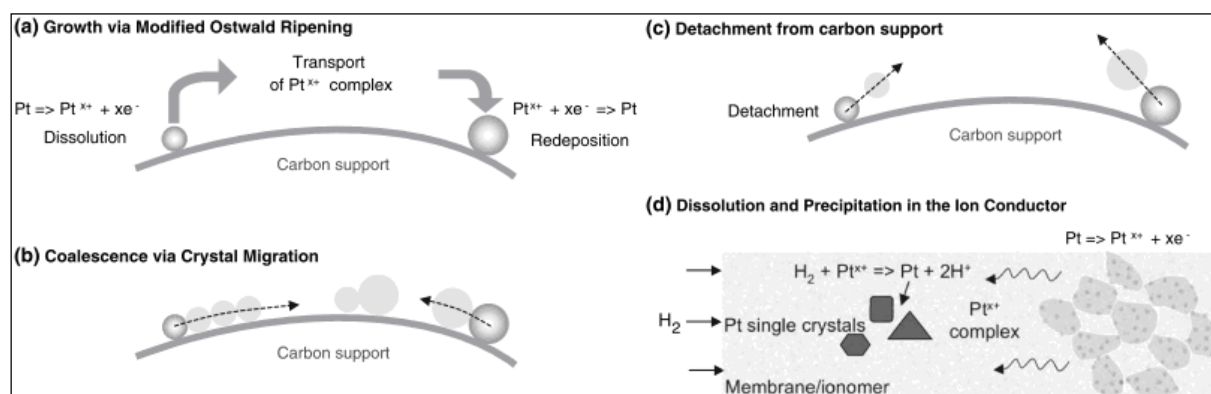


Figure 1-26. Mechanisms explaining the instability of Pt nanoparticles in low-temperature fuel cells [61].

d. Main issues concerning the electrodes

Carbon black is one of the most popular catalyst support materials due to the good cost/performance/durability ratio it offers. Despite this, it is still necessary to better understand its degradation mechanisms and to limit carbon aging.

In parallel, new materials which could replace carbon black are investigated:

- **Ordered mesoporous carbons** [65] are constituted of monodispersed mesopores, that is to say homogeneously dispersed pores with a diameter higher than 2 nm. By comparison, carbon black exhibits broad pore size distribution with a significant fraction of micropores (size < 2 nm). The low accessibility of platinum deposited in the micropores limits the electrocatalytic activity. Mesoporous carbons present therefore a higher catalytic activity. Their pore structure makes them good electrical conductors and contributes to enhance mass transfer. In addition, their synthesis is simple and relatively cheap. However, their low degree of graphitization (like carbon black) does not comply with the durability requirements since it makes them prone to oxidize. This can be solved by an artificial graphitization but the manufacturing process becomes more complicated and expensive [66].
- **Carbon nanotubes (CNTs)** [67], [68] present interesting properties which make them suitable candidates as catalyst support material: they are highly conductive, exhibit a large surface area for the catalyst dispersion and are relatively stable in oxidative conditions. While these properties have to be further studied in real fuel cell conditions, the main problem with CNTs remains their manufacturing process and their cost.
- **Ceramic electrode supports** such as titanium oxide [35] or tungsten carbide [69] present usually high stability in fuel cell environment and reasonable electrical conductivity. However, their low surface area results in a low metal dispersion and consequently in a poor electrochemical activity [65].

In the same time, more durable and cheaper catalysts have still to be found. Most of the research focuses currently on:

- **Pt-alloy catalysts.** The use of Pt based binary alloy catalysts such as Pt-Ru, Pt-Co or Pt-Pd and ternary alloy catalysts aims to reduce the amount of platinum in fuel cells while increasing the catalyst activity and durability. Although activity is enhanced compared to pure platinum for some cases [70], their stability in long term operation

remains problematic. Additional metals tend to dissolve and to form cations at the cathode. For instance, once ionized, cobalt migrates in the membrane where the local potential remains too high for its reduction (standard electrode potential of the Co^{2+}/Co : $E_{\text{Co}^{2+}/\text{Co}}^0 = -0.28\text{V}$ vs RHE) [71]. As a result, important damages such as conductivity losses or membrane failure can occur.

- **Noble metal catalysts** such as Au [72] or Pd [73], [74] offer a lower catalyst activity than platinum. However, in the case of palladium, the activity can be improved by using a Pd based binary or ternary alloy. The advantage compared to platinum, is the reduced cost of such catalysts due to their relative abundance. Their durability in fuel cell operating condition has however to be assessed.
- **Non noble catalysts** [75], including metal catalyst such as Ni and Cu and non metal catalysts such as titanium dioxide, vanadium oxide. Research works are still necessary to improve the activity of these catalysts. Tests in real use conditions have to be performed to determine their resistance to the fuel cells environment.

Investigations into catalyst supports and catalysts are not disconnected. Thus, in an important number of publications, alternative catalyst support to carbon and alternative catalyst to platinum are studied simultaneously. For example, gold particles supported on carbon nanotubes have been tested [76]. Up to now, no combination provides a real breakthrough.

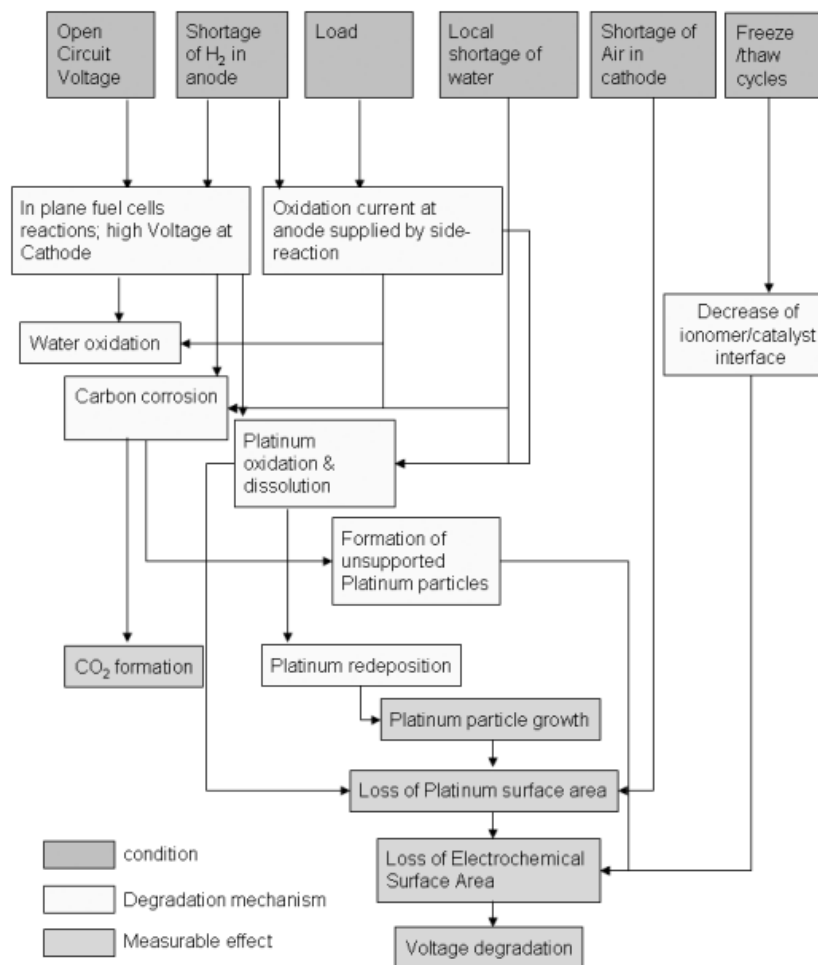


Figure 1-27. Main electrode degradation mechanisms [32].

1.4.4 Membrane

The polymer electrolyte membrane contributes to the fuel cell voltage drop with increasing current density because of the ohmic losses it induces. To reduce these losses, the main tendency is to lower its thickness. However, this can make worse the consequences of chemical as well as physical degradations. Hydrogen or oxygen crossovers become for instance more significant.

In parallel to the reduction of the membrane thickness, the development of new membranes relies on more essential issues such as the reinforcement of their mechanical strength, the reduction of their brittleness in dry state or the increase of the current density [77]. One of the first materials to satisfy well enough the required conditions is Nafion, which was first commercialized in the 1970s. Nafion is a perfluorosulfonic polymer. It consists of a PTFE backbone and pendent fluorodiether sides chains with hydrophilic sulfonic acid end-groups (Figure 1-28). The sulfonic groups are responsible for protons transport while the backbone (or main chain) ensures the mechanical resistance. The main characteristic of such perfluorosulfonic acid (PFSA) membranes is a good chemical stability in both oxidative and reductive environments. The electrical conductivity is highly dependent on the hydration level and therefore a good water management is needed. Other PFSA membranes than Nafion have been developed (Figure 1-28). Although having a better lifetime compared to the first generations, their failure still leads to dramatic performance drop and to the shutdown of the cell because of hydrogen leakage.

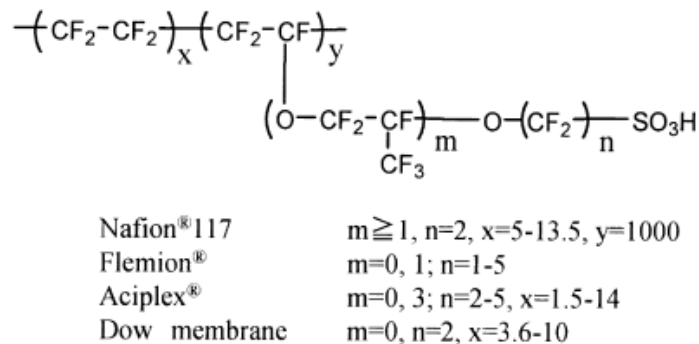


Figure 1-28. Structure of prefluorinated membranes [78].

a. Chemical degradations

Several chemical attacks are involved in PFSA membrane degradations. They all implicate either hydroxyl or hydroperoxyl radicals which presence within the cell results from two different mechanisms. The first one occurs in five steps [79] and is initiated in the anode:

- Hydrogen is splitted into hydrogen radicals on Pt catalyst at the anode:



- Oxygen crosses the membrane and reacts with the hydrogen radicals to form hydrogen peroxide:





- Reactions (1-75), (1-76) and (1-77) take place in the anode only. However, hydrogen peroxide can diffuse in the membrane where it can meet a metal impurity (coming from the dissolution of the flow field plate [80], the dissolution of the platinum catalyst or more simply from the manufacturing process), which gives birth to a hydroxyl radical:



- Finally, the hydroxyl radical reacts with another hydrogen peroxide to produce another hydroperoxyl radical, located this time in the membrane:



In the second mechanism, the production of hydrogen peroxide through reactions (1-75), (1-76) and (1-77) is replaced by a production due to an incomplete reduction of the oxygen. The reaction takes place either in the cathode when its potential is low enough or directly on platinum particles which have already migrated through the PEM (see §1.4.3) [81]:



Oxygen reduction in the membrane can occur in a region where the mixed potential (function of the hydrogen and oxygen partial pressure [82]) reaches a value beyond 0.6V vs RHE, which corresponds to the $\text{O}_2/\text{H}_2\text{O}_2$ standard electrode potential ($E_{\text{O}_2/\text{H}_2\text{O}_2}^0$). Contrary to oxygen reduction at the cathode, it occurs also in open circuit. The formation of hydroperoxyl radicals results then from reactions (1-78) and (1-79), as in the first mechanism.

Then, these radicals attack the membrane according to different mechanisms. Various scenarios have been proposed in the literature like the main chain unzipping [83], consisting in three steps (Figure 1-29):

- Step 1: a hydroxyl radical reacts with an acid end group. This leads to the emission of carbon dioxide and water, the end group becoming a perfluorocarbon radical.
- Step 2: the perfluorocarbon radical reacts with a hydroxyl radical to form a hydrogen fluoride. The end group becomes an acid fluoride.
- Step 3: the acid fluoride reacts to produce another hydrogen fluoride and during this final step, an identical acid end group than in step 1 is formed.

As long as side chains are not reached, step 1 starts again once step 3 is terminated. When a side chain is encountered, its separation from the main chain occurs as depicted on the Figure 1-29.

The main chain unzipping can be initiated by defects like C-H or C=C bonds, created for instance during the manufacturing process [84].

Chen et al. [85], [86] analysed the content of the exhaust gases and water in both anode and cathode of a cell maintained in open circuit and performed post-mortem analyses of the membrane structure. They found a release of fluorine HF that was attributed to the degradation of the ionomer main chains. In addition, they also detected species such as SO_4^{2-} , H_2SO_2 , H_2SO_3 and trifluoroacetic acid (TFA) which are characteristic of a second degradation mechanism concerning the side chains and side chains end groups.

The membrane chemical attacks increase with the hydrogen crossover [87]. According to Sethuraman et al. [88], this situation occurs preferentially when the humidity inside the membrane is low and the temperature is high. A sudden drop of the cell voltage is usually observed (Figure 1-30) while the hydrogen crossover starts to increase dramatically (Figure 1-31) [89].

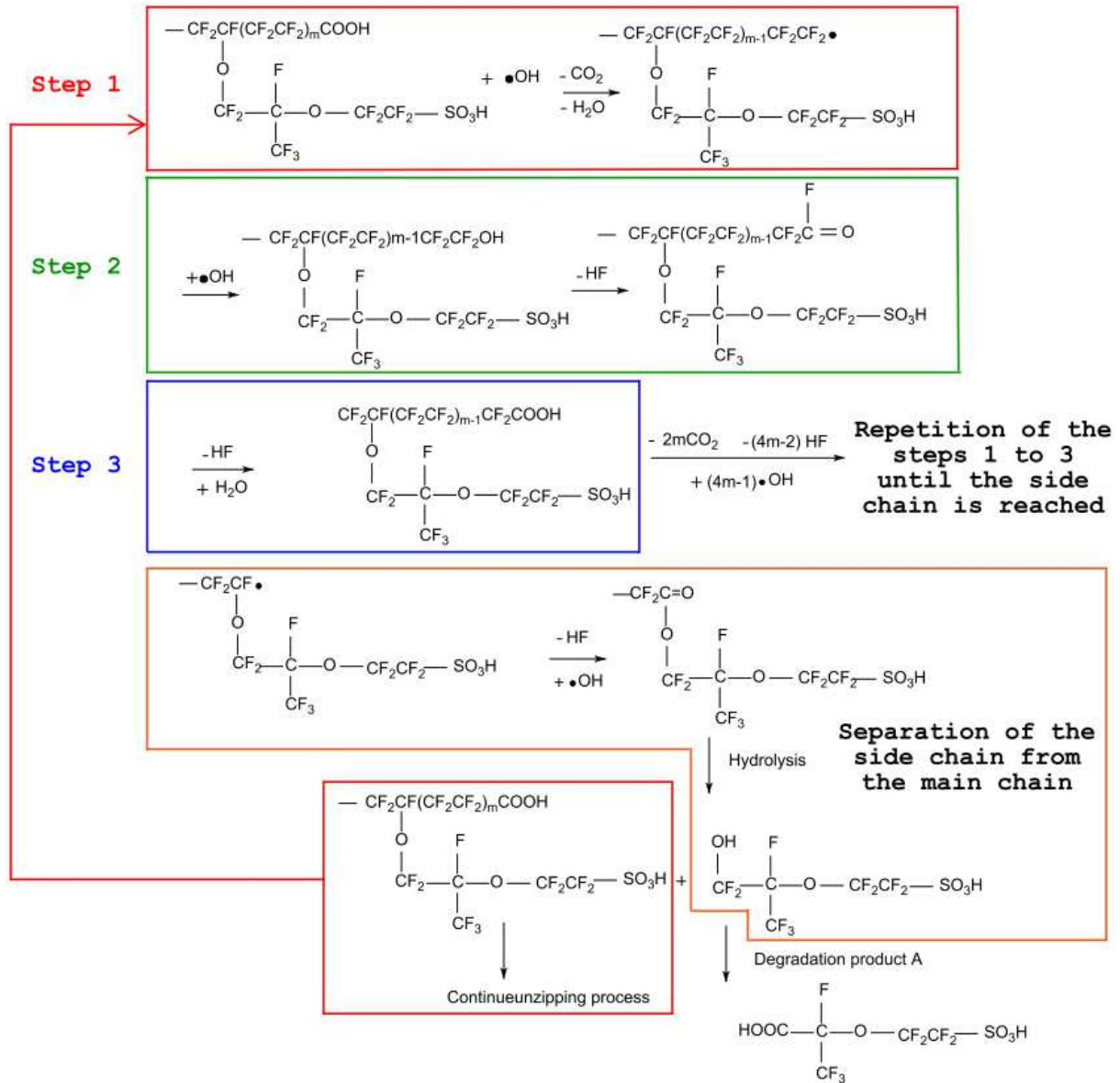


Figure 1-29. Main chain unzipping scenarios, adapted from [85].

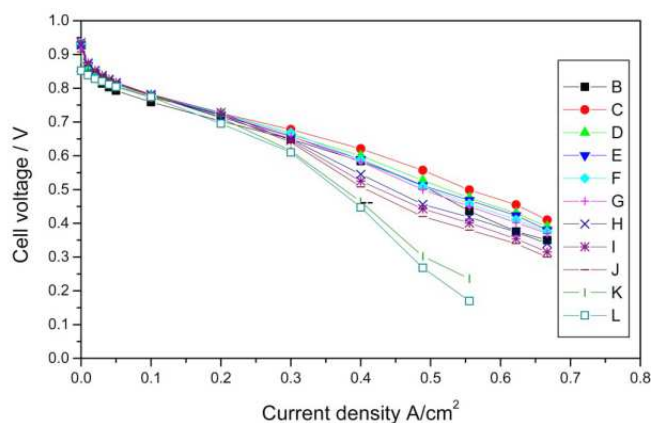


Figure 1-30. I-U curves of a cell during a current hold test at 300 mA/cm^2 . Cell operated at 75°C with H_2 and air fully humidified and at atmospheric pressure [89]. (B) 31, (C) 313, (D) 751, (E) 1154, (F) 1641, (G) 1900, (H) 2088, (I) 2108, (J) 2402, (K) 2544, and (L) 2700 h.

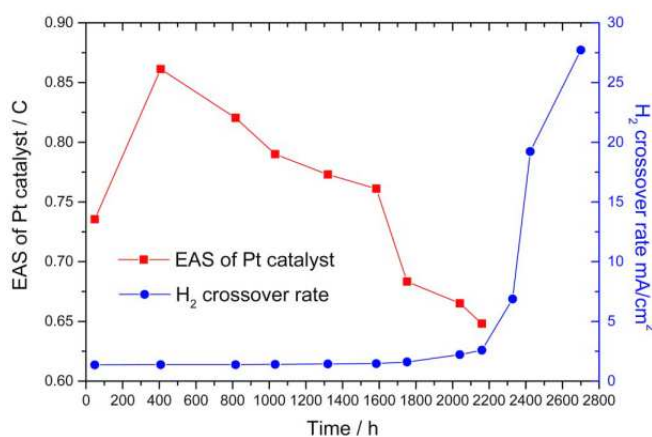


Figure 1-31. H_2 crossover current density evolution during a fuel cell current hold test at 300 mA/cm^2 . Cell operated at 75°C with H_2 and air fully humidified and at atmospheric pressure [89].

Finally the last type of chemical degradation is the pollution of the membrane by cations. The SO_3^- end groups of Nafion side chains are responsible for the transport of the protons from the anode to the cathode. Cations resulting from the manufacturing process, from the oxidation of the flow field plates or that of the catalyst tend to replace protons at the SO_3^- sites since their affinity is higher. For example, cobalt used with platinum to enhance the catalytic activity in the electrode is known to dissolve and to diffuse in the membrane. As its standard potential electrode is low ($E_{\text{Co}^{2+}/\text{Co}}^0 = -0.28\text{V}$ vs RHE), it cannot be reduced anymore and occupy SO_3^- sites [71]. The conductivity of the membrane is then reduced both because of the inactivity of a portion of SO_3^- sites and because of the decrease of water activity induced by this pollution [90].

b. Mechanical degradations

During operation, the membrane undergoes temperature and humidity variations. Both generate mechanical stresses. When these variations are repeated, the mechanical resistance of the membrane decreases and cracks or pinholes can appear.

Figure 1-32 depicts the mechanical properties of several MEAs submitted to stress test after 100 cycles between 30% RH and 100% RH at 65°C [91]. Microcracks were observed on the surface of these samples. The number of cycles imposed to the MEA is a determining parameter in the membrane strain limit: the membrane mechanical resistance decreases with the number of humidity cycles.

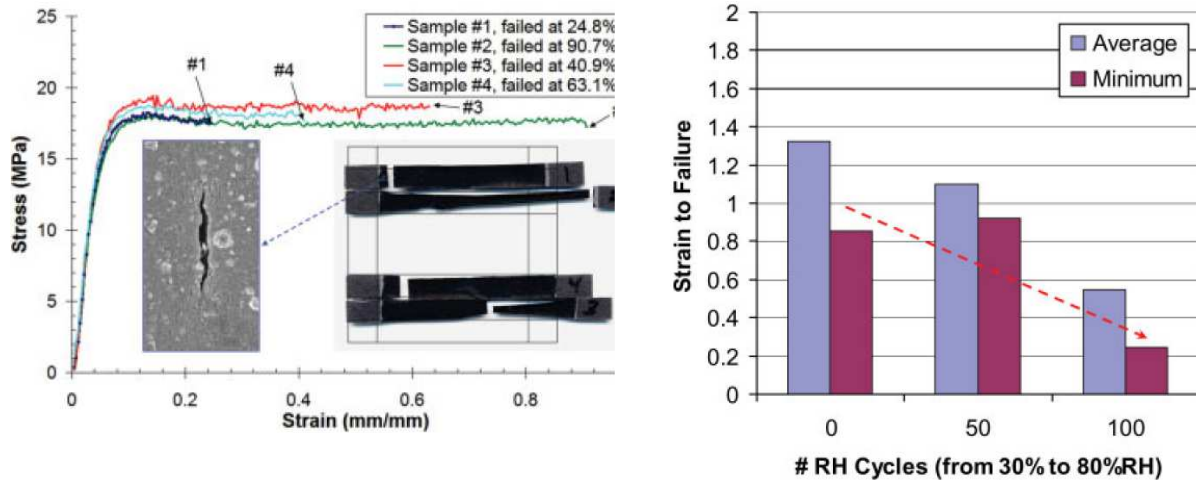


Figure 1-32. Left: stress–strain curves of the membrane after 100 cycles between 30% and 80% RH at 65°C and SEM images of the cracks. Right: average and the minimum values of the strain-to-failure as functions of the number of cycles between 30% and 80% RH [91].

The membrane mechanical resistance is also lower when the temperature increases (Figure 1-33).

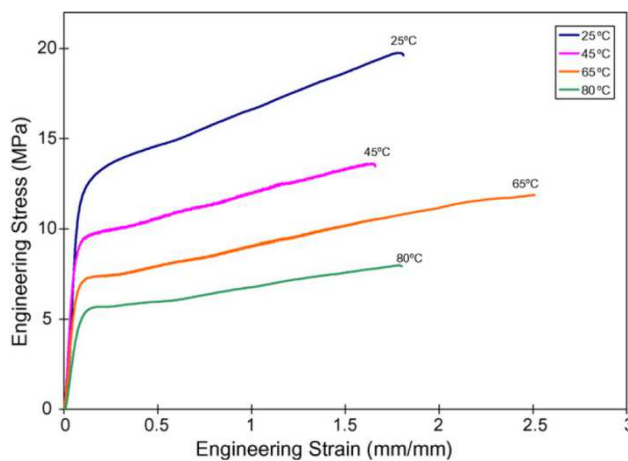


Figure 1-33. Stress–strain curves of Nafion NR111 membrane at 50% RH and various temperatures [92].

c. Main issues related to membrane durability

The structural properties of PFSA membranes [93] are still in the process of improvement. In the future, one can expect a better resistance to chemical attacks, to mechanical stresses and an increase of their performances [77]. Manufacturing processes initially developed for thick membranes are also revised to improve the initial properties of thinner membranes [83].

Alternatives to PFSA membranes are also under investigation. Most of the research concentrates on partially fluorinated membranes, non-fluorinated hydrocarbon membranes, non fluorinated aromatic membranes and acid base blend membranes. The advantages and disadvantages of each of these technologies are listed in Table 1-2.

Despite efforts to find new solutions, Nafion or its PFSA equivalent versions (including short side chain membrane like Aquivion) remain by far the most used polymer electrolyte.

Category	Structure	Physical properties	In situ performance
Perfluorinated membranes (pf)	<ul style="list-style-type: none"> Fluorinated backbone like PTFE Fluorocarbon side chain Ionic clusters consisting of sulfonic acid ions attached to the side chains 	<ul style="list-style-type: none"> Membranes are strong and stable in both oxidative and reductive environments 	<ul style="list-style-type: none"> Membrane is durable upto 60,000 h Proton conductivities in well humidified membranes are 0.2 S/cm at PEMFC operating temperatures Cell resistance of 0.05 Ω cm² for 100 μm thick membrane with voltage loss of only 50 mV at 1 A/cm² is achievable
Partially fluorinated membrane	<ul style="list-style-type: none"> Fluorocarbon base Hydrocarbon or aromatic side chain grafted onto the backbone, which can be modified 	<ul style="list-style-type: none"> Membranes are relatively strong in comparison to pf, but degrade fast 	<ul style="list-style-type: none"> Less durable than perfluorinated ones Low performance On suitable modification, yield membranes with comparable proton conductivities
Non-fluorinated hydrocarbon membranes	<ul style="list-style-type: none"> Hydrocarbon base, typically modified with polar groups 	<ul style="list-style-type: none"> Membranes posses good mechanical strength Poor chemical and thermal stability 	<ul style="list-style-type: none"> Poor conductors of protons Exhibit low durability on account of swelling obtained by incorporation of polar groups into the polymer matrix
Non-fluorinated aromatic membranes	<ul style="list-style-type: none"> Aromatic base, typically modified with polar/sulfonic acid groups 	<ul style="list-style-type: none"> Good mechanical strength Chemically and thermally stable even at elevated temperatures 	<ul style="list-style-type: none"> Good water absorption Relatively high proton conductivity is attainable Conductance of SPPBP at 65 mol% of sulfonation is 10⁻² S/cm that is retained at temperatures above 100 °C
Acid-base blend membranes	<ul style="list-style-type: none"> Incorporation of acid component, into an alkaline polymer base 	<ul style="list-style-type: none"> Stable in oxidizing, reducing and acidic environments High thermal stability 	<ul style="list-style-type: none"> Good dimensional stability Exhibit proton conductivity comparable to Nafion® Durability of the membranes is still to be proven

Table 1-2. Structure and properties of different membranes under investigation for PEMFC applications [77].

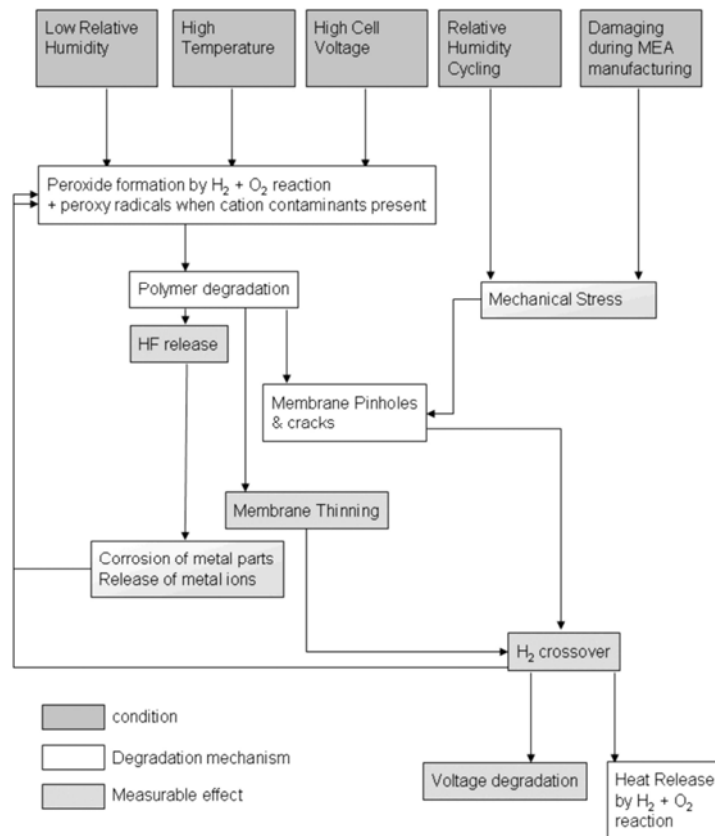


Figure 1-34. Degradation conditions, mechanisms and effects for PFSA membranes [32].

1.5. Conclusion

In the current context of energy crisis, fuel cells appear as an interesting alternative to internal combustion engines and batteries. Although promising due to their high efficiency, PEMFCs fail however to meet durability and reliability targets and this as well for automotive as for stationary applications.

This first chapter aims to detail the components of a PEMFC and their respective roles in the energy conversion process. This description is necessary to understand how a damage caused to one of these components can affect the cell operation. The different degradation mechanisms usually encountered in the literature can be sorted by components: MPL, GDL, electrodes, membrane, flow field plates. This classification highlights that several mechanisms can occur (chemical attack, pollution, mechanical stress) depending on the operating conditions (OCV, fuel starvation, potential hold). In addition, it appears that the products of some degradations mechanisms can also be harmful. As some of these products (platinum, metal cations) can migrate in the cell, damages in one component can therefore affect other components. There is then a “contagion effect” which explains why the cell failure can arise so rapidly.

An important part of research focuses on the improvement of the materials used as electrode support, catalyst or membrane. Some examples of alternative materials are presented with their advantages and disadvantages. So far, no appropriate combination of such alternative materials meeting the objectives of performances, cost and durability has been found.

The use of current materials in fuel cell can also be optimized to reduce the degradations. In chapter 2 and 3, some characteristics of Ion Power MEAs were tuned: anode or cathode platinum loading or carbon specific surface were modified and the influence of these changes on the mechanisms leading to degradations was assessed; first for single start-ups (§2.8.2) and then during long term aging protocols (§3.6).

Two diagnosis tools, EIS and CV, were also presented in this first chapter. In chapter 2, EIS and CV are completed by CO₂ measurements using a NonDispersive InfraRed (NDIR) sensor (§2.2). In chapter 3, post-mortem analyses are also performed to analyse the degradations and to confirm the results of CV, EIS and measurements of CO₂ emissions (§3.7.2). CV and EIS are particularly useful when they are used in a segmented cell like those presented in the second chapter. On top of that, segmented cell enable the measurement of internal currents occurring during start-ups and shut-downs performed in open circuit.

2 Electrochemical Description of Start-up and Shut-down

Some operating conditions are known to severely damage the fuel cell MEA, for instance OCV hold, potential cycles, start-ups and shut-downs. While the corresponding degradation mechanisms are generally well identified, few information is available concerning their spatial distribution within the cell, apart from those provided by post-mortem analyses. The in-situ local monitoring of the degradation evolution is therefore a challenge that segmented fuel cells can help to achieve. Combined with appropriate techniques like Electrochemical Impedance Spectroscopy or Cyclic Voltammetry, the segmentation of the electrode current collector can be applied to fuel cell diagnosis as well as to the validation of the cell design [94] or to the optimisation of the cell performance [95]. Its use by an increasing number of research groups confirms its numerous advantages [95], [96], [97].

In this chapter, attention is paid to single start-ups and shut-downs. The first section focuses on the analysis of start-ups and more particularly on internal currents. While these currents were already observed by several groups [98], [99], [100], they were neither used to identify nor to quantify the degradations mechanisms. In a second step, another description of start-ups is presented under the form of a potentials distribution analysis based on the work of Shen et al. [101]. This analysis aims to complete the internal current description and to point out where and which kind of degradations should occur.

In a second section, an attempt is made to distinguish between the different contributions of internal currents to damages like Pt or carbon oxidation (reverse currents). For this, the 2D segmented cell developed to investigate start-ups is first presented with its dedicated test bench. The variation of the charges deduced from the reverse currents is then studied depending on the hydrogen flow rate and compared to the carbon dioxide emissions measured in the cathode gas exhaust. With another cell equipped with local Reference Hydrogen Electrodes, local anode and cathode potentials are detailed.

In a third section, the results of similar investigations carried out about the shut-down procedure are presented.

Finally, complementary experiments were implemented in the framework of a partnership with the LANL in Los Alamos: Ion Power MEAs were used to study the impact of component specifications (carbon support, platinum loading in the anode and cathode) on the internal currents and CO₂ emissions during single start-ups and shut-downs.

Although the MEAs used in this collaboration do not have identical specifications, they showed tendencies similar to those observed with the Johnson Matthey MEAs.

2.1. Description of start-ups

2.1.1 Principle and internal currents

During the start-up of a PEMFC, the anode compartment is divided momentarily into an upstream part occupied by fresh hydrogen and a downstream part filled with the gas which was used to flush the anode: air or nitrogen (Figure 2-1). The boundary between the downstream and the upstream parts moves from the inlet to the outlet of the anode compartment with a velocity that is governed by the hydrogen flow rate. Reiser et al. [98] first related start-ups to phenomena which could accelerate the decay of fuel cells. They showed

that electrochemical reactions took place in both electrodes even when the start-up was performed in open circuit. More specifically, they proposed the following mechanism:

- In the upstream part of the anode compartment (called the active part in the following), hydrogen is oxidized at the anode and oxygen is reduced at the cathode. These reactions correspond actually to the normal operation of a fuel cell.
- In the downstream part of the anode compartment (called the passive part in the following), oxygen is reduced in the anode and oxidation reactions occur in the cathode outlet. According to Reiser et al., oxidations involve water and carbon, this last reaction being responsible for the degradations caused by start-ups. When nitrogen was used to flush the anode, the reduction reactions in the anode outlet were attributed to oxygen crossover from the cathode side through the membrane. As shown at the end of §2.1.2 and in §4.2, platinum oxides can also contribute to the reduction reactions.

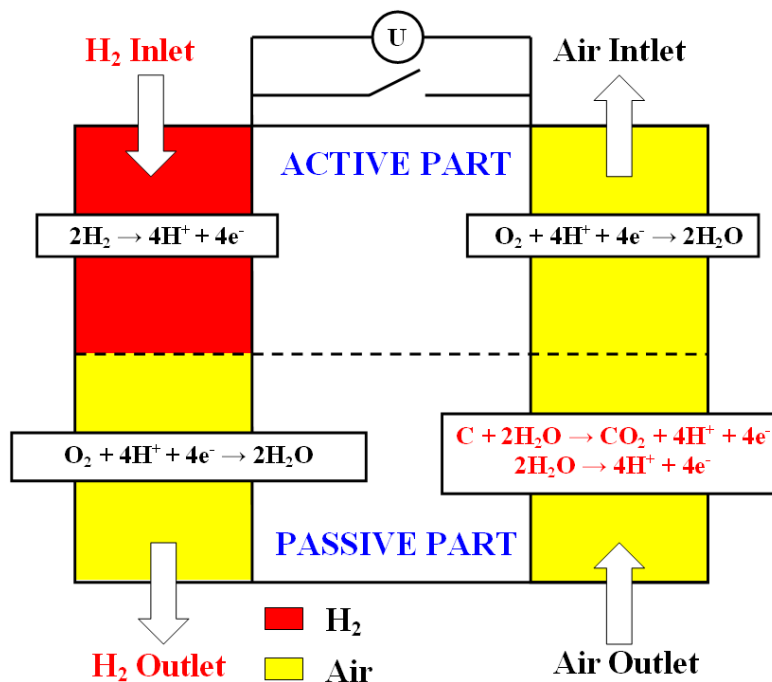


Figure 2-1. Reactions occurring during fuel cell start-ups according to Reiser et al. [98], the anode compartment being initially filled with air.

To demonstrate this mechanism, Reiser et al. built a dual cell which consisted in two cells electrically connected together, but with separated gas supply as depicted in Figure 2-2. The first one operated normally: hydrogen was supplied to the anode and air to the cathode. In the second cell however, air was supplied to both compartments. This configuration reproduced and maintained the conditions which appear transiently during a start-up in a unique cell. During these experiments, currents between the anodes and cathodes of the two cells were measured, which confirmed that redox reactions took place at each of the four electrodes. In the following, these currents are referred to as internal currents and those flowing in the passive part only (cell 2 in the present case) as reverse currents (by reference to the fuel cell normal operation). After a few hours, the performances of cell 2 decreased strongly while those of cell 1 remained high in comparison.

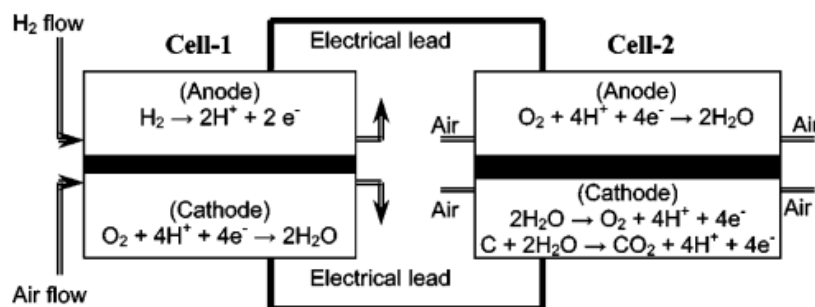


Figure 2-2. Schematic of a dual cell configuration used to simulate the reverse-current conditions. Two 25 cm^2 active area polymer electrolyte fuel cells were used [98].

Another experiment realised by Reiser et al. consisted in supplying simultaneously half of the parallel straight flow channels of an anode with hydrogen while the other half was fed with N_2 or 4% O_2 in N_2 (i.e: H_2 , N_2 or a mixture of N_2 and O_2 were flowing in parallel along the anode compartment, Figure 2-3). The cathode compartment was supplied with air. The cell was maintained at 65°C during 6 hours in open circuit conditions. Post mortem analyses of the MEA were then realised at different locations (Figure 2-4).

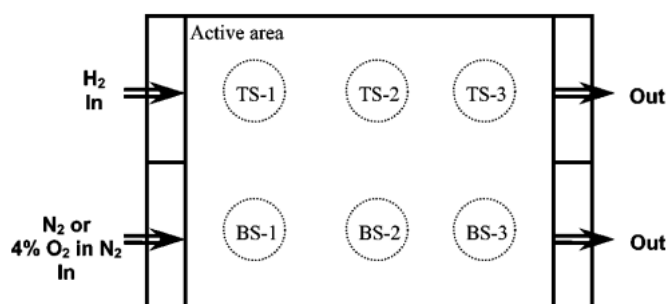


Figure 2-3. Schematic of anode side gas flow configuration in a 320 cm^2 active area polymer electrolyte fuel cell used for reverse-current experiments by Reiser et al. [98]. Anode flow fields with straight parallel channels were used. Half of the anode channels were fed with hydrogen, and the others were fed with N_2 or 4% O_2 in N_2 . The TS-1, TS-2, TS-3, BS-1, BS-2, and BS-3 indicate the six locations chosen for the cross-sectional EMPA images after testing.

Results of the post-mortem analysis showed that the cathode was thinner in the regions where no hydrogen was present in the anode (BS-1, BS-2). This tends to reinforce the conclusion of Reiser et al. concerning the nature of the electrochemical reactions occurring during a start-up: degradations result from carbon oxidation in the part of the cathode located at the opposite of the hydrogen starved region in the anode. Evidence of carbon oxidation was also brought by other research groups who measured in real time the emissions of CO_2 in the air exiting the cathode during start/stop cycles in a fuel cell where the anode compartment was initially filled with air [102], [103], [104], [105].

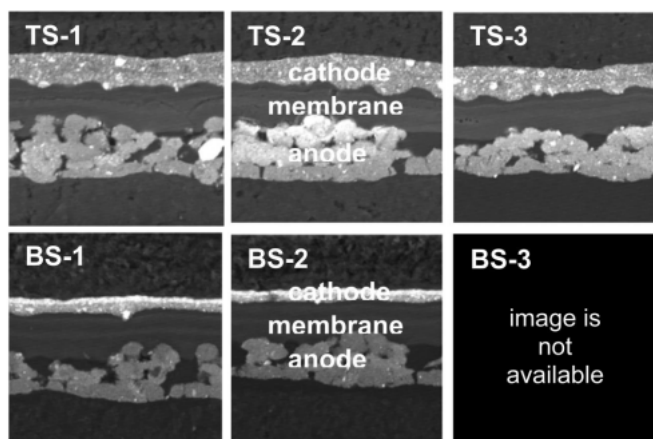


Figure 2-4. Cross-sectional EMPA images after 6 h of reverse-current testing. The location is mapped in Figure 2-3 [98].

Although it provided many valuable information, the use of dual cell configurations [47], [98], [106] did not enable the space and time resolution required to observe the hydrogen/air front progression along the anode compartment. The internal currents measured were therefore not representative of those occurring in a real cell during start-up (or shut-down). Instrumented cells made it possible to overcome this issue. Their specification lies in their segmented current collectors which enable the local collection of the internal currents and this in real time during start-ups (or shut-downs). The time and space resolution of the hydrogen/air front progression is then only limited by the size of the collectors and by the acquisition system [96] (high frequency acquisition systems are required). Maranzana et al. [100] used a 2D cell (i.e: a cell with straight parallel channels) segmented in the cathode to record the internal currents during a start-up (Figure 2-4). The result showed a strong inhomogeneity of the internal currents depending on the position along the cell.

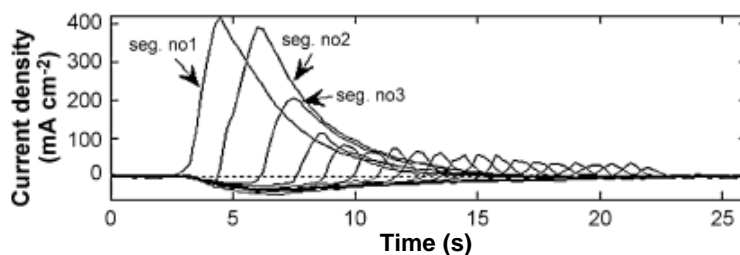


Figure 2-5. Internal currents recorded by Maranzana et al. [100].

Similar current density profiles were also observed by Siroma et al. [99] although the geometry of their cell was different (Figure 2-6).

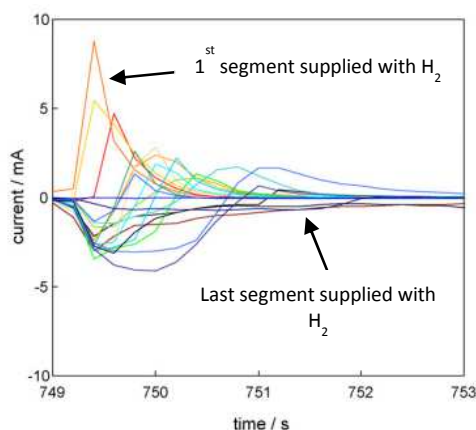


Figure 2-6. Internal currents recorded by Siroma et al. [99].

Another criterion to take into consideration is the geometry of the flow field plates and especially that of the channels. Combined with the hydrogen flow rate, these parameters determine the resident time of the hydrogen/air front, which is also the time during which reverse currents occur. The longer this time, the more the cathode is likely to be damaged.

Internal currents during start-up and shut-down can also be observed using a segmented cell with a more complex geometry than straight parallel channels. In the framework of the H2E program, a segmented cell was designed and built in the fuel cell group of the LEMTA to study the local behavior of MEAs which equipped stacks from Axane (Air Liquide). In this case, the flow field plates have a serpentine geometry as depicted in Figure 2-7.



Figure 2-7. Design of the flow field plate from Axane.

While the geometry of the flow field is different from a 2D cell, current density profiles were close to those obtained by Maranzana et al. (Figure 2-8) and those presented later in this document. However, the internal currents pattern presented irregularities (compared to those obtained using a cell with straight parallel channels) certainly due to the more complicated motion of the hydrogen/air front within the cell. Therefore, the 2D segmented cell appears to be more adapted to the study of the degradation mechanisms induced by start-up and shut-down when one wishes to focus on the electrochemistry rather than on the fluid dynamics.

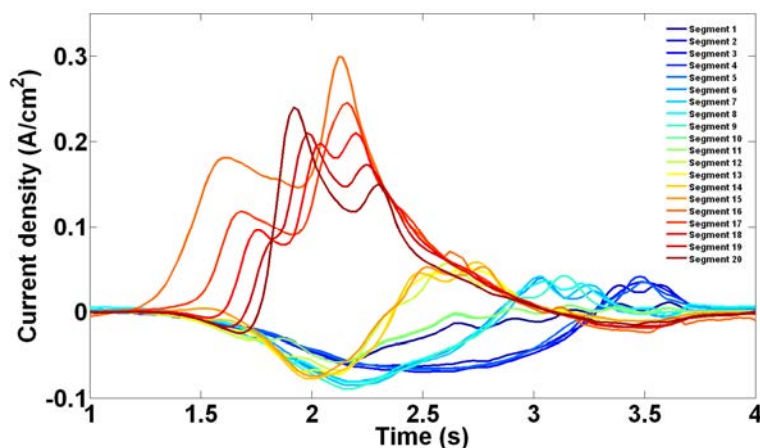


Figure 2-8. Current density profiles obtained with the cell of Axane during a Start-up in air at 12 slph.

In complement to this experimental approach, Maranzana et al. also attempted to simulate numerically the phenomena leading to the internal currents [107]. In addition to the faradic reactions proposed by Reiser et al., they added a capacitive contribution to the reverse currents, which gives numerical current density profiles similar to the experimental ones.

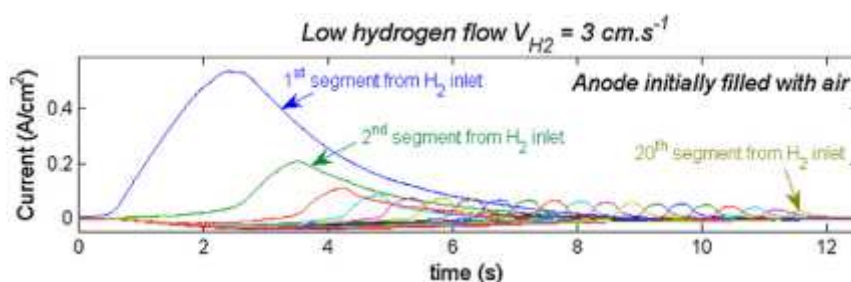


Figure 2-9. Simulated internal currents vs time during Start-up with an anode compartment initially filled with air. $T = 22^{\circ}\text{C}$ [107].

More recently, Schneider et al. [108] demonstrated that internal currents can also occur in the in-plane direction (Figure 2-10). When injected in the anode compartment, H_2 flows preferentially along the channels and diffuses in a second step under the land that is to say underneath the rib, through the GDL. The reverse currents are in this case localized in the land and are more pronounced for broader ribs. This should result in more pronounced degradations under the ribs than below the channel. The instrumented cell used in the present work does not allow such measurements. However, in chapter 3, evidence of higher degradations under the rib is brought by post-mortem analysis of an MEA submitted to repeated start-ups.

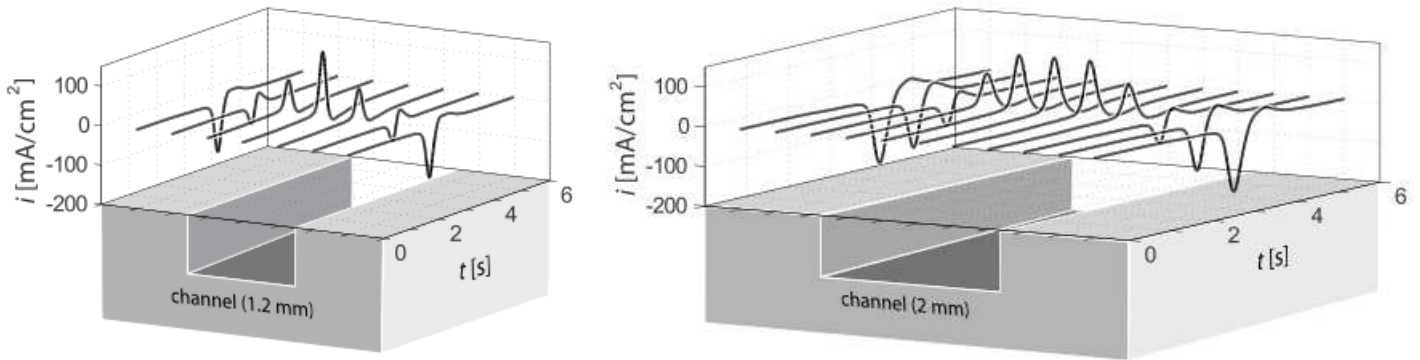


Figure 2-10. In-plane current transients during start-up of a H_2 /air PEMFC with fully humidified gases. The local current transients are shown for a 1.2 mm channel (left) and a 2 mm channel fuel flow field (right, channel:land ratio 1:1) [108].

During shut-down, the opposite phenomenon appears: air is introduced in the anode inverting first the channels. It diffuses then underneath the rib through the GDL. This time, the reverse currents are located under the channels (Figure 2-11) where degradations should be enhanced.

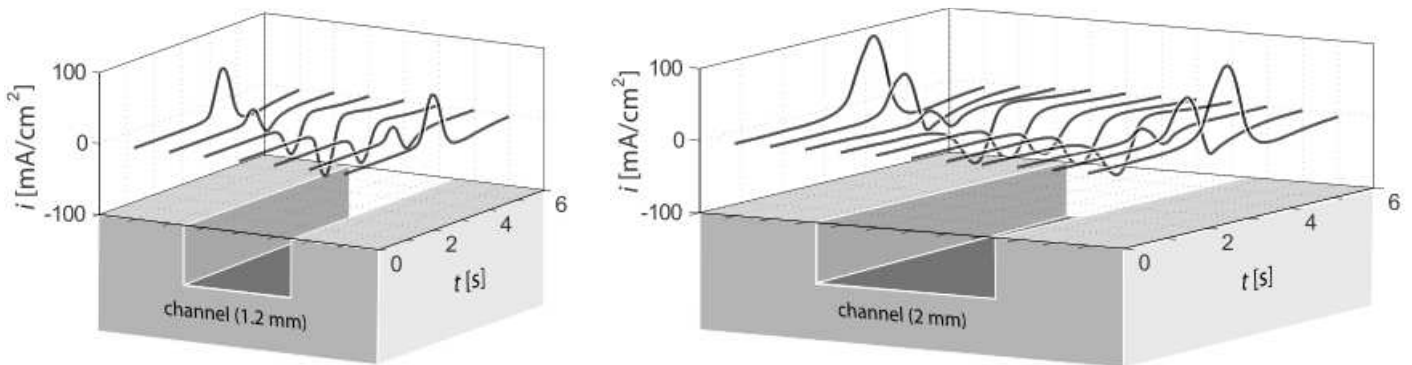


Figure 2-11. In-plane current transients during shut-down of a H_2 /air PEMFC with fully humidified gases. The local current transients are shown for (left) a 1.2 mm channel and a 2 mm channel fuel flow field (right, channel:land ratio 1:1) from [108].

2.1.2 Description of potential evolution during start-ups

Another approach to describe start-ups consists in studying the potentials distribution in the cell. In parallel to internal currents measurements, Reiser et al. also modeled the mechanisms they described. The result of a numerical simulation obtained with this model is presented in Figure 2-12; the anode compartment is assumed half-filled with hydrogen. Three potentials were expressed with reference to the standard hydrogen electrode:

- The anode metal potential V_m^a
- The cathode metal potential V_m^c
- The electrolyte potential V_e (ϕ in Figure 2-12). V_e is assumed constant in the direction perpendicular to the electrolyte.

Two regions can be distinguished: upstream from the hydrogen/air front (region A or active part) and downstream (region B or passive part). Due to the high conductivity of metal at the

anode and cathode, V_m^a and V_m^c remained constant in these two regions and equal to 0V and 0.85 V respectively. However, the electrolyte potential V_e varied. In region A, V_e was close to V_m^a while in region B, V_e dropped to -0.593 V, which resulted in a high interfacial potentials difference between the cathode metal and the electrolyte: $V_m^c - V_e = 1.443V$. Such potentials difference in the cathode enables strong oxidation reactions.

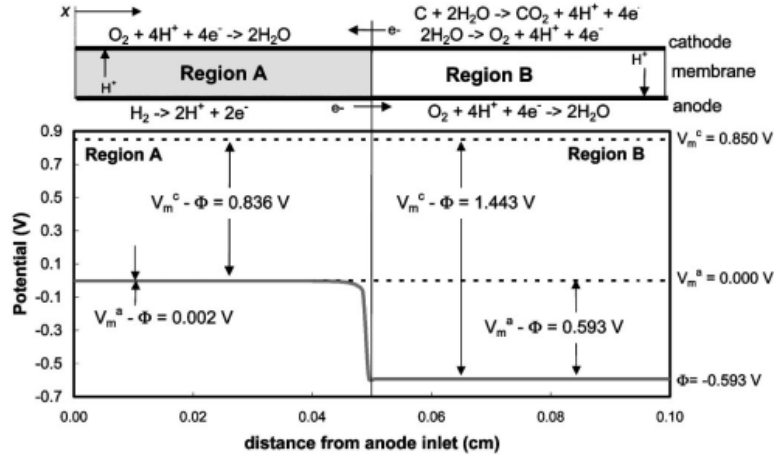


Figure 2-12. Potential distribution in a cell during a start-up in air with reference to the Reference Hydrogen Electrode (RHE), from [98].

To verify the results predicted by the model of Reiser et al., Shen et al. [101] measured in real time the potential distribution during start-ups in a 5 cm² cell. All the mentioned potentials are relative to the reference hydrogen electrode. The membrane potential V_e was measured thanks to copper wires sandwiched inbetween two Nafion 212 membranes (a correction was brought to take into account the potential induced by the copper wires). The potential they measured was an average of the potentials on both sides of the membrane (Figure 2-13):

$$V_e = \frac{V_e^c + V_e^a}{2} \quad (2-1)$$

At 1 A/cm², the potentials V_e^a and V_e^c on both sides of the membrane were close to each other ($V_e \pm 50$ mV; with a Nafion conductivity of 1.10^{-2} S/cm and membranes width = 50 μ m). During start-ups or shut-downs, V_e reached values of several hundreds of mV, which allowed neglecting the electrolyte potential variations perpendicular to the electrolyte $V_e \approx V_e^a \approx V_e^c$. Thereafter, this approximation is used for every value of the current to facilitate the argumentation. The wires were installed in the upstream and the downstream part of the cell to put forward the non homogeneity of the membrane potential along the anode. The description in term of potentials distribution proposed by Shen et al. can be analysed using the equivalent electrical circuit presented in Figure 2-13. This circuit includes charge transfer resistances corresponding to the electrochemical reactions considered by Reiser et al. and double layer capacities as added by Maranzana et al. The electrical equivalent circuit in Figure 2-13 is also used in §0 to validate the potential distribution observed by Shen et al. in the segmented cell.

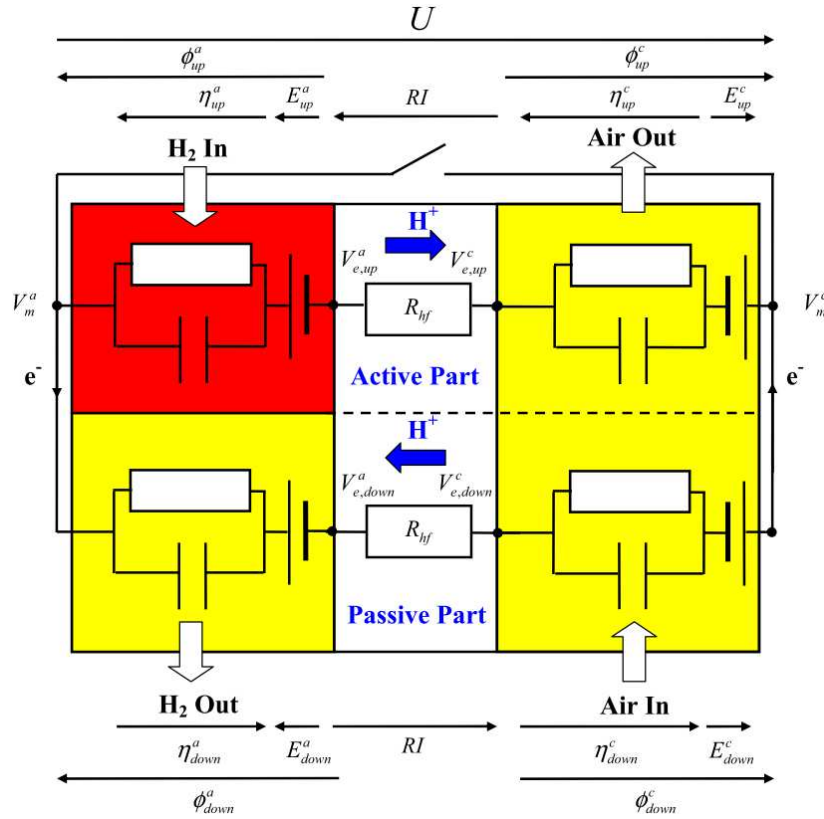


Figure 2-13. Electrical equivalent circuit based on the one proposed by Maranzana et al. [107]. One can see the double layer capacities which contribute to the internal currents.

It must be noted that the initial and final values of the potentials during a start-up in air and a start-up in nitrogen should be similar. Indeed, when the anode remains filled with nitrogen for a long time, the fuel cell voltage decreases to 0 V. This decrease can be attributed to the oxygen permeation through the membrane (from the cathode to the anode).

The fuel cell voltage corresponds to the *difference* between the cathode and anode metal potentials:

$$U = V_m^c - V_m^a \quad (2-2)$$

As far as the electrodes are concerned, their potential ϕ corresponds actually to the *difference* between the metal and the electrolyte potentials (Figure 2-13):

$$\text{In the anode: } \phi^a = V_m^a - V_e^a = E_{Ox(i)/Red(i)}^a + \eta^a \quad (2-3)$$

$$\text{In the cathode: } \phi^c = V_m^c - V_e^c = E_{Ox(i)/Red(i)}^c + \eta^c \quad (2-4)$$

In the following, ϕ^a and ϕ^c are referred to as the anode and cathode potentials, respectively. Since mass transport is neglected and according to Figure 2-13 [107], η stands for the activation overpotential as well as the potential difference applied to the double layer capacity. As a reminder, $\eta < 0$ for a reduction reaction and $\eta > 0$ for an oxidation reaction.

In *Figure 2-14* [101], both electrodes being initially filled with air; the two electrode potentials are equal to:

$$V_m^a = V_m^c = \phi^a = \phi^c = E_{O_2/H_2O} \quad (2-5)$$

And of course, the fuel cell voltage is null (*Figure 2-14*).

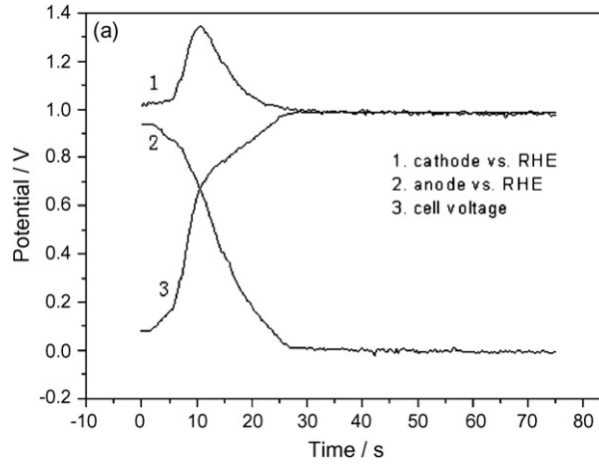


Figure 2-14. Anode potential, cathode potential and cell voltage vs. time during a start-up in air @ 0.12 slph [101]. In this case, anode (cathode) potential refers to the interfacial potential between the anode (cathode) and the electrolyte averaged over the anode (cathode) length (§0).

a. First stage of a start-up

At start-up, two stages can be distinguished. The *first stage* corresponds to an anode partially filled with hydrogen.

Anode metal potential V_m^a and anode potential ϕ^a during start-up

In the anode, the introduction of hydrogen leads to two distinct behaviours:

- In the active part, the anode potential ϕ_{up}^a decreases from about 1 V (O_2/H_2O) to about 0 V (H^+/H_2). This is caused simultaneously by:
 - The decrease of the anode metal potential V_m^a since the cell voltage U increases (*Figure 2-14*);
 - The increase of the electrolyte potential $V_{e,up}$ (*Figure 2-15*).

During this transition, ϕ_{up}^a is higher than E_{H^+/H_2} , which triggers the oxidation of hydrogen.

- In the passive part, the anode metal potential V_m^a drops also (the electric conductivity of carbon being assumed infinite) but since air is still present, the anode potential in this region ϕ_{down}^a remains high. As a consequence, the electrolyte potential $V_{e,down}$ in the passive part decreases (*Figure 2-15*). Despite this decrease, ϕ_{down}^a falls below E_{O_2/H_2O} and oxygen reduction becomes possible.

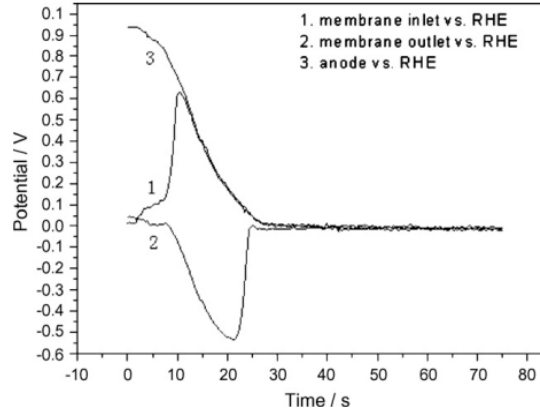


Figure 2-15. Anode potential (in this case, interfacial potential between the anode and the electrolyte was averaged over the anode length, ξ_0), membrane inlet potential $V_{e,up}$ and membrane outlet potential $V_{e,down}$ vs. time during a start-up in air @ 0.12 slph [101].

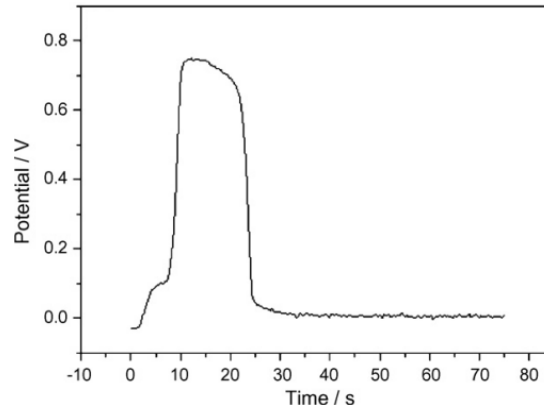


Figure 2-16. Electrolyte potentials difference $V_{e,up} - V_{e,down}$ between the upper and lower part of the cell during a start-up in air @ 0.12 slph [101].

This results in an unbalance between the active and passive parts in such a way that $\phi_{up}^a < \phi_{down}^a$. The intensity of the electrochemical reactions in the upper and lower parts of the anode increases with the difference between ϕ_{down}^a and ϕ_{up}^a . As the anode metal potential is homogeneous over the whole electrode, the difference between these two potentials is equivalent to the difference between $V_{e,up}$ and $V_{e,down}$:

$$\phi_{down}^a - \phi_{up}^a = V_{e,up} - V_{e,down} \quad (2-6)$$

This is represented in Figure 2-16 (right) where the maximum value reached is close to 0.7 V. The cell being in OCV, electrons produced in the active part in the anode can only flow toward the passive part of the same electrode.

We show in chapter 4 (Figure 4-11 in §4.2.1) that, for the sake of simplicity, the capacitive current can be considered as a function of the electrode potential ϕ rather than from the activation overpotential η . Although the anode potential in the upstream part is lower than that in the downstream part ($\phi_{up}^a < \phi_{down}^a$), they both decrease during start-up (§0 and §4.2.3).

Therefore, the double layer capacities participate to the reverse currents in these two regions (also this in the active part).

b. Cathode metal potential V_m^c and cathode potential ϕ^c during start-up

The modifications of the electrolyte potential resulting from the injection of hydrogen have also an impact on the cathode side. The higher electrolyte potential in the active part $V_{e,up}$ induces a drop of the cathode potential ϕ_{up}^c . In parallel, the lower electrolyte potential in the passive part $V_{e,down}$ results in a higher cathode potential ϕ_{down}^c in this region so that $\phi_{down}^c > \phi_{up}^c$. Reduction and oxidation are therefore possible in the active and passive part respectively.

It is important to note that ϕ_{down}^c can exceed the O_2/H_2O standard potential electrode which makes this region very oxidating (values close to 1.6 V can be measured – see Figure 2-17 and §0). These results are in agreement with the estimation of Reiser et al. who found a cathode potential in the downstream part of 1.443V (Figure 2-12).

In the cathode, the capacity located in the active part participates to the forward currents ($\phi_{up}^c < E_{O_2/H_2O}$) while this in the passive part participates to the reverse currents ($\phi_{down}^c > E_{O_2/H_2O}$).

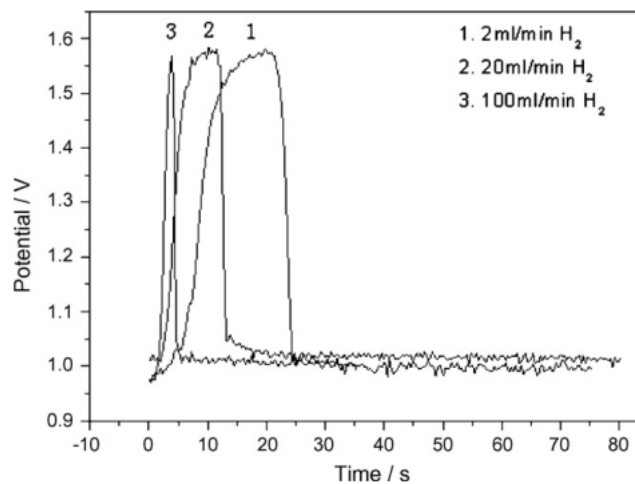


Figure 2-17. Cathode potential in the passive part ϕ_{down}^c during a start-up @ 0.12 slph, from [101].

As the cell is in OCV, electrons produced in the passive part of the cathode can only flow toward the active part. This flow corresponds to the negative or reverse currents (by reference to the normal fuel cell operation) which can be observed using a segmented or a dual cell.

An alternative and stationary representation of the complete potentials distribution is proposed in Figure 2-18 when hydrogen partially fills the anode compartment. In this representation, the electrolyte potential is not anymore considered as constant in the direction perpendicular to the membrane ($V_e^c \neq V_e^a$). The active and passive parts are represented separately but one can see that for both of them the fuel cell voltage U (in red) is homogeneous (the two parts being electrically connected). In addition, the current intensity through the membrane in the active part is the same as the one in the passive part (but in the opposite direction). If the membrane resistance is homogeneous and equal to R_e , this is

equivalent to consider that the potential differences across the membrane in the active and passive part are opposite (in blue):

$$U_{e,up} = V_{e,up}^a - V_{e,up}^c = V_{e,down}^c - V_{e,down}^a = -U_{e,down} \quad (2-7)$$

Value of Electrochemical potentials and overpotentials can then be added so that $\phi_{down}^c > \phi_{up}^c$ and $\phi_{up}^a < \phi_{down}^a$.

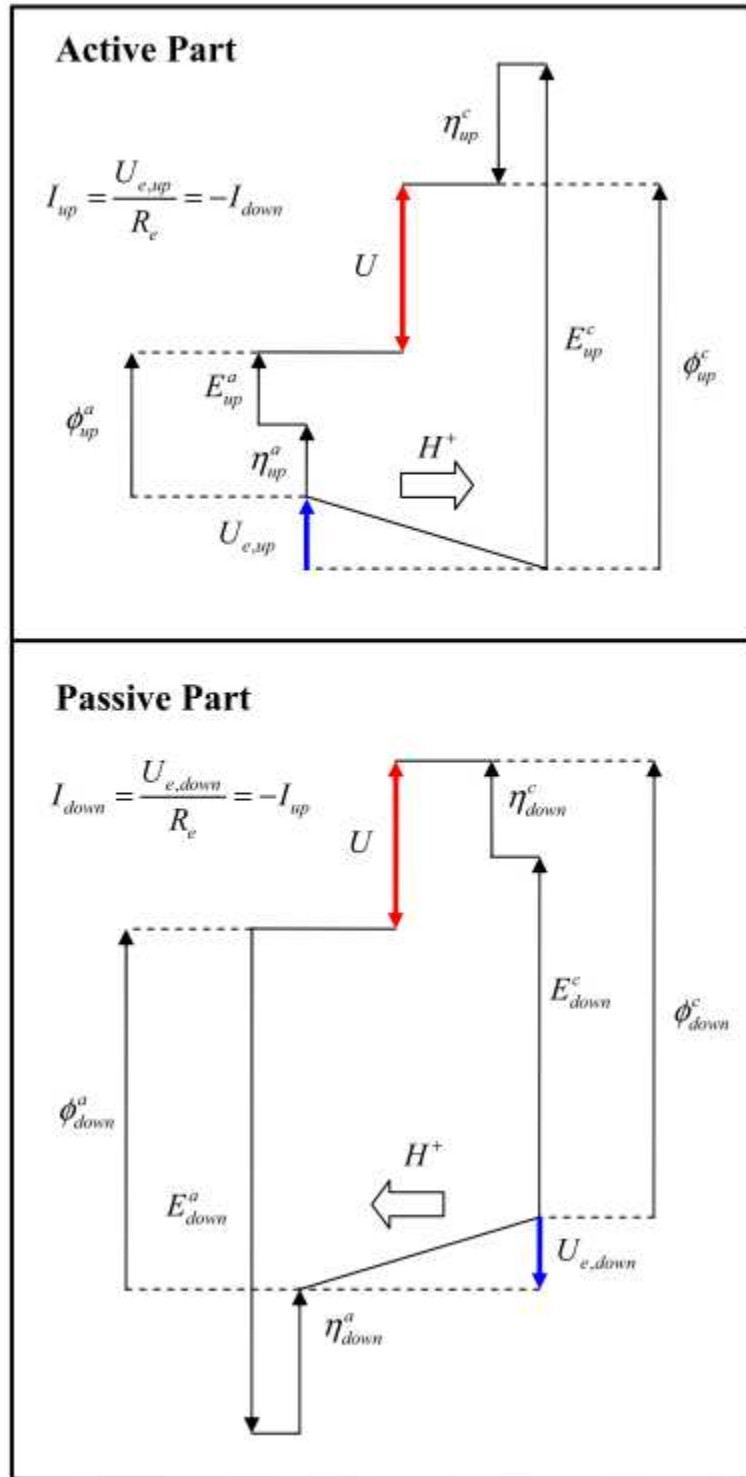


Figure 2-18. Potentials distribution during the first stage of the start-up of a cell.

c. Second stage of a start-up

The *second stage* of a start-up corresponds to an anode completely filled with hydrogen. In Figure 2-19, it begins the instant the second segment becomes active. At this time, the standard electrode potential of the 2nd segment decreases progressively from E_{O_2/H_2O} to E_{H^+/H_2} in the anode. This initiates simultaneously:

- The decrease of the anode potential in the 2nd segment ϕ_{down}^a which tends toward that of the 1st segment $\phi_{up}^a \approx 0V$.
- The increase of the electrolyte potential in the 2nd segment $V_{e,down}$. This leads to the decrease of the cathode potential in the second segment ϕ_{down}^c , which tends to that of the 1st segment ϕ_{up}^c .
- The redistribution of the charges accumulated in the capacities of the two segments at the cathode (the current flowing in the opposite direction of the current measured during the first stage, §0 and Figure 4-22 in §4.2.3).
- The homogenisation of the platinum oxide content between the first and the second segment resulting from the first stage in the cathode (the corresponding current flowing also in the opposite direction of the current measured during the first stage). This phenomenon is modelled in chapter 4 (§4.2.3).
- The transient increase of the fuel cell voltage above the open circuit voltage referred to as fuel cell overshoot (Figure 2-20, §0 and chapter 4).

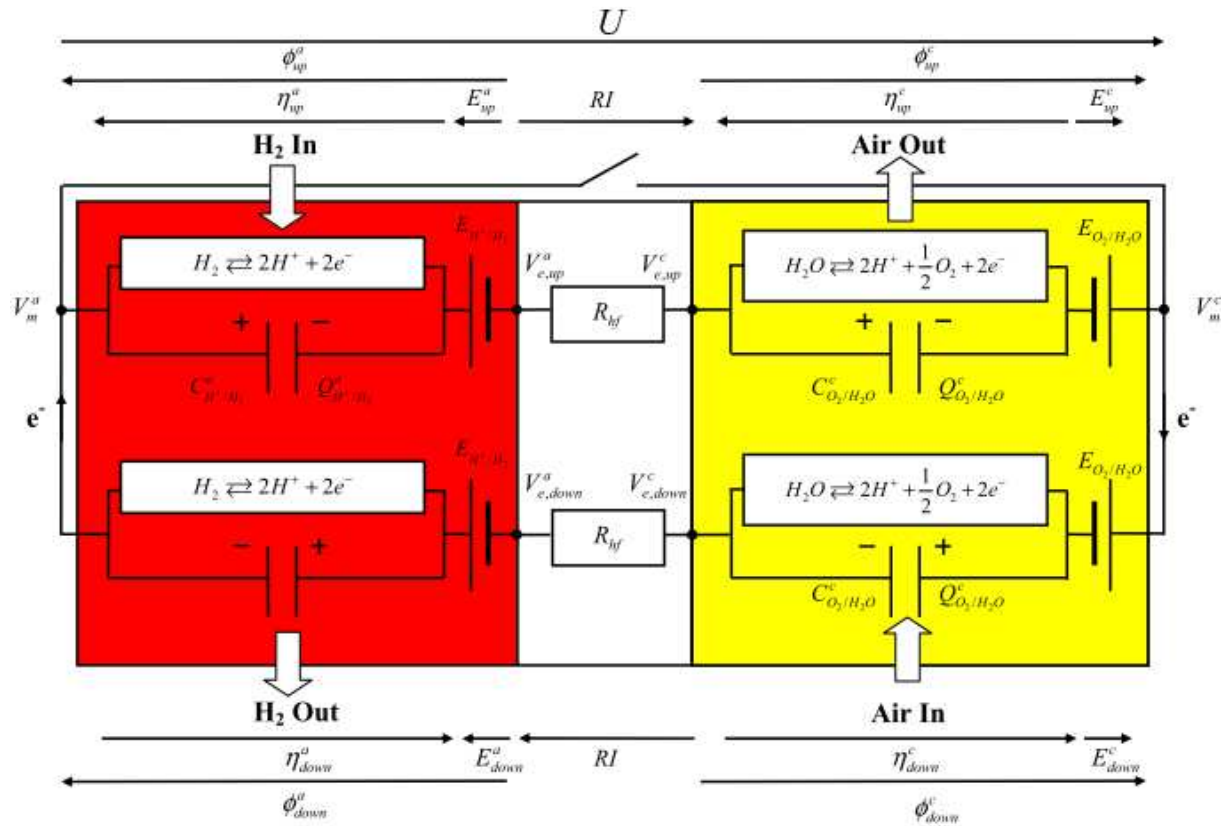


Figure 2-19. Equivalent electrical circuit corresponding to a start-up with the anode initially filled with air – Second stage, anode completely filled with hydrogen.

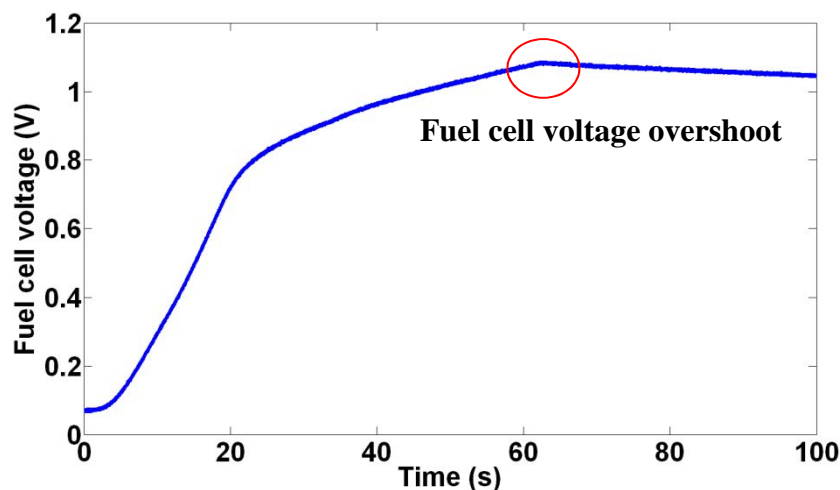


Figure 2-20. Fuel cell voltage measured with the 2D segmented cell during a start-up with the anode initially filled with nitrogen – experimental results measured with a hydrogen flow rate set to 0.2 slph. Air and hydrogen humidified to 100% RH, fuel cell temperature set to 50°C.

The confirmation by Shen et al. that ϕ_{down}^c reaches high values during the first stage of a start-up opens a discussion about the oxidation reactions taking place in this region. Indeed, no hydrogen can react here unless it crossed the membrane previously. The cyclic voltammetry measurements show that hydrogen permeation stands for only a few mA/cm² while reverse currents can be of the order of several hundreds of mA/cm². Reiser et al. considered only carbon oxidation and water splitting but several other reactions can also occur in this potential range, in particular those involving platinum [31]:

N°	Reaction	Standard Potentiel	E^0 (pH=4)
1	$Pt+H_2O=PtO+2H^++2e^-$	$E^0=0.980-0.0591pH$	$E^0=0.7436$
2	$PtO+H_2O=PtO_2+2H^++2e^-$	$E^0=1.045-0.0591pH$	$E_0=0.8086$
3	$PtO_2+H_2O=PtO^{3+}+2H^++2e^-$	$E^0=2.000-0.0591pH$	$E_0=1.7636$
4	$Pt^{2+}+H_2O=PtO+2H^+$	$\log(Pt^{2+})=-7.06-2pH$	$\log(Pt^{2+})=-15$
5	$Pt=Pt^{2+}+2e^-$	$E^0=1.188+0.0295\log(Pt^{2+})$	$E_0=0.7437$
6	$Pt=Pt^{2+}+2e^-$	$E^0=0.963+0.0295\log(Pt^{2+})$	$E_0=0.5187$
7	$Pt^{2+}+2H_2O=PtO_2+4H^++2e^-$	$E^0=0.837-0.1182pH-0.0295\log(Pt^{2+})$	$E_0=0.8085$
8	$Pt^{2+}+2H_2O=PtO_2+4H^++2e^-$	$E^0=1.062-0.1182pH-0.0295\log(Pt^{2+})$	$E_0=1.0335$

As far as carbon is concerned, the oxidation of oxygen surface groups can also be considered (§1.4.3). Furthermore, reversible or non degrading oxidation reactions are likely to participate to the reverse currents too. The identification of the different origins of the reverse currents is necessary to discriminate those which are harmful for the fuel cell.

In the next section, the segmented cell and the test bench developed by the LEMTA for the study of start-ups and shut-downs are presented. A first identification of the different contributions to the reverse currents is then attempted.

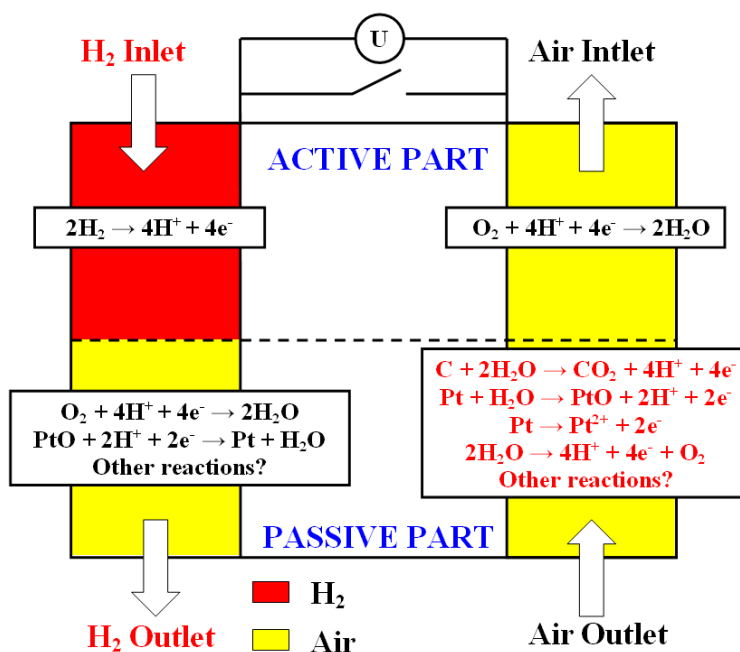


Figure 2-21. Reactions occurring during start-up, the anode compartment being initially filled with air.

2.2. 2D segmented cell and test bench

The experimental results presented in the following were obtained with the test bench depicted in Figure 2-22. This bench was developed in order to monitor a unique cell with 20 segments. Figure 2-23 shows pictures of this cell. The anode flow field plate was in gold plated aluminum. Except for the results presented in section §2.3, the anode plate was not segmented and it was also used to control the temperature in the cell thanks to a cooling circuit and a thermostated bath (Lauda RE104 – E100). The cathode compartment was machined in a polycarbonate plate (transparent but non conductive) and the current collection was made by 20 electrically insulated segments (Figure 2-23). The four 15 mm, 1 mm thick gold plated brass strips used for each segment delimit five parallel air channels (the depth and width of the 5 straight parallel channels are 0.7 mm × 1 mm, at the cathode and at the anode). Kapton sheets (2.3 mm × 1 mm × 80 μm) were used to isolate each strip from the adjacent ones. The four strips of each segment were electrically connected outside the cell, which amounts to averaging the current over the membrane width.

Gases were supplied through 7 mass flow controllers, which allowed selecting a broad range of flow rates. Hydrogen and air were introduced in the cathode and anode compartment in counter-flow. The gas lines also allowed flushing the anode with nitrogen or air, and the cathode with nitrogen. Each gas flowed first through a discharge tube before being introduced into the cell in order to improve the response of the mass flow controllers. All gases were humidified. When the cell was in regular operation, the local current densities reached up to 2 A/segment: these local current densities were measured thanks to 20 shunt resistors of 5 mΩ (Figure 2-24) and recorded by a data processing and acquisition system (National Instrument SCXI multiplexer) at a frequency of 200Hz. When voltammograms were recorded, the maximum current densities were of the order of 20 mA/segment and they were measured using Hall current sensors (CT 0.1-P - LEM - ±200mA). Cyclic voltammetry required also a power source (3A-20V) which was set in parallel with the cell and the load

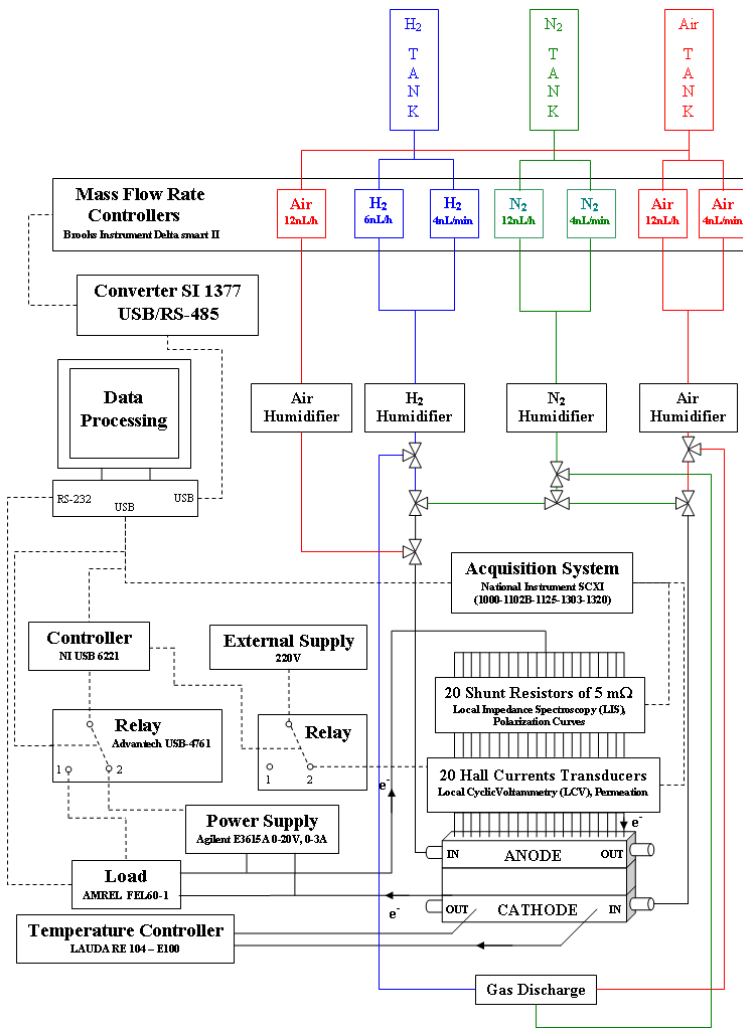


Figure 2-22. Gas lines and data acquisition and processing system.

150 μm PTFE gaskets were inserted between the MEA and the flow field plates. The plates were held together thanks to a set of 40 BoLts tightened to a torque of about 2.5 Nm.

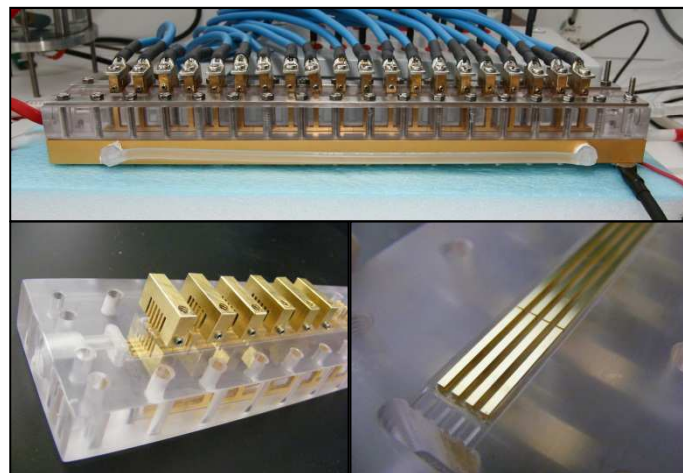


Figure 2-23. Segmented cell and close-up on the current collection strips.

A Labview program enabled to control the mass flows and the operation of the valves as functions of the experimental data: temperature, voltage and local currents. Local impedance spectroscopy was performed in galvanostatic mode with a frequency range of 0.25 to 800 Hz and with an amplitude of the (total) current oscillation equal to 5% of the steady state value (with a National Instrument USB 6221 load controller).

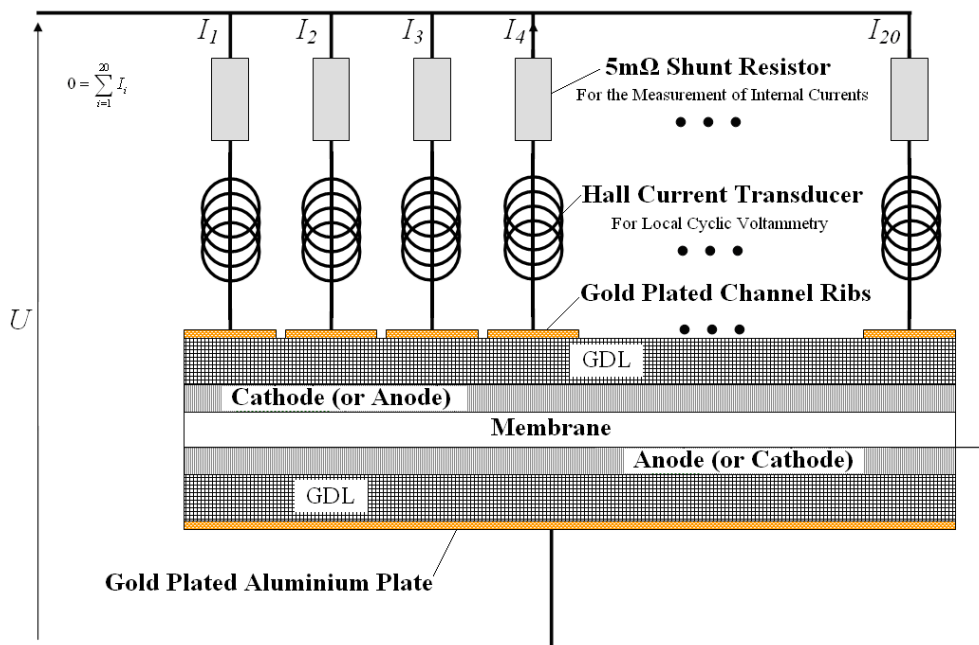


Figure 2-24. Segmented cell electrical connections.

The CO₂ emissions were measured during fuel cell steady state and transient operation using a single beam Infrared Multi-Component Analyzer -CAI 600 series-. The air feeding the fuel cell was filtered using soda lime to eliminate carbon dioxide at the cathode inlet. The cathode exhaust gases were thoroughly dehydrated using a condenser and a home-made Nafion[®] membrane dryer.

The characteristics of the different MEAs tested are listed in Annex 1. If not specified otherwise, the MEA used is a Johnson Matthey with 0.2 mg/cm² of platinum in the anode, 0.6 mg/cm² of platinum in the cathode and a 30 μm thick PFSA membrane.

2.3. Charge balance

Internal currents measured at one electrode provide information about the flow of the protons in the direction perpendicular to the membrane. However, one cannot exclude a priori the possibility that some of the protons produced in the active part of the anode flow along the membrane to react with oxygen present in the passive part of the cell (Figure 2-25).

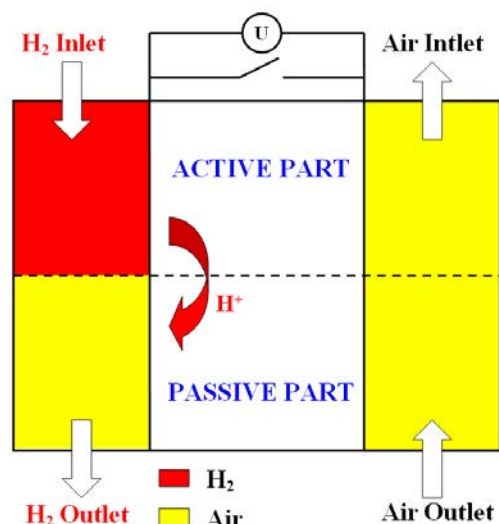


Figure 2-25. Reactions occurring during start-up assuming possible flow of protons along the membrane from the active to the passive part of the anode compartment (initially filled with air).

This information can be obtained using a cell segmented on both electrodes and by comparing the internal currents measured on both sides. The results are presented in Figure 2-26.

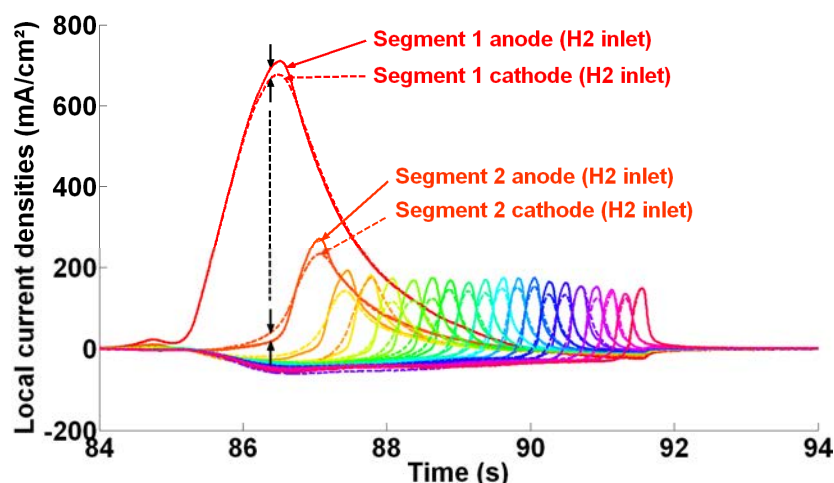


Figure 2-26. Local current densities measured at the anode and at the cathode segments during a start-up with the anode compartment initially filled with air (H_2 flow rate = 2 slph, air flow rate = 20 slph). Air and hydrogen humidified to 100% RH (MEA Johnson Matthey, Pt loading = $0.6 \text{ mg}_{Pt}/\text{cm}^2$, cell temperature = 60°C).

The curves in Figure 2-26 show only a small discrepancy between the internal currents measured at the anode and at the cathode. This is probably due to the non-uniformity of the contact resistances between the collecting strips and the gas diffusion layers, which leads to a redistribution of the electrons between successive segments: one can check that the difference between the anode and cathode currents is exactly compensated from one segment to another. Moreover, the total amount of charge produced at the anode is the same as the one consumed at the cathode (the difference is below 3%). Consequently, the flow of protons along the membrane can be considered as negligible: using a fuel cell segmented at the cathode only is sufficient to measure accurately the internal currents.

The assessment of the number of segments needed to achieve a satisfying measurement of the internal currents is presented in §0.c. The reproducibility of the internal currents measurement is evaluated in §2.8.2.b.

2.4. Start-up with the 2D segmented cell

Potentials distribution

A first series of potential measurements were performed using the 2D segmented cell to check the results of Shen et al. [101]. For this, the first and the last segments were electrically disconnected from the rest of the cell (Figure 2-27): we used isopropanol and a cotton swab to remove a thin strip of electrodes and GDL between segment 1 and 2 and between segment 19 and 20. The MEA was purchased from Johnson Matthey (see Annex 1).

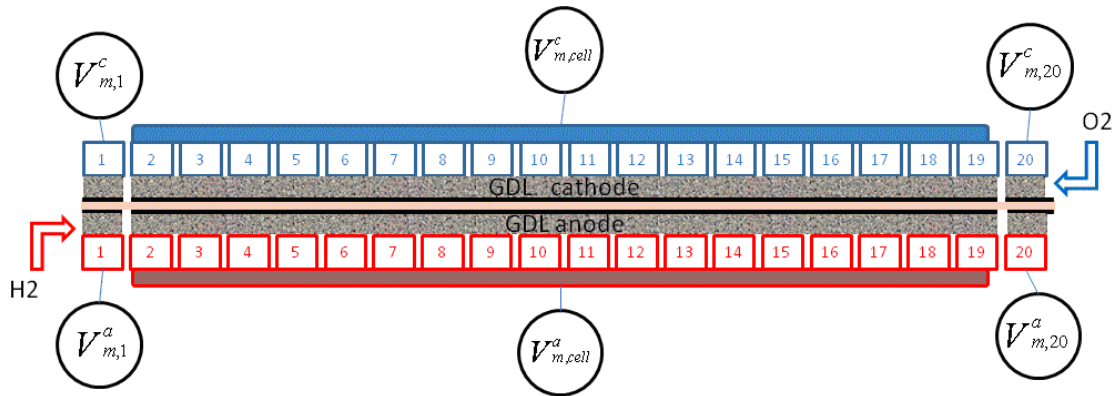


Figure 2-27. 2D Segmented cell with first and last segments electrically disconnected.

The electrical equivalent circuit corresponding to this cell is depicted in Figure 2-28. During a start-up, the lateral current I_L flowing in the direction of the membrane plane between the 20th and the 19th segments was assumed null:

$$I_L = 0 \text{ A} \quad (2-8)$$

As a consequence, the cathode potential of the 19th segment is given by:

$$\phi_{19}^c = V_{m,cell}^c - V_{m,20}^c + \phi_{20}^c \quad (2-9)$$

Since the last segment was electrically disconnected from the others, there was no overpotential at the anode and cathode ($\eta_{20}^a = \eta_{20}^c = 0\text{V}$), which means that before start-up (when both compartments were filled with air) the potentials were equal to the equilibrium potential of the O₂/H₂O oxidoreduction reactions E_{O_2/H_2O} . Actually, we had mixed potentials of about 1V:

$$\phi_{20}^a = \phi_{20}^c \approx 1\text{V} \quad (2-10)$$

Thus, by measuring $V_{m,cell}^c - V_{m,20}^c$, it was possible to estimate the cathode potential of the 19th segment. The anode potential of the 19th segment was also accessible:

$$\phi_{19}^a = V_{m,cell}^a - V_{m,20}^a + \phi_{20}^a \quad (2-11)$$

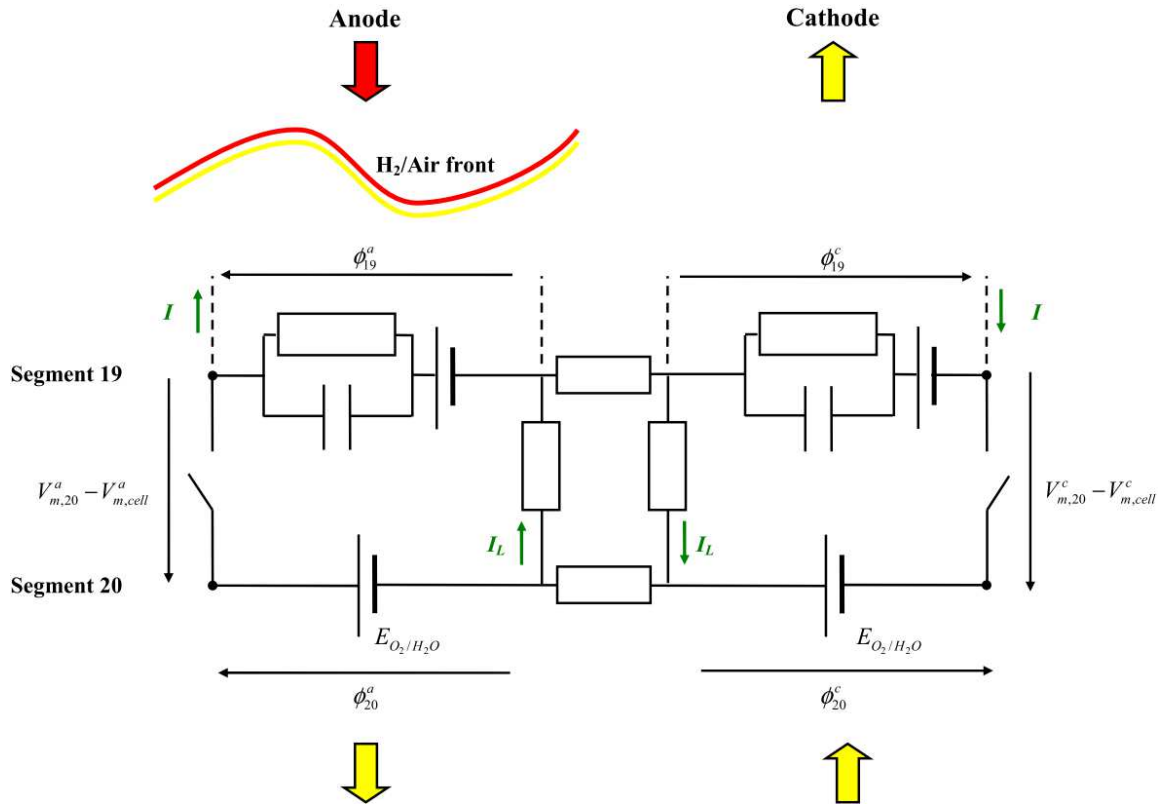
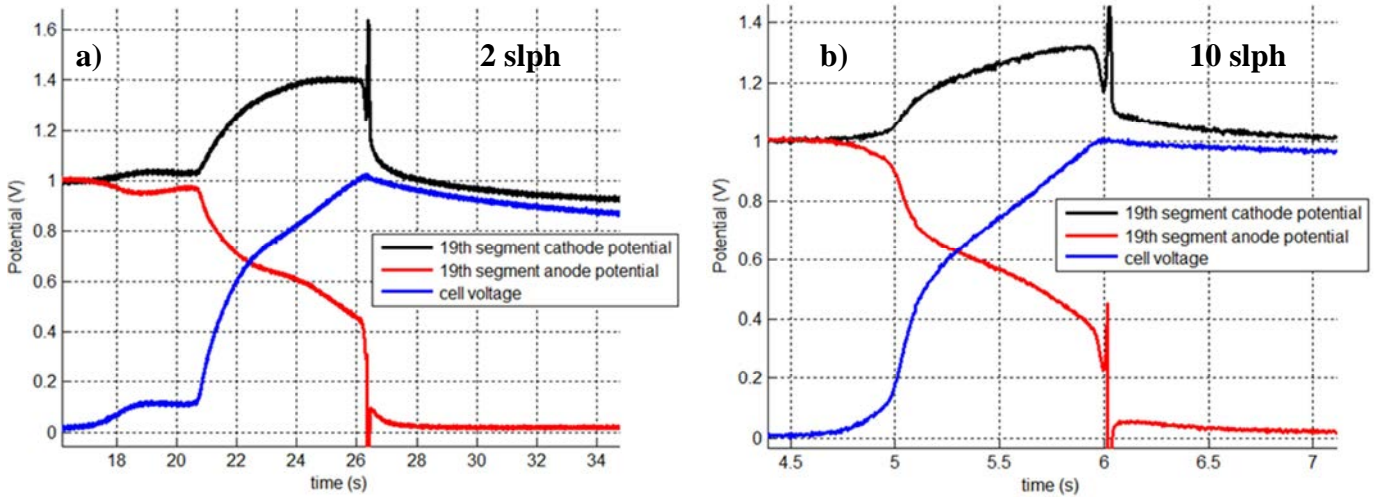


Figure 2-28. Electrical equivalent circuit of the 2D segmented cell close to the hydrogen outlet during a start-up by injection of hydrogen in air. The last segment was electrically disconnected from the rest of the cell.



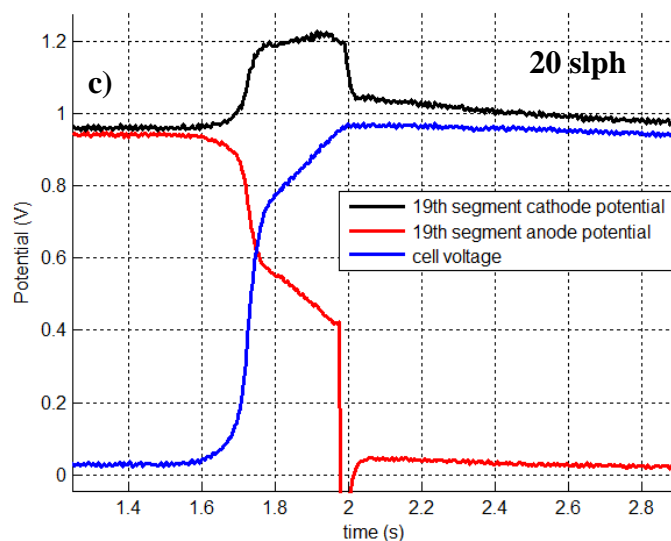


Figure 2-29. Anode and cathode potentials ϕ_{19}^a and ϕ_{19}^c in the 19th segment and fuel cell voltage vs. time during start-up. Injection of hydrogen in air at a) 2 slph, b) 10 slph and c) 20 slph.

Figure 2-29 shows that the values of the anode and cathode potentials ϕ_{19}^a and ϕ_{19}^c measured in the 19th segment were close to those obtained by Shen et al. in the downstream part of their cell (Figure 2-17). The hydrogen flow rate seems to play a role in the the maximum value reached: at 2 slph, the cathode potential ϕ_{19}^c exceeded shortly 1.6 V while at 20 slph, it barely went over 1.2 V. Performing a start-up at low hydrogen flow rate combines thus the disadvantages of reaching higher cathode potential and remaining in this condition for a long time.

This first method only allowed an estimation of the anode and cathode potential in the 19th segment. Therefore, a new cell was developed and built to measure local potentials all along the gas channels thanks to local reference hydrogen electrodes (Figure 2-30). The MEA used with this cell had a membrane broader than the active surface (Figure 2-31). 20 gas diffusion electrodes, electrically insulated from each other, were placed on the top of the membrane which protruded from the anode. A supplementary channel was machined in the anode flow field plate. This channel was only used to supply the 20 GDE with hydrogen, even when the anode compartment was flushed or filled with air (Figure 2-32). Thus, each of them could be regarded as a local Reference Hydrogen Electrode. To prevent gas permeation, a gasket was placed between the channel supplying the local RHE and the anode channels. The cathode was also segmented to measure the internal currents during start-up.

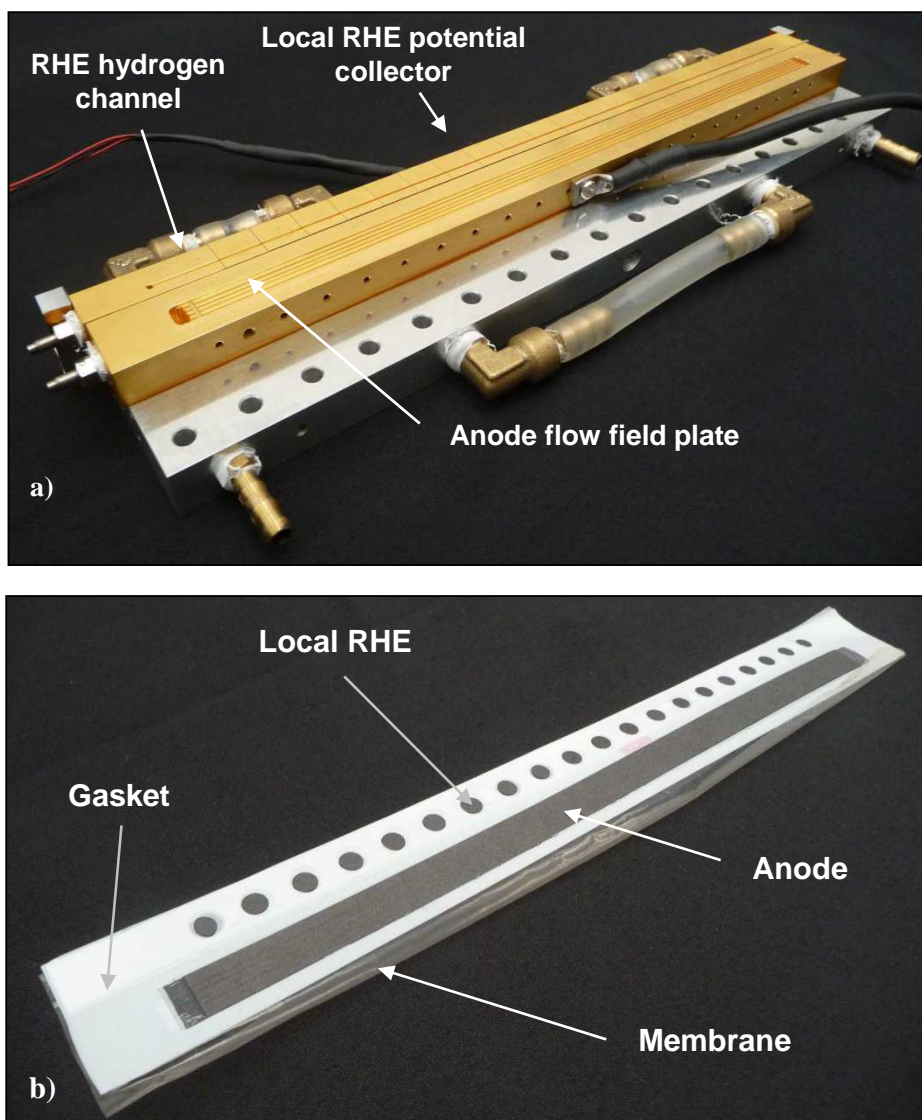


Figure 2-30. a) Anode side of the cell: the anode flow field plate was completed by a segmented plate used for the hydrogen supply and the potential collection of the local Reference Hydrogen Electrodes (RHE). b) The anode active layer and the RHE shared the same membrane. A gasket prevented gas leakage between the RHE and the anode compartment.

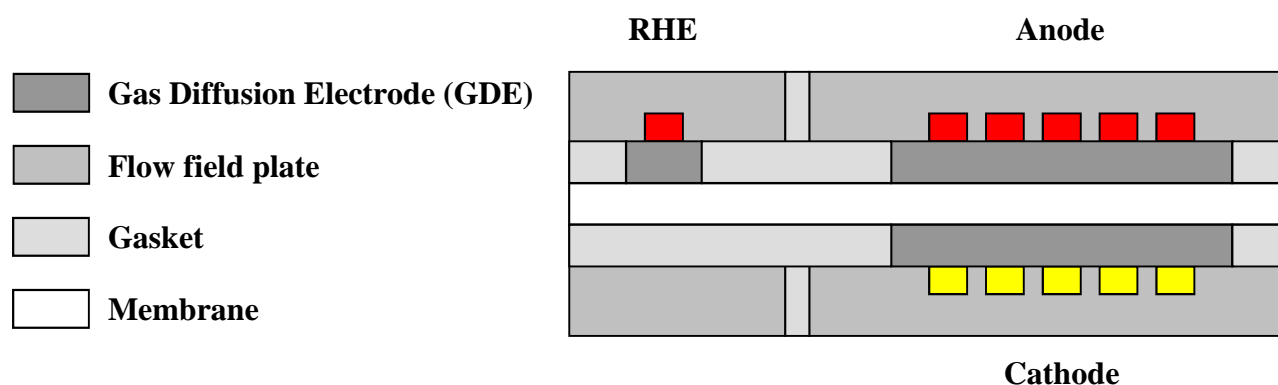


Figure 2-31. Cross-section of the fuel cell equipped with local Reference Hydrogen electrodes.

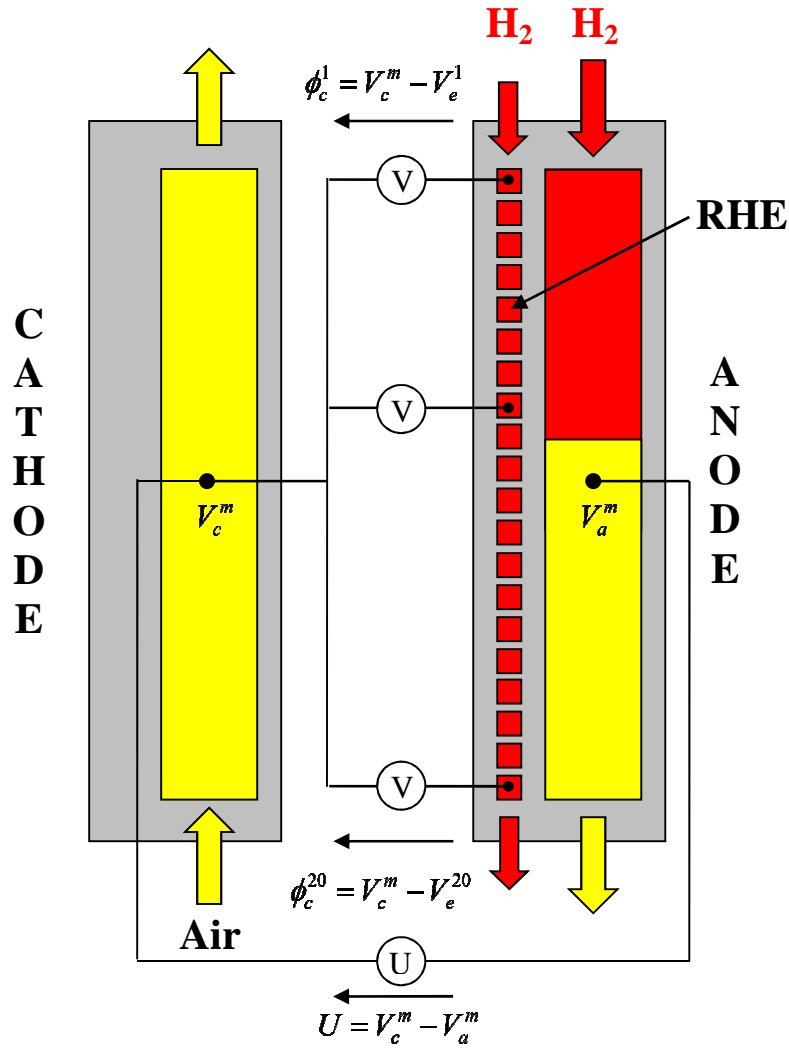


Figure 2-32. Schematic of the segmented cell equipped with local reference hydrogen electrodes (RHE) during a start-up by injection of hydrogen in air in the anode compartment. Anode and cathode are represented side by side.

One can define the local RHE potential $\phi_{RHE}(i)$ by:

$$\phi_{RHE}^i = V_m^{RHE}(i) - V_e^i = 0V \quad (2-12)$$

With $V_m^{RHE}(i)$ the local metal potential and V_e^i the local electrolyte potential of the i^{th} RHE. ϕ_{RHE}^i was assumed constant.

Therefore, the metal potential of the RHE was locally equal to that of the membrane:

$$V_m^{RHE}(i) = V_e^i \quad (2-13)$$

The local cathode potential $\phi_c(i)$ can be expressed as:

$$\phi_c(i) = V_c^c - V_m^{RHE}(i) \quad (2-14)$$

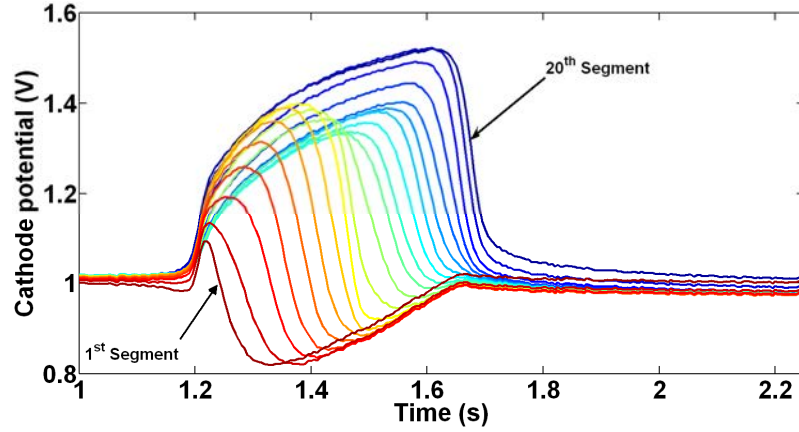


Figure 2-33. Experimental local cathode ϕ_c^n potential during a start-up by injection of hydrogen in air at 10 slph.

And knowing the fuel cell voltage $U = V_m^c - V_m^a$, one can access the local anode potential $\phi_a(i)$:

$$\phi_a(i) = \phi_c(i) - U \quad (2-15)$$

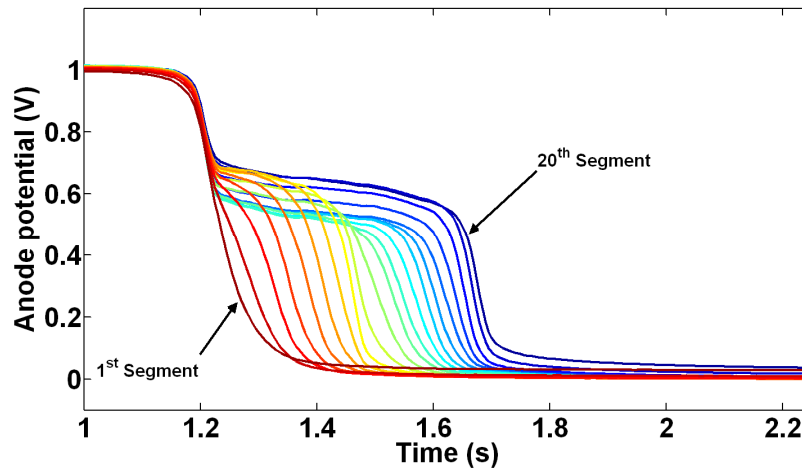


Figure 2-34. Experimental local anode ϕ_a^n potential during a start-up by injection of hydrogen in air at 10 slph.

By comparison, Shen et al could measure a non zero potential difference between the metal potential of their RHE V_m^{RHE} and the potential of the electrolyte in the active $V_{e,up}$ and passive $V_{e,down}$ parts (Figure 2-15). Contrary to our experimental set-up, they did not segment their RHE. The interfacial potential between the metal and the electrolyte should then be given by:

$$\phi_{RHE} = V_m^{RHE} - \frac{1}{N} \sum_i^N V_e^i = 0V \quad (2-16)$$

Or:

$$V_m^{RHE} = \frac{1}{N} \sum_i^N V_e^i \quad (2-17)$$

However, their measurement of the cathode potential remained valid since they proceeded as follow:

$$\begin{aligned}\phi_c^{down} &= (V_m^c - V_m^{RHE}) - (V_{e,down} - V_m^{RHE}) \\ \phi_c^{down} &= V_m^c - V_{e,down}\end{aligned}\tag{2-18}$$

Another possible comparison with the work of Shen et al. consists in considering the electrolyte potential difference between the upper and lower part of the cell: $V_{e,up} - V_{e,down}$ (Figure 2-16). This difference could also be expressed using the cell equipped with local RHE, for instance between the 1st and the 20th segments (Figure 2-35):

$$V_e^1 - V_e^{20} = \phi_c^{20} - \phi_c^1\tag{2-19}$$

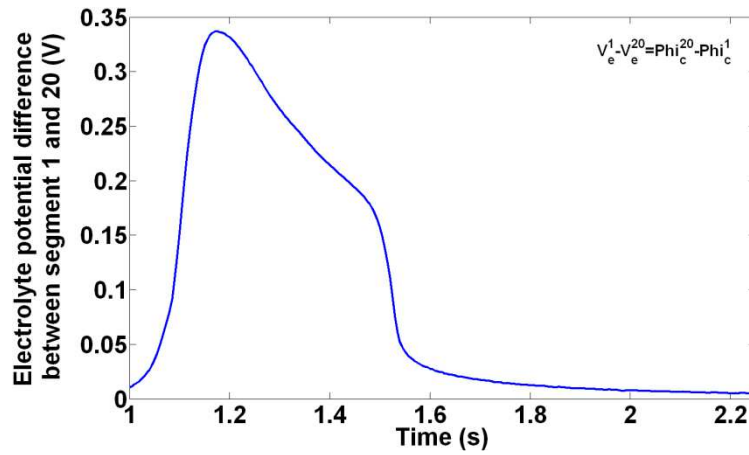


Figure 2-35. Electrolyte potential difference between segment 1 and 20 (V) measured during a start-up by injection of hydrogen in air at 10 slph.

While the values reached are different, the variation of the electrolyte potential difference between the upper and lower part of the cell we measured was similar to that observed by Shen et al. A quantitative comparison would require to use strictly similar cell and hydrogen injection flow rate.

The local measurement of anode and cathode potentials opens up interesting possibilities such as the realisation of anode and cathode polarization curves. Local impedance spectroscopy can also be applied simultaneously to both electrodes. This information could be useful to identify the respective contribution of each electrode to the degradation mechanisms but also to the performance of the cell. Such studies are to be considered as perspectives of this Ph.D (chapter 5)

Local current densities and charges during a start-up

a. Internal currents

When a fuel cell is started-up, the gas shift induces the appearance of potential differences between the active and passive parts ($\phi_{up} \neq \phi_{down}$) but also within the membrane ($V_{e,up} \neq V_{e,down}$). Due to these driving forces, electrical charges are set in motion. The 2D segmented cell

enabled the measurement of these charge transfers within the cathode. Figure 2-36 shows the evolution of the local current densities measured in all cathode segments during different start-ups: in air or in nitrogen and using different hydrogen injection flow rates. Note that the current density profiles were similar for all of them. However, differences appeared in term of characteristic time (i.e, start-up duration) and maximum values (Figure 2-36). Thus for a given hydrogen flow rate, a start-up in air led to higher current densities than a start-up in nitrogen. Likewise, for identical gas filling initially the anode, the local current densities increased with the hydrogen flow rate. This was particularly noticeable for the first segment.

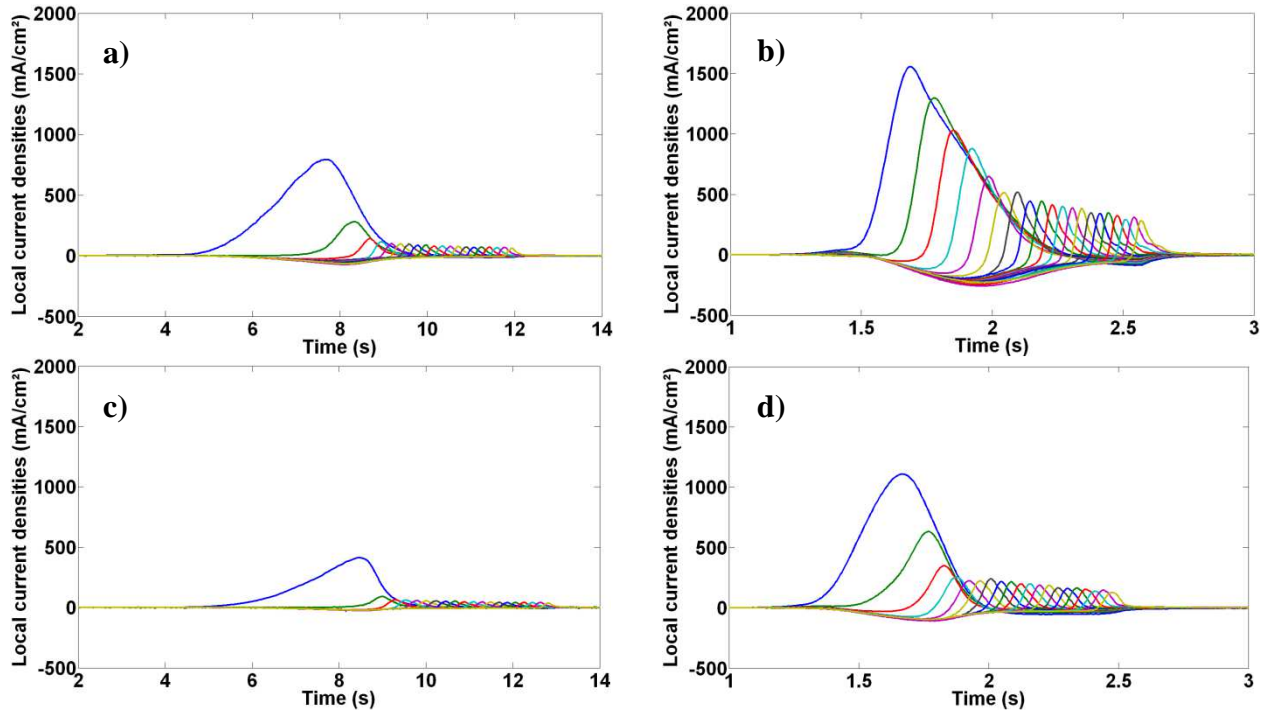
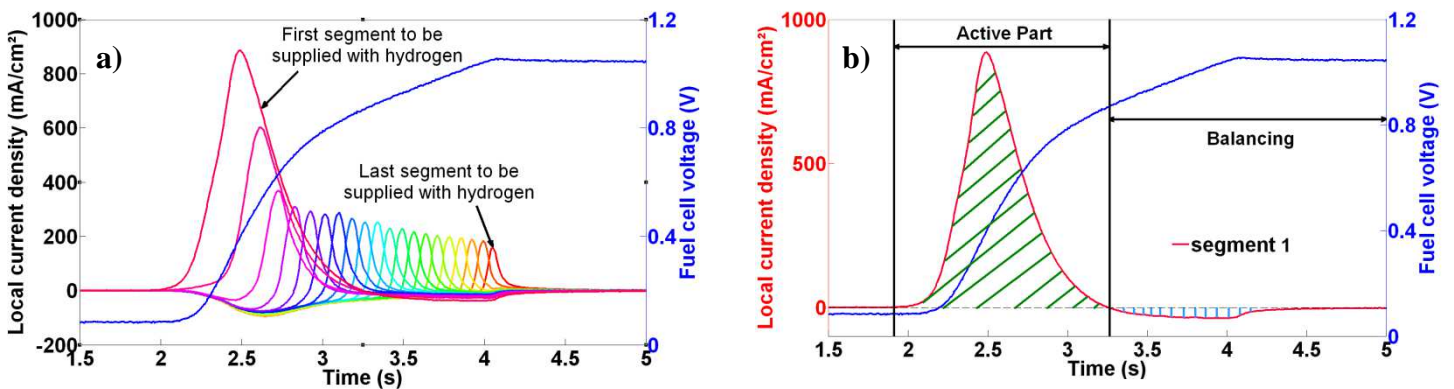


Figure 2-36. Local current density profiles for a) Start-up in air, hydrogen flow rate=2slph; b) Start-up in air, hydrogen flow rate=10slph; c) Start-up in nitrogen, hydrogen flow rate=2slph; d) Start-up in nitrogen, hydrogen flow rate=10slph (MEA Johnson Matthey, Pt loading = 0.6mgPt/cm², cell temperature = 60°C).

Figure 2-37 a) shows the evolution of the local current densities measured in all cathode segments during a start-up with the anode initially filled with nitrogen. In the following, the focus is put on current density profiles measured in the first segment supplied with hydrogen (Figure 2-37 b)), in a segment located at equal distance from the anode inlet and outlet (Figure 2-37 c)) and in the last segment (Figure 2-37 d)).



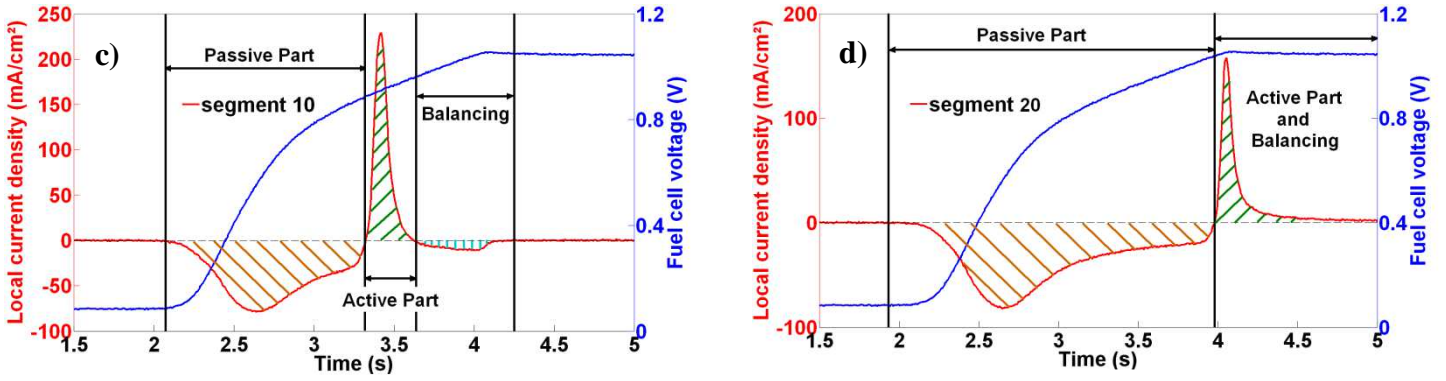


Figure 2-37. a) Current density measured in each of the 20 cathode segments and fuel cell voltage increase (vs. time) during start-up. Anode initially filled with nitrogen; hydrogen flow rate set to 5 slph. Air and hydrogen humidified to 100% RH (MEA Johnson Matthey, Pt loading = 0.6mgPt/cm², cell temperature = 60°C). b) Current density in the anode first segment and fuel cell voltage (vs. time) during start-up. c) Current density in the anode 10th segment (of 20) and fuel cell voltage (vs. time) during start-up. d) Current density in the anode last segment and fuel cell voltage (vs. time) during start-up.

The first segment supplied with hydrogen was always active while all the others became successively active once in the presence of hydrogen. As there is also a capacitive contribution to the internal currents, a redistribution of charges occurred when the faradic reactions stopped. At this time, the first segment released some of the electrons it had accumulated at the cathode - which corresponds to a negative current in Figure 2-37 b) and c) whereas the inverse phenomenon occurs in the last segment. As shown later, this redistribution of charge was also due to the homogenisation of the platinum oxide content through the cathode catalyst layer (a platinum oxide gradient was created during start-up, see §4.2.3).

b. Definition and identification of the charges

The balance of charge showed that the time and space integral of the negative currents was strictly equal to that of the positive currents. Starting from these considerations, it is possible to define three types of charge exchange during the start-up sequence:

- (i) Passive charges, corresponding to the integral of the negative currents (reverse currents) measured in the passive part of the fuel cell (orange striped area in Figure 2-37 c) and d)),
Locally:

$$Q_P(seg(i)) = S_{seg} \cdot \int_{Passive_part} j_{seg(i)} \cdot dt < 0 \quad (2-20)$$

And globally:

$$Q_P = \sum_{i=1}^{20} Q_P(seg(i)) = S_{seg} \cdot \sum_{i=1}^{20} \int_{Passive_part} j_{seg(i)} \cdot dt < 0 \quad (2-21)$$

- (ii) Balancing charges, exchanged during the redistribution stage once all segments became active; the negative balancing charges correspond to the blue striped area in Figure 2-37 b) and c),

Locally:

$$Q_B(seg(i)) = S_{seg} \cdot \int_{Balancing} j_{seg(i)} \cdot dt < 0 \quad (2-22)$$

And globally:

$$Q_B = \sum_{i=1}^k Q_B(seg(i)) = S_{seg} \cdot \sum_{i=1}^k \int_{Balancing} j_{seg(i)} \cdot dt < 0 \quad (2-23)$$

- (iii) Active charges, corresponding to the integral of the positive current measured in the active part minus the positive balancing charges (equal in absolute value to the negative balancing charges).

Locally:

$$Q_{green_area}(seg(i)) = S_{seg} \cdot \int_{Green_area} j_{seg(i)} \cdot dt \quad (2-24)$$

$$Q_A(seg(i)) = Q_{green_area}(seg(i)) - Q_B(seg(i)) > 0 \quad (2-25)$$

And globally:

$$Q_{green_area} = \sum_{i=1}^{20} Q_{green_area}(seg(i)) = S_{seg} \cdot \sum_{i=1}^{20} \int_{Green_area} j_{seg(i)} \cdot dt \quad (2-26)$$

$$Q_A = Q_{green_area} - Q_B > 0 \quad (2-27)$$

At a local scale, it is worth mentioning that the time and space integral of the negative currents differ from that of the positive currents.

$$Q_A(seg(i)) + Q_B(seg(i)) + Q_P(seg(i)) \neq 0 \quad (2-28)$$

The location of the segments between the hydrogen inlet and outlet results in differences in the charges exchanged as defined in equations (2-20), (2-22), (2-25) (Figure 2-38).

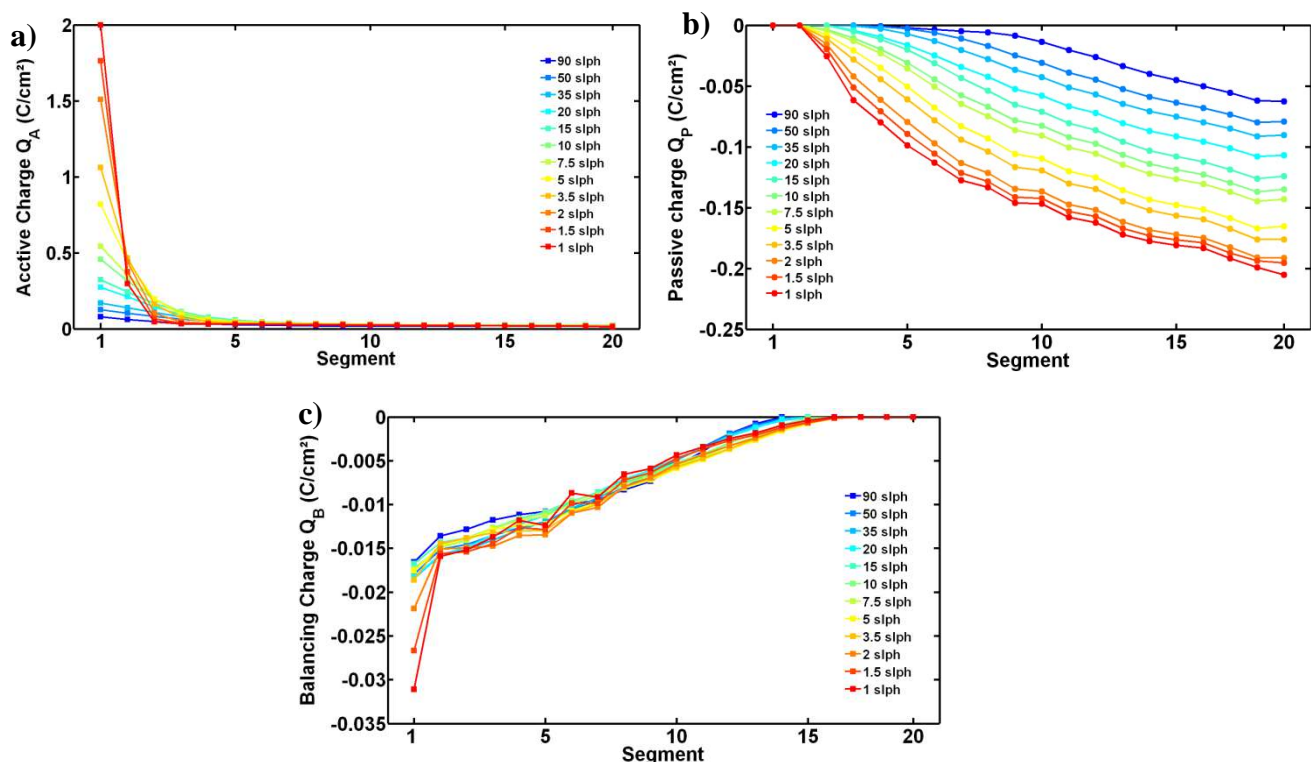


Figure 2-38. Local active a), passive b) and balancing c) charges exchanged over each segment vs. the hydrogen flow rate. Single start-ups in air (MEA Johnson Matthey, Pt loading = $0.6\text{mgPt}/\text{cm}^2$, cell temperature = 60°C).

The charges corresponding to the positive currents Q_A were mainly produced by the first and second segments following the hydrogen inlet. The currents flew homogeneously through the segments located in the passive region (Figure 2-37). However, the segments located close to the hydrogen outlet remained passive a longer time than those located upstream. As a consequence, higher values of Q_p were recorded close to the anode outlet. The amount of balancing charges was higher close to the anode inlet, possibly because the double layer capacities were the most charged.

As most of the degradations occur in the passive region, the study of the charge resulting from the reverse currents is of primary interest. This is the marker we use in the next sections. It is referred to as **the charge exchanged**.

c. Limitation concerning the charges measured

The hydrogen injection flow rate is the main parameter characterising a start-up but it must be mentioned that the velocity of the hydrogen/air or hydrogen/nitrogen front is not a straightforward function of it. The observation of the front velocity was made possible starting from the internal currents: during a start-up, the segments are first passive and they become active once supplied with hydrogen. The transition corresponds to a change in the direction of the current flowing through each segment. Thus, it was possible to follow the motion of the hydrogen/air or hydrogen/nitrogen front within the cell (Figure 2-39).

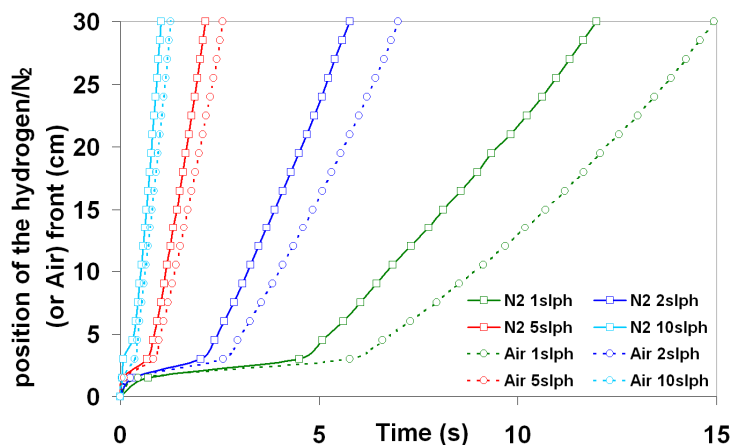


Figure 2-39. Position of the hydrogen/air or hydrogen/nitrogen front versus time during start-up at different hydrogen flow rate.

Table 2-1 lists the effective velocities of the hydrogen/nitrogen and hydrogen/air fronts. They were estimated from the shift in the direction of the internal currents during single start-ups performed with three different values of hydrogen injection flow rate. They can be compared to theoretical velocities corresponding to the filling of the gas channels plus the GDL by hydrogen (the porosity of the GDL was set to 0.84). From the comparison between theoretical and effective velocities, it appears that:

- The GDL has to be taken into account;
- Even so, the theoretical velocities remain below the effective values.

The most probable explanation for this difference is that the consumption of hydrogen slowed down the front. This hypothesis is consistent with Figure 2-39, which shows that the motion of the front was slower for the two first segments where, according to Figure 2-38, hydrogen consumption was the highest. This could also explain why the effective velocity of the hydrogen/nitrogen front was faster than that of the hydrogen/air front for identical hydrogen injection flow rates. Indeed, the next section shows that a start-up by injection of hydrogen in nitrogen involved fewer charges than by injection of hydrogen in air (the presence of nitrogen limiting the reduction reactions in the passive part of the anode).

H ₂ flow rate (slph)	Velocity (m/s)			
	Theoretical channel	Theoretical channel +GDL (420μm, $\epsilon_{GDL} = 0.84$)	Effective Start-up in N ₂	Effective Start-up in Air
2	0.16	0.09	0.05	0.04
10	0.79	0.43	0.29	0.24
20	1.59	1.28	0.59	0.50

Table 2-1. Theoretical and effective velocities during start-up in air and in nitrogen at different hydrogen injection flow rates.

The difference between the effective and theoretical times needed by the hydrogen front to completely fill the anode compartment corresponds to an additional volume of hydrogen which can be converted into an electrical charge (assuming that all this hydrogen reacts electrochemically). Surprisingly, this equivalent charge was much higher than that actually measured with the forward currents (see the last four columns of Table 2-2). Several reasons can explain this strong difference:

- Hydrogen can chemically reacts with oxygen.
- Internal currents occurred within a same segment between land and channel. Such internal currents have been evidenced by Schneider et al [108] (§2.1.1).
- Internal currents could also occur between the inlet and the outlet part of a segment. The accuracy of charge measurements was therefore assessed by considering the charge exchanged between the active and passive parts of the cell as a function of the number of segments along the cell (the total length of the air and hydrogen channels is 30 cm). Figure 2-40 shows that there is a threshold value (10 segments of 3 cm in length) below which the charge exchanged is clearly underestimated because internal currents within each segments are not measured. According to these results, dividing the cell into 10 segments leads to a measurement error lower than 1% (compared to 20 segments).
- The results of start-up simulations presented in the fourth chapter show that the charge calculating from the forward currents to evaluate the hydrogen consumption underestimate the effective value (Figure 4-26).

However, no quantitative data allowed concluding which of these contributions is the main responsible for the hydrogen consumption.

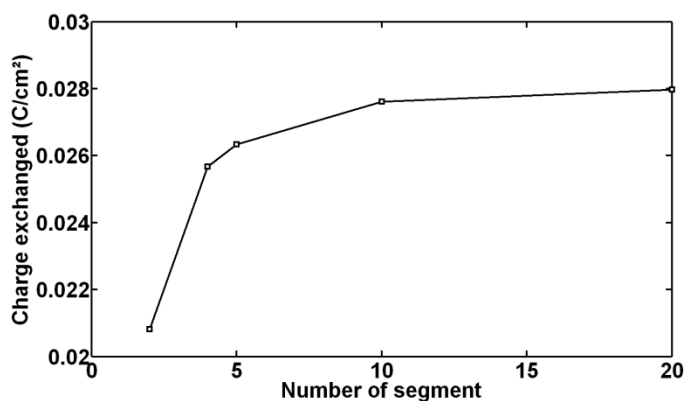


Figure 2-40. Charge exchanged vs. the number of segment along the cell. Start-up were realised by injecting 10 slph of hydrogen in air-filled anode.

Once hydrogen had flown through the first three segments, the front moved regularly until it reaches the outlet of the anode. During this second phase, very small amounts of hydrogen were consumed (Figure 2-38 a)) and the velocity of the front remained nearly constant.

Flow rate (slph)	filling time (s)				Δt (eff-theo) (s)		Equivalent charge density (C/cm ²)		Effective charge (C/cm ²)	
	Theoretical		Effective		$\Delta t_{N_2} = t_{N_2} - t_{theo}$	$\Delta t_{air} = t_{air} - t_{theo}$	Δt_{N_2}	Δt_{air}	SU in N ₂	SU in Air
	channels	channels + GDL	SU in N ₂ t_{N_2}	SU in air t_{air}						
2	1,89	3,8	6	7,5	2,2	3,7	0,33	0,55	0,06	0,11
10	0,38	0,76	1,03	1,25	0,28	0,49	0,21	0,37	0,04	0,06
20	0,19	0,38	0,51	0,6	0,13	0,22	0,19	0,33	0,03	0,04

Table 2-2. Theoretical and effective filling times. Equivalent charge densities calculated from the difference between the effective and theoretical filling times.

d. Charge exchanged vs. hydrogen injection flow rate

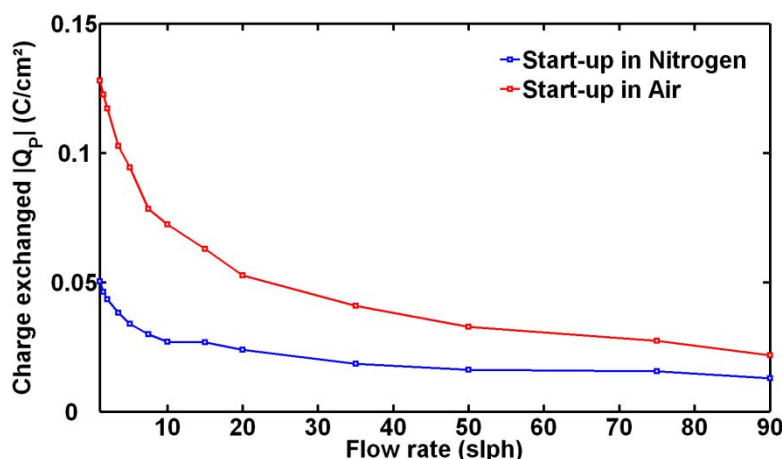


Figure 2-41. Charge exchanged $|Q_P|$ during start-ups vs. hydrogen injection flow rate. Anode initially filled with nitrogen or air. All gases humidified to 100% RH (Johnson Matthey MEA, Pt loading = $0.6\text{mgPt}/\text{cm}^2$, cell temperature = 60°C).

Although the increase of the hydrogen injection flow rate led to higher current densities during start-up (Figure 2-36), Figure 2-41 shows that the total amount of charges exchanged decreased.

This evolution has to be related to the kinetic of the faradic reactions. While capacitive currents are almost instantaneously generated ($\tau = R_{hf} \cdot C_{dla} = 1\text{ms}$ with C_{dla} the anode capacity estimated to $100\text{ F}/\text{m}^2$ with the EIS and the R_{hf} the high frequency resistance of about 1.10^{-5} ohm.m^2), certain electrochemical reactions are slow (§4.2.1). At low hydrogen flow rate, the hydrogen front in the anode moved slowly enough so that the reactions with low kinetics like carbon oxidation in the passive part of the cathode could occur. When the front moved faster, the extent of these reactions was then more limited. At high hydrogen flow rate, the capacitive currents should thus become predominant compared to the faradic ones. This is supported by the fact that the two curves in Figure 2-41 tend toward the same limit at high hydrogen flow rate and by the numerical simulation of start-ups presented in §4.2.3.

Figure 2-41 also shows the significant impact of the gas filling initially the anode compartment on the amount of charges exchanged during the start-up sequence: it was much lower in the presence of nitrogen. In a first approximation, if nitrogen was the only species considered in the passive part of the anode, no reduction reactions would occur there and reverse currents would have thus been only capacitive. This would explain why the charge exchanged was more important when air was used since in this case electrochemical reactions were enabled. In practice, electrochemical reactions involving platinum, carbon or oxygen permeating through the membrane still occurred when nitrogen is present in the passive part (§4.2.3). However due to the low platinum loading in the anode and the slow permeation of oxygen, these reactions were rather limited except, for the slowest start-ups. Indeed, when hydrogen was injected in nitrogen at 2 slph for instance, the start-up lasted about 6 seconds (Table 2-2): with an oxygen permeation current of about $5\text{ mA}/\text{cm}^2$, the corresponding contribution of oxygen to the charge density was of about $0.03\text{ C}/\text{cm}^2$, which is not negligible anymore.

Moreover, the curves in Figure 2-41 are in agreement with the results of Shen et al., who observed also a strong correlation between the hydrogen injection flow rate and the time the cathode potential remained high in the passive part: the higher the flow rate, the shorter the

potential is maintained at its maximum value Figure 2-42. The cathode potential of segment 19 in § 0 also confirmed this observation (Figure 2-29).

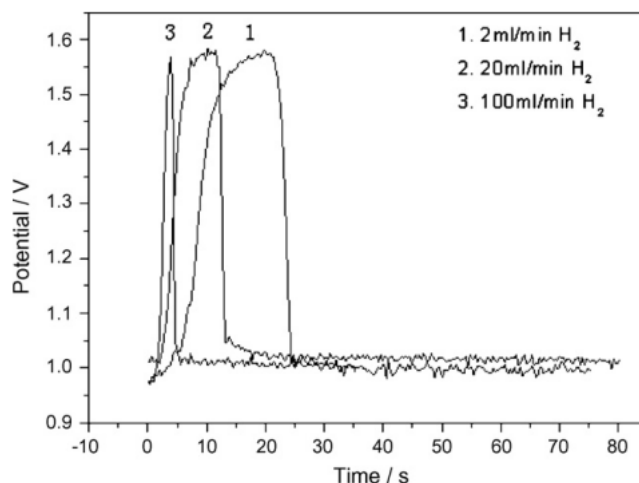


Figure 2-42. Cathode potential in the passive part ϕ_{down}^c during a start-up @ 0.12 slph, from [101].

Another consequence of the hydrogen flow rate variation is shown in Figure 2-43: the voltage overshoot diminished when the hydrogen flow rate increased. It must be mentioned that the experiments were performed from the high to the low hydrogen flow rates and by alternating air and nitrogen flushes: consequently, the results of the last measurements (the lowest hydrogen flow rates) were probably affected by the corrosion of the cathode carbon support.

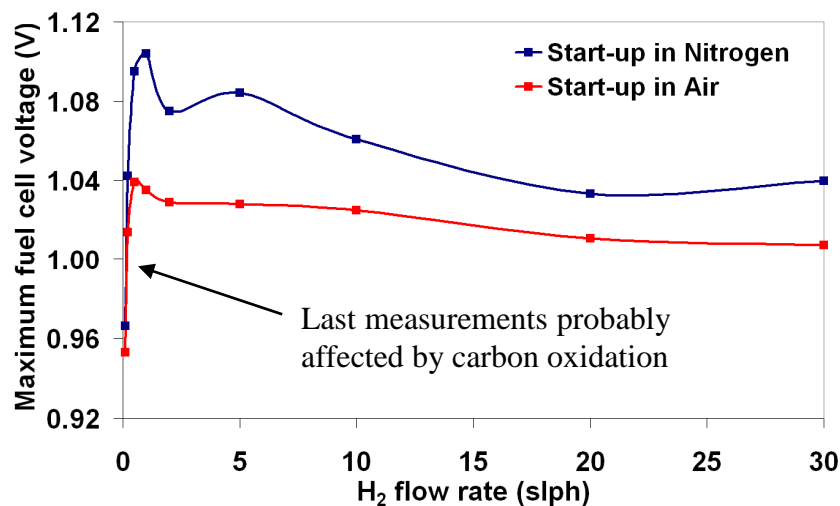


Figure 2-43: Fuel cell voltage overshoot measured during start-up in nitrogen and in air vs. hydrogen flow rate. Air and hydrogen humidified to 100% RH, fuel cell temperature set to 60°C.

Although low in absolute value the voltage overshoot may be significant in some cases. 0.1 V represents 10% of the steady state OCV, and 15% to 20% of the fuel cell voltage in operation. Thus, a 100 cells stack designed for working at 0.6 V/cell (60 V/stack) could reach an OCV of 110 V at start-up, a value 80% higher than in regular operation. A simple way to reduce the

fuel cell voltage overshoot during start-up consists in increasing momentarily the hydrogen flow rate.

2.5. Carbon dioxide in cathode exhaust gases

In order to investigate the contribution of carbon oxidation to the reverse currents, a Non-Dispersive Infrared Sensor (NDIR) was connected to the cathode gas exhaust (see §2.2). Start-ups in air and nitrogen were performed at different hydrogen flow rates. The corresponding carbon dioxide emissions are presented in Figure 2-44.

The first observation is that the peaks were strongly dependent on the nature of the gas filling initially the anode compartment: the production of CO_2 was much lower with nitrogen. The peaks were also higher and broader at low hydrogen flow rates. Similar observations were made by several groups for start-ups in air [102], [103], [104]. Although these results were obtained with different cell designs and different flow rates, they are consistent with those presented here. Gu et al. [103] for instance used a 50 cm^2 fuel cell at 80°C fed with 66% HR air. They measured up to 100 ppm for start-up sequences, with hydrogen injection flow rates set to $140 \text{ sccm} = 8,4 \text{ slph}$ at the anode (air flow rate at the cathode: $1000 \text{ sccm} = 60 \text{ slph}$).

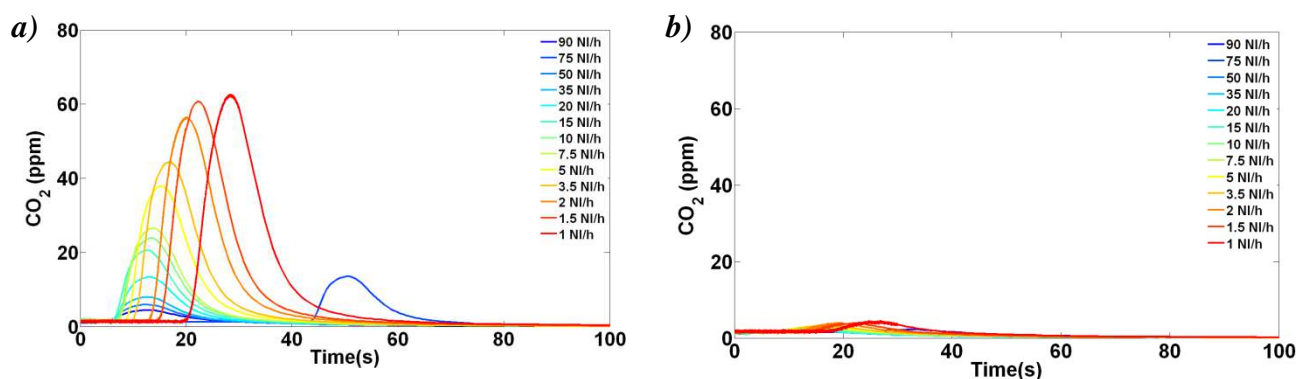


Figure 2-44. Carbon dioxide peaks recorded after start-ups performed with different hydrogen flow rate in air a) and in nitrogen b) (MEA Johnson Matthey, Pt loading = 0.6 mgPt/cm^2 , cell temperature = 60°C).

The results of the integration of the carbon dioxide peaks are presented in Figure 2-45.

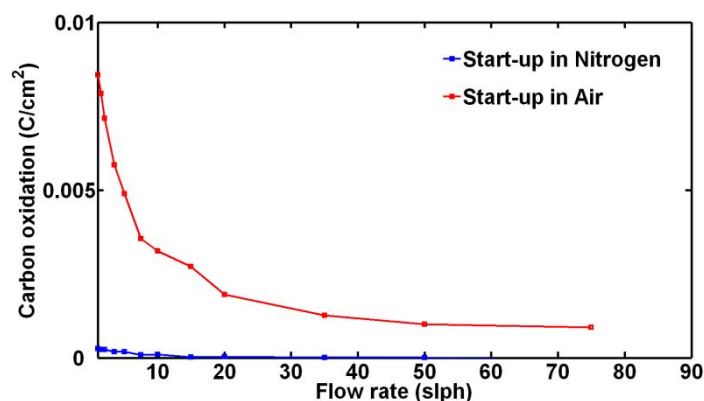


Figure 2-45. Charge produced by the oxidation of carbon and calculated from the CO_2 measured in the cathode gas exhaust during single start-up in air and in nitrogen at different hydrogen flow rates (MEA Johnson Matthey, Pt loading = 0.6 mgPt/cm^2 , cell temperature = 60°C).

The evolution with the hydrogen flow rate of the charges corresponding to the carbon dioxide emissions was similar to that of the charges exchanged (Q_p). This observation applies to start-ups in air and in nitrogen. However, the carbon oxidation measured during a start-up in air represented at most 10% of the charges exchanged (Figure 2-46). Other electrochemical reactions in the downstream part of the cathode have therefore to be taken into account. According to the description made in the first chapter (§1.4.3) and the results presented in chapter 3, platinum dissolution and redeposition has to be considered. Such reactions were confirmed by the ECSA induced by repeated start-ups and by the post mortem observations of a Pt band in the membrane or bigger platinum particles in the catalyst layer (§3.4). Non-degrading faradic reactions are also conceivable like water splitting or reversible platinum oxidation as during a cyclic voltammetry. These reactions are described in more details in §4.2.3.

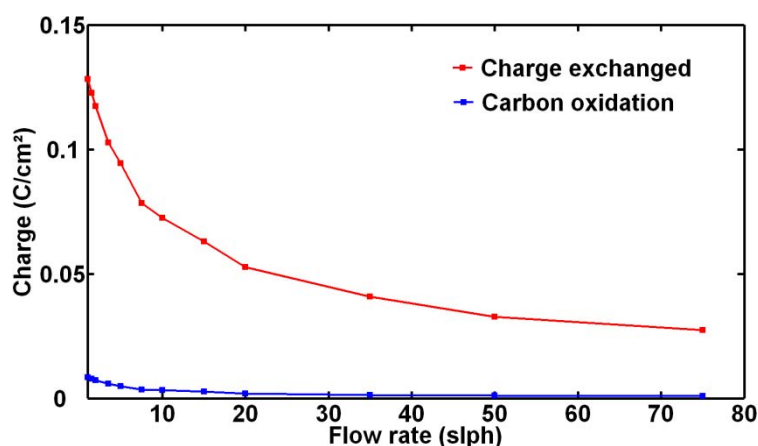


Figure 2-46. Charges exchanged during start-ups in air at different hydrogen injection flow rates (red). Carbon oxidation calculated from the cathode exhaust gas measurements during start-ups at different hydrogen flow rates (blue).

2.6. Shut-down with air

In this section, shut-downs are described using the same approach than used previously for start-ups with the objective to highlight similarities and differences.

2.6.1 Principle

We considered shut-down protocols consisting in injecting air (or nitrogen, see §2.7) in the anode compartment which was thus divided momentarily into an upstream part occupied by air and a downstream part filled with hydrogen (Figure 2-47). Compared to a start-up, the locations of redox reactions were inverted: in the upstream part (which became the passive part), oxidation occurred in the cathode and reduction in the anode. In the downstream part, oxidation took place in the anode and reduction in the cathode. Despite this inversion, similar reactions have to be expected. However, due to the presence of hydrogen in the anode, platinum was initially in a reduced form when air was injected. Then, the increase of the anode potential induced the oxidation of platinum, which by-passed the oxidation reactions taking place in the opposite part of the cathode (production and consumption of the protons occurred simultaneously in the passive part of the anode, Figure 2-47). As a consequence,

internal currents were limited compared to start-ups (a detailed comparison is done in §2.6.4). In the case of start-ups, platinum and oxygen were both reduced in the passive part of the anode (Figure 2-21). This mechanism was first proposed by Gu et al. [103]. It is in good agreement with our observations, as well for potential evolution (§2.6.2) as charges exchanged (§2.6.3).

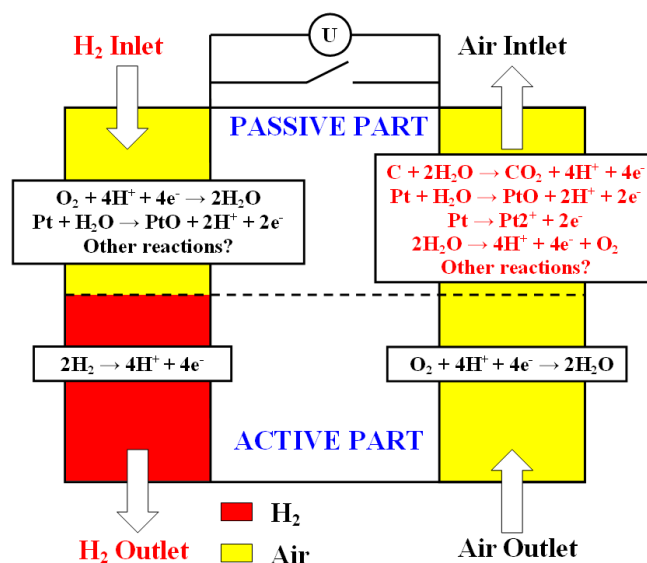
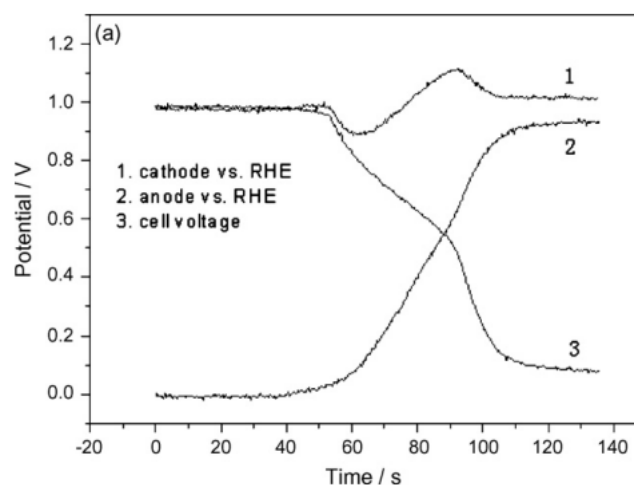


Figure 2-47. Reactions occurring during shut-down, the anode compartment being initially filled with air

2.6.2 Potential evolution during shut-down

The shut-down of a cell by injection of air in the anode compartment led to a decrease of the voltage from about 1V to 0V. Like for start-ups, Shen et al. [101] monitored the potential of the anode and cathode metal with reference to a RHE during the progress of the air front (Figure 2-48). Air being continuously supplied to the cathode, the potential of the metal in this electrode remained close to the reversible potential of the O_2/H_2O couple ($V_m^c \approx E_{O_2/H_2O}$). The diffusion of air in the anode induced an increase of the anode metal potential V_m^a until it reached the same value than in the cathode.

Figure 2-48. Evolution of the anode V_m^a and cathode V_m^c metal potentials and cell voltage during a shut-down by diffusion of air in the anode [101]. In this case, anode (cathode) potential refers to the interfacial potential between the anode (cathode) and the electrolyte averaged over the anode (cathode) length (§0).



In addition to the anode and cathode metal potential, the membrane potential was also monitored with reference to a RHE during the shut-down (Figure 2-49). The potentials evolution were similar to those observed during start-up. The membrane potential in the region still supplied with hydrogen $V_{e,down}$ (lower part of the cell in our case, referred to as inlet by Shen et al.) stayed close to the anode potential ($V_m^a \approx V_{e,down}$) as long as no oxygen was present. On the contrary, the membrane potential in the region already filled with air in the anode $V_{e,up}$ dropped. This makes the anode potential ϕ_{up}^a increase up to 1V.

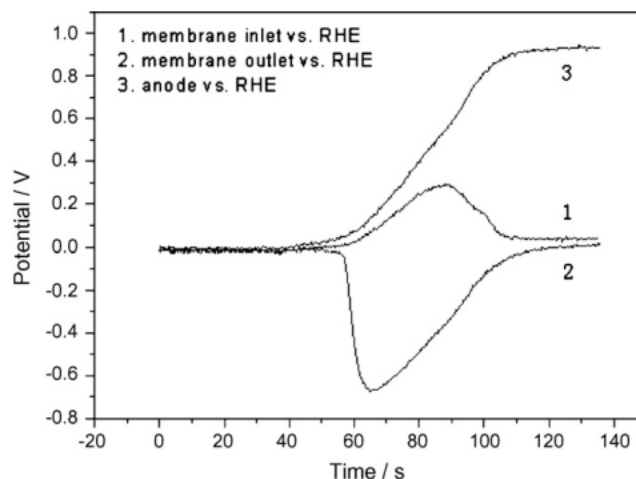
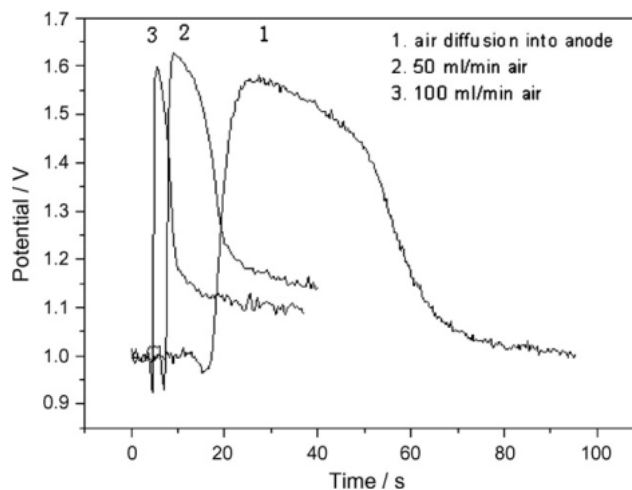


Figure 2-49. Membrane inlet (H_2 -air region, $V_{e,down}$), outlet (air-air region, $V_{e,up}$) and anode metal (V_m^a) potentials (in this case, interfacial potential between the anode and the electrolyte averaged over the anode length, ξ_0) when air diffuses from the anode outlet.

A consequence of the drop of $V_{e,up}$ in the upper part of the cell was the increase of the cathode potential ϕ_{up}^c in this region. This is represented in Figure 2-50 in the case of shut-downs performed with three different air flow rates. Like for start-ups, the maximum values reached were close to 1.6 V, the value of the cathode potential increasing when the air flow rate was reduced. In such conditions, degradations due to carbon oxidation or platinum oxidation are very likely.

Figure 2-50. Cathode potential ϕ_{up}^c in the region filled by air on the anode side for shut-downs at different air flow rate, from [101].



2.6.3 Local Current densities

The evolution of the local current densities measured in all the segments during a shut-down (with air) is depicted in Figure 2-51. As for start-ups, three different cases are more specifically detailed: the first segment supplied with air (Figure 2-51 b)), a segment located at an equal distance from the anode inlet and outlet (Figure 2-51 c)) and the last segment (Figure 2-51 d)).

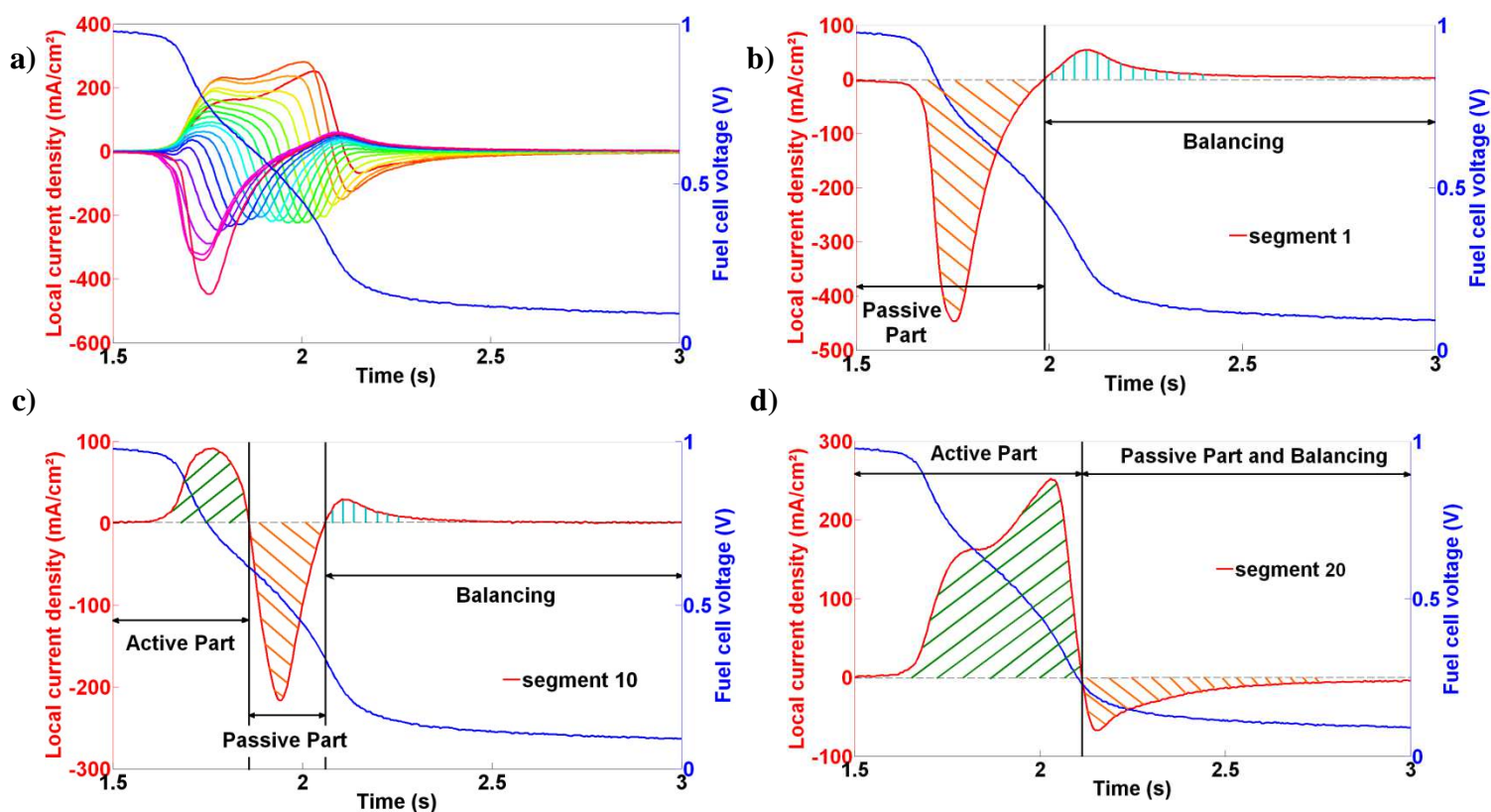


Figure 2-51. a) Current density measured in each of the 20 cathode segments and fuel cell voltage decrease (vs. time) during shut-down. Air was used to flush the anode at a flow rate set to 20 slph. Air and hydrogen were humidified to 100% RH (MEA Johnson Matthey, Pt loading = 0.6 mgPt/cm², cell temperature = 60°C). b) Current density in the anode first segment and fuel cell voltage vs. time during shut-down. c) Current density in the anode 10th segment (of 20) and fuel cell voltage vs. time during shut-down. d) Current density in the anode last segment and fuel cell voltage vs. time during shut-down.

While the shape of these curves differed from those measured during start-ups, two distinct stages could be identified. The first stage corresponded this time to the anode partially filled with air. The first segment supplied with air was always passive while all the others became successively passive once in the presence of air. The second stage began when the faradic reactions stopped. Then, due to the capacitive contribution to the global current, a redistribution of charges occurred. The corresponding currents could only be distinguished in the first segments, under the form of positive currents (blue striped area in Figure 2-51 b) and c)). The redistribution could be due also to the homogenisation of the platinum oxide content in the cathode. Indeed, a platinum oxide gradient must be created in the cathode between the upstream and downstream part. Contrary to start-ups, this process may occur in the anode too

since the platinum evolves from the reduced to the oxidized form (during start-up there is no platinum oxide homogenisation in the anode since the platinum particles are completely reduced at the end, §4.2.3).

The same types of charges than for a start-up can be defined:

- (i) Active charges corresponding to the positive currents measured in the active part of the fuel cell (green striped area in Figure 2-51 c) and d)). Contrary to a start-up, their value was directly accessible,

Locally:

$$Q_A(seg(i)) = S_{seg} \cdot \int_{Active_part} j_{seg(i)} \cdot dt > 0 \quad (2-29)$$

Globally:

$$Q_A = \sum_{i=1}^{20} Q_A(seg(i)) = S_{seg} \cdot \sum_{i=1}^{20} \int_{Active_part} j_{seg(i)} \cdot dt > 0 \quad (2-30)$$

- (ii) Balancing charges exchanged during the redistribution stage once all segments became passive; the balancing charges correspond to the blue striped area in Figure 2-51 b) and c) and were positive (negative for start-up),

Locally:

$$Q_B(seg(i)) = S_{seg} \cdot \int_{Balancing} j_{seg(i)} \cdot dt > 0 \quad (2-31)$$

Globally:

$$Q_B = \sum_{i=1}^{20} Q_B(seg(i)) = S_{seg} \cdot \sum_{i=1}^{20} \int_{Balancing} j_{seg(i)} \cdot dt > 0 \quad (2-32)$$

- (iii) Passive charges corresponding to the negative current measured in the passive part minus the negative balancing charges (equal in absolute value to the positive balancing charges).

Locally:

$$Q_{Orange_area}(seg(i)) = S_{seg} \cdot \int_{Orange_area} j_{seg(i)} \cdot dt \quad (2-33)$$

Globally:

$$Q_{Orange_area} = \sum_{i=1}^{20} Q_{Orange_area}(seg(i)) = S_{seg} \cdot \sum_{i=1}^{20} \int_{Orange_area} j_{seg(i)} \cdot dt \quad (2-34)$$

$$Q_P = Q_{Orange_area} - Q_B < 0 \quad (2-35)$$

The positive balancing charges, represented here by the blue striped area, were not distributed in the same segments as the negative balancing charges ($Q_{B>0}^{seg(i)} \neq -Q_{B<0}^{seg(i)}$), merged with the

passive charges. As there was no way to distinguish between the negative balancing and the passive charges in each segment and as the negative balancing charges were small compared to the passive charges, they were neglected in the following.

$$Q_p(seg(i)) = Q_{Orange_area}(seg(i)) - Q_B(seg(i)) \approx Q_{Orange_area}(seg(i)) < 0 \quad (2-36)$$

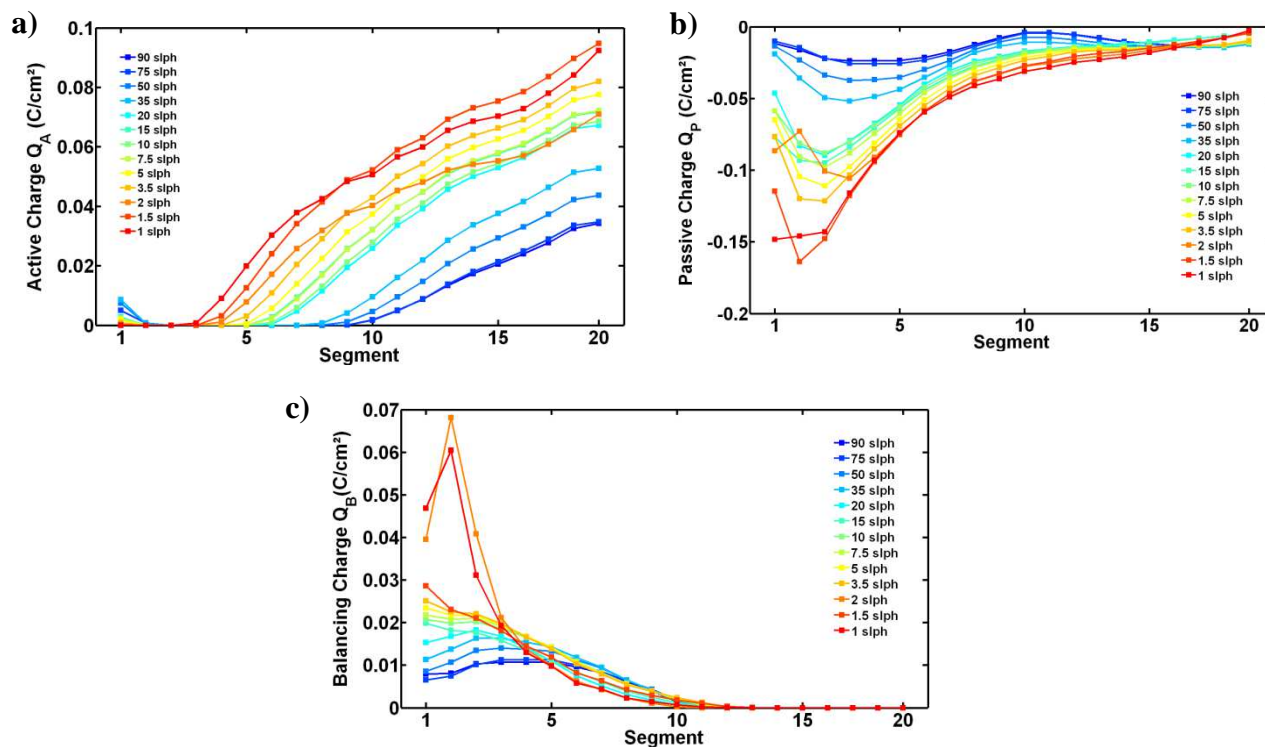


Figure 2-52. Local active a), passive b) and balancing c) charges measured during shut-down. Anode flushed with air at different flow rates (MEA Johnson Matthey, Pt loading = 0.6mgPt/cm², cell temperature = 60°C).

2.6.4 Comparison between start-up and shut-down

Local charges during shut-down were not distributed identically as during start-up (Figure 2-38). Balancing and passive charges were located close to the anode inlet where the segments remained passive the longest time. On the contrary, active charges increased when moving closer to the anode outlet.

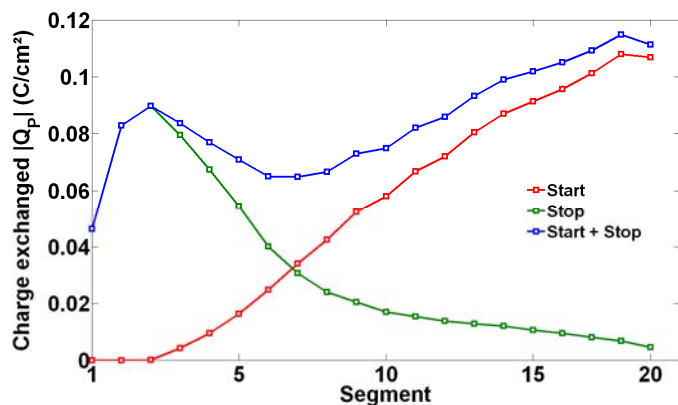


Figure 2-53. Local passive charges measured during start-up with hydrogen injection flow rate set to 10 slph (red). Local passive charges measured during shut-down with air injection flow rate set to 10 slph (green) and sum of the both contributions (blue) - MEA Johnson Matthey, Pt loading = 0.6 mgPt/cm², cell temperature = 60°C.

As passive charges (referred to as charge exchanged like for start-up) result from the reverse currents, they are responsible, at least partially, for the cathode degradations occurring during start-up and shut-down. Due to the distributions of the charges exchanged, it can be expected that the extent of the degradations generated in the cathode by start-up increases progressively from the inlet to the outlet of the anode compartment (**Figure 2-53**). On the contrary, the degradations induced by shut-down in the cathode should concern mainly the closest segments to the anode inlet where air was introduced. This local aging was confirmed by the experiments presented in chapter 3 (§3.5).

As shown in Figure 2-54 more charges were exchanged between the active and passive parts during a start-up than during a shut-down. During a shut-down, the platinum oxidation in the passive part of the anode by-passed the oxidation reactions occurring in the opposite part of the cathode [103] (Figure 2-47). In other words, some protons were produced (platinum oxidation) and consumed (oxygen reduction) directly in the passive part of the anode, which resulted in a lower charge exchanged (during start-up, platinum and oxygen were both reduced in the passive part of the anode).

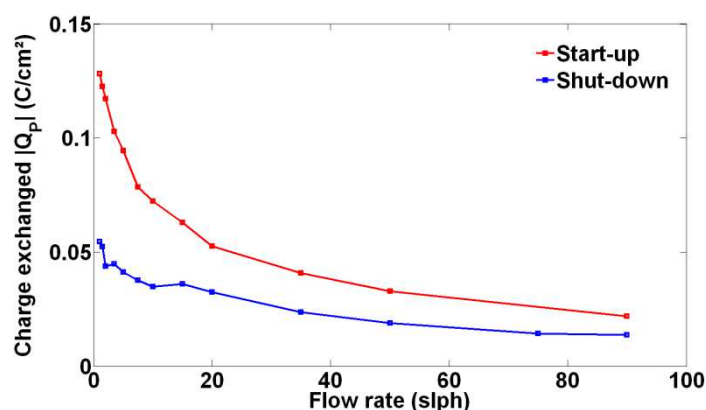


Figure 2-54. Charge exchanged during start-ups and shut-downs performed at different flow rate (MEA Johnson Matthey, Pt loading = 0.6mgPt/cm², cell temperature = 60°C).

2.6.5 Carbon dioxide measurement in the cathode exhaust gas

During shut-down by injection of air in the anode, carbon dioxide was released in the cathode exhaust gas (Figure 2-55). The CO₂ peaks were higher and broader for lower air flow rates. Compared to start-up, the CO₂ emissions during shut-down were less intense for equivalent gas injection flow rate. However, CO₂ emissions continued for quite a significant time after the cell voltage reached 0 V (at 2 slph, air needed around 12 seconds to fill completely the anode compartment). This phenomenon was only observed with the Johnson Matthey MEA: no CO₂ emissions were recorded after the peak with the Ion Power MEA. The homogenisation of the platinum oxide gradient along the cathode resulting from the first stage of the shut-down (§2.1.2) can be done either by reducing some of these platinum oxides or by oxidizing platinum (§4.2.3). Among the possible reactions, PtOH^s reduction leads to carbon oxidation (4-18): this could explain the long lasting CO₂ emission with the Johnson Matthey MEA.

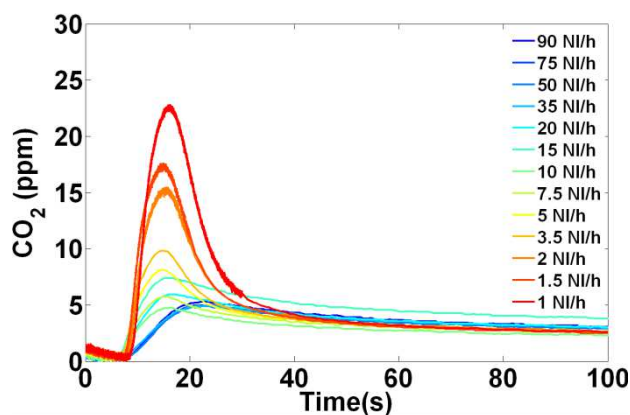


Figure 2-55. Carbon dioxide peaks recorded after shut-downs performed at different air flow rates in hydrogen with a Johnson Matthey MEA.

Since carbon oxidation leads to the release of four electrons according to reaction (1-72), CO_2 emissions can be converted into charges. For shut-downs, this conversion was done by considering only the first 50 seconds following the introduction of air in the anode compartment in order to take only the CO_2 emitted during the peaks into account. A comparison between the charges resulting from carbon oxidation during start-up and shut-down is presented in Figure 2-56.

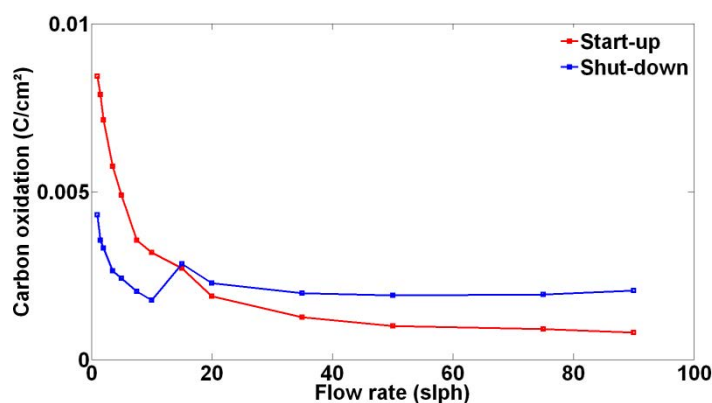


Figure 2-56. Carbon oxidation vs. flow rate during start-ups and shut-downs performed with different gas injection flow rates

Above 10 slph, no CO_2 peak was clearly noticeable. Therefore, the interpretation of the values obtained at the highest air flow rate was difficult. Below 10 slph, distinct peaks appeared and one can observe that shut-downs induced less oxidation than start-up. This result is consistent with the lower charge exchanged during shut-downs than during start-ups.

The evolution of carbon oxidation with the air injection flow rate was similar to that of the charge exchanged. However, carbon oxidation represented only a small fraction of these charges (at most one tenth, Figure 2-57).

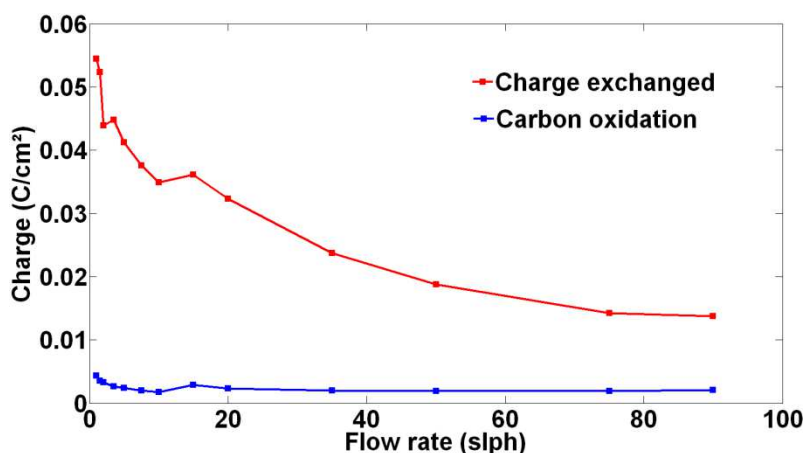


Figure 2-57. Charges exchanged during shut-downs at different air injection flow rates (red). Charges corresponding to carbon oxidation calculated from the carbon dioxide emission measured in the cathode exhaust gas during shut-downs at different air flow rates (blue).

Recently, *Kreitmeier et al.* [109] succeeded in measuring the CO₂ emissions along the channel during start-up and shut-down procedures. It appeared that the distribution of the carbon dioxide emissions (Figure 2-58) was in good agreement with those of the charge exchanged during start-up and shut-down (Figure 2-53).

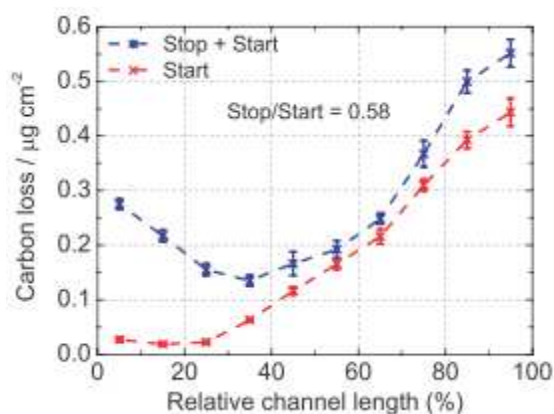


Figure 2-58. Local carbon losses per start/stop experimentally determined at 80°C, ambient pressure, 70% RH and a nominal anode gas velocity of 0.6 m/s [109].

In addition, these authors found a carbon loss ratio between shut-down and start-up of 0.58 for an anode gas velocity of 0.6 m/s. We measured also a value close to 0.6 in term of charge exchanged when the gas injection flow rate was comprised between 20 slph and 30 slph (which corresponds to a gas velocity of about 0.6 m/s, Figure 2-59). However, it must be noted that this ratio was a function of the gas injection flow rate (gas velocity) with two distinct phases:

- Below 20 slph, the ratio increased with the gas injection flow rate but remained below 0.6;
- From 20 slph, the ratio remained approximately constant around 0.6.

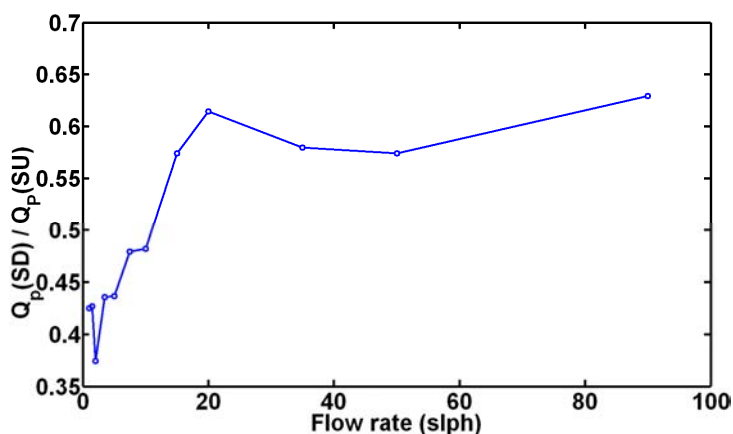


Figure 2-59. Charge exchanged ratio between shut-down and start-up performed with the same anode anode gas injection flow rate.

2.7. Shut-down with nitrogen

When nitrogen was supplied to the anode compartment, no internal currents were recorded. The only evidence of the shut-down is the slow decrease of the fuel cell voltage, which could be explained by:

- The removal of hydrogen due to the nitrogen flow in the anode;
- Oxygen permeation through the membrane, which could chemically react with hydrogen or oxidize platinum.

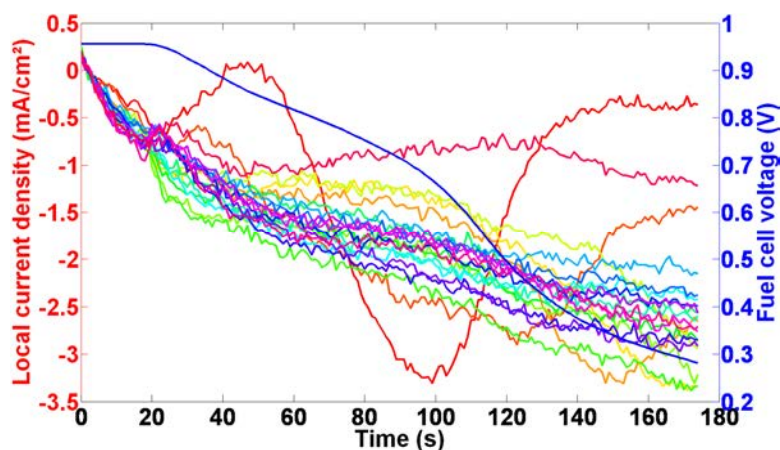


Figure 2-60. Local current density and voltage evolution during a shut-down with nitrogen at 2 slph. These values are not significant compared to those obtained during a shut-down with air.

According to measurements made in the cathode exhaust gas (Figure 2-61), shut-down with nitrogen do not lead to carbon dioxide emissions, or in very limited amount.

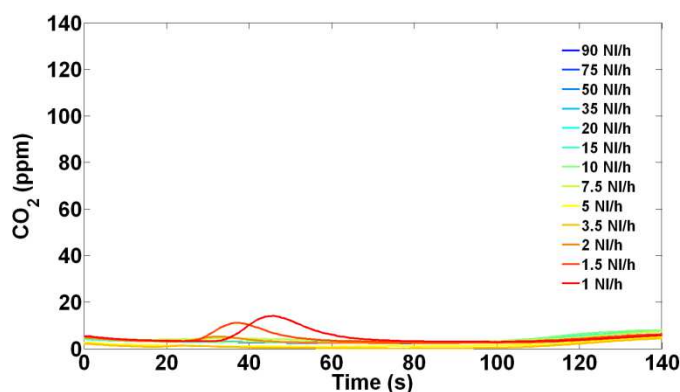


Figure 2-61. Carbene dioxide peaks recorded after shut-downs done at different nitrogen flow rate in hydrogen.

2.8. Comparison of start-ups and shut-downs performed with different MEAs

The charge exchanged during fuel cell start-ups or shut-downs depends on different parameters such as the gas used to flush the anode compartment or its injection flow rate. Attention can also be paid to the structure of the MEA. In the frame of a collaboration between the LEMTA and the LANL, MEAs with different characteristics were investigated during single start-ups and shut-downs. Some examples of these investigations are given in this section.

2.8.1 General comparison (multiple MEAs)

Experiments were carried out with six different MEAs coming from three different manufacturers: Johnson Matthey, Paxitech and Ion Power. Their specifications are summarized in Annex 1. The main differences between these MEAs concerned the carbon supporting the electrode, the platinum loading, the membrane characteristics and those of the GDL.

Considering these significant differences, their comparison from a quantitative point of view may not be not relevant. However, it is interesting to observe whether they react similarly when submitted to identical start-ups procedures. For all these experiments, the current density profiles were comparable to those described in §0. The charges exchanged could be measured for each MEA (Figure 2-62).

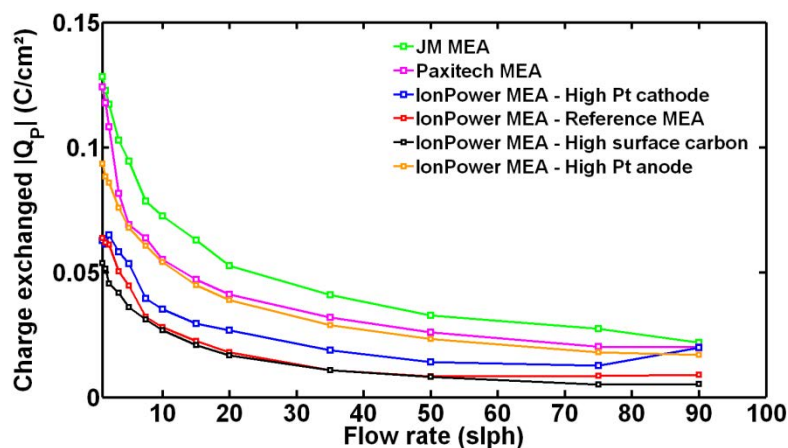


Figure 2-62. Evolution of the charges exchanged during start-ups in air vs hydrogen flow rate for the six MEAs.

Despite the diversity of MEAs, their responses to start-ups performed at different hydrogen flow rates were similar. In addition, for start-ups performed at a given hydrogen flow rate (20 slph), the distribution of the charge exchanged was alike (Figure 2-63).

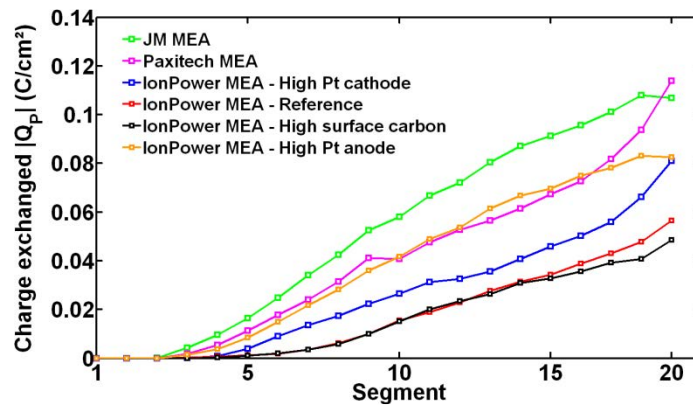


Figure 2-63. Distribution of the charge exchanged during start-ups in air with 20 slph hydrogen injection flow rate for the six MEAs.

The results in Figure 2-62 and Figure 2-63 indicate that similar mechanisms were at work in all cases, although with different magnitudes.

2.8.2 Specific comparison (Ion Power MEAs)

The project with the LANL aimed to analyse the impact of MEA structural changes on the degradations induced by start-ups and shut-downs. This time, only Ion Power MEAs were considered. In order to compare the results, a reference MEA was chosen which specifications are (Annex 1):

- Anode platinum loading : 0.08 mg/cm² (0.03 mg/cm² according to XRF spectroscopy);
- Cathode platinum loading: 0.2 mg/cm² (0.27 mg/cm² according to XRF spectroscopy);
- Carbon at cathode : Vulcan XC-72 (240 m²/g).

The other MEAs differed from the reference MEA by a unique parameter: anode or cathode platinum loading and surface carbon area at the cathode. The influence of the GDL or MPL thickness in the anode and cathode for instance was out of the scope of this work.

a. Charge exchanged and CO₂ emissions during individual start-ups and shut-downs

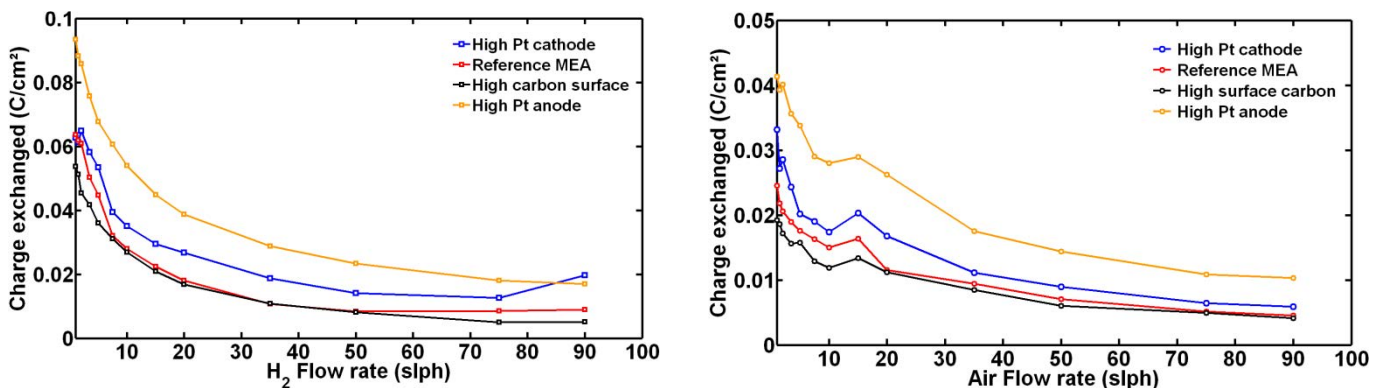


Figure 2-64. Charge exchanged during single start-ups (left) and shut-downs (right) vs. gas injection flow rate for the Ion Power MEAs.

According to the results presented in Figure 2-64, only the MEA with a higher Pt loading at the anode differed significantly from the three others, with more charge exchanged. On the contrary, doubling the cathode Pt loading or tripling the carbon specific surface do not result in any noticeable change in the charge exchanged. This means that the anode is probably the limiting electrode for the reverse current, which is not surprising considering that the main reaction taking place in the passive region is the oxygen reduction. This conclusion applies to start-ups as well as to shut-downs.

The addition of platinum modifies probably the activation barriers and activation overpotential distribution. At a given fuel cell voltage, increasing the platinum loading in the anode allows reducing the activation barrier of the electrochemical reactions which occur there and therefore the overpotential needed. Meanwhile, the activation overpotentials for the electrochemical reactions in the cathode can increase and produce more charges too. Examples of potential evolutions are summarized in Figure 2-65 (the increase of the cathode platinum loading is also considered).

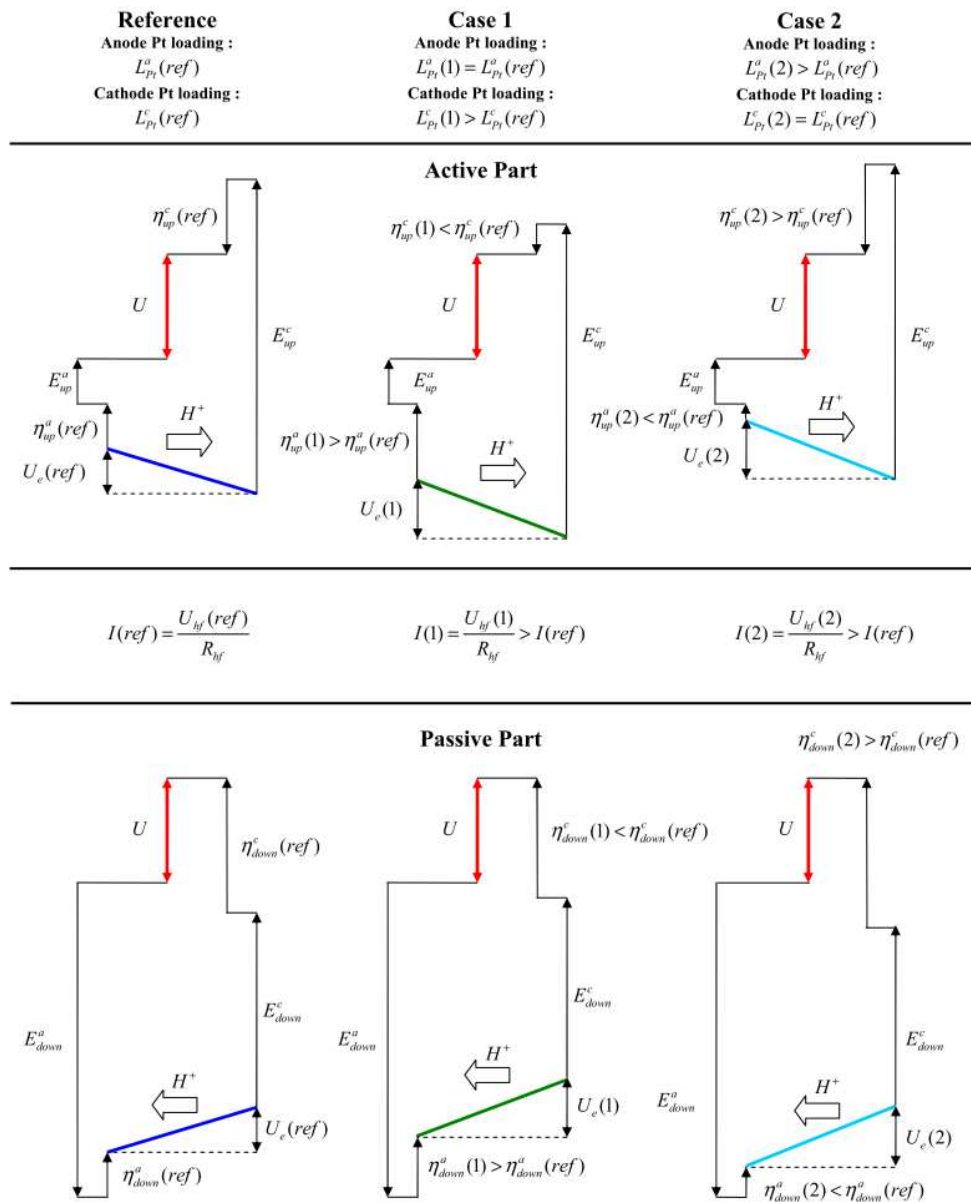


Figure 2-65. Potentials distribution in active and passive part of a cell during a start-up.

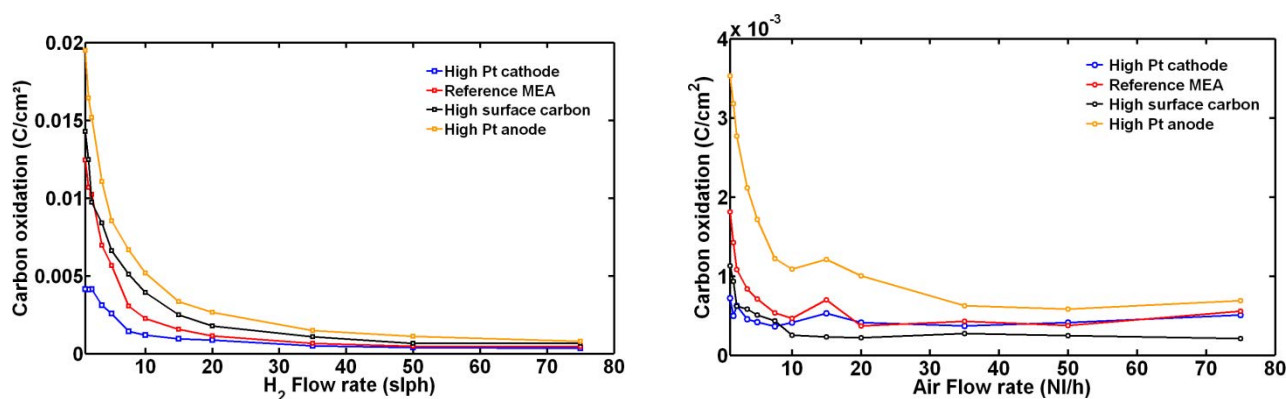


Figure 2-66. Charge corresponding to carbon oxidation and estimated from the carbon dioxide measured in the cathode exhaust gas during single start-ups (left) and shut-downs (right) for the different Ion Power MEAs.

Figure 2-66 depicts the evolutions of the CO₂ emissions as functions of the hydrogen or air injection flow rates. Contrary to the charge exchanged, one can notice a clear difference in the behavior of the four MEA: the CO₂ emissions were between 15 to 50% higher with the high surface carbon (800 m²/g amorphous carbon) than with the reference electrode (240 m²/g Vulcan XC72) and about 50% higher with a higher Pt loading at the anode (0.18 mg_{Pt}/cm² against 0.08 mg_{Pt}/cm² with the reference MEA); on the contrary, increasing the Pt loading at the cathode (0.44 mg_{Pt}/cm² against 0.2 mg_{Pt}/cm² with the reference MEA) made it possible to limit significantly the CO₂ emissions. The main conclusions that can be drawn from these results are the followings:

- The increase of the CO₂ emissions with the Pt loading confirms that the anode is the electrode that governs the reverse currents and thus carbon corrosion at the cathode. During start-ups, a higher Pt loading favors oxygen and Pt reduction in the passive part of the anode compartment, and consequently carbon corrosion in the passive part of the cathode compartment. The similar behaviors observed during start-ups and during shut-downs tend to show that the impact of direct Pt oxidation in the passive part of the anode compartment has no significant effect, either on the reverse currents or on carbon corrosion.
- As expected, amorphous carbon with a high specific surface was more sensitive to corrosion during start-ups. The CO₂ emissions were only 10 to 15% above those measured with the reference MEA for the lowest hydrogen injection flow rate (1 slph) but about 50% higher with 10 slph (i.e., the value that was used for the aging protocols presented in §3.6). Surprisingly, there was no significant impact of a change in the carbon specific surface on CO₂ emissions during shut-downs.
- Although it resulted in a clear augmentation of the charge exchanged (Figure 2-64), the increase of the Pt loading at the cathode also entailed a significant decrease of the CO₂ emissions (Figure 2-66). This means that despite of the link between reverse currents and carbon corrosion illustrated by the similar shape of the curves in Figure 2-64 and Figure 2-65, their response to a change in the MEA specification differs. The main reason for that is the small contribution of the CO₂ emissions to the reverse currents: 0.45 μg/cm² (maximum value measured during start-up using the MEA with high specific surface carbon at the cathode) corresponds for instance to 0.015 C/cm², or 25% of the charge exchanged at the lowest hydrogen flow rate, which can be considered as a maximum (Figure 2-67). The CO₂ emissions contribution to the charge exchange fell to about 7% using the MEA with high Pt loading at the cathode.

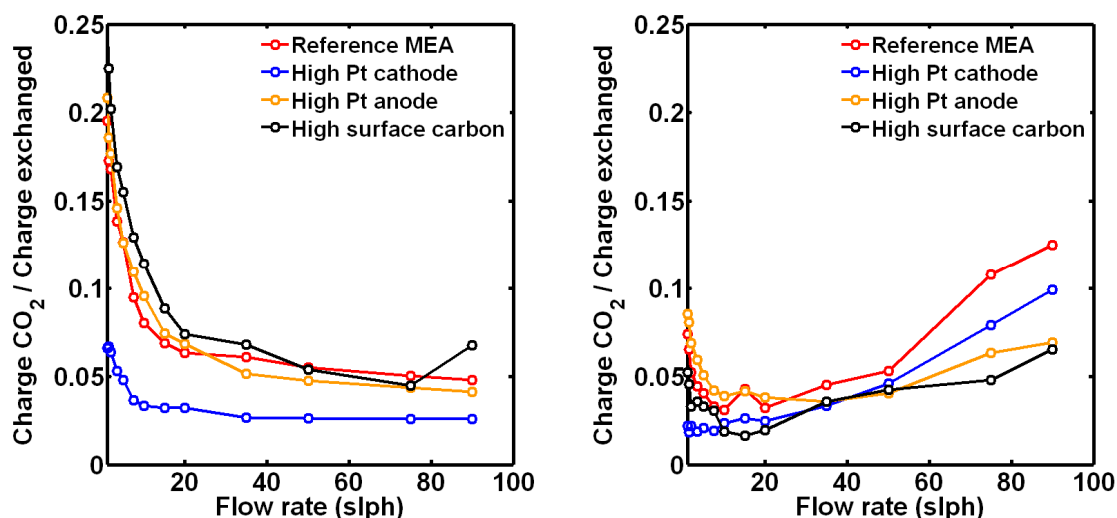


Figure 2-67. Contribution of CO_2 emissions to the charge exchanged per start-up (left) and shut-down (right) vs. gas injection flow rate.

b. Reproducibility

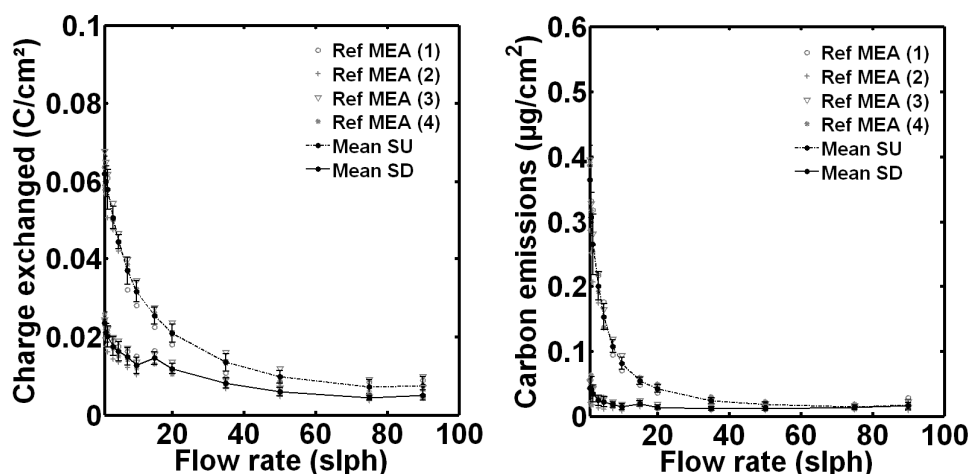


Figure 2-68. Reproducibility tests carried out with five different samples of the reference MEA. Charge exchanged (left) and carbon emission (right plot) vs. gas flow rate. Average and maximum dispersion of the charge exchanged = 0.003 and 0.006 C/cm^2 . Average and maximum dispersion of the carbon emissions = 0.01 and 0.05 $\mu\text{g}/\text{cm}^2$.

The reproducibility of the results was assessed by repeating the measurements of the CO_2 emissions and charge exchanged with four different samples of the reference MEA during single start-ups and shut-downs (Figure 2-68). The aging protocols in §3.6 were performed with air or hydrogen injection flow rates set to 10 slph. For these flow rates, the dispersion of the charge exchanged was of the order of 8% for SU and 16% for SD, while that of the CO_2 emissions (expressed in term of carbon emissions) was of the order of 11% for SU and 33% for SD, which is sufficiently low to consider the variations discussed above as significant. Furthermore, Figure 2-68 shows that the dispersion tended to decrease when the gas injection flow rates increased, although the charge exchanged and CO_2 emissions were lower. This indicates that the higher dispersion observed for the lowest injection flow rates was probably due to physical phenomena and/or variations in the materials properties rather than to the

experimental setup: Table 2-3 gives the voltage (@0.67 A/cm²), the permeation current density and the ECSA of the four reference samples at beginning of life (after the conditioning stage).

Sample	ECSA	Permeation current density	Voltage @0.67 A/cm ²
1	67 m ² /g _{Pt}	1.4 mA/cm ²	0.615 V
2	64 m ² /g _{Pt}	2.0 mA/cm ²	0.599 V
3	63 m ² /g _{Pt}	1.6 mA/cm ²	0.618 V
4	64 m ² /g _{Pt}	1.4 mA/cm ²	0.626 V

Table 2-3. Characteristics of four samples of the reference MEA at beginning of life.

2.9. Conclusion

Fuel cell start-ups and shut-downs were performed by injecting a fresh gas (hydrogen, nitrogen or air) in the anode compartment of a cell in open circuit. This led to the division of the cell in two parts: one where hydrogen was already (or still) presents in the anode compartment (the active part) and one (the passive part) occupied with the new gas (air or nitrogen). The front between hydrogen and the other gas moved from the inlet to the outlet of the anode with a velocity which was governed by the gas injection flow rate.

Reiser et al. [98] evidenced with a dual cell that internal currents occur between the active and passive parts of the cell. A segmented cell developed in this group enabled to measure locally and in real conditions these internal currents. We checked first that they were identical (in term of current density) in the anode and cathode. Then, the different steps of a start-up were identified. All segments (except the first one supplied with hydrogen) are first located in the passive part of the cell and subjected to reverse currents. Then, they become active once in the presence of hydrogen, which means that forward currents appear. The last step begins when hydrogen fills (almost) completely the anode compartment: depending on the position of the segment along the gas channel, forward or reverse currents can be measured, most probably because of the homogenization of the platinum oxide gradient created during start-up along the cathode catalyst layer. This interpretation is confirmed by the numerical results presented in chapter 4 (§4.2.3).

Shen et al. [101] showed that start-ups entail strong variations of the anode and cathode metal potentials. These evolutions are uniform along each electrode. On the contrary, the electrolyte potential is non-uniform: its value differs in the active and passive parts of the cell. Therefore, the potential difference between the metal and the electrolyte (the local electrode potential) is heterogeneous in the direction parallel to the electrode. Recently, an improved version of our segmented cell equipped with local Reference Hydrogen Electrode made it possible to measure the local anode and cathode potentials. This enabled to confirm that high cathode potentials are reached in the segments close to the hydrogen outlet as long as hydrogen does not fill entirely the anode compartment. Such high potentials are known to accelerate carbon corrosion and catalyst degradation.

During shut-downs, similar steps as those occurring during start-ups could be identified, although the internal currents profiles were not alike. Nevertheless, at identical gas injection

flow rate, the internal currents appeared to be much lower. This could be explained by redox reactions involving platinum in the anode: before shut-down, platinum is under a reduced form due to the presence of hydrogen; when air is injected in the anode compartment, oxygen starts to reduce in the passive part of the anode and platinum oxidizes as the local anode potential rises. The oxidation reactions in the passive part of the cathode are therefore bypassed and internal currents are thus limited.

Reiser et al. [98] correlated the degradations occurring in the passive part of a dual cell to the presence of reverse currents. Integrating the reverse currents over time yields a charge which we referred to as charge exchanged. Since it can be a marker of degradations, this charge has been studied at the local and global scales during start-ups and shut-downs performed in different conditions. At the global scale, it appeared to be a function of the residence time of air (or nitrogen) and hydrogen in the anode compartment. At the local scale, the longer the segments remained passive, the higher the charge exchanged was. It was also higher when start-ups were performed in an anode compartment filled initially with air rather than with nitrogen. This observation suggests that reduction reaction in the passive part of the anode may be a rate determining step of the internal currents and therefore of the degradations they entail.

Thinning of the carbon electrode support in the passive part of the cell being one of the degradation generally attributed to start-ups and shut-downs, carbon dioxide emissions were measured using a NDIR sensor. The evolution of the CO₂ emissions with the gas injection flow rate (hydrogen at start-up and air at shut-down) was similar to that of the charge exchanged. In addition, the comparison between the local CO₂ emissions measured recently by Kreitmeier et al. [109] and the local charge exchanged obtained with our cell in similar conditions showed that their distribution were alike. This confirmed that the charge exchanged can be considered as a marker for carbon oxidation (and probably of other degradations). However, the charge corresponding to the CO₂ emissions appeared to contribute only in very limited amount to the charge exchanged (less than 10%). Other faradic contributions, reversible or not, have therefore to be considered.

In the framework of a partnership between the LEMTA and the LANL, the influence of the MEA characteristics was investigated. The increase of the anode or cathode platinum loading resulted in higher charge exchanged. On the contrary, increasing the carbon specific surface of the cathode had no significant influence. Interestingly, the CO₂ emissions did not follow the same tendencies as the charge exchanged: they decreased when the cathode platinum loading was higher. This suggests that platinum oxidation could protect carbon from corroding. However, higher CO₂ emissions were measured when the anode platinum loading and the cathode carbon specific surface were increased.

The following chapter presents the results of aging protocols consisting in the repetition of start-ups and shut-downs, with the objective to characterize the effects of these repetitions on the cell performance, at the global and local scales, and in various conditions.

3 Fuel Cell Aging

In the second chapter, the charge exchanged was identified as a marker of the degradations in the cell and in particular of carbon oxidation in the cathode. At the local scale, this parameter appears to be non-uniform. Therefore, single start-ups and shut-downs, if repeated, must create regions with distinct level of degradations.

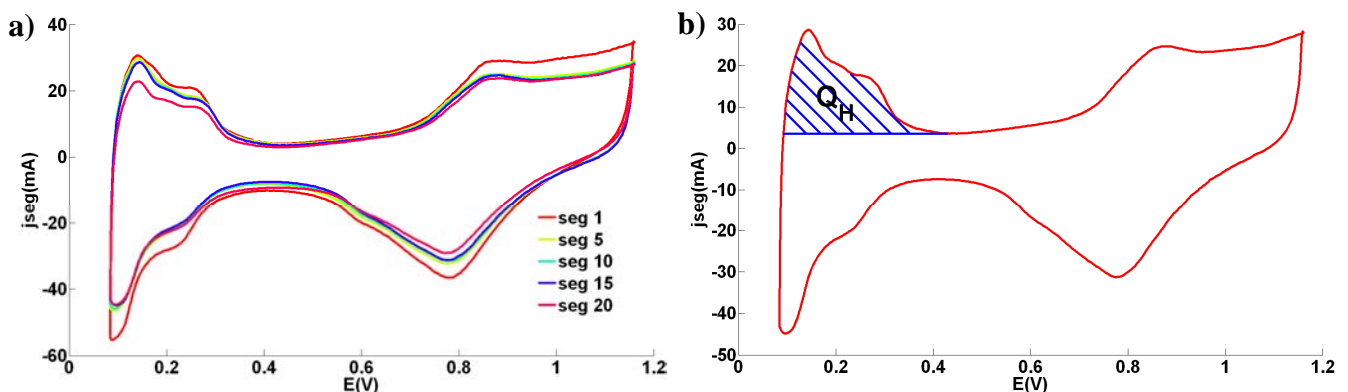
In this chapter, results obtained during long-term aging protocols are presented. These protocols were developed to assess the impact of repeated start-ups and shut-downs on the cell performance. This evaluation was done by monitoring the cell voltage, the local current density and the local ECSA throughout the experiments. The protocols were specifically elaborated to distinguish the respective effects of start-ups and shut-downs. The influence of parameters such as the nature of the gas used to shut-down the cell or its injection flow rate on the performance decay was studied. For comparison, simpler aging protocols consisting in potential cycling were also performed.

The influence of the MEA specifications on the degradation rate was also examined with the objective to optimize their durability.

Finally and in order to learn more about the degradation mechanisms, a Paxitech MEA was aged following a start-up aging protocol and then analyzed ex-situ in the LEPMI.

3.1. Impact of Cyclic voltammetry

The aging protocols set-ups include diagnosis steps such as EIS, CV and the measurement of local polarization curves. While polarization curves and EIS should not generate any significant additional degradation, Linse et al. [26] showed that CV induced the emission of carbon dioxide. Moreover, they demonstrated that the CO_2 emission depended on the platinum content of the electrode and on the potential range which was swept. The resulting damages have therefore to be estimated, to make sure that CV performed for diagnosis purposes does generate much lower degradations than start-ups and shut-downs.



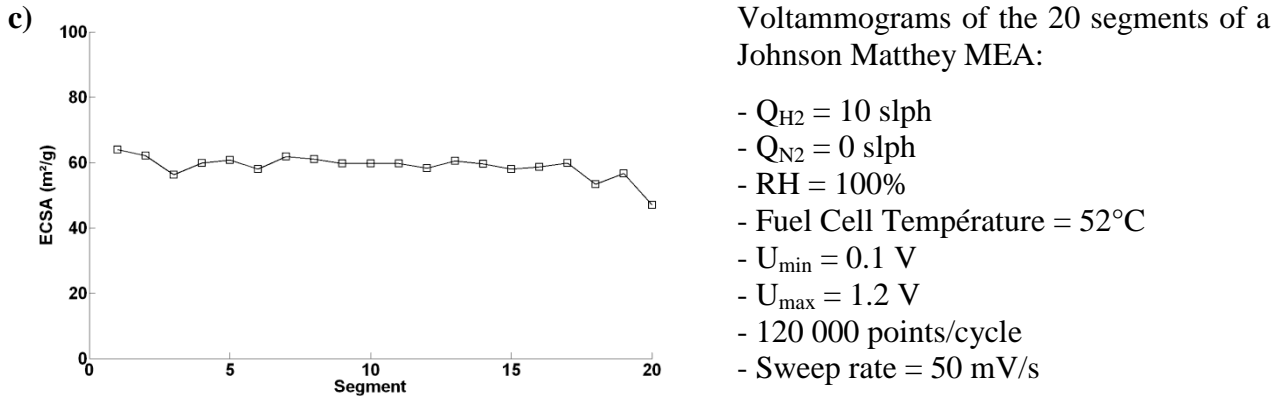


Figure 3-1. a) Cyclic voltammograms of 5 segments. b) ECSA calculation's method. c) ECSA profile along the air channel (new MEA from Johnson Matthey after conditioning stage).

This first protocol consists simply in repeating cyclic voltammetries to assess their impact on fuel cell performances:

- The cell is first conditioned during 24 hours (steady state operations until 1A/cm² with saturated hydrogen and air, $S_{air} = 3$, $S_{H_2} = 1.4$, temperature set to 52°C, ten oxygen starvations at 0.5A/cm²);
- A sequence of 300 cyclic voltammetries is then carried out, each of them consisting in two potential scans (which makes a total of 600 scans). The current densities are recorded during the second scan. The CV were performed as described in §1.3.1. However, since the cell is segmented, the current responses to the potential variations were recorded locally. This leads to the acquisition of twenty voltammograms (5 of them are represented in Figure 3-1 a) and the Platinum surface Area can be estimated for each segment with the method described in §1.3.1 (Figure 3-1 b)). The ECSA profile of a MEA at beginning of life is plotted in Figure 3-1 c).
- A characterization sequence is performed after each 15 cyclic voltammetries, with the following steps:
 - Operation of the fuel cell at constant current density (0.5 A/cm² during 300 s);
 - Electrochemical Impedance Spectroscopy (EIS) with measurement of the spectra locally for each segment;
 - Measurement of the fuel cell polarization curve and simultaneously, those of each segment.

It must be noted that the accelerated aging protocols presented in the following sections (§3.3, §3.4, §3.5) include 272 start-up/shut-down sequences. The cyclic voltammograms being measured every 17 sequences, this corresponds to only 16 voltammograms, plus one following the conditioning stage.

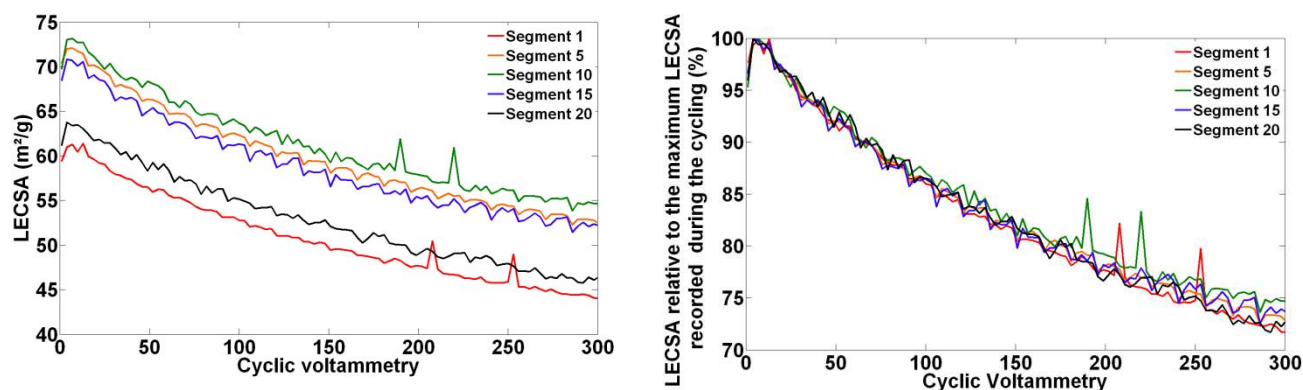


Figure 3-2. Evolution of the local ECSA of five segments vs. the number of cyclic voltammetries performed (1 cyclic voltammetry = 2 scans between 0.1V and 1.2V). Absolute values (left) and relative values with reference to the maximum (right).

Figure 3-2 depicts the evolution of the local ECSAs vs. the number of cyclic voltammetries performed. The results are quite uniform over the MEA surface, except for segments 1 and 20 located at both ends of the cell (probably because the actual surface of the MEA was slightly lower than expected). However, their behaviour is similar to those of the other segments. For clarity, only the values corresponding to segments 1, 5, 10, 15 and 20 are shown.

The evolution of the local ECSA occurs in two phases:

- The first one corresponds to a homogeneous increase. It lasts for about ten voltammetries (20 potential scans). A probable explanation of this behaviour can be the extension of the conditioning stage to the first potential scans. Indeed, the current density does not exceed 1 A/cm² during the conditioning stage and since the platinum load is relatively high (0.6 mg_{Pt}/cm²), some platinum particles may not be (fully) activated. Some of the not, or partially activated particles may become fully activated during the first cyclic voltammetries.
- The second phase corresponds to a uniform and steady decrease: the local ECSAs drop by about 25% of their maximum values after 300 cyclic voltammetries.

Several mechanisms can cause such a decrease. As mentioned previously, carbon dioxide is released when a cyclic voltammetry is carried out. This results possibly in the detachment from the carbon support [110], [111], [112] of some platinum particles that lose subsequently their activity. Local EIS reveals a slight and homogeneous decrease of the double layer capacities (Figure 3-3), known to be sensitive to the carbon corrosion [113]. However, it must be noted that this decrease is only of about 17F/m² that is to say 5% of the initial value. The ECSA drop is consequently much more pronounced than that of the double layer capacity. Its uniform decrease shows that carbon corrosion occurs homogeneously over the cell surface.

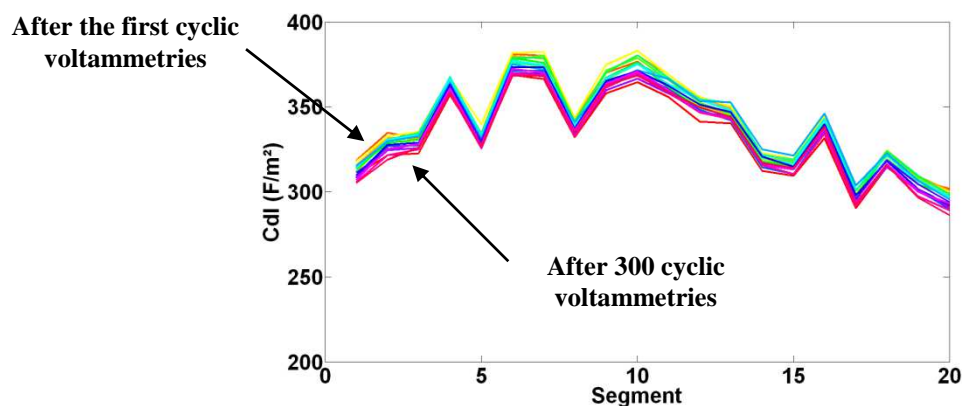


Figure 3-3. Decrease of the local double layer capacities resulting from series of cyclic voltammetry (1 cyclic voltammetry = 2 potential scans between 0.1V and 1.2V).

Other mechanisms can possibly be involved in the ECSA drop:

- The formation of a stable platinum oxide layer. However, this possibility appears unlikely even after a high number of cyclic voltammeteries: the lower potential limit, set to 0.1V should ensure the reduction of platinum.
- Pt dissolution/redeposition at the micrometre scale (long-range Ostwald ripening).
- Pt dissolution/redeposition at the nanometre scale (short-range Ostwald ripening);
- The migration/coalescence of Pt nanoparticles.

Pt dissolution and redeposition at the micrometer scale, or long-range Ostwald ripening, is a process which was already studied during cyclic voltammetry by Yasuda et al. [114]. They noticed a strong decrease of the ECSA after 500 voltammetry cycles with potential sweeps between 0.1 V to 1.2 V. MEA post-mortem analyses revealed the presence of platinum particles in the membrane close to the membrane/electrode interface (Pt band). The quantity of platinum in the PEM was correlated with the value of the upper potential limit: the higher it was, the more platinum would dissolve [60]. Moreover, the length platinum can migrate in the PEM seemed to be determined by the hydrogen crossover and the diffusion coefficient of Pt ions through the membrane [115] (see §1.4.4).

Potential sweep of a cathode filled with nitrogen was also implemented by Borup et al. [116]. The decrease of the ECSA they observed was in good agreement with the results obtained by Yasuda et al. but instead of focusing on Pt migration through the membrane, they studied the catalyst present in the electrode. They correlated the ECSA loss to the increase of the platinum particles growth. Two main mechanisms seem to be at the origin of this phenomenon: the dissolution and redeposition of the platinum particles (Ostwald ripening) and their coalescence due to their lack of bonds with the carbon substrate. The first mechanism corresponds either to short-range Ostwald ripening, that is to say particle to particle diffusion of Pt cations at the nanometre scale or to long-range Ostwald ripening. The second mechanism is possibly enhanced by carbon oxidation since platinum particles less anchored to their carbon support are thus more prone to move and to agglomerate. In addition, the growth of platinum particles is heterogeneous through the cathode thickness according to Shao-Horn et al. [117].

The decrease of the ECSA observed in this work is lower than that observed by Borup et al. and Yasuda et al (a decrease of about 25% of our initial active surface after 600 potential scans against 60% for Borup et al. and more than 60% after 500 scans for Yasuda et al.). Apart from the composition of the electrode (which was not given in detail in the previous works), the main explanation is probably the temperature of the cell, which was set to 80°C against 50°C in our case. As shown in the paper of Borup et al., the temperature plays a predominant role in the platinum particle growth process. The ECSA decrease should therefore be accentuated in their experiments. Since no post-mortem analyse of our MEA has been done after cyclic voltammetry cycles, it is difficult to identify and to quantify the different degradations mechanisms. We can however observe on the voltammogram evolution (Figure 3-4) that the loss of ECSA is mainly due to a loss of the {110}Pt surface.

No information is available concerning the distribution of the degradation in the cathode thickness with our segmented cell. We can only conclude that they were homogeneously distributed along the gas channel.

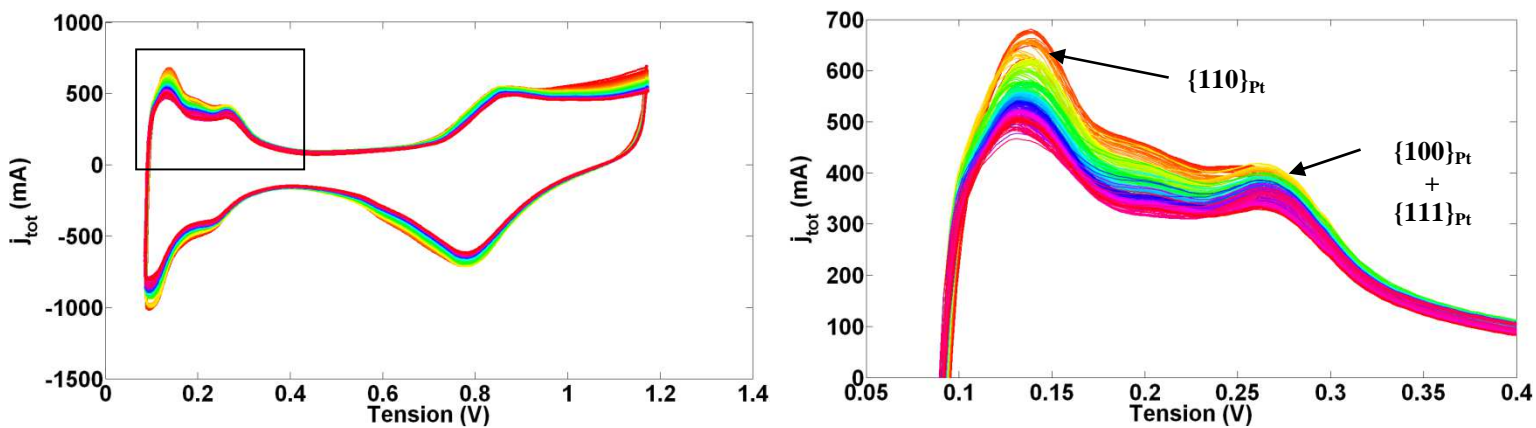


Figure 3-4. Cyclic voltammogram evolution during cyclic voltammetry cycles (left) - close-up on the hydrogen desorption peaks (right).

Table 3-1 gives the evolution of the fuel cell voltage at 0.1 A/cm², 0.5 A/cm² and 1 A/cm²: the ECSA decrease has no repercussion on the fuel cell voltage. The cathode being well loaded with platinum, it remained probably enough ECSA to produce the required current. Possible ways to highlight the relationship between the loss of ECSA and a voltage evolution could be to apply more cycles, to use a lower cathode platinum loading and to monitor the voltage evolution at higher current density.

Intensity (A/cm ²)	0.1	0.5	1	ECSA (m ² /g)
Voltage after the 1 st voltammetry (V)	0.833	0.699	0.567	67.8
Voltage after the last voltammetry (V)	0.836	0.711	0.572	51.6
ratio (%)	100.4	101.7	100.9	76.1

Table 3-1. Evolution of the voltage during cyclic voltammetry cycles.

In the start-up and shut-down aging protocols described in the following sections, only 16 cyclic voltammeteries were performed to monitor the Platinum surface area. Considering the results presented in this section, it can be reasonably assumed that these 16 voltammeteries will have a negligible impact on the fuel cell performance.

3.2. Aging protocols

3.2.1 Start-up and shut-down aging protocols

As seen in the second chapter, carbon dioxide emissions are correlated with the hydrogen injection velocity at start-up and shut-down: higher flow rates are less harmful. In addition, the gas used to shut-down the cell also plays a significant role, air leading to much more CO₂ emissions than nitrogen. However, carbon oxidation may not be the only damaging electrochemical reaction occurring during start-up and shut-down. As seen in §2.5 and §2.6.5, it stands for only a small fraction of the charge exchanged (reverse currents). In order to gather more information, two sets of protocols were established (Table 3-2).

Start-up aging protocols:

These protocols put forward the degradations due to start-ups. This is enabled by starting the cell with low hydrogen flow rate and then purging with high air or nitrogen flow rate (20 slph).

Four start-up aging protocols are realised:

- start-ups by injection of 2 slph hydrogen in air;
- start-ups by injection of 10 slph hydrogen in air;
- start-ups by injection of 2 slph hydrogen in nitrogen;
- start-ups by injection of 10 slph hydrogen in nitrogen.

Shut-down aging protocols:

These protocols put forward the degradations due to shut-downs. This is enabled by starting the cell with high hydrogen flow rate (20 slph) and then purging with low air or nitrogen flow rate.

Four shut-down aging protocols are implemented:

- shut-downs by injection of 2 slph air in hydrogen;
- shut-downs by injection of 10 slph air in hydrogen;
- shut-downs by injection of 2 slph nitrogen in hydrogen;
- shut-downs by injection of 10 slph nitrogen in hydrogen.

The gas flow rates used at start-up and shut-down are kept constant during the whole protocol.

3.2.2 Potential cycling protocol

In addition, two complementary protocols are carried out. They consist in replacing the shut-down and the restart of the cell by a OCV hold. In this case, the cell remains always fed with hydrogen and air and the voltage is cycled between OCV and 0.62V (voltage at 0.5 A/cm²) for the first protocol and 0.58V (voltage at 1 A/cm²) for the second one. This corresponds to Accelerated Stress Tests (AST) commonly used to aged PEMFC. These two additional protocols aims to evaluate the potential cycling contribution to the degradations resulting for start-ups and shut-downs.

The different aging protocols are detailed in Table 3-2.

Protocol N°	Type	Gas for the purge	Flow rate during the start-up (slph)	Flow rate during the shut-down (slph)	Intermediate required current density (A/cm ²)
1	Potential cycle protocol	Replaced by a potential hold at OCV			0.5
2	Potential cycle protocol	Replaced by a potential hold at OCV			1
3	Start-up aging protocol	Nitrogen	2	20	0.5
4		Nitrogen	10	20	
5		Air	2	20	
6		Air	10	20	
7	Shut-down aging protocol	Nitrogen	20	2	
8		Nitrogen	20	10	
9		Air	20	2	
10		Air	20	10	

Table 3-2. Details of the implemented protocols.

3.2.3 Protocol structure

In order to make them comparable, all experiments were based on the same structure:

- The cell is conditioned during about 24 hours as described in the cyclic voltammetry aging protocol (§3.1). The cell is operated at 52°C with saturated gas. $S_{\text{air}} = 3$, $S_{\text{H}_2} = 1.4$;
- 272 cycles (either start-up/shut-down or OCV hold) are realised. This step lasts 300s, which corresponds to the time needed by the fuel cell voltage to drop to 0.1V during a shut-down with nitrogen (this duration was quite independent of the nitrogen flow rate);
- In-between each start-up and shut-down or OCV hold, the cell has to provide 0.5A/cm² during 300 seconds. This value was increased to 1A/cm² in §3.3 for the aging protocol n°2;
- Every 16 start-ups or OCV hold, a characterization was performed, including:
 - Local Polarization Curve;
 - Local Electrochemical Impedance Spectroscopy (LEIS);
 - Local cyclic Voltammetry (LCV);
 - Measurement of the internal currents during an additional start-up/shut-down cycle.

In the potential cycle protocols, the start-up/shut-down cycle of the characterization phase was replaced by an OCV hold.

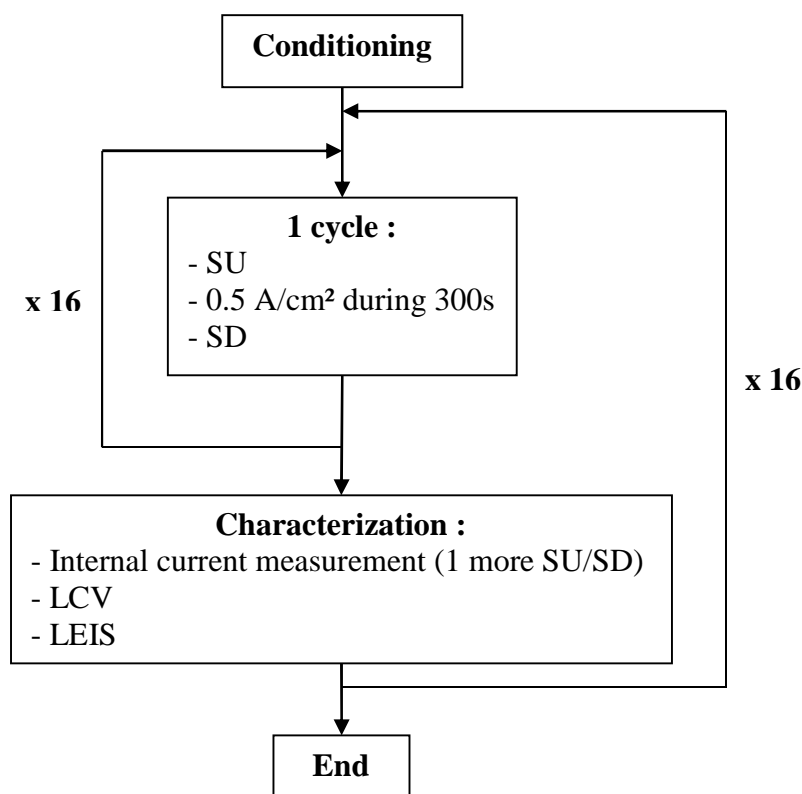


Figure 3-5. Schematic representation of a start-up or shut-down aging protocol.

3.3. Potential cycling

Potential cycling is one of the most common fuel cell accelerated stress tests, probably because it is easy to implement. While it is often realised under the form of cyclic voltammeteries, we chose here to let the cathode filled with air to observe degradations occurring in conditions close to real use operation. Potential cyclings are often considered as representative of start-ups and shut-downs [1]. The results presented in this section will therefore be compared with those obtained during real start-up and shut-down aging protocols.

Descriptions of in-situ local degradations during potential cycles are quite rare in the literature. Weng et al. [118] for instance used a 92 cm² segmented cell with six serpentine flow channels in co-flow mode to study the influence of the potential cycles on the local performances. They realised 450 cycles, which consisted in alternating operation at 0.07 A/cm² and 0.7 A/cm², each current step lasting 10 minutes. During this protocol, they observed the appearance of heterogeneities in the local polarization curves as well as in the ECSA. They attributed these heterogeneities to the operating conditions (hydrogen and air relative humidities set to 60% RH) which generated flooding and therefore fuel starvation events in the downstream part of their cell. The cell was operated at 60°C.

In our case, potential cycles induced a homogeneous decrease of the ECSA (Figure 3-6) which, with regards to the result of Weng et al., tends to indicate that no local fuel starvation took place. The homogeneous degradations observed in Figure 3-6 should therefore result from uniformly distributed phenomena.

Nevertheless, the ECSA losses were more pronounced when the potential cycling was done between OCV and 0.58V (which corresponds to a current density of 1 A/cm²) than between OCV and 0.62V (which corresponds to a current density of 0.5 A/cm²). The ECSA drops seemed also linearly dependent on the number of cycles (at least for the first 272 sequences). For protocol 1 (OCV – 0.5 A/cm²), the global loss was of about 7.8 m²_{Pt}/g_{Pt} after 272 cycles, which represents 12% of the maximal ECSA value or a loss of 285 cm²_{Pt}/g_{Pt}/cycle. For protocol 2 (OCV – 1 A/cm²) these values were higher. The global loss was of about 10.1 m²_{Pt}/g_{Pt} after 272 cycles, which represents 14.3% of the initial value or a loss of 370 cm²_{Pt}/g_{Pt}/cycle.

These results are of the same order of magnitude as those obtained with repeated cyclic voltammeteries. After 272 scans (136 cycles) between 0.1V and 1.2V, the global ECSA had decreased of 12.4 m²_{Pt}/g_{Pt}, which represents 17.7% of the initial value or 456 cm²_{Pt}/g_{Pt}/scan.

The difference in the degradation rates can be explained by the conditions in which potential variations were applied:

- By steps and in air filled cathode for the potential cycles;
- By linear sweep in nitrogen filled cathode during cyclic voltammetry.

In addition, the lower potential limit was set to 0.1V for the cyclic voltammetry aging protocol while it reached a minimum of 0.58V only in the case of the OCV cycling protocol. Linse et al. [26] showed that the lower potential limit during a potential cycling is a key parameter for the carbon oxidation: more CO₂ emissions were measured when the lower potential limit was low. The CO₂ emissions were also related to the upper limit of the potential scan: the higher this limit, the more CO₂ was measured. The voltammetry reached up to 1.2V while during OCV cycling protocol, the fuel cell voltage never exceeded OCV.

The ECSA losses for protocol 1 (OCV – 0.5 A/cm²) and 2 (OCV – 1 A/cm²) are then assumed governed mostly by platinum dissolution and redeposition (long and short Ostwald ripening, §1.4.3).

	Global	ECSA at BOL (m ² _{Pt} /g _{Pt})	Maximal ECSA (m ² _{Pt} /g _{Pt})	Final ECSA (m ² _{Pt} /g _{Pt})	ECSA loss (m ² _{Pt} /g _{Pt}) ⁽¹⁾	Relative ECSA loss (%) ⁽¹⁾	ECSA loss/cycle (cm ² _{Pt} /g _{Pt}) ⁽¹⁾
Protocol	OCV - 0.5 A/cm ²	62.7	64.7	56.9	7.8	12.0	285.1
	OCV - 1 A/cm ²	70.2	70.2	60.1	10.1	14.3	369.8
	Cyclic Voltammetry ⁽²⁾	67.5	70	57.6	12.4	17.7	455.9

Table 3-3. Global ECSA evolution during the different potential cycle agings. (1) with reference to the maximum ECSA. (2) evaluated on 272 scans which makes only 136 cycles as defined in the cyclic voltammetry aging protocol.

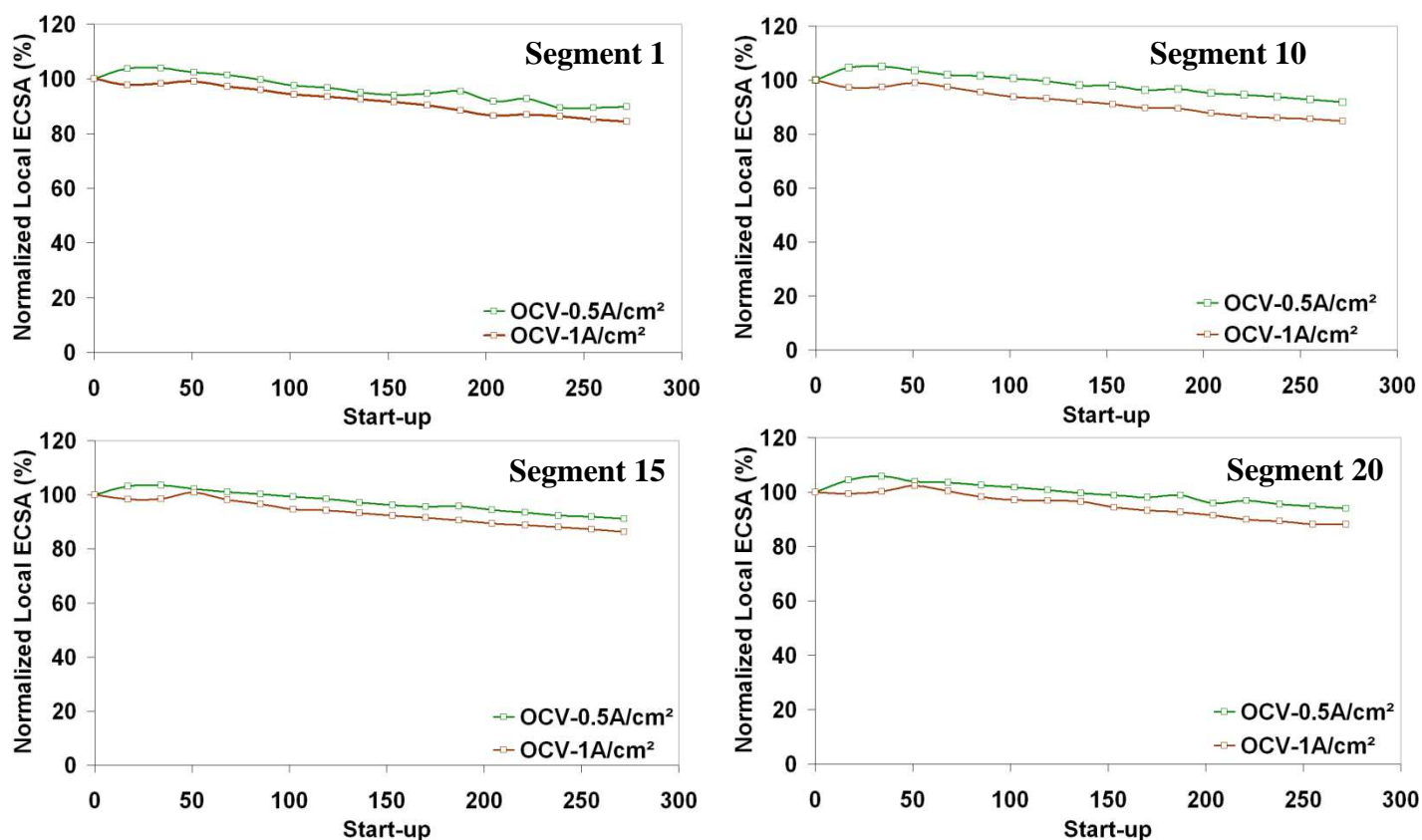


Figure 3-6. LECSA of segment 1, 10, 15, 20 measured during potential cycle aging protocols at 0.5 A/cm² and 1 A/cm² (here represented depending on the an equivalent number of start-up: 1 start-up = 1 OCV hold).

Even if global damages were important, their homogeneous distribution over the cell surface limits their impact in term of performance. Indeed, no evolution of the fuel cell voltage was noticed during these experiments. Likewise, no clear evolution of the local current densities was evidenced: the ability of each segment to deliver the required average current density remained unchanged even after 272 cycles: due to their high cathode platinum loading (0.6 mg_{Pt}/cm²), the Johnson Matthey MEAs were not very sensitive to these limited platinum losses.

3.4. Start-up aging

Results presented hereafter correspond to the start-up aging protocols performed by injecting low or high hydrogen flow rates in nitrogen or air (protocols 3, 4, 5 and 6).

3.4.1 ECSA evolution

The monitoring of the local ECSA (Figure 3-7) provided various informations:

- The ECSA tended to increase for almost all the protocols during the first start-ups. As already mentioned in §3.1, this evolution may correspond to an extension of the conditioning stage. Therefore, the analysis of the agings should be realised outside of this period.

- Except for the first start-ups, all aging protocols led to a decrease of the global platinum active surface (Annex 2).
- As expected, the ECSA drop was more pronounced when air was used instead of nitrogen to purge the cell (Annex 2). In this case, the reduction reactions in the passive part of the anode are limited (§2.1.1) and so are the oxidation reactions in the opposite part at the cathode. The reduction reactions probably occur because of oxygen which permeates through the membrane (§0) or because of the reduction of platinum oxide. The formation of these oxides could be enabled by oxygen crossover before the cell was restarted.
- The ECSA drop was more marked when hydrogen was introduced slowly in the anode compartment (Annex 2). This evolution can be correlated with those of the global charge exchanged (§0) and carbon dioxide emissions (§2.5): more carbon corrosion at low hydrogen injection flow rate must result in more platinum particle detachments from the carbon support (§1.4.3). Introducing hydrogen slowly in the anode maintains high the cathode potential a longer time in the passive part of the cell [101]. Thus, long and short range Ostwald ripening should also be accentuated.
- The ECSA drop was not homogeneous (Annex 3 and Annex 4): the segments located close to the hydrogen outlet always suffered from a faster platinum loss rate. The ECSA drop was up to four times more pronounced in the last (20th) segment than in the first one. It must be noted that over the first segments, the platinum losses observed during the start-up aging protocols performed with nitrogen are close from those obtained during the potential cycle aging protocols. For these segments, degradations can therefore be attributed mostly to potential cycling rather than to internal currents (forward currents in this case).

Despite the high air injection flow rate used to purge the cell, shut-downs still seem to generate ECSA losses in the first segment (where air was used to flush the anode) during the start-up aging protocols in air. Some improvements of the shut-down procedure can be considered to avoid these degradations:

- The gas injection flow rate could be increased during the flush.
- The purge could be done in two steps: first by flushing the anode compartment with nitrogen and then with air.

These two solutions were actually combined in §3.6 with significant results. Nevertheless, even if shut-downs induce a bias during the aging protocols (using air for the purge), it does not impede the observation of degradations resulting from start-ups.

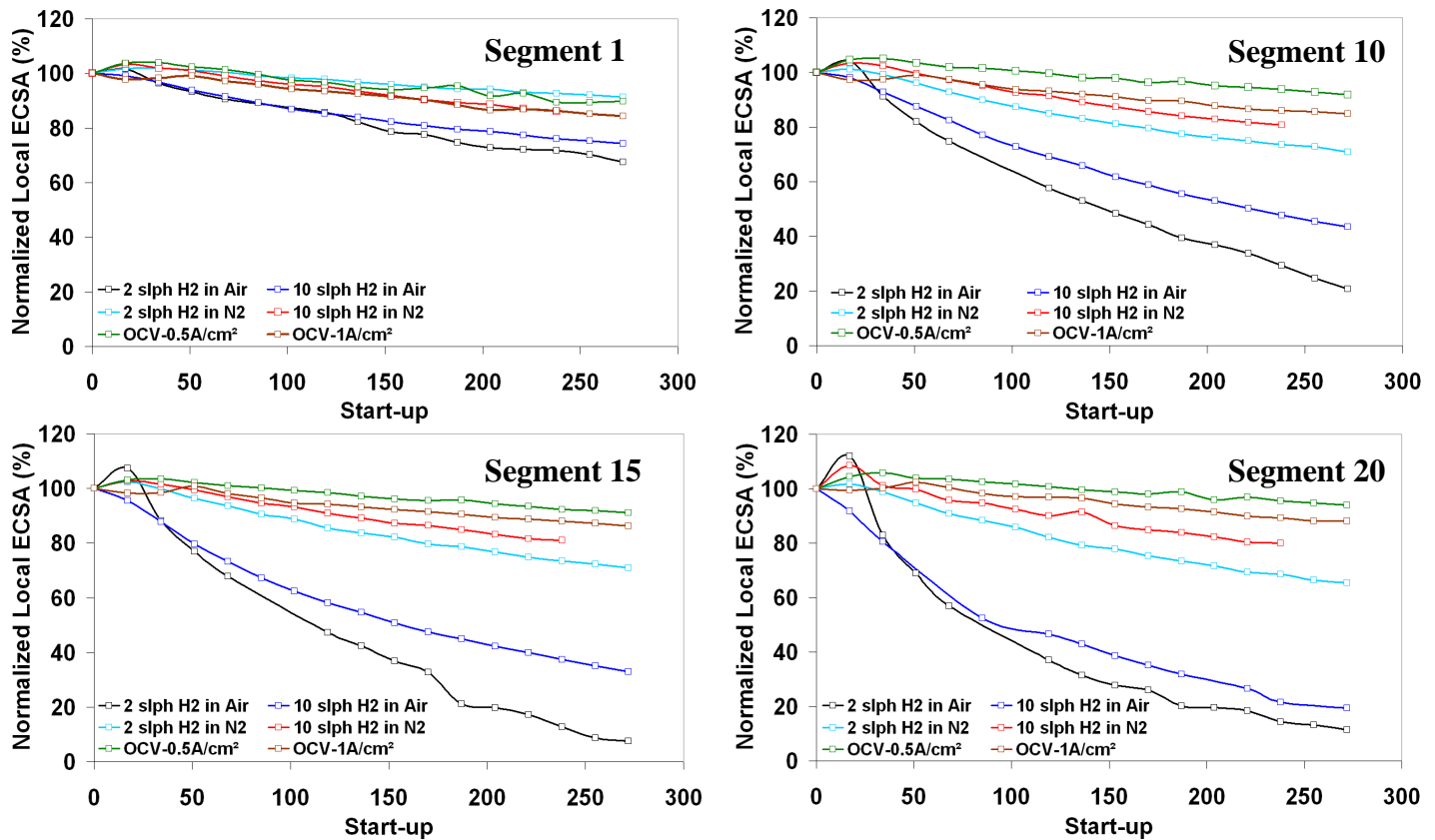


Figure 3-7. LECSA of segment 1, 10, 15, 20 measured during potential cycling aging protocols between OCV and voltage at 0.5 A/cm² or 1 A/cm² and during start-up aging protocols by injection of 2 slph or 10 slph hydrogen in nitrogen or air.

3.4.2 Charge exchanged evolution

Complementary information was provided by the global and local charges exchanged, which were measured every 17 start-ups and linearly interpolated during the intermediate sequences. The evolution of the global charge exchanged during the aging protocols is depicted in Figure 3-8:

- Their values at the beginning of the aging protocols were consistent with those obtained in §0.
- During the course of the aging protocols, they tended to diminish at a rate which increased with their value at beginning of life (BOL): drops were more pronounced when performing start-ups in air at low hydrogen injection flow rate.

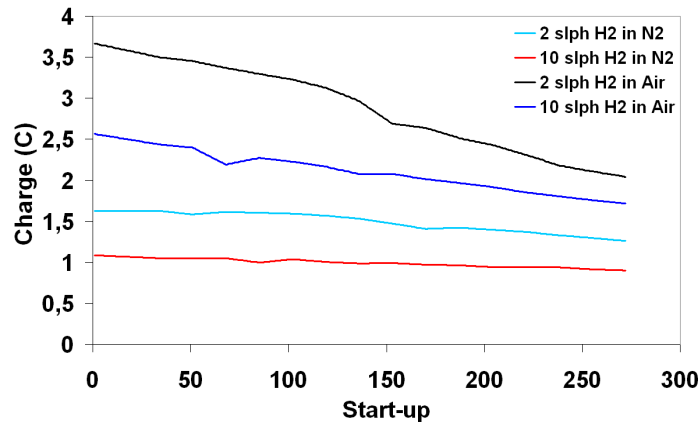


Figure 3-8. Evolution of the charge exchanged for start-up aging protocols by injection of 2 or 10 slph hydrogen in nitrogen or air at the global scale.

In the case of the start-up aging protocol by injection of 2 slph hydrogen in air, one can observe that the charge exchanged evolution was also a function of the position of the segment along the cell: it was more pronounced near the hydrogen outlet (Figure 3-9).

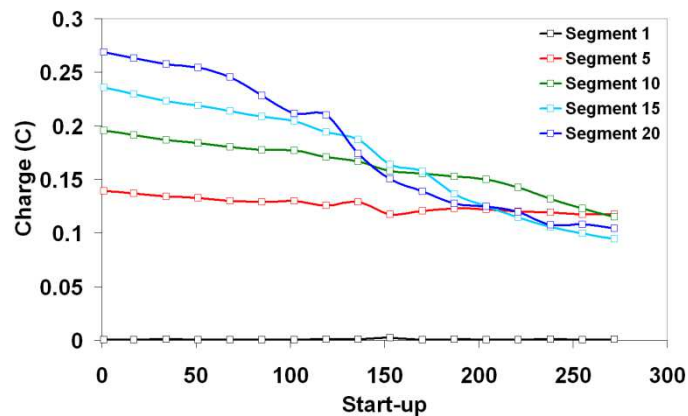


Figure 3-9. Local charges exchanged in segment 1, 5, 10, 15 and 20 during a start-up aging protocol by injection of 2slph hydrogen in air.

3.4.3 Charge exchanged vs. ECSA

The comparison of Figure 3-7 with Figure 3-8 and Figure 3-9, shows that the ECSA drop is more important when more charges are exchanged between the active and passive part of the cell. Thus, the global charge exchanged during each aging protocol was integrated over the number of start-ups and compared to the global ECSA (Figure 3-10).

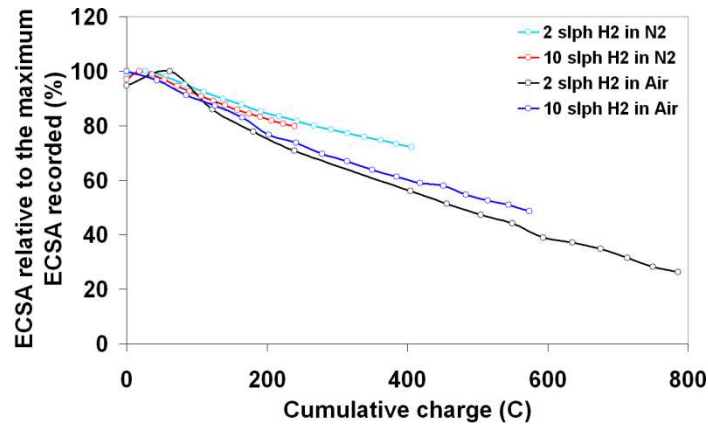


Figure 3-10. ECSA relative to the maximum ECSA recorded vs the cumulative charge exchanged during the start-up aging protocols by injection of hydrogen in nitrogen or air at 2 slph and 10 slph at the global scale.

Figure 3-10 shows that the cumulative charge exchanged and the ECSA loss were linearly correlated for every aging protocol. However, the slopes differs whether hydrogen was injected in air or in nitrogen. For instance, the ECSA loss per cumulative charge exchanged was of about $1.35 \text{ m}^2_{\text{Pt}}/\text{g}_{\text{Pt}}/(\text{C}/\text{cm}^2_{\text{MEA}})$ when 2 slph hydrogen was injected in nitrogen while it was of about $1.63 \text{ m}^2_{\text{Pt}}/\text{g}_{\text{Pt}}/(\text{C}/\text{cm}^2_{\text{MEA}})$ in air. This difference may be explained by:

- Carbon oxidation, which certainly affected the MEAs aged by repeating start-ups in air but not (or to a lesser extent) those which were aged by repeating start-ups in nitrogen. In §2.5, we observed that carbon oxidation was nearly negligible during single start-ups in nitrogen. This reaction contributes to the charge exchanged and should also impact the ECSA since it leads to the detachment of platinum particles.
- The cathode potential ϕ_c , which reaches higher values when start-ups were performed in air than when they were performed in nitrogen (§4.2.3). Therefore the long and short range Ostwald ripening should be less significant with nitrogen.

Interestingly, the influence of the hydrogen injection flow rate on the slope of the curves in Figure 3-10 appears to be limited. However, the final cumulative charge exchanged as well as the ECSA loss were higher when the hydrogen injection flow rate used was low. This may be related to the time the cathode potential remains high (Figure 2-17 in §2.1.2).

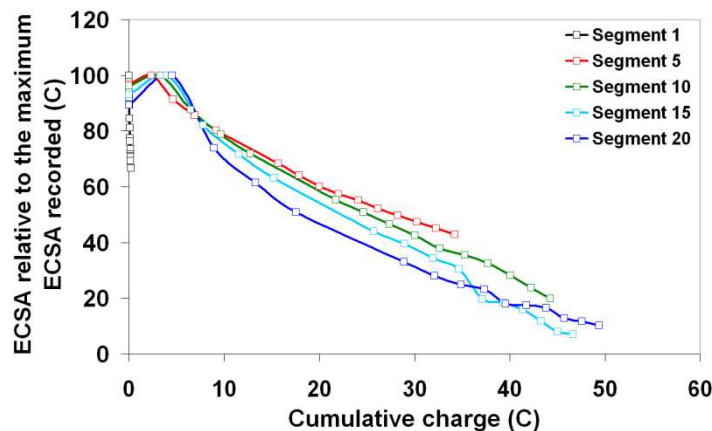


Figure 3-11. LECSA relative to the maximum LECSA recorded vs local cumulative charge exchanged during the start-up aging protocol by injection of 2 slph hydrogen in air.

Figure 3-11 presents at a local scale the evolution of the ECSA as a function of the cumulative charge exchanged during the start-up aging protocol performed by injection of 2 slph hydrogen in air. One can observe that:

- The local ECSA loss per cumulative charge exchanged corresponds to that of the global ECSA loss $\pm 10\%$ (for segment 5 to 20 where degradations are mainly due to start-ups).
- The final ECSA loss and cumulative charge exchanged depend on the position of the segment along the cell: they are more pronounced near hydrogen outlet, the higher their values (§2.1.2). This trend is not so obvious for segments 15 and 20 in Figure 3-11 since they had lost almost all their ECSA at the end of the protocol. However, this trend was observed during the other start-up aging protocols which induced more progressive degradations.

These observations can be complemented by those in §3.7, which reveals a more pronounced thinning of the cathode catalyst layer close to the hydrogen outlet due to carbon corrosion: a result which could be expected considering the correlation between charge exchanged and carbon dioxide emission described in §2.5 (*Figure 2-53* and Figure 2-58). The high cathode potential maintained longer in the segment close to the hydrogen outlet could be responsible for these evolutions (§4.2.3).

Finally, almost no charge was exchanged in segment 1 because it stayed always active during start-ups. In this case, the ECSA loss could be attributed to the shut-downs but the charge exchanged during these operations was not considered (that is why the curve corresponding to this segment is different in Figure 3-11). In §3.5, where shut-down aging protocols are presented, the contributions of start-up and shut-down are both taken into account in the cumulative charge exchanged for its comparison with the ECSA (Figure 3-20 and Figure 3-21).

3.4.4 Performance evolution

Figure 3-12 represents the fuel cell voltage during every start-up aging protocol at different current densities. Two groups can be distinguished:

- The start-up aging protocols by injection of hydrogen in nitrogen. During these protocols the fuel cell voltage remained stable between 0.1 A/cm² and 1 A/cm², this despite the heterogeneous ECSA losses described in §3.4.1.
- The start-up aging protocols by injection of hydrogen in air. The fuel cell voltage dropped during these protocols. The drop was accelerated by the decrease of the hydrogen injection flow rate. The evolution was also more pronounced at high current density.

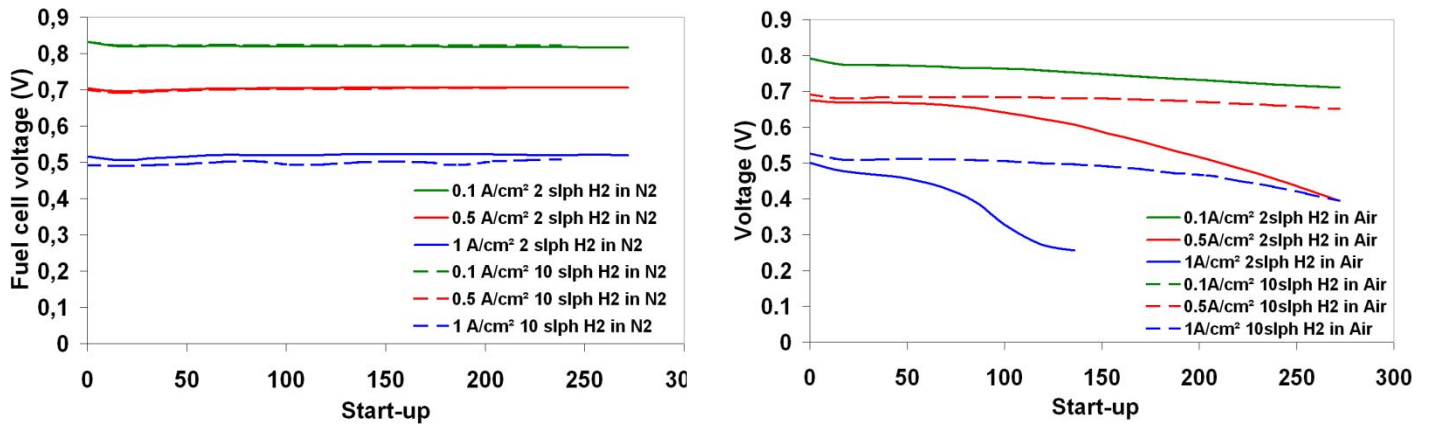


Figure 3-12. Voltage evolution at 0.1 A/cm², 0.5 A/cm² and 1 A/cm². Start-up aging protocols by injection of hydrogen in nitrogen (left) and air (right) at 2 slph and 10 slph.

Figure 3-13 shows the evolution of the local current densities profiles at an average current density of 0.5 A/cm² for the start-up aging protocols by injection of 2 and 10 slph hydrogen in air. While homogeneous at BoL, local current densities became rapidly heterogeneous along the gas channel. The segments the most affected were those with the highest local cumulative charges exchanged (§3.4.2) and where ECSA dropped the most (that is to say the segments close to the hydrogen outlet, §3.4.1). The local current density losses were compensated by an increase of the current density in the segments close to the hydrogen inlet. At the end of the start-up aging protocol by injection of 10 slph hydrogen in air, 6 segments were not able to provide the required averaged current density (0.5 A/cm²). They were 11 when start-ups were performed by injecting 2 slph hydrogen in air.

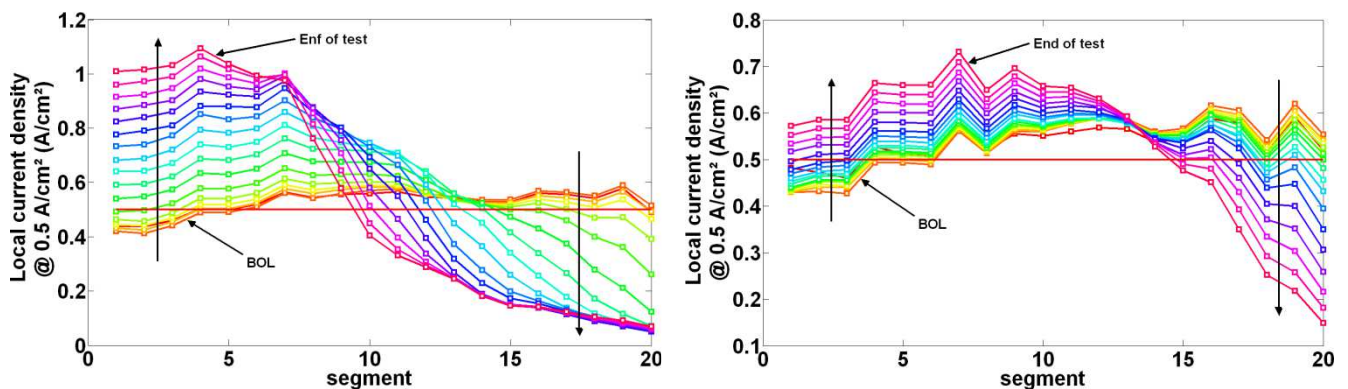


Figure 3-13. Local current densities evolution at an average current density of 0.5 A/cm². Start-up aging protocols by injection of hydrogen in air at 2slph (left) and 10 slph (right).

Concerning the start-up aging protocol by injection of hydrogen in nitrogen, no evolution of the local current densities was observed, this even when they were measured at a higher average current density (1 A/cm²). Carbon oxidation, which was more significant in the case of start-ups in air, seems therefore to play a determining role in the performance drop. However, the cathodes of the Johnson Matthey MEAs being well loaded in platinum (0.6 mg_{Pt}/cm²), important platinum losses are probably necessary before their impact on the performances becomes noticeable.

3.4.5 Further investigations into start-up aging protocol by injection of hydrogen in nitrogen

Starting from these results, a longer aging protocol was implemented to find the threshold value of the local ECSA below which performances were affected. This protocol included 2500 start-ups, realised by injecting hydrogen in nitrogen at 2 slph. The local ECSA continued to decrease after the end of the previous (and shorter) protocol with the same tendencies: the segments close to the hydrogen outlet were the most affected (Figure 3-14).

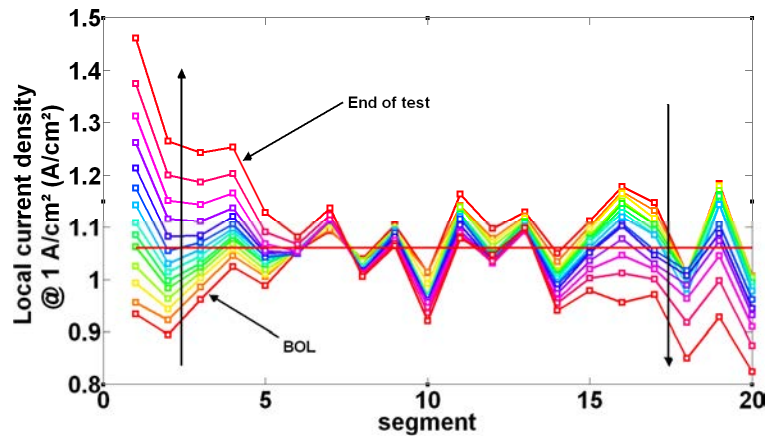


Figure 3-14. Local current densities (average current density of $1\text{A}/\text{cm}^2$) during the long term aging protocol by injecting hydrogen in nitrogen at 2slph.

After 2500 start-ups, the ECSA of the last segment fell below 5% of its maximum value while that of the first segment was still above 40% (Figure 3-15).

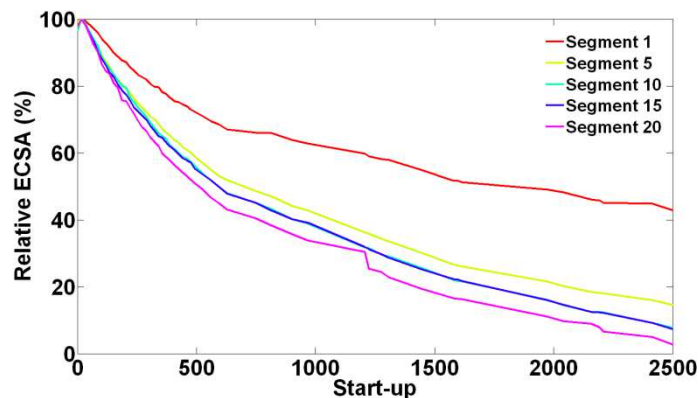


Figure 3-15. Local ECSA evolution during the long term start-up aging protocol by injecting hydrogen in nitrogen at 2slph.

Contrary to the first and shorter protocol, the fuel cell voltage decreased significantly (Figure 3-16). The decrease rate was more pronounced when the average current density was higher. The local current densities evolution was also more marked (Figure 3-14). It can be assumed that contrary to the cyclic voltammetry cycles (§3.1), the heterogeneity of the LECSA losses over the MEA surface accelerates the voltage drop.

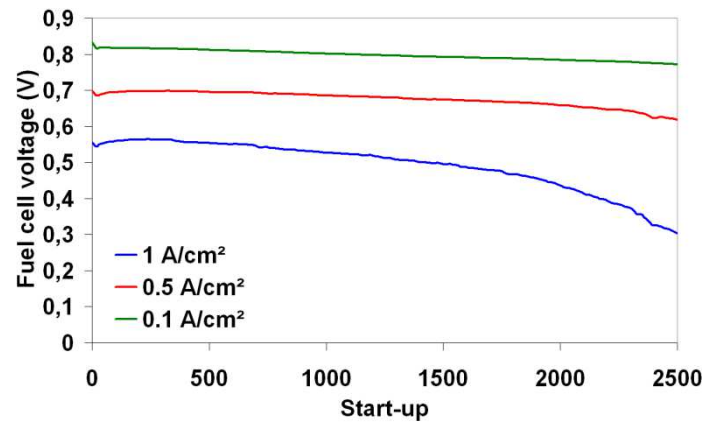


Figure 3-16. Cell voltage evolution at different global current densities during the long term start-up aging protocol (injection of 2 slph of hydrogen in nitrogen).

At the beginning of the aging, degradations were balanced by phenomena which maintained the performances constant, like the decrease of the global high frequency resistance R_{hf} (Figure 3-17): its variation was of about $8 \cdot 10^{-3} \Omega \cdot \text{cm}^2$ between the first and the 1000th start-up. At 1 A/cm^2 , this corresponds to a gain of $8 \cdot 10^{-3} \text{ V}$ (most of this gain occurred before the 500th start-up). After 2000 start-ups, R_{hf} augmented significantly in the segments located near the hydrogen outlet (Figure 3-17) while it still decreased slowly at the other end of the MEA. Platinum lost near the hydrogen outlet being assumed to migrate - at least partially - in the membrane (long range Ostwald ripening leading to the formation of a Pt-band, §1.4.4 and §3.7.2), it can catalyse reactions which modify the membrane structure and thus its conductivity, which can result eventually in its failure (§1.4.4).

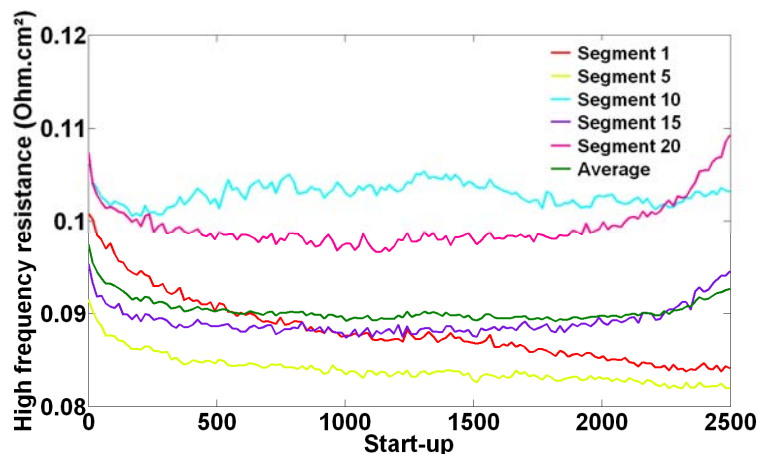


Figure 3-17. High frequency resistance evolution during the long aging protocol by injecting hydrogen in nitrogen at 2 slph.

Additional information can be brought by local EIS. For instance, the time evolution of the local capacities appeared to be correlated to that of the LECSAs (Figure 3-18).

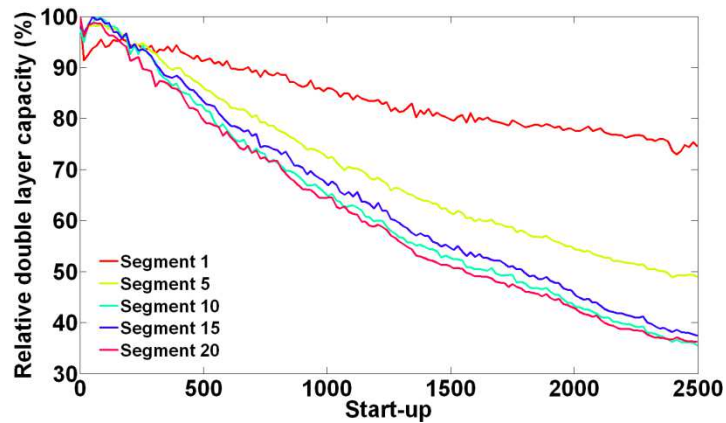


Figure 3-18. Relative double layer capacities evolution during the long aging protocol by injecting hydrogen in nitrogen at 2slph.

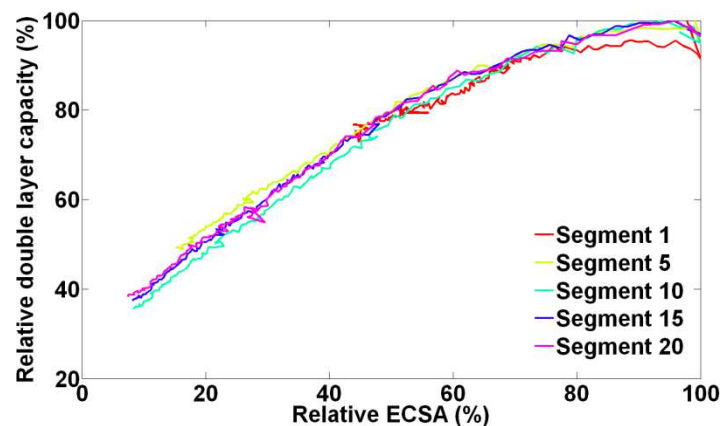


Figure 3-19. Relative capacities evolution in function of the relative LECSA evolution during the long aging protocol by injection of hydrogen in nitrogen at 2slph.

Start-ups in nitrogen, like start-ups in air induced heterogeneous performance losses which entailed different levels of local degradations. These degradations could be observed through the platinum active surface evolution or that of the double layer capacity, which were correlated according to Figure 3-19. Actually, since start-ups in nitrogen are not supposed to oxidize carbon (or only in very limited amount), the double layer capacity losses are assumed to be caused by the loss of platinum (resulting from long and short range Ostwald ripening). By extension, the charge exchanged being correlated with the local ECSA, it is also assumed to be correlated with the double layer capacity. For the segment 1, the charge exchanged should be this resulting from shut-downs.

3.4.6 Conclusion about start-up agings

The results presented in §3.4 shows that:

- Start-ups entailed a heterogeneous aging of the MEA, which can be observed through the local evolution of the ECSA or that of the double layer capacity. These evolutions appear to be correlated with that of the cumulative charge exchanged.
- The extent of the degradations and thus of the performance loss depends on the gas used to flush the anode compartment. More damages were observed when hydrogen was injected in an anode compartment filled with air than with nitrogen. In this case,

high cathode potentials are measured (§0), which entails carbon oxidation and ECSA drop. According to §2.6.5, carbon oxidation should be negligible in the case of start-ups performed by injection of hydrogen in nitrogen. In addition, lower cathode potentials limit long and short range Ostwald ripening.

- The decrease of the hydrogen injection flow rate accelerates the fuel cell performance decay since it maintains high the cathode potential over a longer time (in the passive part of the cell).

The comparison of the potential cycle protocols (§3.3) with the start-up aging protocols (§3.4) revealed that they result in different degradation mechanisms: potential cycling protocols induced a uniform aging of the MEA and the ECSA losses were lower than those obtained in real start-up conditions.

3.5. Shut-down aging

In chapter 2 (§2.6.3), Figure 2-54 indicates that the total charge exchanged during a start-up with injection of 20 slph of hydrogen in air is close to that obtained during a shut-down with a 2 slph air injection flow rate. The approach which consists in implementing slow shut-downs to enhance their effects on degradations should then be limited. Even if start-ups are realised using a high hydrogen injection flow rate, both start-ups and shut-downs are expected to affect simultaneously the performance (aging) of the cell.

Thus, for the shut-down aging protocol by injection of air at 2 slph in the anode compartment (protocol 9), the local charges exchanged generated by start-ups were taken into account. In Figure 3-20, which represents the evolution of the local cumulative charges exchanged during the aging protocol, one can observe that the contribution of start-ups is of the order of 40% of that of shut-downs, although hydrogen is injected with a velocity ten times faster than air.

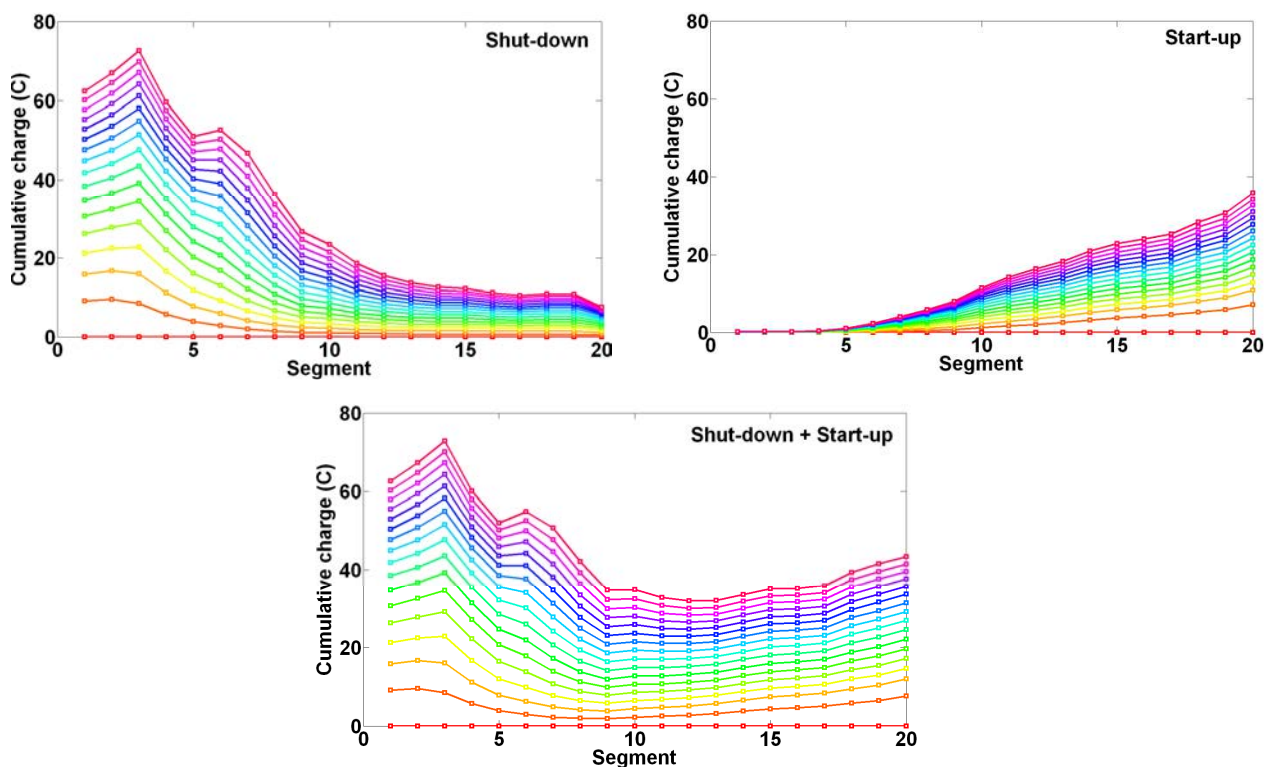


Figure 3-20. Local cumulative charges exchanged during shut-downs with air at 2 slph (top left), start-ups with hydrogen at 20 slph (top right) and during the both (bottom).

The evolution of the local ECSAs during this protocol is given in Figure 3-21.

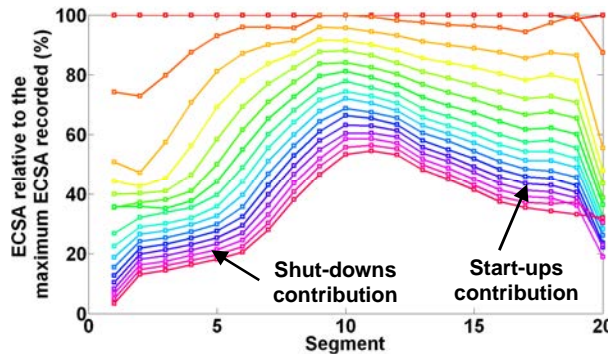


Figure 3-21. Evolution of the local ECSA relative to the maximum ECSAs recorded during the shut-down aging protocol by injecting air at 2 slph in the anode compartment.

According to Figure 3-20 and Figure 3-21, the higher the cumulative charge exchanged, the higher the local ECSA drop. The respective contributions of start-ups and shut-downs can be well distinguished on the local ECSA profiles.

Figure 3-22, where local ECSA drop is plotted vs the local cumulative charge exchanged, allows confirming the correlation between these two parameters. Except at the beginning of the aging protocol and for some singular points, the local ECSA loss vs. the cumulative charge exchanged is similar for all segments, including the first one where the charge exchanged during shut-downs is taken into account (which was not the case in Figure 3-11). In the present case, shut-downs lead to higher platinum active surface loss than start-up because the gas injection velocities were chosen adequately.

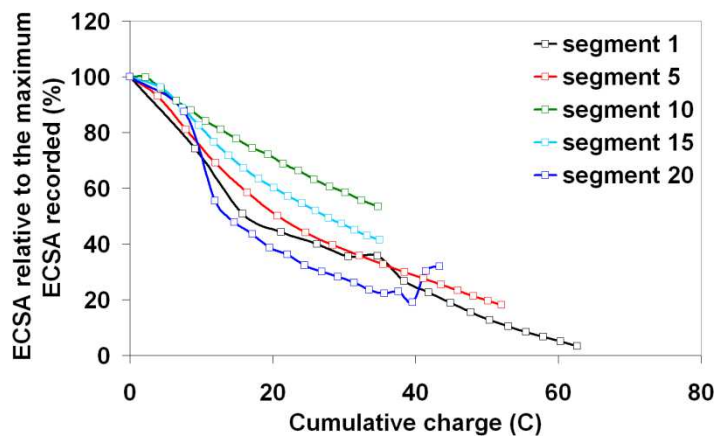


Figure 3-22. ECSA relative to the maximum value recorded vs the cumulative charge resulting from the reverse currents during the shut-down aging protocol with air at 2 slph and during its equivalent start-up aging protocol at a global (left) and local (right - shut-down aging protocol only) scale.

The correlation between ECSA and cumulative charge exchanged is also valid at a global scale. The comparison between the start-up aging protocol performed by injecting hydrogen in air at 2 slph and the shut-down aging protocol with 2 slph of air in hydrogen (Figure 3-23) confirms that the ECSA losses are similar. However, higher values were measured during the start-up aging protocol.

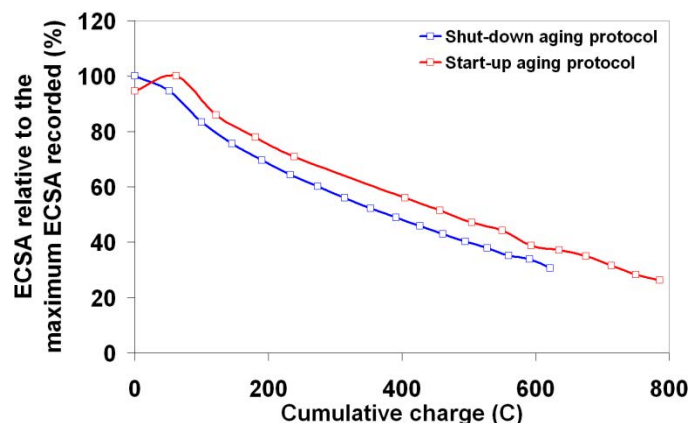


Figure 3-23. ECSA relative to the maximum ECSA recorded vs the total cumulative charge exchanged during the shut-down aging protocol (injection of 2 slph of air in hydrogen) and during the start-up aging protocol (injection of 2 slph hydrogen in air).

Figure 3-24 shows that degradations the most significant decrease of the local current density was observed close to the segment 1 where air was introduced for the purge. This decrease was compensated by the higher current density in the closest segments from the hydrogen outlet, which was sufficient to maintain an average current density of 0.5 A/cm² during the whole aging protocol. However, after 119 start-ups, the cell was not able anymore to provide an average current density of 1 A/cm². In Figure 3-25, the evolution of the local current densities relative to their initial values at an average current density of 0.5 A/cm² brings some complementary information:

- Between the beginning-of-life (BoL) and the middle-of-life (MoL), the segments located close to the air inlet at the anode (segment 1) were damaged by shut-downs. Their current densities decreased but the other segments compensated homogeneously the losses.
- Between the middle-of-life and the end-of-life, one more segment failed to provide 0.5 A/cm² (the 7th). The compensation by the other segments was this time heterogeneous: the segments in the middle of the cell supported most of the current density redistribution. The segments close to the hydrogen outlet were certainly affected by degradations resulting from start-ups. These degradations are assumed to be more progressive than those occurring during shut-downs, which explains why their effects were delayed.

The contribution of shut-downs to the degradation seems therefore to prevail over that of start-ups. At the end of this aging protocol, the first seven segments provide less than the average current density (0.5 A/cm²). As a reminder, eleven segments were in this situation in the equivalent start-up aging protocol (Figure 3-13).

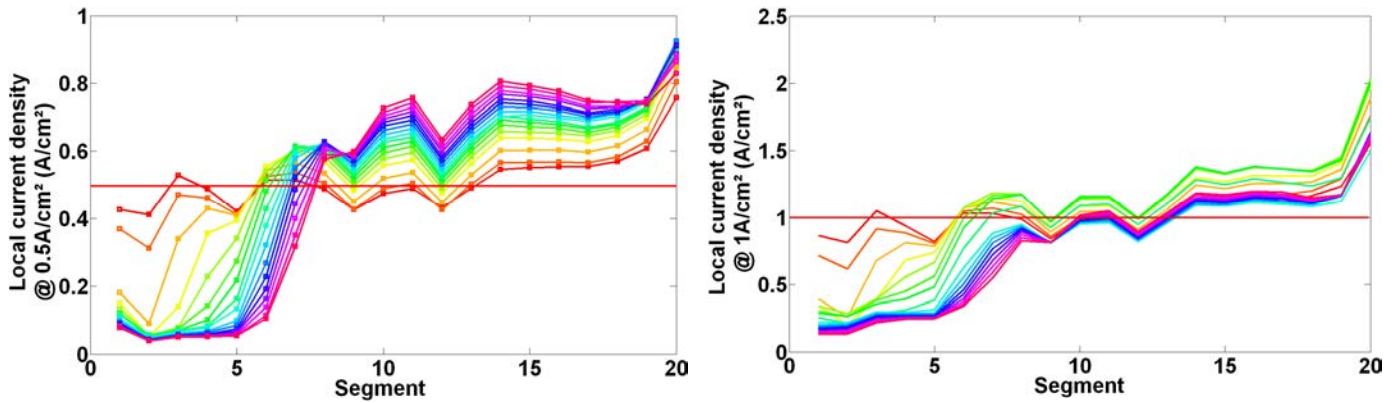


Figure 3-24. Evolution of the local current densities during the shut-down aging protocol with air at 2 slph.

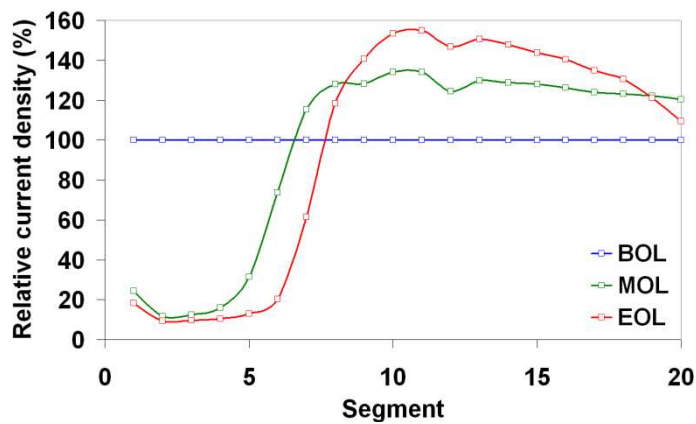


Figure 3-25. Local current densities evolution relative to their initial values at an average current density of 0.5 A/cm² during the shut-down aging protocol by injecting air in hydrogen at 2 slph (Beginning of Life, Middle of Life and End of Life).

Concerning the performances, Figure 3-26 indicates that the voltage drop occurred more rapidly at 1 A/cm² during the shut-down than during the start-up aging protocol. However, this result is to qualify: the faster voltage drop in the case of the shut-down aging protocol was due to the simultaneous effect of shut-downs and start-ups (during the start-up aging protocol, the shut-downs did not generate significant degradations and the segments close to the purge inlet could support longer the current density losses of the segments close to the hydrogen outlet). It is very likely that the result would be much different if the start-up contribution to the degradation could be further minimized in the shut-down aging protocol. This is why in the next section, which compares the Ion Power MEAs with different specifications, the start-ups are realised in two steps during the shut-down aging protocols:

- Once the anode compartment purged with low air flow rate, it is purged with nitrogen at high flow rate (90slph).
- Start-up is then performed by injecting 90 slph of hydrogen in nitrogen.

One can also remark that even if the start-up and shut-down effects were combined during the shut-down aging protocol, damages induced by the start-up aging protocol still became predominant at 0.5 A/cm² around the 200th start-up.

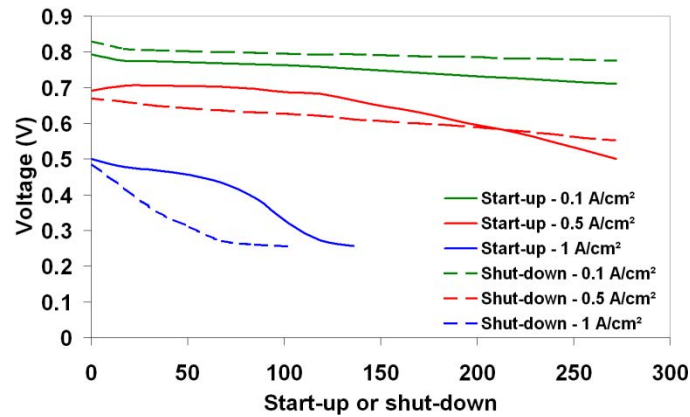


Figure 3-26. Cell voltage evolution at average current density of 0.1, 0.5 and 1 A/cm² during start-up and shut-down aging protocols realised with a gas injection flow rate set to 2 slph.

3.6. Start-up and shut-down aging with different MEAs

Regarding the results in §2.8.2, distinct evolutions are expected between MEAs with different specifications when submitted to the same aging protocols. In this section, only Ion Power MEAs described in §2.2 were used. As a reminder, these MEAs differ from a reference MEA by a unique parameter only: anode or cathode platinum loading, or carbon specific surface (Annex 1).

Two different aging protocols (start-up vs. shut-down) were employed to distinguish between the SU and SD effects on degradation rates and performance losses: in the start-up aging protocol, the hydrogen injection flow rate (in the air-filled anode compartment) was set to 10 slph and the shut-down effects were minimized by injecting nitrogen during each shut-down. In the shut-down aging protocol, the air injection flow rate (in the hydrogen-filled anode compartment) was set to 10 slph and the fuel cell was started-up again only after carefully flushing the anode compartment with nitrogen, which minimized the start-up effects. In both cases, the fuel cell was operated at a fixed current density of 0.67 A/cm² for 5 minutes between two consecutive SU/SD sequences in order to monitor the performance decrease. The ElectroChemical Surface Area (ECSA) was measured after every 30 SU/SD sequences. The two protocols were stopped once the ECSA had decreased by about 50% (40% in the case of the MEA with a higher Pt loading at the cathode).

3.6.1 Impact on the whole cell

Figure 3-27 presents the evolution of the cell voltage as a function of the number of SU or SD performed. As expected from the previous data, one can see that start-ups have a stronger impact than shut-downs. At beginning of life (BoL), the voltage of the reference MEA was the lowest, which is not surprising considering that increasing the carbon specific surface, cathode Pt loading or the anode Pt loading improves generally the fuel cell performance. However, the voltage decreased more rapidly with the MEA having a higher Pt loading at the anode and with that having a higher specific surface carbon at the cathode.

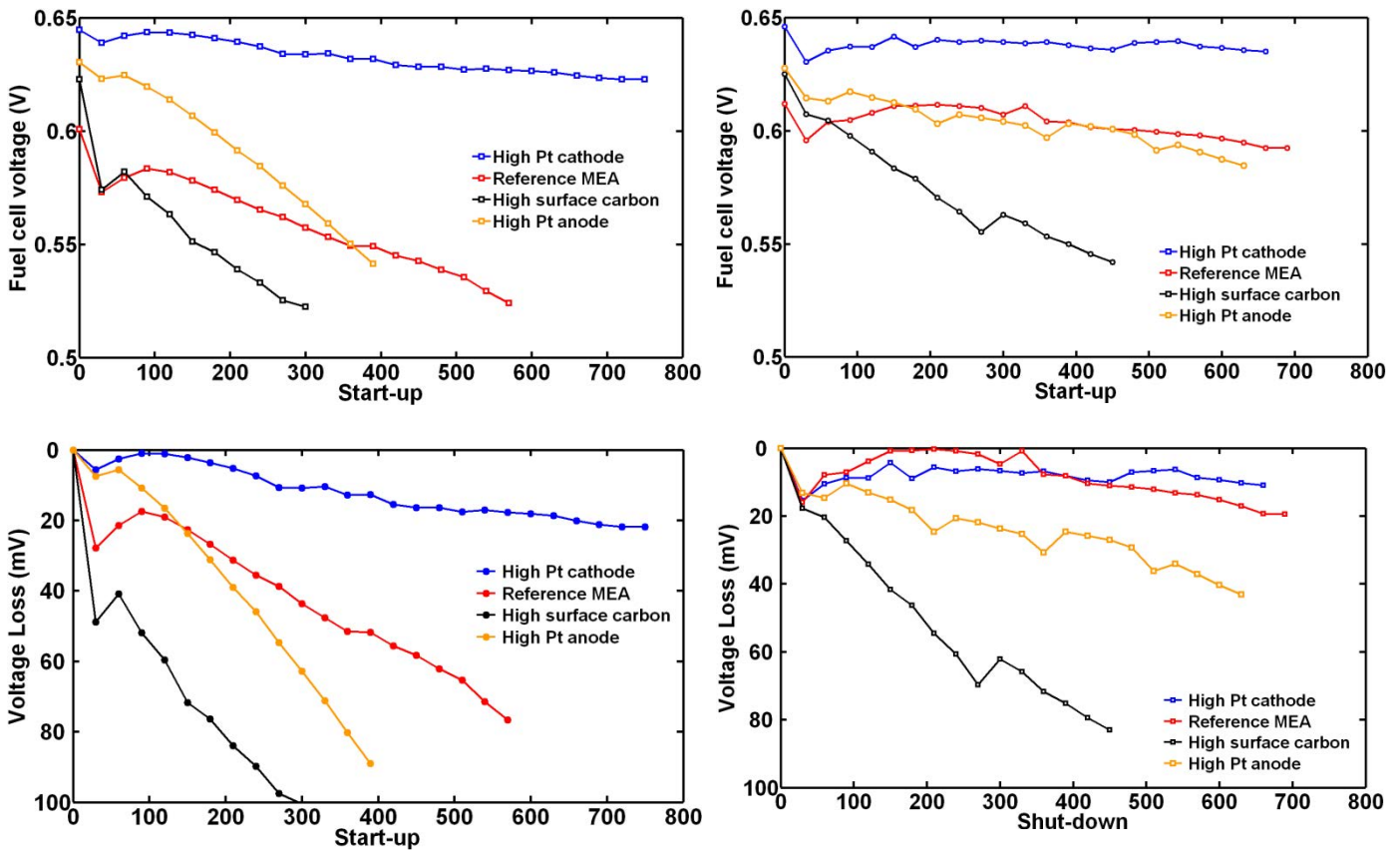


Figure 3-27: Top: Evolution of the fuel cell voltage at an average current density of 0.67 A/cm^2 for different MEA during the start-up aging protocol by injection of 10 slph hydrogen in air (left) and during the shut-down aging protocol by injection of air in hydrogen at 10 slph (right). Bottom: fuel cell voltage loss for the start-up (left) and shut-down (right) aging protocols.

This behavior is consistent with the highest CO_2 emissions measured with these MEA (§2.8.2). The best performance and durability were obtained with the MEA having a higher Pt loading at the cathode. Again, this result is consistent with the lowest CO_2 emissions measured with this MEA. As shown in Figure 3-28, the CO_2 emissions remained lower than with the other MEA during the whole of the aging protocols. Nevertheless, in all cases the CO_2 emissions decreased significantly during the first 200 or 300 cycles. This evolution can be linked to the decrease of the ECSA, to the increase of the graphitized/amorphous carbon ratio, or to the progressive passivation of carbon because of partial oxidation. On the other hand at beginning of life, the electrodes may contain less anchored or less stable carbon particles, which are thus more prone to oxidize.

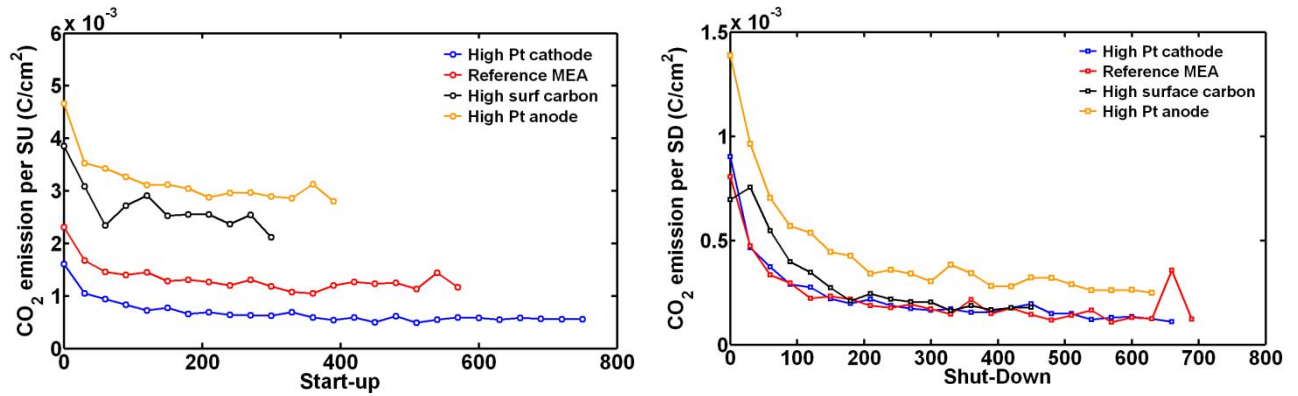


Figure 3-28: Evolution for the different MEA of the CO₂ emission during the start-up aging protocol by injection of hydrogen in air at 10 slph (left) and during the shut-down aging protocol by injection of 10 slph air in hydrogen (right).

Figure 3-29 presents the evolution of the MEA ECSA (expressed in m^2_{Pt}/m^2_{MEA} to facilitate comparisons) as a function of the number of SU or SD performed. Although the ECSA decreased regularly in all cases, there were significant differences between the MEA (Table 3):

- At beginning of life (during the first 90 cycles), the MEA with a high Pt loading at the anode showed the fastest ECSA drop, which is consistent with the previous observations about charge exchanged (Figure 2-64 in §2.8.2) and CO₂ emissions (Figure 2-66 and Figure 3-28). The ECSA drop was slower for the MEA with a high Pt loading at the cathode than for the reference MEA, which is also consistent with the previous results. However, the ECSA decrease rate of the MEA with high specific surface carbon at the cathode was significantly lower than that of the reference MEA, although the charge exchanged (Figure 2-64 - gas injection flow rate of 10 slph) and CO₂ emissions (Figure 2-66 and Figure 3-28) were higher or similar.
- The observations are slightly different considering the whole of the aging protocols (300 SU or SD cycles): high Pt loading at the cathode still offers efficient protection against ECSA drop while high Pt loading at the anode has the opposite effect; on the other hand, the ECSA decrease rate measured with the MEA with high specific surface carbon at the cathode becomes similar to that observed with the reference MEA.

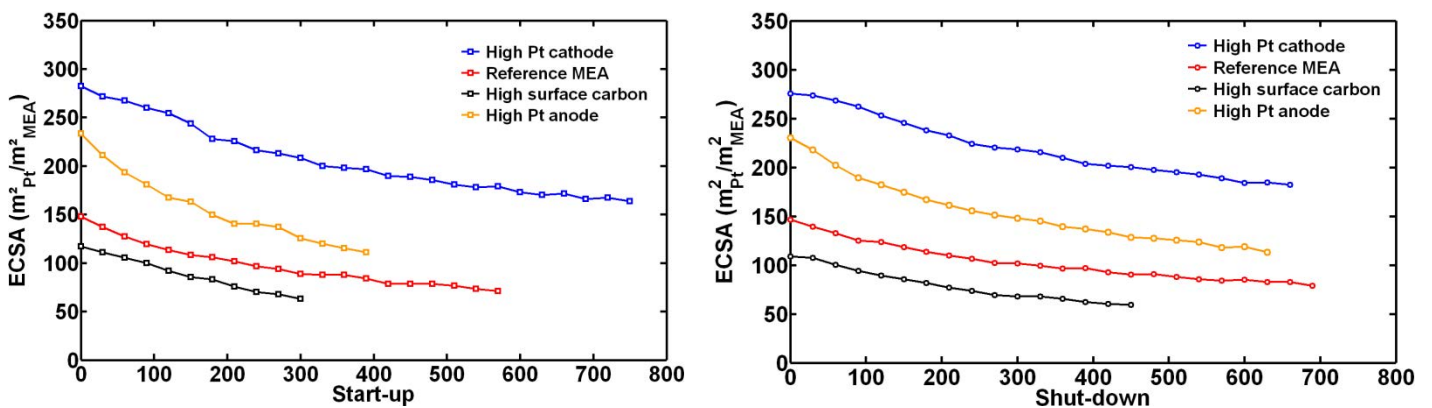


Figure 3-29: Evolution for the different MEA of the ECSA expressed in m^2_{Pt}/m^2_{MEA} during start-up aging protocol by injection of hydrogen in air at 10 slph (left) and during shut-down aging protocol by injection of air in hydrogen at 10 slph (right).

According to Figure 3-28, using high specific surface carbon at the cathode led to CO₂ emissions 50% to 100% higher than with the reference MEA but to lower or similar decrease of the ECSA (*Table 3-4*). These results mean that carbon corrosion has probably a limited impact on the ECSA: Pt particles detachment from the carbon support may not be the predominating phenomena compared to short-range Ostwald ripening, long-range Ostwald ripening, or migration/coalescence. Our results even suggest that at the beginning of the SU aging protocol, carbon corrosion limits the ECSA drops. According to *Table 3-5* and *Figure 3-27* however, high specific surface carbon had a dramatic impact on the degradation of the cell performance, most likely because of structural changes in the electrodes at the micro-scale, like those evidenced for instance by Dubau et al. [71] or Gasteiger et al. [119]. Carter et al. showed recently that 10% wt. of carbon loss was enough to severely damage the electrode porosity [120]. In our case, 0.1 μg/cm²/SU carbon loss measured by CO₂ emissions (*Figure 3-28*, MEA with high specific surface carbon at the cathode) correspond to a total loss of about 0.03 mg/cm² after 300 SU, or 4% of the initial mass of carbon at the cathode (about 0.8 mg/cm²). However, the portion of solid carbon leaving the cell washed away by liquid water is probably significant.

These conclusions can be summarized in the last two columns of *Table 3-5*, showing that the impact of ECSA losses on fuel cell voltage (@ 0.67 V) can vary in a large extent depending on the protocol applied (SU or SD) and MEA specification: from 0 to 2823 μV/cm²_{Pt}/cm²_{MEA}.

MEA	ECSA drop rate at BoL (90 cycles)		Average ECSA drop rate (300 cycles)	
	Start-up	Shut-down	Start-up	Shut-down
Reference MEA	-0.32 cm ² _{Pt} /cm ² _{MEA}	-0.24 cm ² _{Pt} /cm ² _{MEA}	-29 cm ² _{Pt} /cm ² _{MEA}	-23 cm ² _{Pt} /cm ² _{MEA}
Higher cathode Pt loading	-0.21 cm ² _{Pt} /cm ² _{MEA}	-0.13 cm ² _{Pt} /cm ² _{MEA}	-17 cm ² _{Pt} /cm ² _{MEA}	-13 cm ² _{Pt} /cm ² _{MEA}
Higher anode Pt loading	-0.43 cm ² _{Pt} /cm ² _{MEA}	-0.34 cm ² _{Pt} /cm ² _{MEA}	-35 cm ² _{Pt} /cm ² _{MEA}	-26 cm ² _{Pt} /cm ² _{MEA}
Higher carbon specific surface	-0.19 cm ² _{Pt} /cm ² _{MEA}	-0.18 cm ² _{Pt} /cm ² _{MEA}	-30 cm ² _{Pt} /cm ² _{MEA}	-22 cm ² _{Pt} /cm ² _{MEA}

Table 3-4. ECSA drop rates at beginning of life (during the first 90 cycles) and during the first 300 cycles.

MEA	Average voltage loss (300 SU)	Average voltage loss (300 SD)	$\Delta V/\Delta_{\text{ECSA}}$ (300 SU)	$\Delta V/\Delta_{\text{ECSA}}$ (300 SD)
Reference MEA	-124 μV/SU	-50 μV/SD	1283 μV/cm ² _{Pt} /cm ² _{MEA}	652 μV/cm ² _{Pt} /cm ² _{MEA}
Higher cathode Pt loading	-47 μV/SU	not significant	829 μV/cm ² _{Pt} /cm ² _{MEA}	not significant
Higher anode Pt loading	-238 μV/SU	-63 μV/SD	2040 μV/cm ² _{Pt} /cm ² _{MEA}	727 μV/cm ² _{Pt} /cm ² _{MEA}
Higher carbon specific surface	-248 μV/SU	-207 μV/SD	2480 μV/cm ² _{Pt} /cm ² _{MEA}	2823 μV/cm ² _{Pt} /cm ² _{MEA}

Table 3-5. Average voltage drop per SU or SD during the first 300 cycles and voltage drop per ECSA loss.

3.6.2 Local impact along the gas channel

Figure 3-30 shows the time evolution of ECSA profiles measured along the gas channels during start-up and shut-down aging protocols performed with the reference MEA. 570 SU and 690 SD were necessary to lose about 50% of the initial value of the (average) ECSA. The segments suffering the most from fuel starvation were located close to the hydrogen outlet (air inlet) during start-ups and close to the hydrogen inlet (air outlet) during shut-downs. As expected, the most severe ECSA drops were measured in these regions. The impact of this heterogeneous aging can be observed through the time evolution of the local polarization curve: the decay of the performance was more pronounced in the region staying the longest in presence of oxygen in the anode compartment (Figure 3-31, top).

Similar results were observed using MEA with high Pt loading at the anode and with high specific surface carbon at the cathode, the only difference lying in the duration of the protocols: 390 SU or 630 SD were needed to lose 50% of the ECSA in the first case and 300 SU or 450 SD in the second case.

However, the MEA with high Pt content at the cathode showed a different behavior. Not surprisingly, the time required to reach a significant ECSA loss was more important (about 750 SU or SD for a 40% drop). Because of the lower charge exchange and CO₂ emissions, the ECSA drop was also much more homogeneous with a difference below or equal to 6 percentage points between segments 15-20 (43% average drop for SU and 31% average drop for SD) and segments 1-5 (40% average drop for SU and 37% average drop for SD). By comparison, the difference between segments 15-20 (59% average drop for SU and 40% average drop for SD) and segments 1-5 (46% average drop for SU and 54% average drop for SD) was between 13 (for SU) and 14 (for SD) percentage points with the reference MEA (Table 3-6). Figure 3-31 (bottom) shows that the aging impacts only slightly the local performances, except for segment 20 in the case of start-ups (and segment 1 in the case of shut-downs): these segments did not suffer from fuel starvation and were never subjected to reverse currents. Consequently, the decrease of performances is probably linked with the repetition of high intensity (up to 1.5 A/cm² at SU) forward currents conjugated with low cathode potential -leading for instance to the formation of H₂O₂-, which effects predominated over those of reverse currents, carbon corrosion and catalyst oxidation occurring in the passive part of the cell.

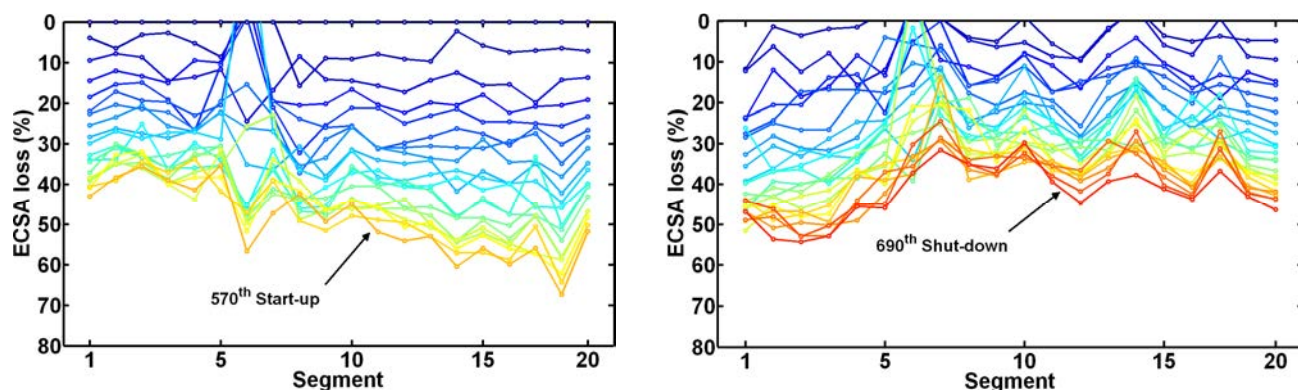


Figure 3-30. Time evolution of ECSA profile along the gas channels for the reference MEA during start-up (left) and shut-down (right) aging protocols.

MEA	%ECSA drop at anode outlet over the whole aging protocols (average values segment 1-5)		%ECSA drop at anode inlet over the whole aging protocols (average values segment 15-20)	
	Start-up	Shut-down	Start-up	Shut-down
Reference MEA	46	54	59	40
Higher cathode Pt loading	40	37	43	31
Higher anode Pt loading	31	56	62	46
Higher carbon specific surface	21	42	36	27

Table 3-6. Comparison of %ECSA drop at anode inlet and outlet over the whole aging protocols

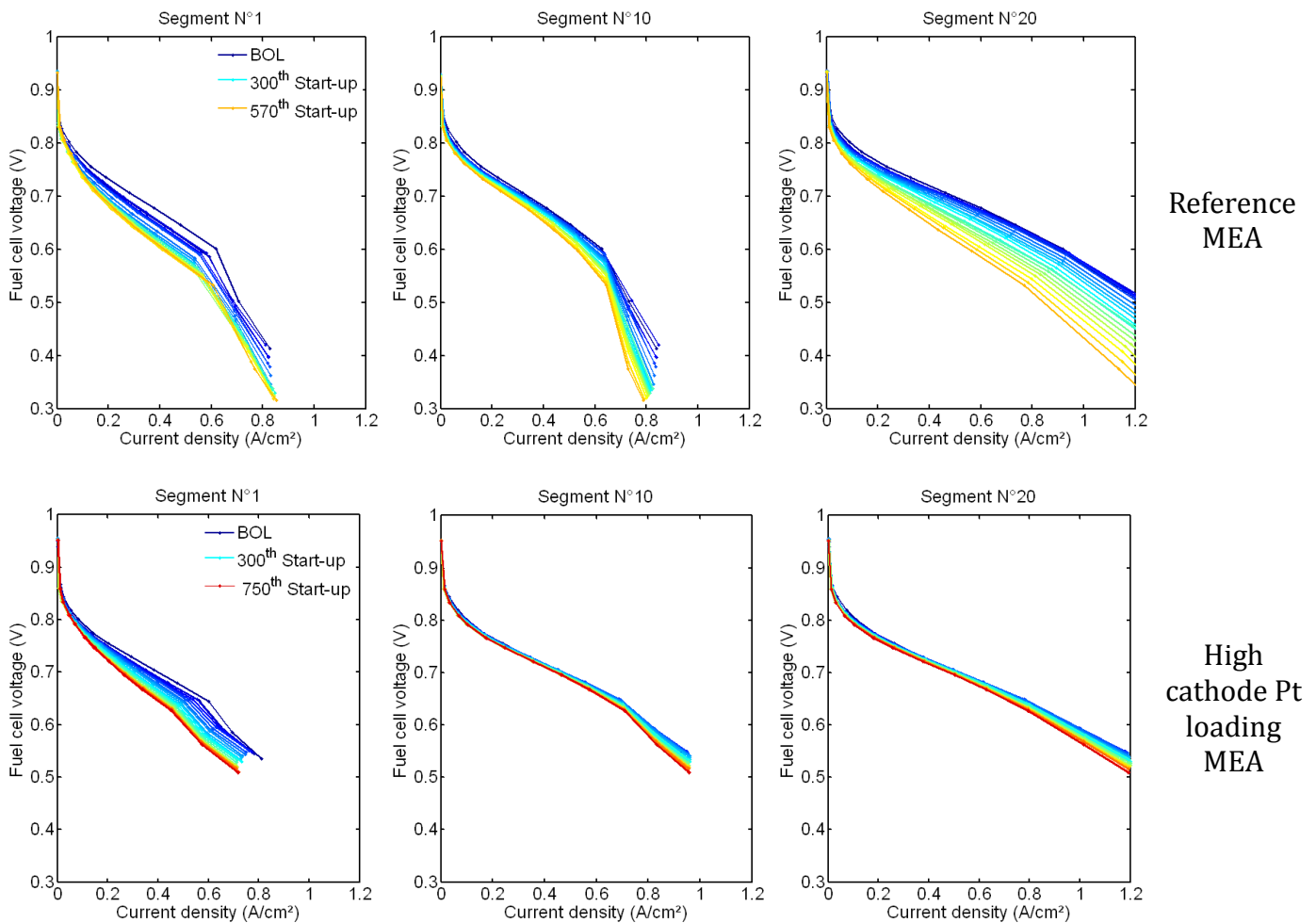


Figure 3-31. Top: time evolution of local polarization curves measured in segment 1 (strongest ECSA drop in Figure 3-30), 10 and 20 (lowest ECSA drop in Figure 3-30) during start-up aging protocol. Reference MEA. Bottom: time evolution of local polarization curves measured in segment 1, 10 and 20 during start-up aging protocol. MEA with high cathode Pt loading. The ECSA drop was slow and homogeneous.

3.7. Post-mortem analyses of aged MEA

In order to gather more data about the degradations taking place during start-up aging protocols, post-mortem analyses of aged MEAs were carried out in the LEPMI (part of this work was made during the Ph.D of Julien Durst). This time, experiments were conducted on Paxitech MEAs which we were free to analyse. Identical protocols than those implemented previously were used. The results presented hereafter were obtained for the start-up aging protocol by injection of 2 slph hydrogen in air.

3.7.1 In-situ aging analysis

It is first important to note that the results obtained in-situ with the Paxitech MEAs were similar to those obtained with the Johnson Matthey MEAs (Figure 3-32):

- Global decrease of the ECSA but with a higher rate for the segments close to the hydrogen outlet.
- Higher amount of charge exchanged measured in the segments close to the hydrogen outlet.
- Similar correlation between local ECSA evolution and local cumulative charge exchanged as that obtained with the Johnson Matthey MEA.
- Decrease of the local current densities where the local ECSA losses and the local cumulative charges exchanged are the higher (close to the hydrogen outlet).

It can therefore be assumed that the same degradation mechanisms occurred in both MEAs.

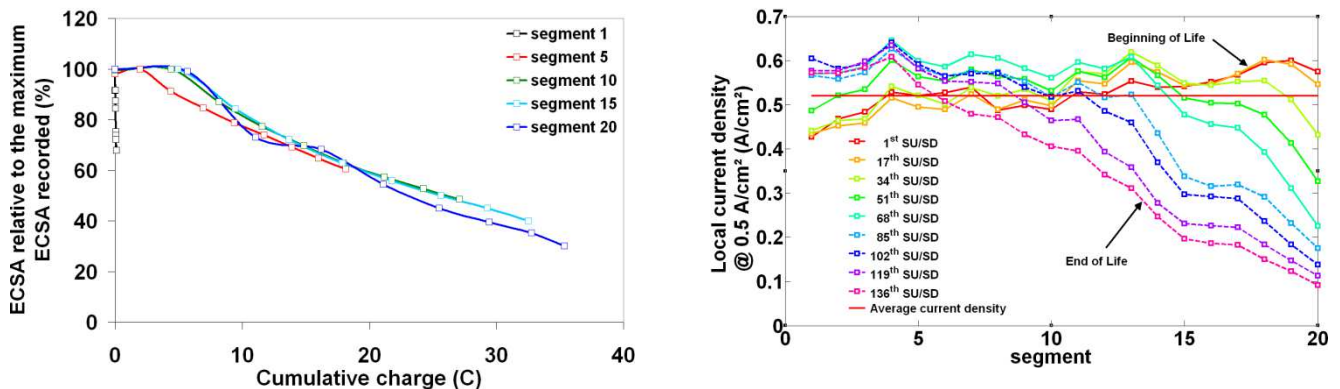


Figure 3-32. ECSA relative to the maximum value recorded vs cumulative charge resulting from the reverse current during a start-up aging protocol by injection of 2 slph hydrogen in air (left). Local current density evolution at an averaged current density of 0.5 A/cm² during the same protocol (right). The profiles are represented by solid lines when the required averaged current density is produced by the cell, and by dashed lines otherwise.

However, the performances of the Paxitech MEA were very sensitive to the degradation induced by the start-up aging protocol. As a consequence, only 136 start-ups have been performed.

3.7.2 Post-aging analysis

a. Inlet vs. outlet degradation heterogeneities

The first analyses focused on the degradation distribution along the cell. SEM images of MEA cross section all along the channel length ($d_{\text{cathode}} = 9.5 \pm 1 \mu\text{m}$; $d_{\text{membrane}} = 28 \pm 1 \mu\text{m}$; $d_{\text{anode}} = 4 \pm 0.5 \mu\text{m}$) were recorded as a function of the position (Figure 3-33).

While the pristine MEA displays a uniform thickness for all its components, the cross-sections of the aged MEA revealed that the active layers aged heterogeneously along the MEA length. Close to the cathode outlet, at segment 5 (Figure 3-33.B), the region that operated mostly actively during the SU events, the MEA looks very similar to its pristine state ($d_{\text{cathode}} = 7 \pm 1 \mu\text{m}$; $d_{\text{membrane}} = 28 \pm 1 \mu\text{m}$; $d_{\text{anode}} = 4 \pm 0.5 \mu\text{m}$), with only a little amount of Pt crystallites precipitated as a Pt-band in the PEM. The morphology of the MEA is different when looking closer to the cathode inlet (e.g. segment 15 on Figure 3-33.C and segment 18 on Figure 3-33.D). The reduced cathode thickness ($d_{\text{cathode}} = 3 \pm 1 \mu\text{m}$) signs the severe carbon corrosion rates that took place in the part operating mostly passively during the SU, while no/insignificant variations of either the PEM ($d_{\text{membrane}} = 27 \pm 1 \mu\text{m}$) or the anode ($d_{\text{anode}} = 4 \pm 0.5 \mu\text{m}$) thicknesses are monitored. The decrease of the cathode thickness is concomitant with the apparition of a dense Pt-band located in the PEM, which explains part of the decrease of the ECSA recorded *in situ* in these regions of the MEA.

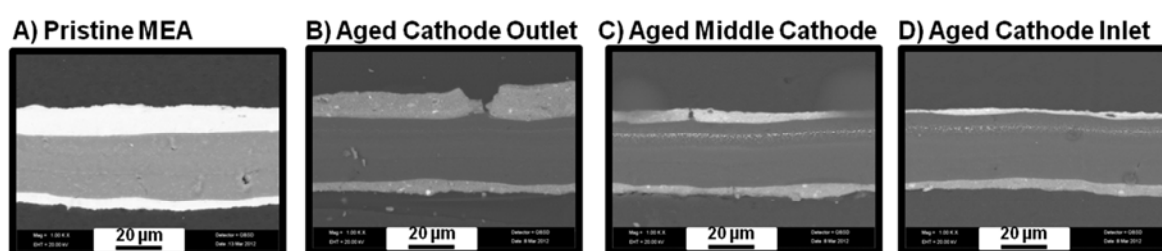


Figure 3-33. SEM images recorded in back-scattered mode (magnification $\times 1000$) of (A) a pristine MEA and of the MEA, aged under repeated 136 SU/SD cycles, taken at (B) segment 5, (C) segment 15 and (D) segment 18. The upper electrodes are the cathodes.

b. Channel vs. land degradation heterogeneities

In addition, when looking with more accuracy to the segments that have aged close to the cathode inlet, another level of heterogeneity appears: after removing the GDL from the cathode, residual portions of the micro-porous layer were left on the top of the active layer, as seen with the top view of the aged MEA (Figure 3-34).

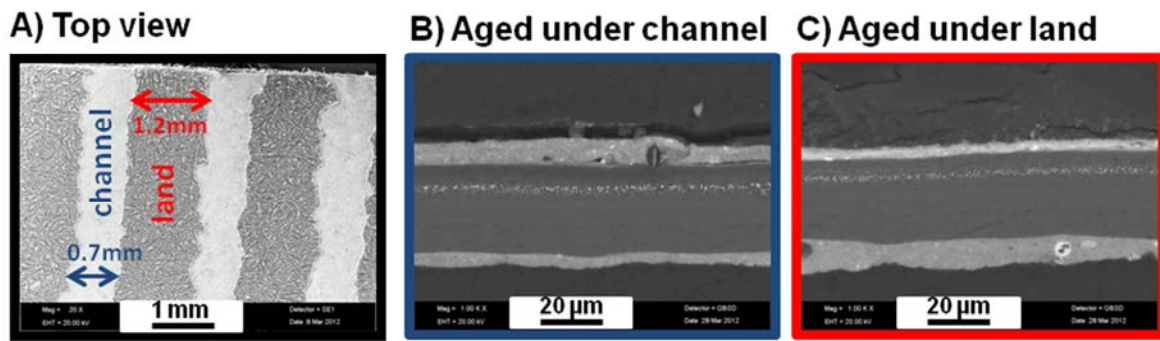


Figure 3-34. SEM images in back-scattered mode of (A) the top view of the aged MEA taken under segment 18 and the cross-sections of the two distinct regions in segment 18: (B) under a channel and (C) under a land respectively. The upper electrodes in (B) and (C) are the cathodes.

The position and dimensions of these MPL residues match with the part of the MEA that has operated under a land. The rationale for the local presence of residual portions of the MPL is open to discussion. The hypothesis of a high compression of the MEA under the channel, which would induce mechanical damages within the MEA structures, can be discarded, as this phenomenon is neither seen at the cathode outlet (segment 1), where fuel starvation events are absent, nor on the anode side. Such local degradation of the MPL was only monitored close to the cathode inlet. Therefore, such MPL residues are clearly a fingerprint of the land region, and are used in the following as a marker to enable performing locally-resolved characterization techniques.

Based on SEM images taken close to the cathode inlet, the cathode appears more degraded (at the micro-scale) under a land (Figure 3-34.C) than under a channel (Figure 3-34.B): the remaining cathode is smaller ($d_{\text{cathode}} = 3.3 \pm 0.5 \mu\text{m}$ under a land vs. $d_{\text{cathode}} = 4.9 \pm 1.5 \mu\text{m}$ under a channel) and appears brighter, signing the higher Pt content/lower carbon content. Interestingly, the Pt-band in the PEM is located at approximately the same position, sign of similar H_2 and O_2 partial pressure ratio under a land or under a channel [82]. Here it is also worth saying that such differences between channels and lands were not observed close to the cathode outlet, the region that has been spared from fuel starvation events.

The development of such channel vs. land heterogeneities, in regions where harsh carbon corrosion rates occurred following fuel starvation events, match perfectly with the findings of Schneider and von Dahlen [108] (§2.1.1): the portions of cathode facing an anode land region are expected to suffer longer fuel starvation events than those facing anode channel regions, due to the time needed by hydrogen to diffuse below the land (§2.1.1). As the anode and cathode bipolar plates are symmetric and the anode lands face the cathode ones in the present cell setup, faster degradation rates are witnessed for the land regions of the cathode. Moreover, the humidified conditions used in this study ($\text{RH} > 90\%$ and $T = 50^\circ\text{C}$) slower oxygen diffusion as compared with dry conditions, therefore exacerbating channel vs. land heterogeneities [108].

Although the preliminary SEM observations of Figure 3-34 clearly demonstrated heterogeneous rate of aging at the micro-scale between channel and land regions, more insights at the nano-scale can be achieved to identify the impact of these degradation heterogeneities on the local morphology of the Pt and C particles: Figure 3-35 displays a series of TEM micrographs of ultramicrotomed slices sampled in the MEA region aged close

to the cathode inlet (segment 18). As expected from the SEM micrographs (micro-scale, Figure 3-34), this region underwent major structural changes at the nano-scale. Like for the SEM observations, these changes can be discussed as a function of the position during the aging, either under a channel (Figure 3-35.B) or a land (Figure 3-35.C).

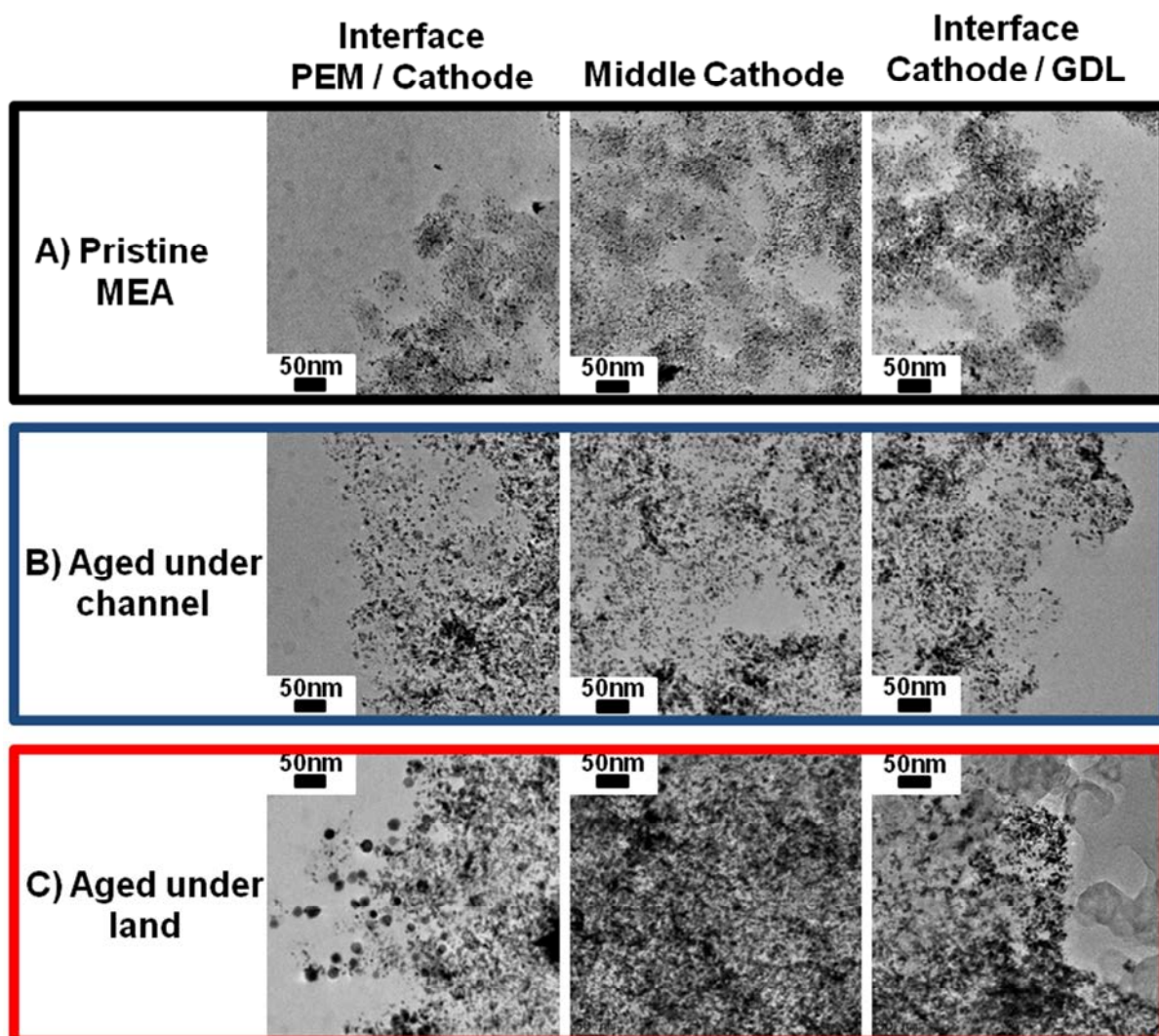


Figure 3-35. TEM images of ultramicrotomed samples (magnification $\times 50000$) taken through the cathode thickness *i.e.* from the PEM/cathode interface to the Cathode/GDL interface, of (A) a pristine MEA and of (B, C) two samples of MEA aged at segment 17 of the segmented cell (close to the cathode inlet). The analyzed samples in (B) and (C) were aged under a channel and a land respectively.

In the channel region (Figure 3-35.B), the overall increase of the mean particle size of the catalyst is obvious. This increase seems homogeneous through-the-plane of the cathode, *i.e.* from the PEM|cathode interface to the cathode|GDL interface, as seen from the local particle size distribution (Figure 3-36.B). The mean volume-averaged diameter of the aged catalyst particles is $d_v = 4.8$ nm, whatever the location through the cathode thickness. These insignificant through-the-plane degradation heterogeneities of the cathode catalyst agree with the results of Dubau *et al.* [71].

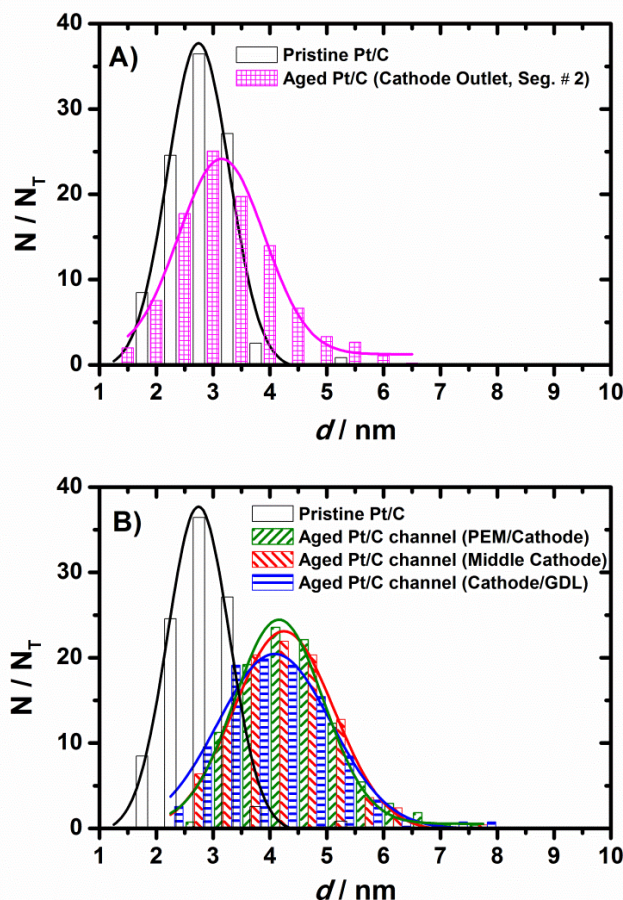


Figure 3-36. Particle size distribution (PSD) of fresh (in black) and aged Pt/C catalysts, calculated based on TEM images taken at high magnification ($\times 200000$). The PSD of the aged cathode catalyst are measured (A) close to the cathode outlet (in pink) and (B) close to the cathode inlet either at the PEM/Cathode interface (in green), or in the middle of the cathode (in red), or at the Cathode/GDL interface (in blue).

It is also interesting to compare the particle size distribution of the cathode catalyst aged close to the cathode outlet (Figure 3-36.A) with that of the cathode catalyst aged close to the cathode inlet under a channel (Figure 3-36.B): the mean particle size is higher close to the inlet. The increased mean particle size in this area compared to the cathode outlet proves that fuel starvation events were well present under channels. However, they proceeded in a much lower extent than under lands, as highlighted in the following. Actually, when looking at the CL overall structure, there seems to be minor changes of the cathode CL porosity and Pt/C morphology in this region at first sight: the FIB-SEM experiments carried out in this specific region confirmed the minor changes in terms of the void volume (Figure 3-37.B) with respect to the pristine electrode.

The impact of the aging on the land regions of cathode located close to the air inlet is completely different than for channel regions in the same area, a few micrometres away. First, large Pt particles, ranking from 20 to 40 nm diameter, coexist with a high range of agglomerated particles at the PEM|cathode interface. Only agglomerated particles are found when moving toward the cathode|GDL interface. It is worth mentioning that not enough

isolated Pt particles could be found throughout the cathode CL to draw accurate local or global particle size distribution (at least 400 particles are required to have enough statistics) similar as in Figure 3-36.B. All the classical degradation mechanisms leading to ECSA losses are evidenced here: (i) agglomeration of Pt nanoparticles upon collisions due to carbon corrosion, (ii) Pt dissolution/redeposition onto larger particles, and (iii) 3D-Ostwald ripening (§1.4.3). It appears difficult to distinguish which from these three contributions predominates in the loss of ECSA.

The carbon support was also severely degraded by the aging test. First, the remaining carbon support appears completely amorphous, a first sign of severe carbon corrosion rates [121]. The TEM images are compatible with a complete loss of porosity throughout the whole electrode thickness (Figure 3-35). This result is in agreement with the work of Carter *et al.* [120], who concluded that only 10% wt. of carbon loss is necessary to fully loose the electrode porosity. Note that the $0.2 \mu\text{g cm}^{-2} \text{SU}^{-1}$ carbon loss measured by CO_2 emissions (§ 3.1) correspond in the present case to a total loss of about 0.02 mg cm^{-2} , *i.e.* 5% of the initial mass of carbon at the cathode (0.4 mg cm^{-2}). However, it must be kept in mind that the carbon loss is highly heterogeneous and that the portion of solid carbon leaving the cell washed away by liquid water may be significant.

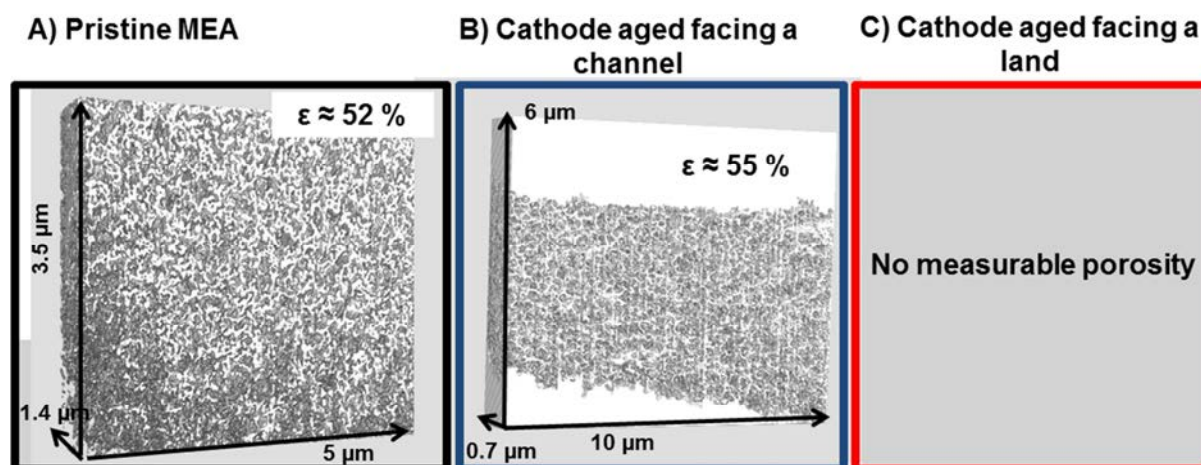


Figure 3-37. Snapshots of the 3D reconstruction, using FIB-SEM, of the cathode catalyst layers (CL) of (A) the pristine MEA and of (B) the MEA aged under a channel close to the cathode inlet.

The ultramicrotomed slice of the aged MEA was also observed with a FEG-SEM in STEM mode (Figure 3-38). It was striking to observe that, due to the lower electron acceleration voltage of a SEM compared to a TEM, the electron beam was not able to cross over the portion of cathode aged under a land (the electrode looks darker compared to the portion of cathode aged facing a channel). As all ultramicrotomed slices have the same thickness ($e = 70 \text{ nm}$), this indirectly signs the more absorbing/dense electrode structure in the cathode aged under a land (richer in Pt/poorer in light elements such as C, F or S). This last result is partly confirmed with locally-resolved X-EDS measurements, displayed over the SEM pictures (Figure 3-38). The quantification of the X-EDS signal was done for the Pt, F, S and O signals, using a similar procedure as in Dubau *et al.* [71]. When comparing the two regions in Figure 3-38, it clearly appears that the Pt content is larger in the cathode aged under a land. This confirms the higher rate of release of carbon compared to platinum from the electrode structure during multiple SU events. Thus, the electrode thickness diminishes (it becomes

denser) and the Pt content remains stable overall, therefore apparently increasing when ratioed to the amount of remaining carbon. Interestingly, in the case of the region of the cathode aged under a land, the Pt content increases undoubtedly when moving from the PEM|cathode to the cathode|GDL interface, which might sign the higher carbon corrosion rates close to the cathode|GDL interface. Since fuel starvation events are rapid and intense potential disturbance events, there are reasons to believe that a distribution of the potential profile sets up through the electrode thickness during such events, even though this hypothesis has not been verified experimentally yet.

When combining these results with the more marked range of agglomerated and large particles, it can be concluded that this region (under a land) experimented more carbon corrosion during SU and SD events than (i) the cathode outlet and (ii) the neighbouring part of the cathode that aged under a channel.

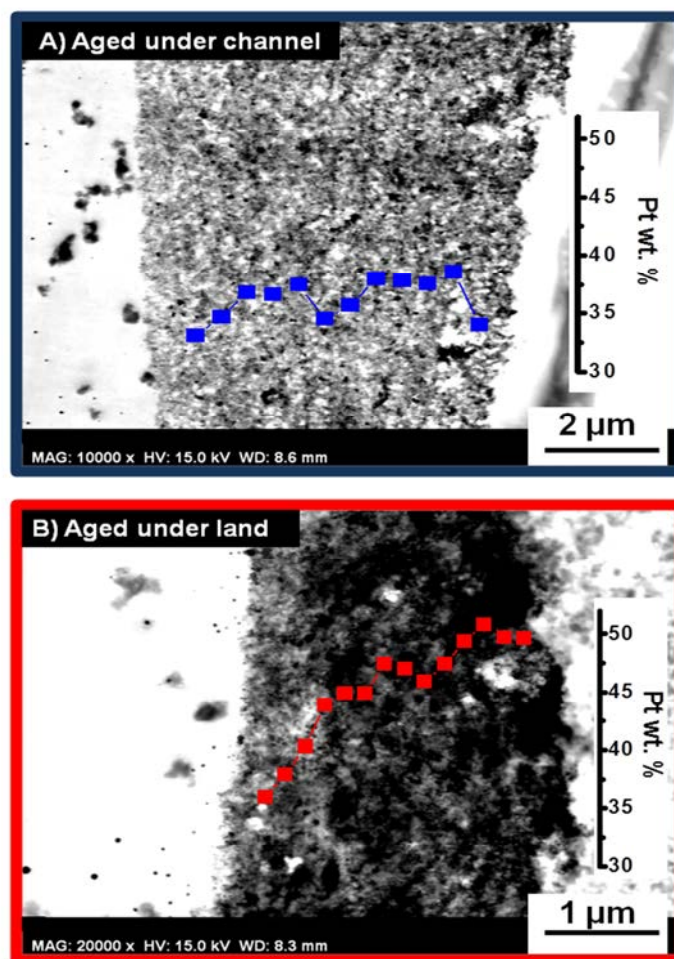


Figure 3-38. FEG-SEM images recorded in STEM mode of the two MEA ultramicrotomed samples aged either (A) under a channel (magnification $\times 10000$) or (B) under a land (magnification $\times 20000$). Both PEM|Cathode interfaces are located on the left of the images. The locally resolved Pt weight percent, measured with locally X-EDS analyses similar as in Dubau et al., are superimposed on the FEG-SEM images. The contribution of carbon to the X-EDS signal was not considered for the calculation in the Pt weight percent.

Regarding the similar in-situ results of Johnson Matthey, Ion Power and Paxitech MEAs when submitted to start-up aging protocols, the observations made in this section with the Paxitech MEA should be comparable to those which could be obtained with the two others MEAs.

3.8. Conclusion

In the second chapter, internal currents occurring during start-up and shut-down were described and the charge exchanged was defined. This parameter, which can be measured locally in a segmented cell, was pointed out as a marker of the degradation in the cell.

This chapter presents results of aging protocols consisting in the repetition of start-ups and shut-downs. The monitoring of the local current density and of the local ECSA during the experiments made it possible to locate the degradations and to characterize their evolution. Cyclic voltammeteries performed to monitor the local ECSA did not participate significantly to these degradations.

The results obtained in this chapter confirmed those of the second chapter:

- The common residence time hydrogen and of oxygen (whether in air, in nitrogen because of membrane crossover or under the form of Pt oxides) in the anode compartment during start-ups or shut-downs governs the decay of the cell performance.
- Start-ups performed with identical gas injection flow rate as shut-downs generated more damages.
- The degradations observed locally (ECSA and current density drops) were related to the charge exchanged. For identical MEA, the charge exchange provides therefore valuable information about the dangerousness of the conditions under which start-ups and shut-downs are realised.

However, it was also shown that an increase of the charge exchanged resulting from modifications in the characteristics of the MEA does not imply that the performance decay will be faster. This was evidenced by the aging experiments performed with a Ion Power MEA with a high cathode platinum loading. Although the charge exchanged was the highest, this MEA was also the most durable. On the contrary, the increase of the carbon specific surface or the anode platinum loading reduced significantly the MEA lifetime.

Post-mortem analyses of Paxitech MEA carried out in the LEPMI confirmed the non-uniform degradation of the cathode between the hydrogen inlet and outlet, which was observed in-situ during start-up aging protocols. The thinning of the cathode catalyst layer clearly evidenced carbon oxidation. The increase of the average platinum particle diameter was characteristic of short range Ostwald ripening and the Pt-band formed in the membrane of long range Ostwald ripening. In addition, the damages also appeared non-uniform between land and channel (close to the hydrogen outlet, on the cathode side): regions of the MEA located under a land were much more affected than those under a channel, in particular close to the cathode/GDL interface where carbon oxidized faster than close to the PEM/cathode interface. This result is consistent with the reverse currents measured by Schneider et al. [108] in the land region during start-up. However, it must be kept in mind that such heterogeneities may be linked specifically to the Paxitech MEA, and/or to the geometry of the segmented cell: straight

parallel channels tend most probably to slow down the diffusion of gases under the land compared to (more usual) serpentine flow fields.

Finally, two kinds of mitigation strategies make it possible to reduce degradations induced by start-ups and shut-downs:

- Adapting the fuel cell operating conditions, for instance by injecting gases with high velocity in the anode compartment or by using nitrogen to purge the cell instead of air.
- Tuning the MEA specifications: increasing platinum loading or lowering carbon specific surface in the cathode can improve significantly the durability. Up to now, these modifications were realised separately but they could be combined to minimize the damaging effects of start-ups and shut-downs.

4 Numerical Simulation of Start-up

In the second chapter, it was evidenced that CO₂ emissions in the cathode exhaust gases stand for at most 10% of the reverse currents. The identification of the missing contributions is important to know if they can be attributed to reactions likely to participate to the degradations. This requires first to distinguish the capacitive and the faradic currents, which is difficult to achieve with the experiments only.

Other approaches are thus necessary, among which the numerical simulation of the physical phenomena taking place during start-ups or shut-downs. This approach was already considered by Maranzana et al. [107]. Their objective was mainly to differentiate the faradic from the capacitive contribution to the internal currents. They used elementary electrical equivalent circuits (EEC) to represent each segment, which they assembled to form a segmented cell. The conditions applied to the elementary circuit, that is to say gas concentrations, were varied to simulate start-up procedures. This method is briefly described at the beginning of this chapter (§4.1). However, Maranzana et al. did not intend to identify the different faradic contributions to the internal currents: the faradic current they simulated accounted for all the reactions taking place during start-up as a whole.

In this chapter, a new approach is proposed with the use of a generic electrode model in the elementary electrical equivalent circuit. This generic electrode model can be used indistinctly to simulate an anode or a cathode and considers the different electrochemical reactions independently from each other (§4.2.1). These reactions and their kinetic are defined in the first part of this chapter. Then, the transport mechanisms (1D in the direction perpendicular to the electrodes) within the MEA are described. Finally, the setting of the different parameters involved in the electrode model is realised by fitting experimental polarization curves and voltammograms (§4.2.2). Some parameters were also taken from the literature. In this regard, it must be mentioned that some redox reactions were not considered in the model because of the lack of information about their kinetic. For instance, the ex-situ study of the formation of oxygen containing carbon surface groups [122] could help completing our model. The results of 2D simulations of start-ups are discussed from a qualitative as well as quantitative point of view (§4.2.3).

Although shut-downs could be simulated with this model, they are not presented in this chapter, which must be considered as a first milestone validating the numerical model.

4.1. Previous numerical model

4.1.1 Presentation

The model proposed by Maranzana et al. was based on elementary electrical equivalent circuits assumed to be valid whatever the direction of the electrical current. An elementary EEC was constituted by two electrodes, each including:

- A charge transfer resistance, accounting for the activation overpotential resulting from the redox reactions. In the interest of simplification, the charge transfer resistance was assumed constant in time and space.
- A double layer capacity.

It must be noted that the charge transfer resistances in the anode and cathode were different. Moreover, they were operative only when the elementary EEC was located in the active part of the cell.

No Warburg impedance was considered since mass transport limitations were neglected. Charge transfer resistances and double layer capacities were set in parallel. The membrane electrolyte connecting the two electrodes was represented by a high frequency resistance. A standard reversible potential, accounting for the anode and cathode electrochemical reactions

$$E'_0 = E_c - E_a \text{ (Figure 4-2), was set in series with the two electrodes.}$$

With this EEC, the internal currents were lower than the experimental ones. A solution to avoid this limitation consisted in the addition of a “leakage” resistance in parallel to the capacities. Maranzana et al. interpreted this resistance as an activation overpotential originating from redox reactions (carbon oxidation in the cathode for instance). The leakage resistance was assumed constant and it was operative only when the EEC was located in the passive part of the cell.

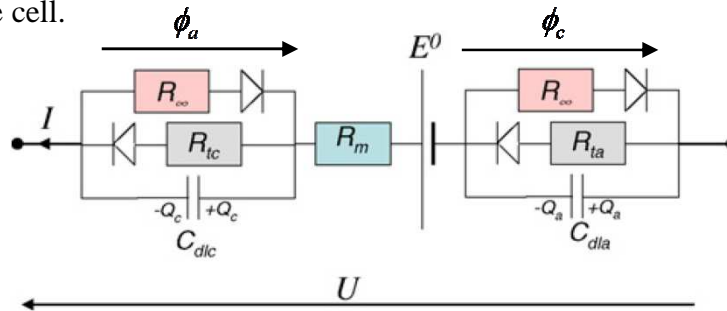


Figure 4-1. Elementary electrical equivalent circuit (EEC).

The elementary EEC were then connected to each other to form a segmented cell so that start-up could be simulated (Figure 4-2). The concentrations in the channels were imposed and the hydrogen/nitrogen front propagation was controlled. The potential could take only two values depending on the gas in the anode compartment:

- With hydrogen, the potential difference E'_0 was assumed equal to 1V;
- With nitrogen, the potential difference E'_0 was assumed equal to 0V.

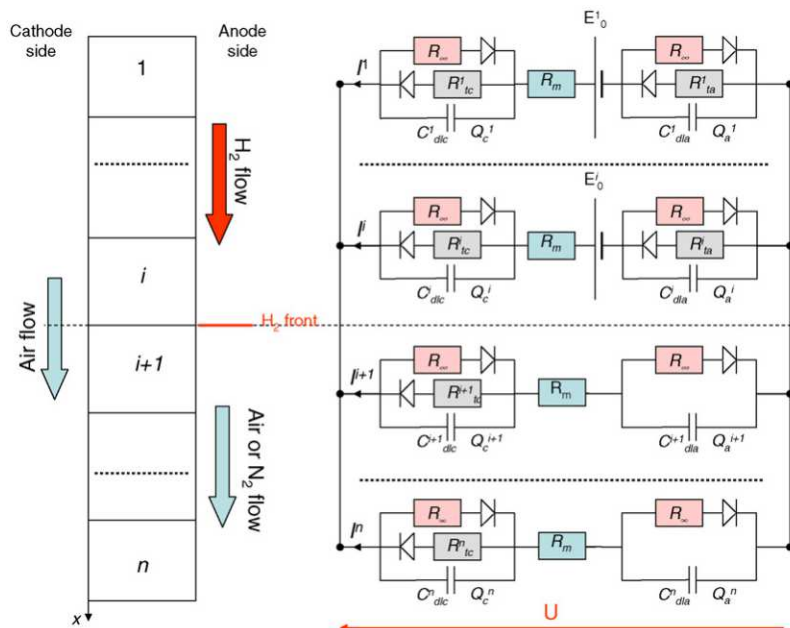


Figure 4-2. Global electrical equivalent circuit of the fuel cell during a start-up [107].

4.1.2 Experimental and numerical results – main limitations of the first model

The experiments presented in the paper of Maranzana et al. were realised using a segmented cell close to that described in chapter 2 (§2.2). The MEA was purchased from Johnson Matthey. It consisted in a 30 μm thick Nafion 212 membrane and in catalyst layers with an average Pt loading of 0.4 $\text{mg}_{\text{Pt}}/\text{cm}^2$ on both sides. The GDL was a 190 μm thick carbon fibre Toray paper (TGP-H-060).

Figure 4-3 compares experimental and simulated internal currents obtained during start-ups by injection of hydrogen with low (3 cm/s) and high (1 m/s) flow rates in nitrogen. Despite of the strong assumptions mentioned above, the numerical and experimental results were close enough to validate the role played by the double layer capacities in the internal currents.

However, the different faradic contributions to the reverse currents could not be distinguished, since the reactions were considered together through one single activation overpotential (the leakage resistance). Assuming that a distinction was possible, a quantification of the contributions (or at least a rough estimation of their order of magnitude) would also require to take into account the electrochemical kinetics.

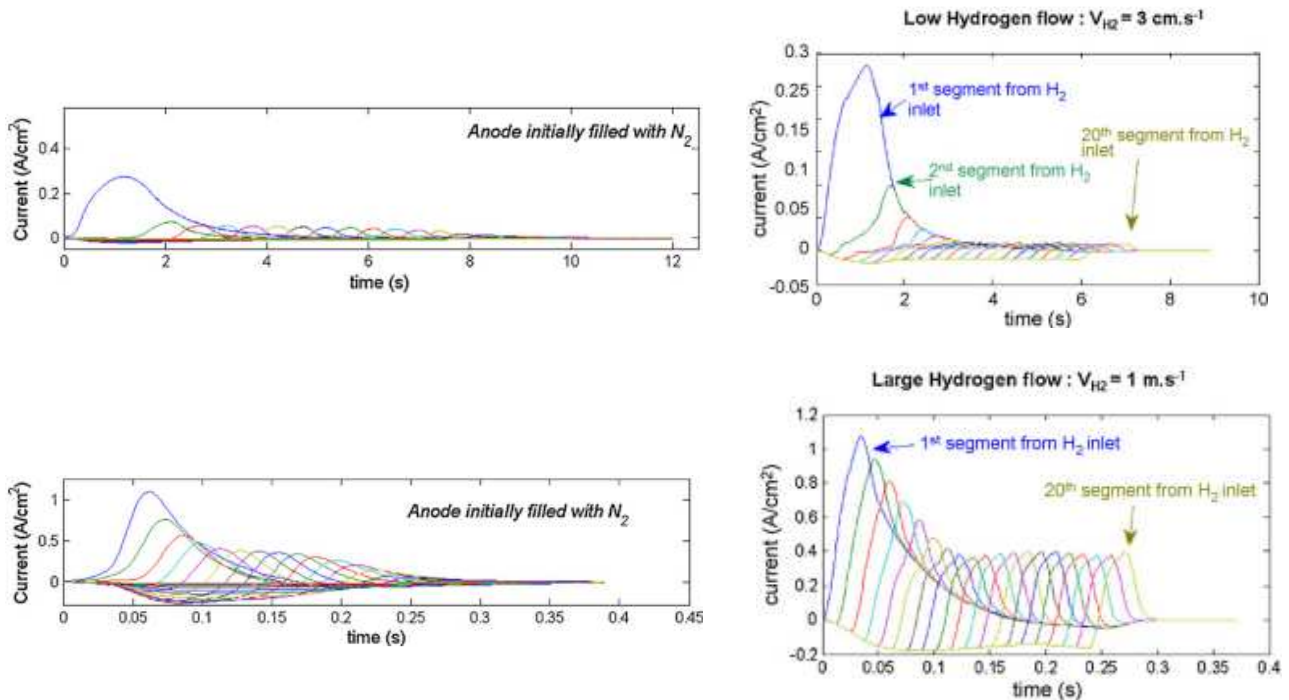


Figure 4-3. (left) Internal currents measured during start-ups in nitrogen using a low (top) and a high (bottom) hydrogen flow rate and their respective numerical simulations (right) with the following parameters setting: $E^0 = 1\text{V}$, $R_m = 0.4 \Omega \cdot \text{cm}^2$, $C_{dla} = C_{dlc} = 0.02 \text{F}/\text{cm}^2$, $R_\infty = 1 \Omega \cdot \text{cm}^2$, $R_{tc} = 0.2 \Omega \cdot \text{cm}^2$ and $R_{ta} = 0.05 \Omega \cdot \text{cm}^2$.

4.2. New numerical model

The new version of the numerical model is based on a structure similar to that proposed initially by Maranzana et al.: elementary electrical equivalent circuit are connected to each other to form a segmented cell. However, instead of differentiating the electrode depending on

their location between anode and cathode and between the active and passive parts, the same generic electrode is used everywhere. This requires to consider all the reactions which can occur in the whole cell in each generic electrode. Then, depending on the electrode potential ϕ that is applied and on gas concentrations, different reactions are activated.

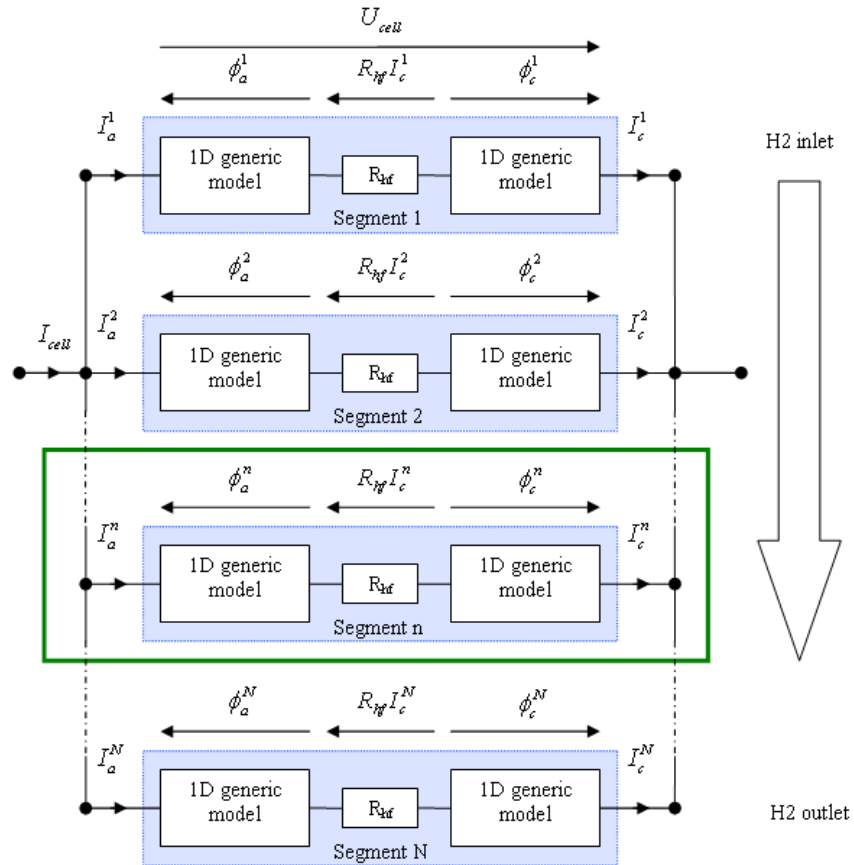


Figure 4-4. New numerical model for the study of start-up in fuel cell. The green frame represents an elementary electrical equivalent circuit.

4.2.1 Generic electrode model

a. Electrochemical and chemical reactions

i Active part

The reactions taking place in a fuel cell under regular operation are well known: hydrogen is oxidized at the anode and oxygen is reduced at the cathode. The pathways associated to these reactions may differ, depending for instance on the activation overpotential or on the platinum active site coverage (§1.2.3). Nevertheless, only the global reactions are considered in the model:



During start-up, when hydrogen is injected in the anode compartment, the strong resulting potential evolutions are likely to induce reactions involving platinum. For instance, platinum is initially in oxidized state in the anode due to the presence of air. When start-up begins, platinum oxides in the active part are reduced because of the sudden drop of the local anode potential (§4.2.3). The reactions implicating platinum play also a significant role in the passive part. They are described in the following section.

ii Passive part

No consensus really exists in the literature about the exact nature of the reactions which take place in the passive part of the cell. Moreover, different reaction pathways than those we retained could be considered. This model is then likely to evolve in the future by integrating new reactions or by improving the simulation of those which were already taken into account. We considered redox reactions involving the two main constituents of electrodes, carbon and platinum, and water which is likely to oxidize at high potential (although in small amount, §4.2.3). Due to the large potential sweeps occurring during start-up, several scenarios are possible (§2.1.2).

Redox reactions involving platinum

A significant amount of platinum can react in the potential range the cell is operating: several studies report that oxidation takes place on the particle surface but also in the subsurface layers [123], [124]. The reactions occurring on particle surface were originally proposed by Conway et al. [123].

- PtOH^s/Pt^s redox reactions on particle surface:



The kinetic of this reaction depends on the amount of free Pt sites, which is accounted for through the Pt^s surface coverage θ_{Pt}^s :

$$\theta_{Pt}^s = \frac{N_{Pt}^s(t)}{N_{Pt}^s} \quad (4-4)$$

With N_{Pt}^s the total number of platinum atoms susceptible to oxidize per cm². According to the mechanism proposed by Conway et al. [123], only a fraction of platinum atoms on the surface can react (see next page). It is considered that atoms on the surface of the particles which can oxidize represent 1/8th of the total platinum atoms in the electrode (*Annex 6*). In the cathode, this ratio corresponds to platinum particles with an average diameter of about 4.5 nm, which is reasonable when the electrode is new (see the particle size distribution in Figure 3-36). $N_{Pt}^s(t)$ is the effective number of Pt atoms on the particle surface per cm².

One can also define the Pt^sOH surface coverage θ_{PtOH}^s by:

$$\theta_{PtOH}^s = \frac{N_{PtOH}^s(t)}{N_{Pt}^s} \quad (4-5)$$

$N_{PtOH}^s(t)$ is the effective number of PtOH molecules on the platinum particle surface per cm².

θ_{Pt}^s and θ_{PtOH}^s vary between 0 and 1.

➤ PtO^s/PtOH^s redox reaction on platinum particle surface:

Once PtOH^s is formed on the surface of platinum particles, it can further oxidize into PtO^s.



The PtO^s surface coverage is defined by:

$$\theta_{PtO}^s = \frac{N_{PtO}^s(t)}{N_{Pt}^s} \quad (4-7)$$

With $N_{PtO}^s(t)$ the effective number of PtO molecules on the particle surface per cm².

The surface coverages θ_{Pt}^s , θ_{PtOH}^s and θ_{PtO}^s are connected by the following equation:

$$1 = \theta_{Pt}^s + \theta_{PtOH}^s + \theta_{PtO}^s \quad (4-8)$$

When $\theta_{Pt}^s = 0$, all the atoms which can oxidize on the particle surface are actually in oxidized state.

➤ PtO^b/Pt^b redox reaction in the bulk of the platinum particle:

According to Conway et al. [123], when the PtOH^s surface coverage reaches a saturation value χ_{PtOH^s} (that is to say when $\theta_{PtOH}^s \geq \chi_{PtOH^s}$) the repulsive interaction between PtOH^s species results in place exchange of OH_{ads} and platinum:



Then, the oxidation can continue:



Experiments realised by Jerkiewicz et al. [124] revealed that contrary to the scenario described by Conway et al, the platinum oxides are not hydrated when the place exchange occurs. Therefore, they proposed a new mechanism for the formation of platinum oxide in the bulk (Figure 4-5): first, water interacts with the platinum surface according to reactions (4-3) and (4-6) to form PtO^s. When the surface coverage of PtO^s reaches a saturation limit χ_{PtO^s} (that is to say when $\theta_{PtO}^s \geq \chi_{PtO^s}$), the repulsive interaction between PtO^s on the surface leads to the place exchange of O_{ads} and platinum.

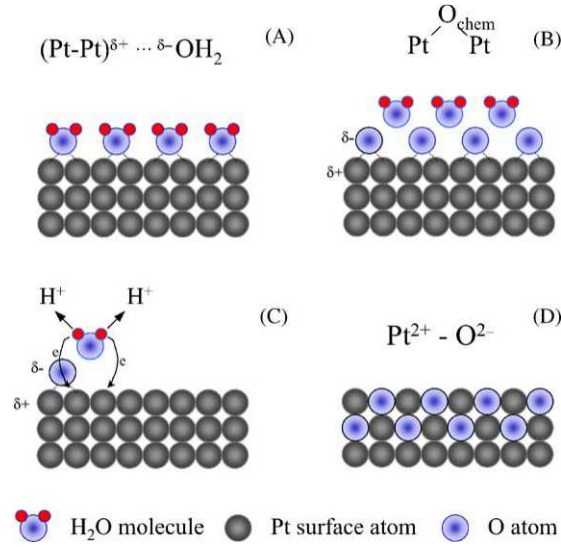
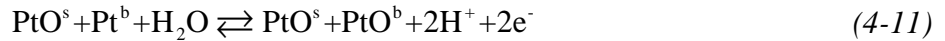


Figure 4-5. PtO growth mechanism proposed by Jerkiewicz et al [124]. (A) interactions of H₂O molecules with the platinum surface that occur in the $0.27 \leq \phi \leq 0.85V$ range. (B) Discharge of a half monolayer of H₂O molecules and subsequent formation of a half monolayer of chemisorbed oxygen (O_{ads}) in the $0.85 \leq \phi \leq 1.15V$ range. (C) Discharge of a second half monolayer of H₂O at $\phi \geq 1.15V$; the process is accompanied by the development of repulsive interactions between $(Pt-Pt)^{\delta+} - O_{ads}^{\delta-}$ surface species that stimulate an interfacial place exchange of O_{ads} and platinum surface atoms. (D) Formation of a quasi-3D surface PtO lattice comprising Pt^{2+} and O^{2-} moieties through the place-exchange process.

This mechanism can be represented by the following equation:



This reaction depends on the free Pt active sites in the bulk, which leads to the definition of platinum and platinum oxide coverage in the bulk θ_{Pt}^b and θ_{PtO}^b :

$$\theta_{Pt}^b = \frac{N_{Pt}^b(t)}{N_{Pt}^b} \quad (4-12)$$

With N_{Pt}^b the total number of platinum atoms susceptible to oxidize in the first sublayer per cm². For the sake of simplicity, this number is equal to that on the surface. $N_{Pt}^b(t)$ is the effective number of platinum atoms in the first sublayer.

$$\theta_{PtO}^b = \frac{N_{PtO}^b(t)}{N_{Pt}^b} \quad (4-13)$$

$N_{PtO}^b(t)$ is the effective number of PtO in the first sublayer. θ_{PtO}^b can be higher than one if a second sublayer is oxidized.

Platinum dissolution

Platinum losses were observed during the start-up aging protocols (§3.4). They can result from platinum dissolution, which leads to the formation of a Pt-band in the membrane (§3.7.2). This dissolution occurs following three possible mechanisms:

- Electro-oxidation of platinum [125]:



- Electro-reduction of platinum oxide [126]:



- Chemical dissolution of platinum oxide [127]:



It is still not clear which of these mechanisms is predominant [127] and the reactions presented above are only indicative.

In §3.7.2, more platinum particles were found in the membrane close to the hydrogen outlet where the cathode potential reaches high values for the longest time. This correlation between the cathode potential and the rate of platinum dissolution means that an electrochemical mechanism is at stake. Two scenarios can be envisaged:

- Platinum dissolution is purely electrochemical: (4-14) and (4-15).
- Platinum oxides are chemically dissolved (like in (4-16)) but their formation resulted from electrochemical reactions, (4-3) and (4-6) for instance.

Although these mechanisms were already described in the literature, the lack of information concerning their kinetics and their negligible contribution to the internal currents led us to exclude them from the model.

Carbon redox reaction

Carbon oxidation evidenced by the measurement of CO₂ in the cathode exhaust gases occurs probably under the effect of electrochemical mechanisms (§2.5). Two processes can be considered: direct carbon oxidation and catalysed carbon oxidation.

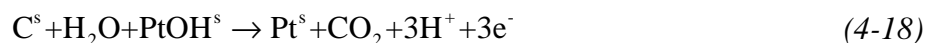
- Direct carbon oxidation

This reaction is not catalysed. It was modelled by Meyers et al. [46]:

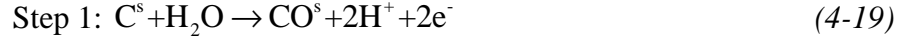


- Catalysed carbon oxidation

This mechanism was proposed by Maass et al. [49]. The global reaction is expressed by:



And it occurs in two steps:



This reaction is referred to as catalyzed but actually it is not. This reference is only used to distinct the direct carbon oxidation from the carbon oxidation that involve platinum (which should normally only play a role of catalyst).

b. Reactions kinetics

General expression

The kinetic of electrochemical reactions is usually expressed by the Butler-Volmer law, which can be written with reference to the standard conditions (§1.2.4):

$$j_{\text{Ox/red}}^{\alpha} = \gamma_{\alpha} j_0^{\text{Ox/red}} \left[\frac{c_{\text{Red}}^{\alpha}}{c_{\text{Red}}^0} \exp\left(\frac{\alpha_{\text{Red}} nF}{RT} (\phi_{\alpha} - E_{\text{Ox/Red}}^0)\right) - \frac{c_{\text{Ox}}^{\alpha}}{c_{\text{Ox}}^0} \exp\left(\frac{-\alpha_{\text{Ox}} nF}{RT} (\phi_{\alpha} - E_{\text{Ox/Red}}^0)\right) \right] \quad (4-21)$$

With α the electrode, anode or cathode.

Similarly to Neyerlin et al [14], we assume that the equilibrium potential can be shifted depending on the concentrations at the electrodes (Figure 4-6) and that this shift should influence the current density. Thus, equation (4-21) becomes:

$$j_{\text{Ox/red}}^{\alpha} = \gamma_{\alpha} j_0^{\text{Ox/red}} \left[\frac{c_{\text{Red}}^{\alpha}}{c_{\text{Red}}^0} \exp\left(\frac{\alpha_{\text{Red}} nF}{RT} (\phi_{\alpha} - E_{\text{Ox/Red}}^{\alpha})\right) - \frac{c_{\text{Ox}}^{\alpha}}{c_{\text{Ox}}^0} \exp\left(\frac{-\alpha_{\text{Ox}} nF}{RT} (\phi_{\alpha} - E_{\text{Ox/Red}}^{\alpha})\right) \right] \quad (4-22)$$

With $E_{\text{Ox/Red}}^{\alpha}$ given by the Nersnt equation:

$$E_{\text{Ox/Red}}^{\alpha} = E_{\text{Ox/Red}}^0 + \frac{RT}{nF} \ln\left(\frac{c_{\text{Ox}}^{\alpha} c_{\text{Red}}^0}{c_{\text{Red}}^{\alpha} c_{\text{Ox}}^0}\right) \quad (4-23)$$

Equation (4-22) can be rewritten by replacing $E_{\text{Ox/Red}}^{\alpha}$ by its expression in equation (4-23):

$$j_{\text{Ox/red}}^{\alpha} = \gamma_{\alpha} j_0^{\text{Ox/red}} \left[\left(\frac{c_{\text{Ox}}^0}{c_{\text{Ox}}^{\alpha}} \right)^{\alpha_{\text{Red}}} \left(\frac{c_{\text{Red}}^{\alpha}}{c_{\text{Red}}^0} \right)^{1+\alpha_{\text{Red}}} \exp\left(\frac{\alpha_{\text{Red}} nF}{RT} (\phi_{\alpha} - E_{\text{Ox/Red}}^0)\right) - \left(\frac{c_{\text{Red}}^0}{c_{\text{Red}}^{\alpha}} \right)^{\alpha_{\text{Ox}}} \left(\frac{c_{\text{Ox}}^{\alpha}}{c_{\text{Ox}}^0} \right)^{1+\alpha_{\text{Ox}}} \exp\left(\frac{-\alpha_{\text{Ox}} nF}{RT} (\phi_{\alpha} - E_{\text{Ox/Red}}^0)\right) \right] \quad (4-24)$$

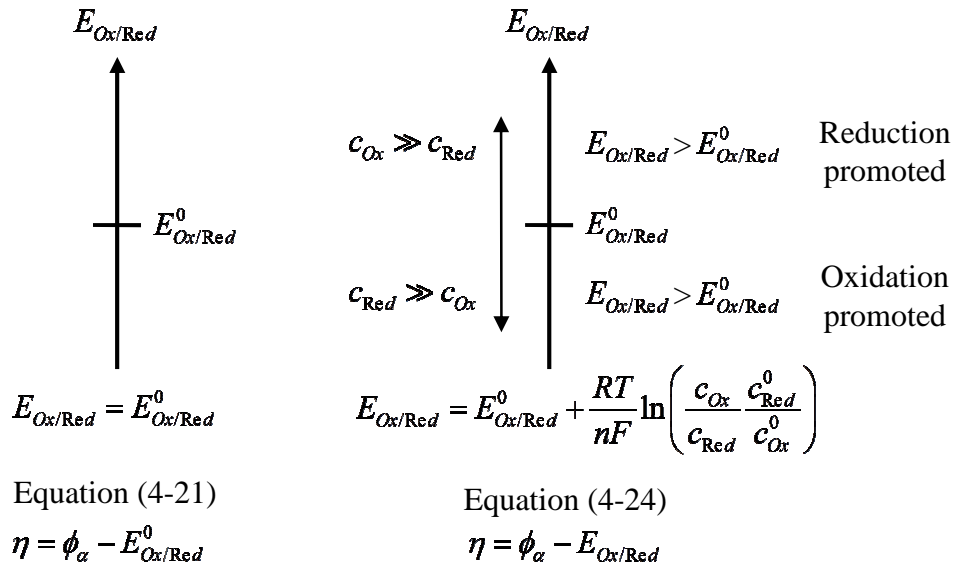


Figure 4-6. Equilibrium potential in equation (4-21) and (4-24) as a function of the oxidant c_{Ox} and reducer c_{Red} concentration at the electrode (by reference to the equilibrium potential in standard conditions).

Thus, each of the redox reactions can be described using:

- The exchange current density ($j_0^{Ox/Red}$),
- The standard electrode potential ($E_{Ox/Red}^0$)
- The charge transfer coefficients (α_{Ox} and α_{Red}).
- The concentration in oxidant c_{Ox}^α and reducer c_{Red}^α at the electrode

H⁺/H₂ redox reactions

According to equation (4-21), the kinetic of the H⁺/H₂ redox reaction becomes:

$$j_{H^+/H_2}^\alpha = \gamma_\alpha j_0^{H^+/H_2} \left[\left(\frac{c_{H_2}^\alpha}{c_{H_2}^0} \right)^{1+\alpha_{H_2}} \exp \left(\frac{\alpha_{H_2} nF}{RT} (\phi_\alpha - E_{H^+/H_2}^0) \right) - \left(\frac{c_{H^+}^0}{c_{H^+}^\alpha} \right)^{\alpha_{H^+}} \exp \left(\frac{-\alpha_{H^+} nF}{RT} (\phi_\alpha - E_{H^+/H_2}^0) \right) \right] \quad (4-25)$$

To maintain the electroneutrality in the membrane, the concentration of protons was kept constant. That is the reason why the proton concentration does not appear in equation (4-25).

O₂/H₂O redox reactions

The expression of the current density for the O₂/H₂O redox reactions depends on the vapour concentration (liquid water is not accounted for). Moreover, the kinetic depends on the surface coverage of platinum. If bare platinum or PtOH^s is available, then:

$$j_{O_2/H_2O(Pt)}^\alpha = \gamma_\alpha j_0^{O_2/H_2O(Pt)} \left[\left(\frac{c_{O_2}^0}{c_{O_2}^\alpha} \right)^{\alpha_{H_2O(Pt)}} \left(\frac{c_{H_2O}^\alpha}{c_{H_2O}^0} \right)^{1+\alpha_{H_2O(Pt)}} \exp \left(\frac{\alpha_{H_2O(Pt)} nF}{RT} (\phi_\alpha - E_{O_2/H_2O}^0) \right) - \left(\frac{c_{H_2O}^0}{c_{H_2O}^\alpha} \right)^{\alpha_{O_2(Pt)}} \left(\frac{c_{O_2}^\alpha}{c_{O_2}^0} \right)^{1+\alpha_{O_2(Pt)}} \exp \left(\frac{-\alpha_{O_2(Pt)} nF}{RT} (\phi_\alpha - E_{O_2/H_2O}^0) \right) \right] \quad (4-26)$$

With:

$$c_{H_2O}^0 = \frac{P_{atm}}{RT} \exp\left(13.669 - \frac{5096.23}{T_h}\right) \quad (4-27)$$

And T_h the temperature of the humidifier (assuming that gases are saturated at the outlet of the humidifiers).

If platinum is covered by an oxide layer (PtO^s), then the kinetic parameters (α_{Ox} , α_{Red} , $j_0^{Ox/Red}$) in equation (4-26) need to be modified:

$$j_{O_2/H_2O}^\alpha = \gamma_\alpha j_0^{O_2/H_2O} \left[\begin{array}{l} \left(\frac{c_{O_2}^0}{c_{O_2}^\alpha}\right)^{\alpha_{H_2O}} \left(\frac{c_{H_2O}^\alpha}{c_{H_2O}^0}\right)^{1+\alpha_{H_2O}} \exp\left(\frac{\alpha_{H_2O} n F}{RT} (\phi_\alpha - E_{O_2/H_2O}^0)\right) \\ - \left(\frac{c_{H_2O}^0}{c_{H_2O}^\alpha}\right)^{\alpha_{O_2}} \left(\frac{c_{O_2}^\alpha}{c_{O_2}^0}\right)^{1+\alpha_{O_2}} \exp\left(\frac{-\alpha_{O_2} n F}{RT} (\phi_\alpha - E_{O_2/H_2O}^0)\right) \end{array} \right] \quad (4-28)$$

Reversible platinum oxidation

The current density resulting from platinum (platinum oxide) successive oxidations (reductions) is a function of the surface coverages $\theta_{Pt}^{s,\alpha}$, $\theta_{PtOH}^{s,\alpha}$ and $\theta_{PtO}^{s,\alpha}$ at the surface of platinum particles:

$$j_{PtOH^s/Pt^s}^\alpha = \gamma_\alpha j_0^{PtOH^s/Pt^s} \left[\begin{array}{l} \theta_{Pt}^{\alpha,s} \left(\frac{c_{H_2O}^\alpha}{c_{H_2O}^0}\right)^{1+\alpha_{Pt}} \exp\left(\frac{\alpha_{Pt^s} F}{RT} (\phi_\alpha - E_{PtOH^s/Pt^s}^0)\right) \\ - \theta_{PtOH}^{\alpha,s} \left(\frac{c_{H_2O}^0}{c_{H_2O}^\alpha}\right)^{\alpha_{PtOH}} \exp\left(\frac{-\alpha_{PtOH^s} F}{RT} (\phi_\alpha - E_{PtOH^s/Pt^s}^0)\right) \end{array} \right] \quad (4-29)$$

Similarly, the kinetic of reaction (4-6) obeys a Butler-Volmer law:

$$j_{PtO^s/PtOH^s}^\alpha = \gamma_\alpha j_0^{PtO^s/PtOH^s} \left[\theta_{PtOH}^{\alpha,s} \exp\left(\frac{\alpha_{PtOH^s} F}{RT} (\phi_\alpha - E_{PtO^s/PtOH^s}^0)\right) - \theta_{PtO}^{\alpha,s} \exp\left(\frac{-\alpha_{PtO^s} F}{RT} (\phi_\alpha - E_{PtO^s/PtOH^s}^0)\right) \right] \quad (4-30)$$

While the adsorbed species differ, the kinetic of platinum oxidation in the bulk proposed by Conway et al. [128] should be similar to that proposed by Jerkiewicz et al. [124]. According to Conway, platinum oxidation rate is an exponentially decreasing function of the platinum oxide coverage θ_{PtO}^s and θ_{PtO}^b . However, their model did not take account of the reduction of PtO formed in Pt. Thus, unlimited growth of PtO on the Pt sublayers could occur. Darling et al. [125] integrated this reduction in their model. We adapted the expression they proposed to the mechanism described by Jerkiewicz:

$$j_{PtO^b/Pt^b}^\alpha = \gamma_\alpha j_0^{PtO^b/Pt^b} \left[\begin{array}{l} \left(1 - \theta_{PtO}^{\alpha,b}\right) \left(\frac{C_{H_2O}^\alpha}{C_{H_2O}^0}\right)^{1+\alpha_{Pt^b}} e^{-\frac{w(\theta_{PtO}^{\alpha,s} + \theta_{PtO}^{\alpha,b})}{RT}} \exp\left(\frac{\alpha_{Pt^b} F}{RT} (\phi_\alpha - E_{PtO^b/Pt^b}^0)\right) \\ - \theta_{PtO}^{\alpha,b} \left(\frac{C_{H_2O}^0}{C_{H_2O}^\alpha}\right)^{\alpha_{PtO^b}} \exp\left(-\frac{\alpha_{PtO^b} F}{RT} (\phi_\alpha - E_{PtO^b/Pt^b}^0)\right) \end{array} \right] \quad (4-31)$$

With w the PtO-PtO interaction (in J/mol).

Carbon redox reaction

Due to the low kinetic of carbon dioxide reduction, only carbon oxidation was considered in the model:

$$j_f^{\alpha,CO_2/C} = \Gamma_\alpha j_0^{CO_2/C} \left(\frac{C_{H_2O}^\alpha}{C_{H_2O}^0}\right)^{1+\alpha_C} \exp\left(\frac{\alpha_C n F}{RT} (\phi_\alpha - E_{CO_2/C}^0)\right) \quad (4-32)$$

With Γ_α the rugosity of the electrode carbon support.

This assumption is also valid for the catalysed carbon oxidation. In addition, it is considered that the rate determining step is the second reaction (4-20), which kinetic depends on the PtOH^s surface coverage:

$$j_f^{\alpha,CO_2/C(Pt)} = \gamma_\alpha j_0^{CO_2/C(Pt)} \theta_{PtOH}^{\alpha,s} \exp\left(\frac{\alpha_{C(Pt)} F}{RT} (\phi_\alpha - E_{CO_2/C(Pt)}^0)\right) \quad (4-33)$$

This assumption can be discussed since in some cases, water involved in the first reaction can also be the limiting reactant.

Figure 4-7 summarizes the different reactions which were integrated in the generic electrode model.

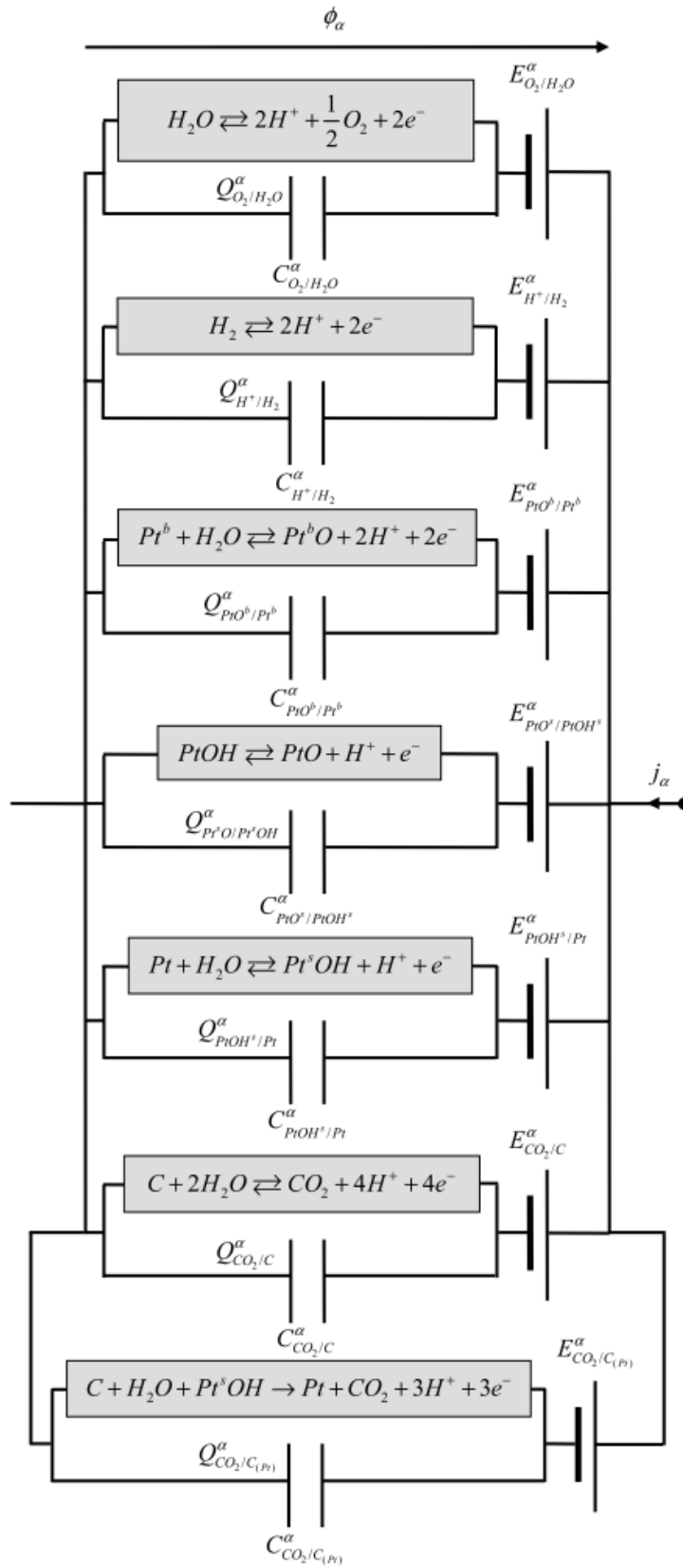


Figure 4-7. Equivalent electrical circuit of an electrode. α stands for the type of electrode considered (anode or cathode)

The electrode model in Figure 4-7 can be depicted using single elements connected in parallel like in Figure 4-8:

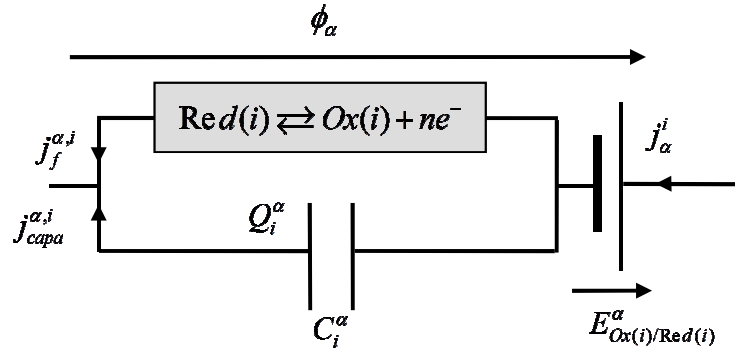


Figure 4-8. Single element in the electrical equivalent circuit of an electrode. α stands for the type of electrode considered (anode or cathode) and i for the reaction.

When the electrode is an anode operating normally (i.e: in the presence of H_2 and oxidation reactions), Figure 4-8 becomes:

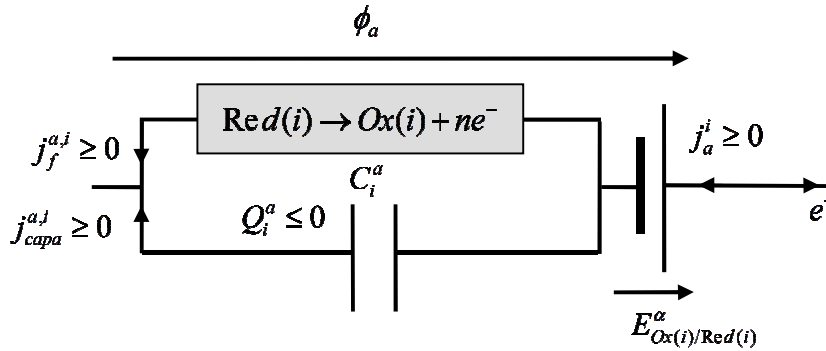


Figure 4-9. Single element in the electrical equivalent circuit of an anode.

When the electrode is a cathode operating normally (i.e: in the presence of O_2 and reduction reactions), Figure 4-8 becomes:

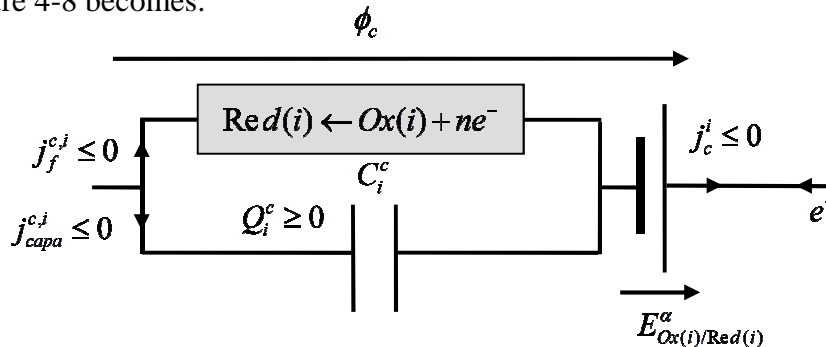


Figure 4-10. Single element in the electrical equivalent circuit of a cathode.

The electrical behaviour of each single element can be described using the Kirchoff's laws. Kirchoff's voltage law leads to:

$$\phi_\alpha = E_{Ox(i)/Red(i)}^\alpha - \frac{Q_i^\alpha}{C_i^\alpha} \quad 1 \leq i \leq m \quad (4-34)$$

And Kirchhoff's current law yields:

$$j_{\alpha}^i = j_{Ox(i)/Red(i)}^{\alpha} + j_{capa}^{\alpha,i} \quad (4-35)$$

The equation (4-35) can be rewritten by making explicit the expression of $j_{capa}^{\alpha,i}$:

$$j_{\alpha}^i = j_{Ox(i)/Red(i)}^{\alpha} + C_i^{\alpha} \frac{d(\phi_{\alpha} - E_{Ox(i)/Red(i)}^{\alpha})}{dt} \quad (4-36)$$

Kirchhoff's current law applied to the whole electrode (Figure 4-7) gives:

$$j_{\alpha} = \sum_{i=1}^m j_{\alpha}^i \quad (4-37)$$

Where m stands for the total number of reactions occurring in the electrode.

And the expression of j_i^{α} in equation (4-37) can be replaced by that in equation (4-36):

$$j_{\alpha} = \sum_{i=1}^m j_{Ox(i)/Red(i)}^{\alpha} + \frac{d\phi_{\alpha}}{dt} \sum_{i=1}^m C_i^{\alpha} - \sum_{i=1}^m C_i^{\alpha} \frac{dE_{Ox(i)/Red(i)}^{\alpha}}{dt} \quad (4-38)$$

Considering that:

$$C_{tot}^{\alpha} = \sum_{i=1}^m C_i^{\alpha} \quad (4-39)$$

Equation (4-38) becomes:

$$j_{\alpha} = \sum_{i=1}^m j_{Ox(i)/Red(i)}^{\alpha,i} + C_{tot}^{\alpha} \frac{d\phi_{\alpha}}{dt} - \sum_{i=1}^m C_i^{\alpha} \frac{dE_{Ox(i)/Red(i)}^{\alpha}}{dt} \quad (4-40)$$

However, it can be considered that the variation with time of the equilibrium potentials are negligible, which makes it possible to simplify equation (4-40):

$$j_{\alpha} = \sum_{i=1}^m j_{Ox(i)/Red(i)}^{\alpha,i} + C_{tot}^{\alpha} \frac{d\phi_{\alpha}}{dt} \quad (4-41)$$

Figure 4-11 shows an adapted version of the electrical circuit in Figure 4-7 accounting for these simplifications.

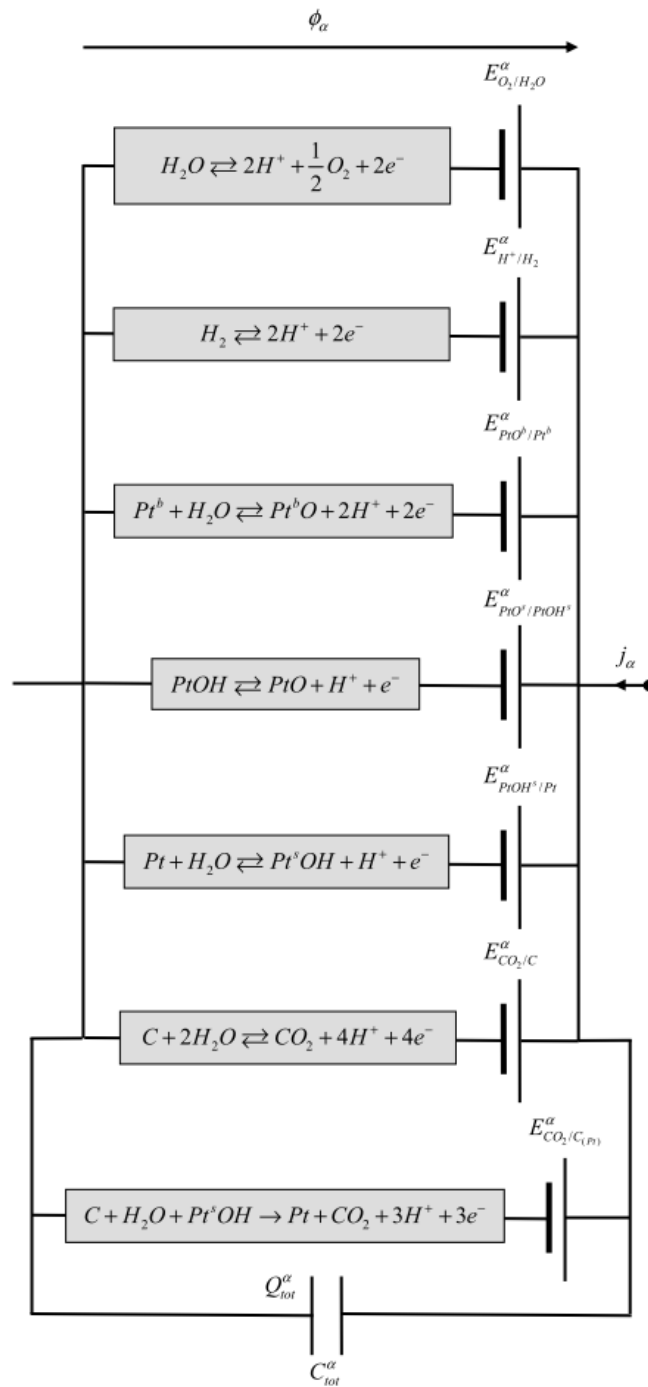


Figure 4-11. Equivalent electrical circuit in Figure 4-7 simplified according to equation (4-41).

c. Mass transport

Several species are implicated in the reactions kinetics. They can be categorized in two groups:

- Gaseous species: hydrogen, oxygen, water and carbon dioxide.
- Solid species: carbon, platinum and platinum oxides (hydrated or not).

Species of the first group are transported from the electrode to the flow field plates or the other way around. The mass transport resistance of the media they have to diffuse through can result in significant concentration variations, which can have an impact on the electrochemical activity of the cell, especially during transient operations such as start-ups and shut-downs. Figure 4-12 represents an electrical equivalent circuit of the mass transport phenomena.

For the gaseous species, different mass transport phenomena were considered in the model and several assumptions were necessary to facilitate the resolution of the equations:

- Concentrations in the channels are known.
- Mass transfer occurs only by diffusion through the GDL and in the membrane (the diffusion is purely resistive in the membrane).
- The diffusion coefficient of species i in the GDL is the effective diffusion coefficient, taking into account both the tortuosity and the porosity of the diffusion media [129].

$$D_{eff,i}^{\alpha,GDL} = \frac{\mathcal{E}}{\tau} D_i^{\alpha,GDL} \quad (4-42)$$

To simplify, $D_{eff,i}^{\alpha,GDL}$ is written $D_i^{\alpha,GDL}$ in the following.

- Gaseous species concentration is assumed uniform through the electrode.

$$c_i^{\alpha,GDL} = c_i^{\alpha} \quad (4-43)$$

- Carbon dioxide concentration in the electrode remains negligible.
- Transport of liquid water is not accounted for. One assumes that liquid water is removed from the electrode without impeding the transport of gaseous species.

Gaseous species can diffuse either through the membrane or through the GDL. Mass fluxes of gaseous species i between the channel and the electrode are considered positive when directed toward the electrode and are expressed by:

$$\varphi_i^{\alpha,channel} = \frac{D_i^{\alpha,GDL}}{e_{GDL}^{\alpha}} (c_i^{\alpha,channel} - c_i^{\alpha}) \quad (4-44)$$

With:

- - c_i^{α} the concentration in the electrode.
- $c_i^{\alpha,channel}$ the concentration in the channel (boundary condition).
- $D_i^{\alpha,GDL}$ the diffusion coefficient of species i through the GDL.
- e_{GDL}^{α} the thickness of the GDL.

The mass flux of gaseous species i between the membrane and the electrode is expressed by:

$$\varphi_i^{\alpha,m} = \frac{D_i^m}{e_m} (c_i^m - c_i^{\alpha}) \quad (4-45)$$

With:

- c_i^m the concentration in the opposite electrode.
- D_i^m the diffusion coefficient of the gaseous species i through the membrane.
- e_m the thickness of the membrane.

d. Mass balance

Each gaseous species involved in one or several electrochemical reactions has to obey the conservation of mass:

$$\left(\varepsilon_\alpha e_\alpha + \varepsilon_{GDL}^\alpha e_{GDL}^\alpha\right) \frac{dc_i^\alpha}{dt} = \frac{j_f^\alpha(i)}{nF} + \varphi_i^{\alpha,channel} + \varphi_i^{\alpha,m} \quad (4-46)$$

With:

- ε_α the porosity of the electrode.
- ε_{GDL}^α the porosity of the GDL.
- $\frac{j_f^\alpha(i)}{nF}$ the electrochemical production or consumption of species i [mol/s/cm²].

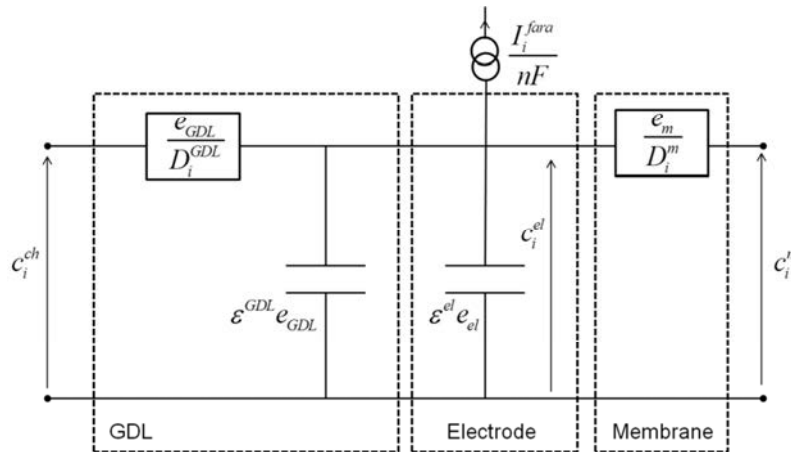


Figure 4-12. Equivalent electrical circuit of the mass transport phenomena for species i .

For oxygen:

$$\frac{j_f^\alpha(O_2)}{nF} = -\frac{j_{O_2/H_2O}^\alpha}{4F} \quad (4-47)$$

For hydrogen:

$$\frac{j_f^\alpha(H_2)}{nF} = -\frac{j_{H^+/H_2}^\alpha}{2F} \quad (4-48)$$

For water:

$$\frac{j_f^\alpha(H_2O)}{nF} = -\frac{j_{H_2O/O_2}^\alpha + 2j_{PtOH^s/Pt^s}^\alpha + j_{PtO^b/Pt^b}^\alpha + j_{CO_2/C}^\alpha + \frac{2}{3}j_{CO_2/C(Pt)}^\alpha}{F} \quad (4-49)$$

Solid species also have to respect the balance of mass. Thus, the PtOH surface coverage is expressed by:

$$\frac{d\theta_{PtOH}^{\alpha,S}}{dt} = \frac{j_{PtOH^s/Pt^s}^{\alpha}}{FN_{Pt}^s} - \frac{j_{PtO^s/PtOH^s}^{\alpha}}{FN_{Pt}^s} - \frac{j_{CO_2/C_{(Pt)}}^{\alpha}}{3FN_{Pt}^s} \quad (4-50)$$

On the surface, the PtO coverage is governed by a single reaction:

$$\frac{d\theta_{PtO}^{\alpha,S}}{dt} = \frac{j_{PtO^s/PtOH^s}^{\alpha}}{FN_{Pt}^s} \quad (4-51)$$

In the bulk, the PtO coverage is given by:

$$\frac{d\theta_{PtO}^{\alpha,b}}{dt} = \frac{j_{PtO^b/Pt^b}^{\alpha}}{2FN_{Pt}^b} \quad (4-52)$$

4.2.2 Parameter setting

To simulate PEMFC operations, two generic electrodes identical to that described in the previous section were connected thanks to a high frequency resistance standing for the membrane (green frame in Figure 4-4 and Figure 4-13). It must be mentioned that the electrode model can be applied to the anode or cathode without distinction (the reactions taking place depend on the potential applied and on the gas concentration in the electrode). The model is referred to as 1 dimensional because transport phenomena are considered only in the direction perpendicular to the MEA.

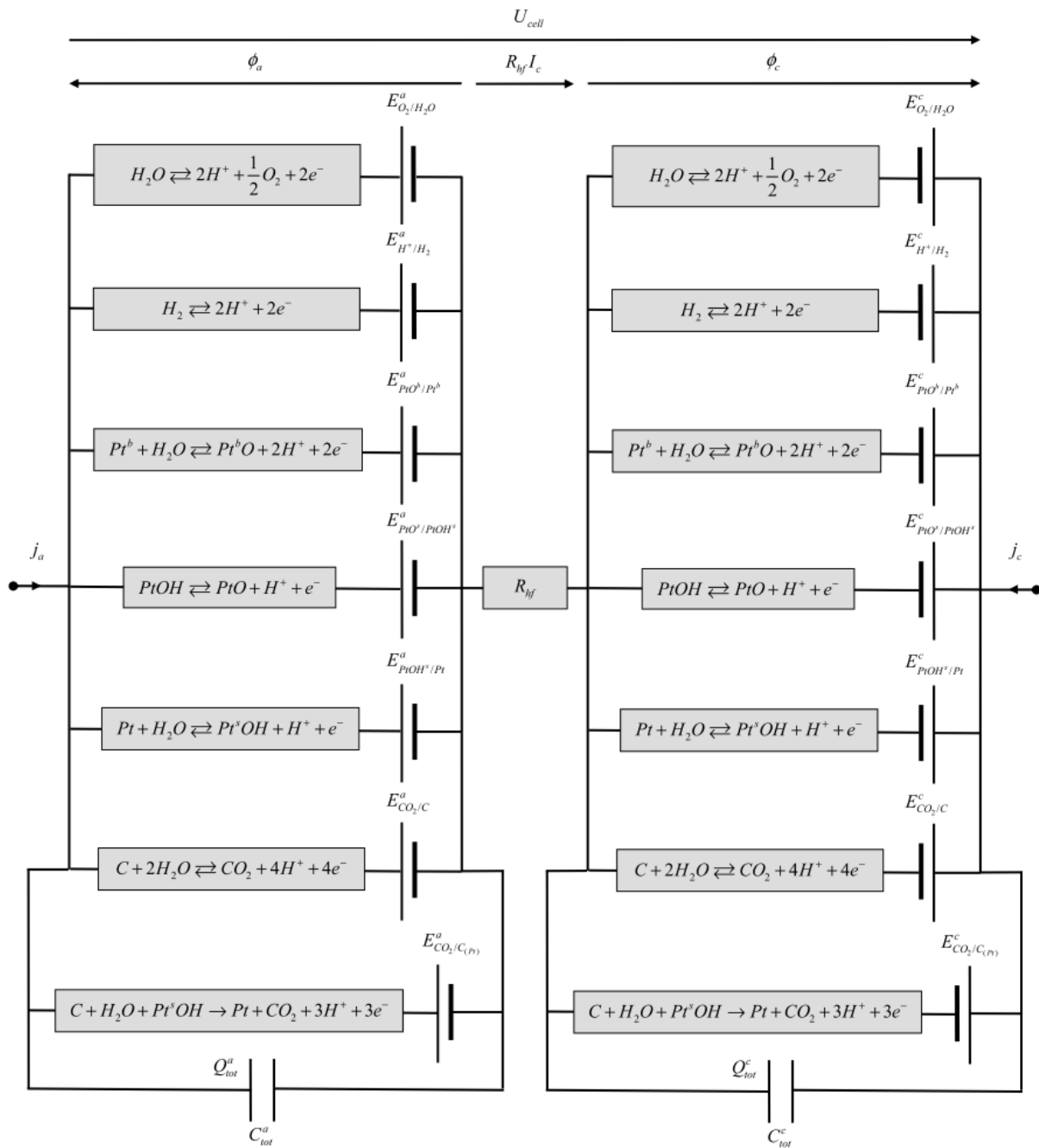


Figure 4-13. Electrical equivalent circuit of the whole MEA of a unique fuel cell segment (or a whole cell).

The accuracy of the numerical simulation of electrochemical and mass transport phenomena depends on the values given to the parameters. Some were found in the literature and others were estimated by fitting experimental results obtained in steady (polarization curve) or transient (cyclic voltammetry – impedance spectroscopy) states. The experiments were realised with a Johnson Matthey MEA similar to that used in chapter 2 and 3 (Annex 1). The experimental conditions were identical to those in chapter 2 (hydrogen, air and nitrogen fully saturated). The fuel cell temperature was set to 80°C. Due to the high number of parameters, some may be correlated which means that several set of parameters can lead to identical or close results.

The system of equations and the resolution method used for the simulation of polarization curves and cyclic voltamograms are detailed in Annex 5.

a. Polarization curve

One set of parameter is chosen so that the experimental polarization curve is correctly fitted by the equivalent circuit presented in Figure 4-13. The simulation is represented in Figure 4-14 with the experimental values.

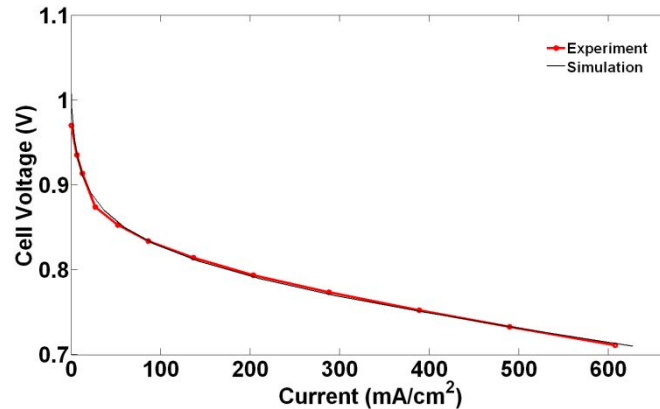


Figure 4-14. Experimental and simulated polarization curves.

b. Cyclic voltammetry

Several indications enable the identification of the kinetic parameters using a voltammogram:

- The position of the current peaks;
- The gap between the forward and backward current peaks;
- The intensity of the peaks.

These data allow the empirical adjustment of parameters relative to the redox reactions. However, several sets of values can be used. For instance, the different platinum oxidations occur simultaneously and their respective contribution can be modified by acting on the reaction rates or on the charge transfer coefficients, this while keeping the resulting global current density constant.

In the scope of this work, the domain of interest is located between 0.4V and 1.2V. This region corresponds actually to the pseudo capacitive region where platinum/platinum oxides can be oxidized/reduced reversibly (assuming that platinum dissolution is negligible). Above 0.5V in Figure 4-15, the simulation fits quite faithfully the experimental curve, which means that the pseudo capacity is properly modeled by one set of parameters (among many others possible). The kinetic parameters related to the carbon oxidation are adjusted according to carbon dioxide emissions measured during the voltammetry ($0.5 \mu\text{g}_C/\text{cycle}/\text{cm}^2$). Similarly to platinum, there are several possible sets of parameters for the catalysed and non catalysed oxidation of carbon which could fit the total carbon dioxide emissions measured. Nevertheless, it appears that if the CO_2 emissions can be accurately simulated during a cyclic voltammetry with a prevalence of non-catalysed over catalysed carbon oxidation, those obtained during a start-up are not realistic compared to the experimental values (not enough carbon is oxidized at high hydrogen injection flow rate and too much at low hydrogen injection flow rate). On the contrary, with a prevalence given to catalysed carbon oxidation,

the simulated CO₂ emissions for both cyclic voltammetry and start-up are in good agreement with the experiments.

The kinetic parameters relative to the hydrogen redox reactions are assessed thanks to the negative and positive peaks between 0.1V and 0.3V. The simulated currents do not fit very well the experimental data but the charge corresponding to the hydrogen sorption and desorption are close in both cases. A better fit would be achieved if the reactions which take place on each platinum face, which have their own kinetic parameters, were modeled (§1.3.1).

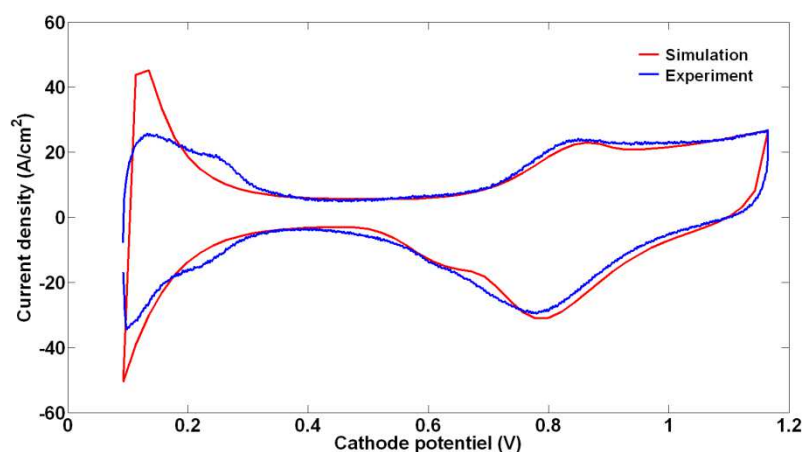


Figure 4-15. Experimental voltammogram (red) and its corresponding numerical simulation (blue).

Once the values of the parameters have been adjusted at a global scale, each reaction can be considered separately. In Figure 4-16, one can see that the influence of some redox reactions is negligible, like for example that of non catalysed carbon oxidation. Oxidation of water is insignificant although the electrode potential is high.

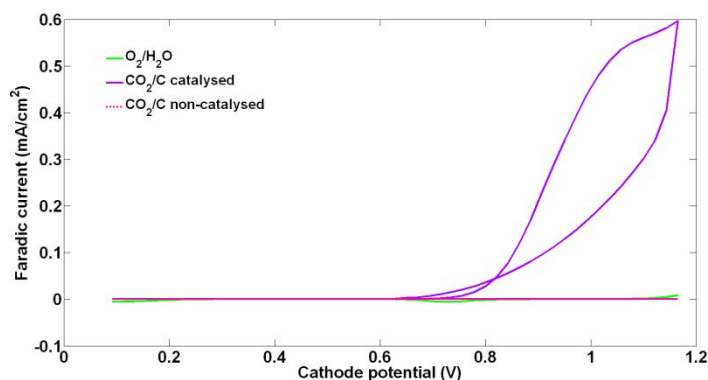


Figure 4-16. Catalysed and non catalysed carbon oxidation and O₂/H₂O redox reactions during a cyclic voltammetry.

On the contrary, platinum oxidation into PtOH^s and PtO^s on the particle surface and into PtO^s in the bulk are predominant at high potential (Figure 4-17). First PtOH^s and then PtO^s are formed between 0.6V and 1V on the platinum particle surface. When about 50% of surface platinum is oxidized, oxidation starts in the bulk (around 0.8V). The whole platinum particles surface is covered by an oxide layer (actually a mixed of PtOH^s and PtO^s) below 1V. At this

time, oxidation in the bulk becomes predominant. When the potential scan is inverted, both $\text{PtOH}^{\text{s}}/\text{Pt}$ and $\text{PtO}^{\text{s}}/\text{Pt}$ ratios return to zero and platinum becomes active again.

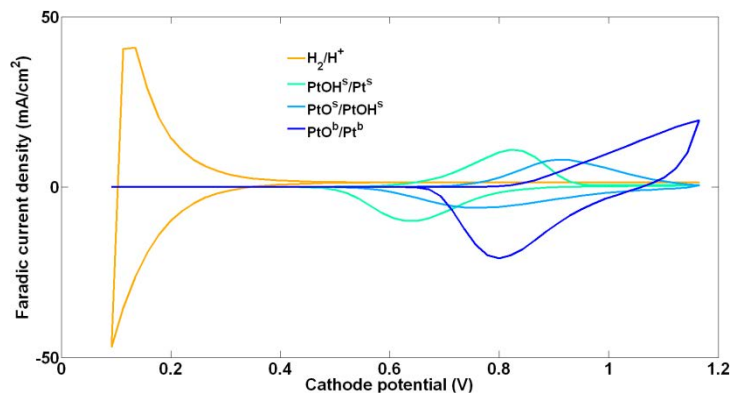


Figure 4-17. Faradic currents during a cyclic voltammetry.

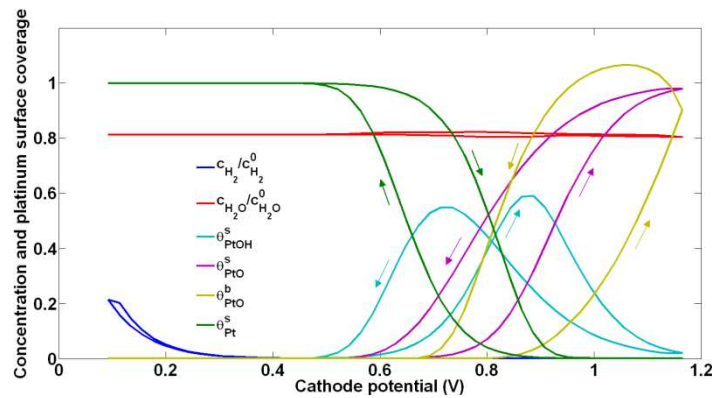


Figure 4-18. Concentrations and platinum surface coverages during a cyclic voltammetry.

Voltammograms provide also information about the hydrogen permeation current (§1.3.1, equation (1-52)). Its value (about 1.5 mA/cm²) was used for the adjustment of the hydrogen diffusion coefficient in the membrane $D_{\text{H}_2}^m$.

Finally, voltammograms also allow estimating the cathode double layer capacity according to equation (1-55) (§1.3.1). The double layer capacity is correlated with the platinum content (Figure 3-19). Since the platinum content in the anode is three times lower than in the cathode, the capacity is assumed to be also three time lower than at the cathode.

		Parameter	Symbol	Value	Unit	Method of estimation					
		Kinetic parameters		H⁺/H₂							
Standard electrode potential	E_{H^+/H_2}^0			1×10^{-4}	V	Hypothesis					
Exchange current density	$j_0^{H^+/H_2}$			200	A/cm ²	Fit volta					
Anode charge transfer coefficient	α_{H_2}			0.3		Fit volta					
Cathode charge transfer coefficient	α_{H^+}			0.3		Fit volta					
Limit current density	$j_{lim}^{H^+/H_2}$			1×10^{10}	A/cm ²	Hypothesis					
O₂/H₂O											
Standard electrode potential						E_{O_2/H_2O}^0	1.15	V	Hypothesis		
On Pt ^s and PtOH ^s	Exchange current density			$j_0^{O_2/H_2O(Pt)}$	3.5×10^{-5}	A/cm ²	Fit polarization curve				
	Anode charge transfer coefficient			$\alpha_{H_2O(Pt)}$	1.09		Hypothesis				
	Cathode charge transfer coefficient			$\alpha_{O_2(Pt)}$	1.09		Fit polarization curve				
	Limit current density			$j_{lim}^{O_2/H_2O(Pt)}$	1×10^{10}		Hypothesis				
On PtO ^s	Exchange current density			$j_0^{O_2/H_2O}$	7.3×10^{-4}	A/cm ²	Fit polarization curve				
	Anode charge transfer coefficient			α_{H_2O}	0.77		Hypothesis				
	Cathode charge transfer coefficient			α_{O_2}	0.77		Fit polarization curve				
	Limit current density			$j_{lim}^{O_2/H_2O}$	1×10^{10}		Hypothesis				
CO₂/C											
Standard electrode potential						$E_{CO_2/C}^0$	0.2	V	Fit		
Non catalysed	Exchange current density			$j_0^{CO_2/C}$	1×10^{-20}	A/cm ²	Fit CO ₂ measurement during volta				
	Anode charge transfer coefficient			α_C	1		Fit CO ₂ measurement during volta				
	Limit current density	$j_{lim}^{CO_2/C}$	1×10^{10}	A/cm ²	Hypothesis						
Catalysed	Exchange current density	$j_0^{CO_2/C(Pt)}$	2×10^{-7}	A/cm ²	Fit CO ₂ measurement during volta						
	Anode charge transfer coefficient	$\alpha_{C(Pt)}$	0.5		Fit CO ₂ measurement during volta						
	Limit current density	$j_{lim}^{CO_2/C(Pt)}$	1×10^{10}	A/cm ²	Hypothesis						

		Parameter	Symbol	Value	Unit	Method of estimation
Kinetic parameters	PtOH ^s /Pt ^s	Standard electrode potential	E_{PtOH^s/Pt^s}^0	0.73	V	Fit volta
		Exchange current density	$j_0^{PtOH^s/Pt^s}$	0.6	A/cm ²	Fit volta
		Anode charge transfer coefficient	α_{Pt^s}	0.45		Fit volta
		Cathode charge transfer coefficient	α_{PtOH^s}	0.3		Fit volta
		Limit current density	$j_{lim}^{PtOH^s/Pt^s}$	1×10^{10}	A/cm ²	Hypothesis
	PtO ^s /PtOH ^s	Standard electrode potential	$E_{PtO^s/PtOH^s}^0$	0.85	V	Fit volta
		Exchange current density	$j_0^{PtO^s/PtOH^s}$	0.8	A/cm ²	Fit volta
		Anode charge transfer coefficient	α_{PtOH^s}	0.2		Fit volta
		Cathode charge transfer coefficient	α_{PtO^s}	0.2		Fit volta
		Limit current density	$j_{lim}^{PtO^s/PtOH^s}$	1×10^{10}	A/cm ²	Hypothesis
	PtO ^b /Pt ^b	Standard electrode potential	E_{PtO^b/Pt^b}^0	0.85	V	Fit volta
		Exchange current density	$j_0^{PtO^b/Pt^b}$	1.3	A/cm ²	Fit volta
		Anode charge transfer coefficient	α_{Pt^b}	0.6		Fit volta
		Cathode charge transfer coefficient	α_{PtO^b}	0.4		Fit volta
		Limit current density	$j_{lim}^{PtO^b/Pt^b}$	1×10^{10}	A/cm ²	Hypothesis
		PtO-PtO interaction	w	19×10^3	J/mol	Hypothesis

Table 4-1. Values of the kinetic parameters and methods used to estimate them.

Parameter	Symbol	Value	Unit	Method of estimation
GDL thickness	e_{GDL}	600	μm	Mean thickness considering 2D transfer under the channel and rib
Anode thickness ⁽¹⁾	e_a	$e_c/2$	μm	Hypothesis
Cathode thickness ⁽¹⁾	e_c	500	μm	Hypothesis
Membrane thickness	e_m	50	μm	JM data
Anode Pt loading	L_{Pt}^a	0,2	mg _{Pt} /cm ²	JM data
Cathode Pt loading	L_{Pt}^c	0,6	mg _{Pt} /cm ²	JM data
Pt Anode rugosity	γ_a	$\gamma_c/3$	m ² /m ² _{MEA}	Hypothesis
Pt Cathode rugosity	γ_c	200	m ² /m ² _{MEA}	Hypothesis
Anode carbon rugosity	Γ_a	$5 * \gamma_a$	m ² /m ² _{MEA}	Hypothesis
Cathode carbon rugosity	Γ_c	$5 * \gamma_c$	m ² /m ² _{MEA}	Hypothesis
Anode capacity	C_{tot}^a	$C_{tot}^c / 3$	F/cm ²	Hypothesis

Parameter	Symbol	Value	Unit	Method of estimation		
Cathode capacity	C_{tot}^c	800	F/cm ²	Fit volta		
Hydrogen reference concentration	$c_{H_2}^0$	$\frac{P_{atm}}{RT}$	mol/m ³	Hypothesis		
Oxygen reference concentration	$c_{O_2}^0$	$0.2 \frac{P_{atm}}{RT}$	mol/m ³	Hypothesis		
Water reference concentration	$c_{H_2O}^0$	Eq. (4-27)	mol/m ³	Hypothesis		
Active platinum on the surface	Anode	$n_{Pt}^{s,a}$	$\frac{L_{Pt}^a S_{MEA}}{8M_{Pt}}$ (2)	mol	Hypothesis	
	Cathode	$n_{Pt}^{s,c}$	$\frac{L_{Pt}^c S_{MEA}}{8M_{Pt}}$ (2)	mol	Hypothesis	
Active platinum in the bulk	Anode	$n_{Pt}^{b,a}$	$\frac{L_{Pt}^a S_{MEA}}{8M_{Pt}}$ (2)	mol	Hypothesis	
	Cathode	$n_{Pt}^{b,c}$	$\frac{L_{Pt}^c S_{MEA}}{8M_{Pt}}$ (2)	mol	Hypothesis	
Oxygen diffusion coefficient	GDL	Anode	$D_{O_2}^{GDL,a}$	0.1×10^{-6}	m ² /s	Hypothesis
		Cathode	$D_{O_2}^{GDL,c}$	1×10^{-6}	m ² /s	Hypothesis
	Membrane	$D_{O_2}^m$	1.5×10^{-10}	m ² /s	Hypothesis	
Hydrogen diffusion coefficient	GDL	Anode	$D_{H_2}^{GDL,a}$	1×10^{-6}	m ² /s	Hypothesis
		Cathode	$D_{H_2}^{GDL,c}$	15×10^{-16}	m ² /s	Hypothesis
	Membrane	$D_{H_2}^m$	1.2×10^{-10}	m ² /s	Hypothesis	
Hydrogen diffusion coefficient	GDL	$D_{H_2O}^{GDL}$	1×10^{-6}	m ² /s	Hypothesis	
	membrane	$D_{H_2O}^m$	1×10^{-10}	m ² /s	Hypothesis	
High frequency resistance	R_{hf}	0.12×10^{-4}	$\Omega.m^2$	Measurement		

Table 4-2. Value of the parameters other than kinetic and methods used to estimate them.

(1) The electrode thickness corresponds in practice to the term $\varepsilon_{\alpha} e_{\alpha} + \varepsilon_{GDL}^{\alpha} e_{GDL}^{\alpha}$ in equation (4-46), which explains why the value is high.

4.2.3 2D transient state modelling of a complete cell

During start-up, the hydrogen injection flow rate is imposed and the propagation of the hydrogen front is governed by the following equation:

$$\frac{c_{H_2}^{a,channel}(x_n, t)}{c_{H_2}^0} = \frac{1}{2} + \frac{1}{2} \operatorname{erf} \left(\frac{t - \frac{x_n}{V_{front}}}{\sqrt{2\tau}} \right) \quad (4-53)$$

With x_n the position of the n^{th} segment and P the total pressure (assumed constant along the channel).

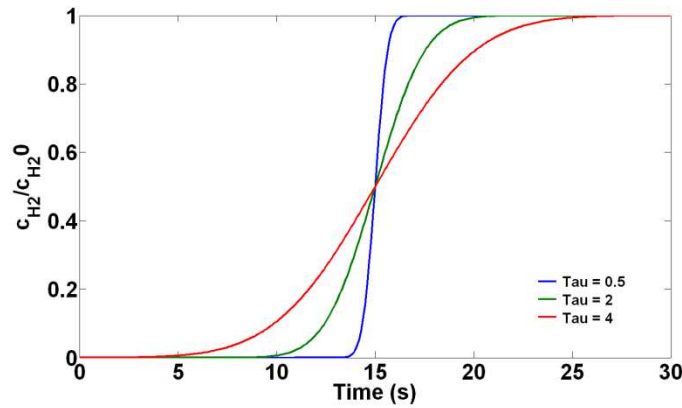


Figure 4-19. $c_{H_2}^{a,channel} / c_{H_2}^0$ ratio for the n^{th} segment calculated for different values of τ using equation (4-53).

Figure 4-19 shows that parameter τ in equation (4-53) controls the rate of concentration change in the channel of a segment. The lower it is, the steeper the front.

The oxygen concentration is given by:

$$c_{O_2}^{channel}(x_n, t) = \frac{P}{RT} - c_{H_2O}^{channel}(x_n, t) - c_{H_2}^{channel}(x_n, t) \quad (4-54)$$

With $c_{H_2O}^{c,channel}(x_n, t)$ imposed.

The numerical simulation of start-up requires to solve at the local scale (i.e: for each segment) the mass conservation equation of each species and the kinetic equation of each reaction. The whole equations system and the numerical method are detailed in Annex 5. The values of the parameter involved in the different equations are those discussed in §4.2.3.

a. Start-up by injection of hydrogen in air

i Internal currents

Figure 4-20 shows that the simulated currents are slightly higher than the experimental ones. A possible explanation could be that during the experiment, some of the internal currents do not transit through the external shunt resistances (§2.2) but through the GDL. Thus the experimental values could be underestimated. One can also notice that the evolutions of the internal currents are smoother in the experiment than in the simulation. To achieve a satisfying numerical solution, τ must be low (for a hydrogen front velocity of 0.5 m/s, $\tau = 5 \text{ ms}$), which corresponds to consider a fast concentration change in the anode channel. In practice, this change appears to be more progressive.

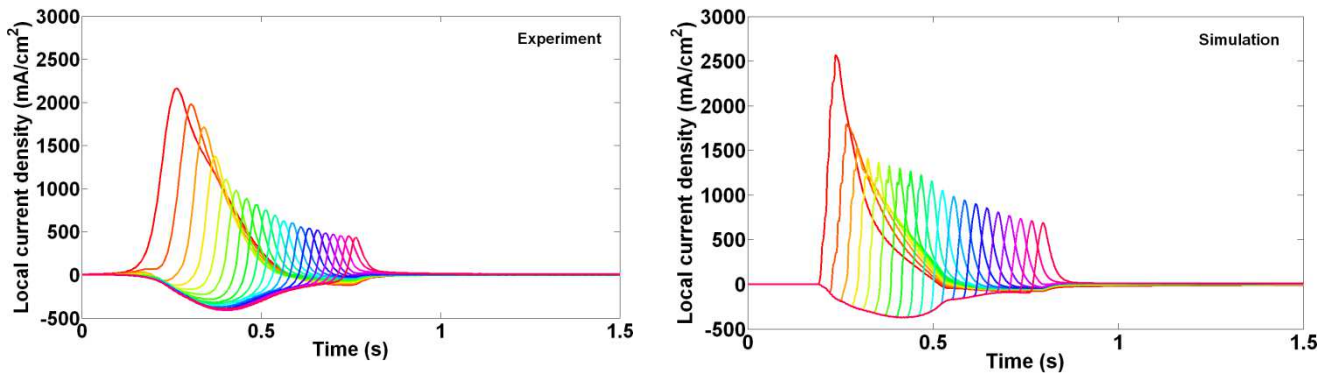
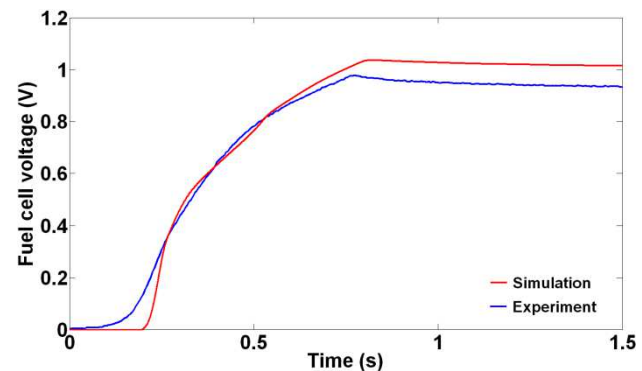


Figure 4-20. Numerical (left) and experimental (right) internal currents during a start-up by injection of hydrogen in air. Hydrogen front velocity set to 0.5 m/s.

While being close, the experimental and numerical evolutions of the fuel cell voltage present some differences (Figure 4-21):

- The sudden change of gas concentration in the numerical simulation leads to a faster evolution of the fuel cell voltage at the beginning of the start-up procedure.
- The final value of the fuel cell voltage is higher than the experimental one. This may indicate that in the model, too much platinum oxides were formed in the cathode during start-up.

Figure 4-21. Numerical and experimental evolution of fuel cell voltage during a start-up by injection of hydrogen in air. Hydrogen front velocity set to 0.5 m/s.



➤ Faradic and capacitive currents

The model enables to analyse the different contributions to the internal currents. A first step consists in separating the capacitive (Figure 4-22) and the faradic (Figure 4-23) contributions. First, one can observe that the anode and cathode capacitive (and faradic) contributions are different. In the anode, the capacitive currents are exclusively negative while in the cathode, their direction depends on the location of the segment and time. Because of the negative capacitive currents, the anode faradic currents are higher than the internal currents presented in Figure 4-20. On the contrary, the cathode faradic currents are always lower than the internal currents.

Then, one can remark that for this value of the hydrogen front velocity, the capacitive currents in the anode are always lower in absolute value than the anode faradic currents (the ratio between capacitive and faradic currents should vary depending on the hydrogen front velocity, §iii). In the cathode, the faradic contribution is predominant in the first segments supplied with hydrogen. However, it decreases strongly along the cell and the capacitive contribution becomes higher than the faradic one close to the hydrogen outlet.

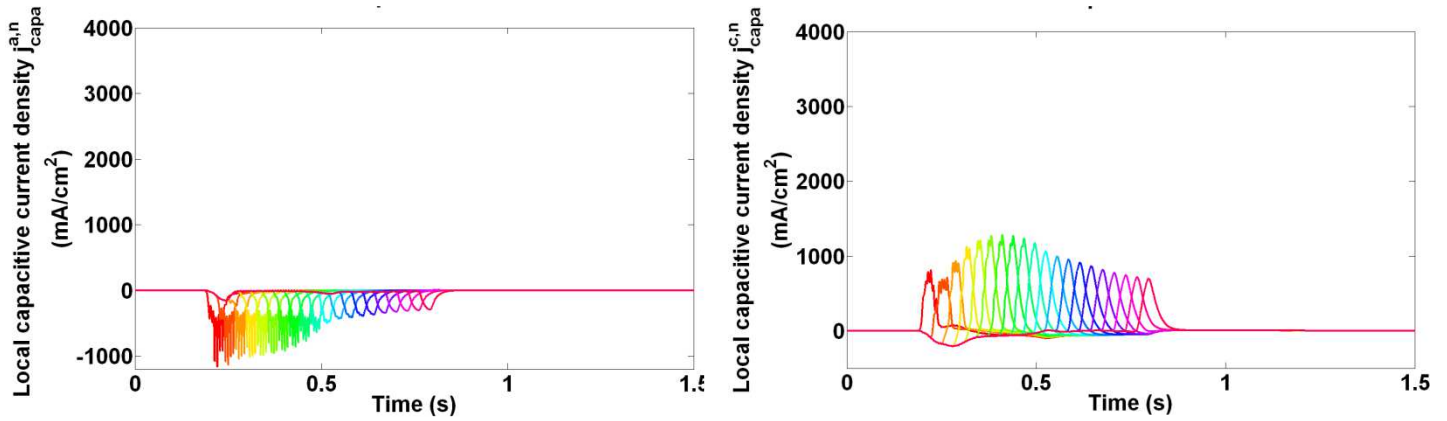


Figure 4-22. Anode (left) and cathode (right) capacitive contributions to the internal currents during a start-up by injection of hydrogen in air. Hydrogen front velocity set to 0.5 m/s. The forward currents are positive.

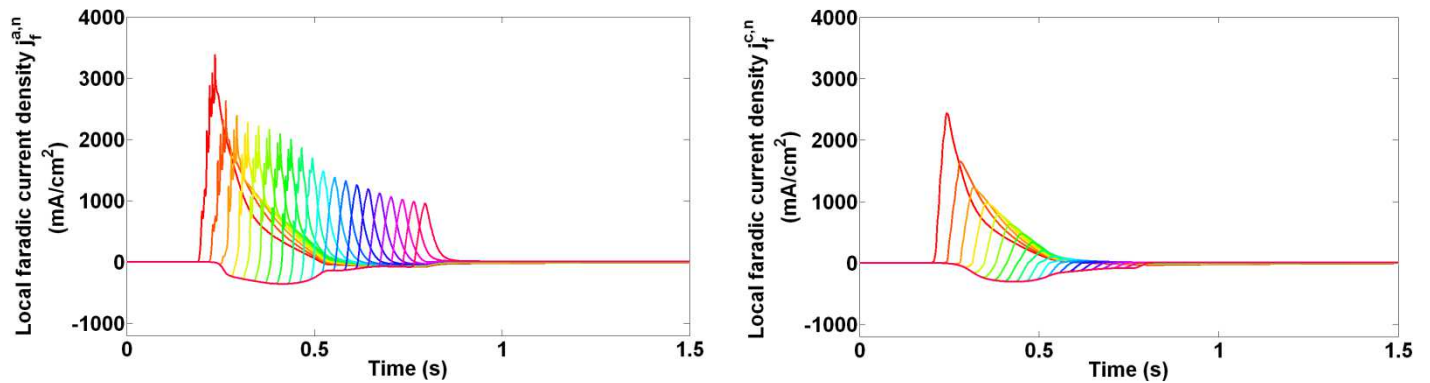


Figure 4-23. Anode (left) and cathode (right) faradic contribution to the internal currents during a start-up by injection of hydrogen in air. Hydrogen front velocity set to 0.5 m/s. The forward currents are positive.

➤ Contributions of the different redox reactions to the faradic currents

A second analysis consists in isolating the various contributions to the faradic currents that is to say to identify the current coresponding to each of the reactions that were modeled. This description is done first in the anode and cathode of a segment located in the middle of the cell (segment 10). Then, we consider the other segments. This analysis of the faradic currents is completed by that of platinum surface coverages and gaseous species concentrations.

❖ Anode reactions

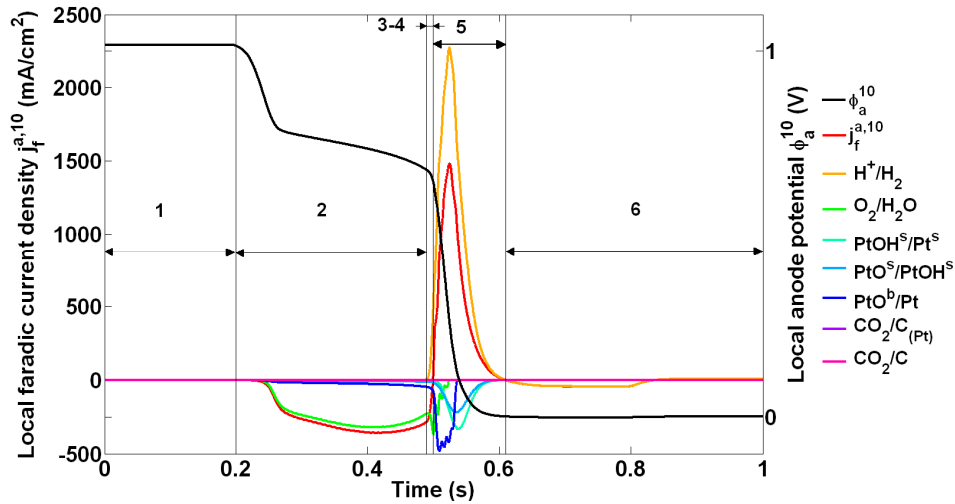


Figure 4-24. Anode faradic currents in segment 10 during a start-up by injection of hydrogen in air. Hydrogen front velocity set to 0.5 m/s. Forward currents are counted positively. Step 3 and 4 are detailed in Figure 4-26.

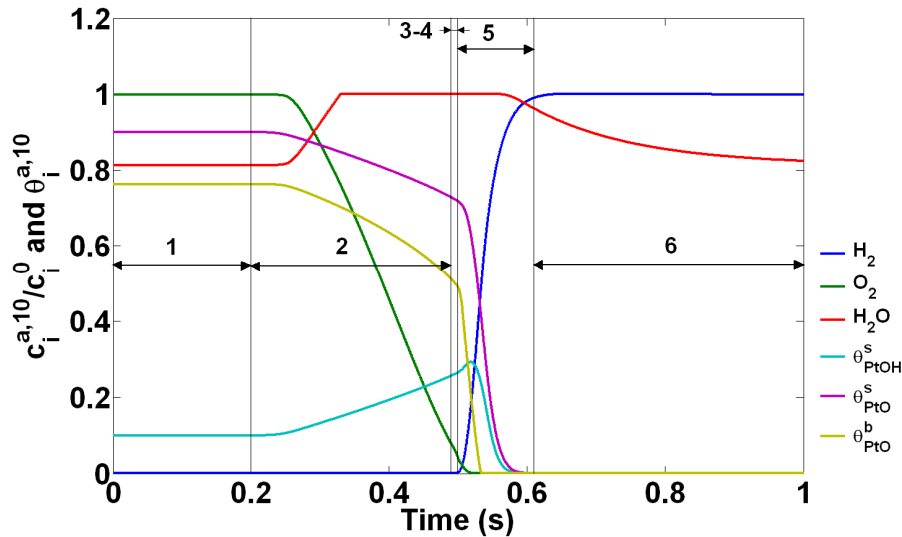


Figure 4-25. Anode platinum surface coverages and gas concentrations by reference to the standard conditions in segment 10 during a start-up by injection of hydrogen in air. Hydrogen front velocity set to 0.5 m/s.

In Figure 4-24 and Figure 4-25, several steps can be distinguished:

1. Before start-up, the surface of the platinum particles is completely oxidized ($\theta_{Pt^s}^{a,10} = 0$) because of the presence of air and high anode potential ϕ_a^{10} . A previous simulation reveals that most of the coverage corresponds to PtO^s but a small fraction corresponds to $PtOH^s$. One can also see that one sublayer of the platinum particles is partially oxidized.
2. When hydrogen is injected in the anode compartment (at 0.2 s) and as long as the front does not reach segment 10 (i.e: up to about 0.5s), only reduction reactions occur. Oxygen is mainly reduced and in a lesser extent PtO^b , PtO^s and $PtOH^s$. As a

consequence, $\theta_{PtO^b}^{a,10}$ and $\theta_{PtO^s}^{a,10}$ decrease while $\theta_{PtOH^s}^{a,10}$ increases since the reduction of PtO^s is favoured compared to that of $PtOH^s$ ($E_{PtO^s/PtOH^s} > E_{PtOH^s/Pt^s}$). The reduction of oxygen and in a lesser extent that of platinum oxides leads to the increase of the water vapour concentration up to saturation.

- Hydrogen oxidation starts once the hydrogen concentration begins to increase in segment 10. In the meantime, the reduction of oxygen and that of platinum oxides continue and still predominate over the other electrochemical reactions. As a result, the net faradic current in segment 10 remains negative (Figure 4-26).
- Step 4 corresponds to the exact moment when the oxidation of hydrogen compensates the reduction of oxygen and platinum oxides. Thus, the net faradic current $j_f^{a,10}$ is null (at about 0.5s, Figure 4-26). One can notice in Figure 4-26 that the time when the net faradic current $j_f^{a,10}$ is null in segment 10 does not correspond to the time when the internal current $j_{int}^{a,10}$ (that is to say the current which can be measured experimentally) is null. In addition, the internal current $j_{int}^{a,10}$ is lower than the current resulting from hydrogen oxidation (because of the negative capacitive contribution). The hydrogen consumption is therefore underestimated when it is evaluated based on internal current (§0.c). The underestimation is represented by the green striped area in Figure 4-26.

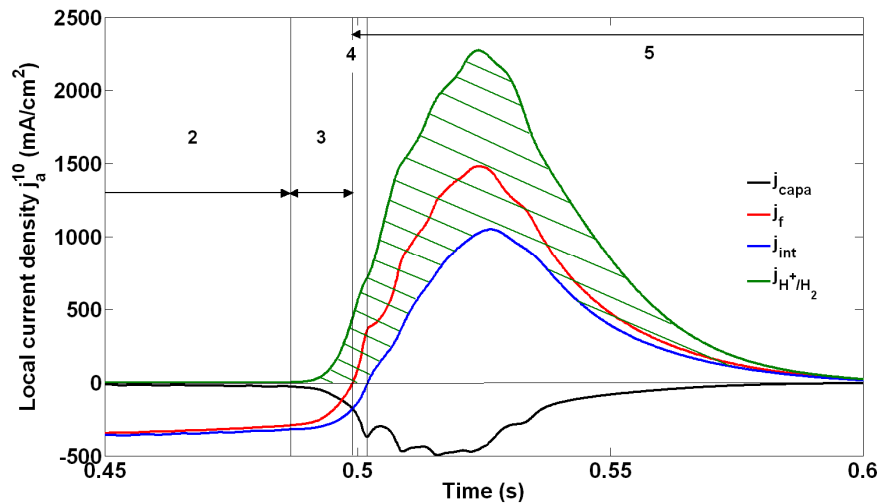


Figure 4-26. Close-up on step 3 and 4 in Figure 4-24. Local capacitive and faradic currents, internal currents (which can be measured experimentally) and currents resulting from the H^+/H_2 oxidoreduction are represented.

- Once the net faradic current is positive, hydrogen oxidation prevails over the reduction reactions. Because of oxidation reactions, the gaseous oxygen initially present in the electrode and GDL is completely consumed before being flushed out by the hydrogen front (Figure 4-25). The PtO^b surface coverage falls to zero. The faradic current resulting from the $PtOH^s$ reduction, which was lower than that resulting from the PtO^s reduction in the previous steps, becomes higher. Water concentration in the electrode decreases slowly since water production due to reduction of platinum oxides does not compensate anymore vapour diffusion through the membrane and the GDL. At the end of step 5, the net faradic current is governed by the passive part of the cell. It decreases progressively and becomes null ($t \sim 0.6$ s in Figure 4-24).

- 6. Only proton reduction reactions occur and the net faradic current is negative. This current is very low (less than 50 mA/cm²) but remains after hydrogen filled completely the anode compartment (see next page).

The evolution of the current density is similar to that described above in most of the segments. However, differences can appear locally:

- step 2 to 4 can be negligible, especially for the segments close to the hydrogen inlet and when the hydrogen injection flow rate is high (Figure 4-27). In such cases, the net faradic current becomes positive at once. Oxygen and platinum oxides are reduced while hydrogen oxidizes simultaneously, as described in step 5.

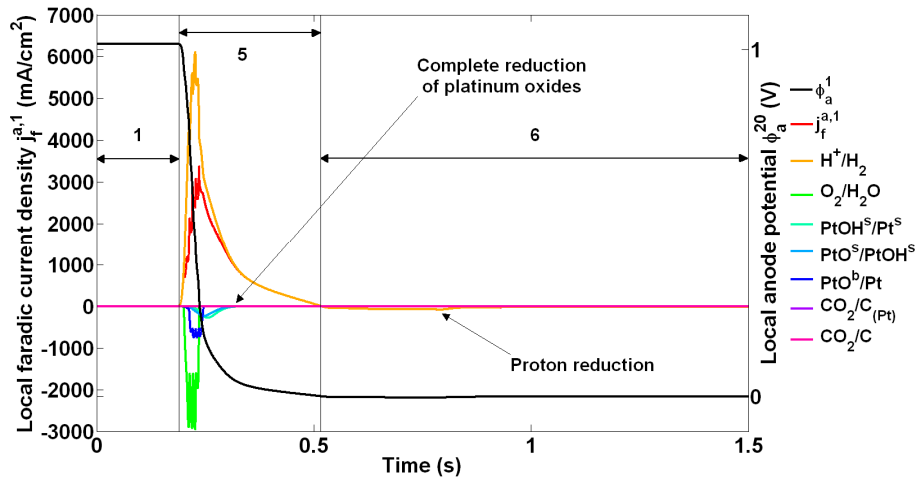


Figure 4-27. Anode faradic currents in segment 1 during a start-up by injection of hydrogen in air. Hydrogen front velocity set to 0.5 m/s. Forward currents are counted positively.

- The complete consumption of oxygen can occur before step 5. For instance, oxygen can be completely consumed in the segments close to the hydrogen outlet, before the hydrogen front reaches them, (i.e: during step 2). If not entirely consumed before or during step 5, oxygen is then removed by hydrogen flow.

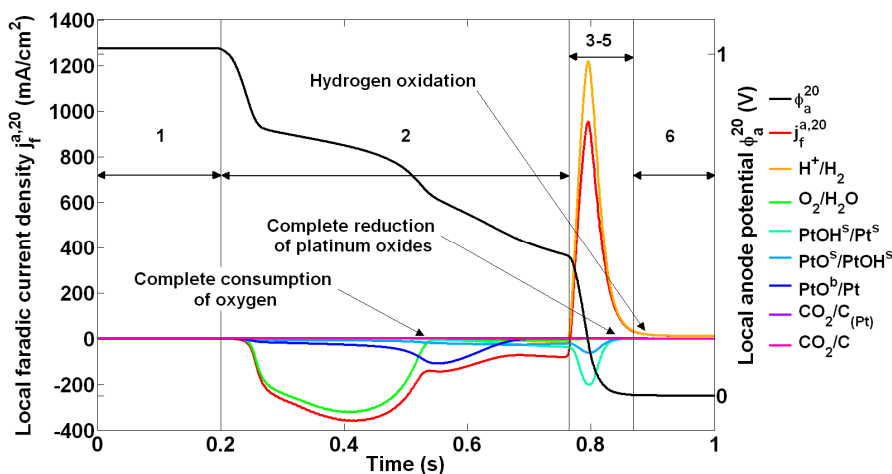


Figure 4-28. Anode faradic currents in segment 20 during a start-up by injection of hydrogen in air. Hydrogen front velocity set to 0.5 m/s. Forward currents are counted positively.

- The very low faradic current remaining in step 6 is necessary for the reduction of the platinum oxide gradient created in the cathode catalyst layer during start-up. It depends therefore on the state of the platinum particles in the cathode. If the oxide coverage is low (which concerns the segments close to the hydrogen inlet, Figure 4-34), reduction will take place at the anode so that oxidation reaction can occur in the cathode (Figure 4-27). On the contrary, if the oxide coverage is high (which concerns the segment close to the hydrogen outlet, Figure 4-34), oxidation reactions will take place in the anode so that reduction reactions can occur in the cathode (Figure 4-28).
- Step 6 depends on the location of the segments. Close to the hydrogen outlet, the net faradic current is positive and corresponds mainly to hydrogen oxidation (Figure 4-28). On the contrary, close to the hydrogen inlet, the net faradic current is negative and corresponds to proton reduction (Figure 4-27). Hydrogen being always oxidized during step 5 (i.e: positive faradic current), step 6 can be easily detected for the segments close to the hydrogen inlet because hydrogen stops to oxidize and protons start to reduce (Figure 4-27). However this transition cannot be well identified for the segments close to the hydrogen outlet since there is not such a transition (Figure 4-28). The positioning of the step 6 for these segments is therefore only indicative.

❖ Cathode reactions

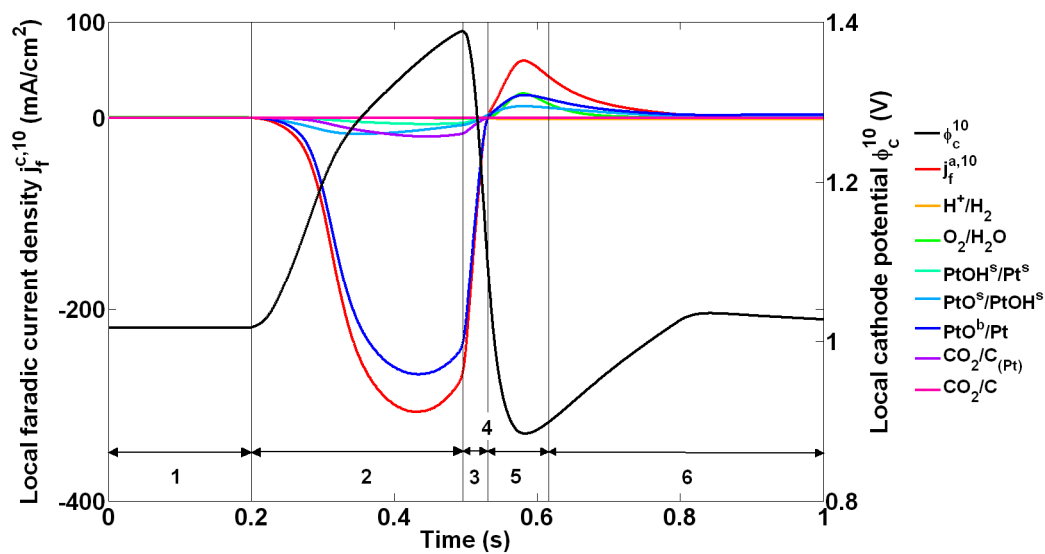


Figure 4-29. Cathode faradic currents in segment 10 during a start-up by injection of hydrogen in air. Hydrogen front velocity set to 0.5 m/s. Forward currents are counted positively.

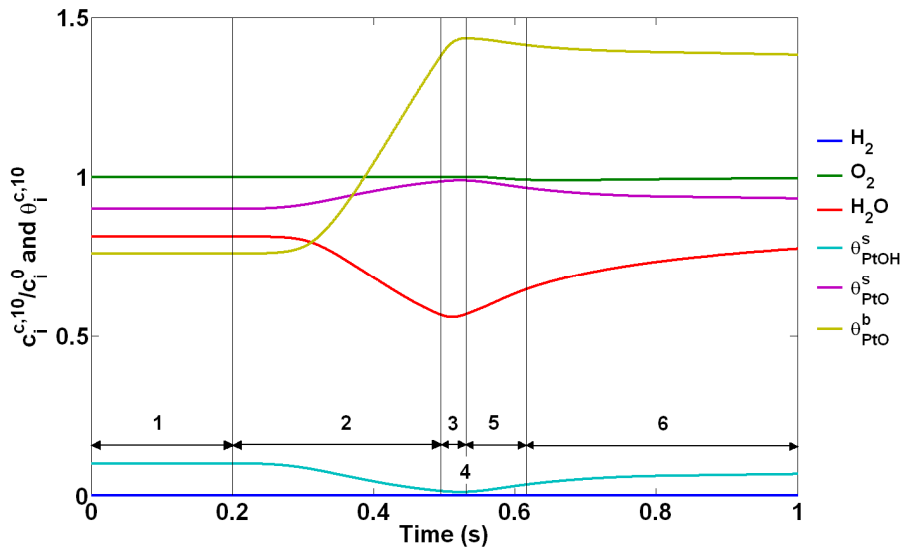


Figure 4-30. Surface coverages and gas concentrations at the cathode by reference to the standard conditions. Segment 10, start-up by injection of hydrogen in air. Hydrogen front velocity set to 0.5 m/s.

According to Figure 4-29 and Figure 4-30, several steps can be identified in the cathode of segment 10 during a start-up:

1. Initial conditions are identical at the anode and at the cathode (both were initially filled with air). On the surface of the particles, platinum is completely oxidized either under the form of PtOHs (about 10% of the platinum oxides) or PtOs (90% of the platinum oxides). These values were obtained by numerical simulation (fuel cell at OCV and both electrodes filled with air).
2. Segment 10 is in the passive region of the cell. The local cathode potential ϕ_c^{10} increases, which enables the oxidation reactions and in particular the formation of PtO^b. Due to the increase of ϕ_c^{10} up to 1.4V, $\theta_{PtO^b}^{c,10}$ reaches almost 1.5, which means that a second sublayer begins to oxidize. In parallel, the small fraction of PtOH^s on the particles surface reacts to form PtO^s. At the end of step 2, PtO^s covers almost all the particle surface: $\theta_{PtO^s}^{c,10} \approx 1$ and $\theta_{PtOH^s}^{c,10} \approx 0$. These reactions consume water, which induces the decrease of the vapour concentration. It must also be noted that carbon oxidation occurs mainly during step 2 when the local cathode potential increases (Figure 4-31). This oxidation results almost exclusively from a catalysed mechanism as described by reaction (4-18). However the current involved remains limited (a few tenths of mA/cm²).

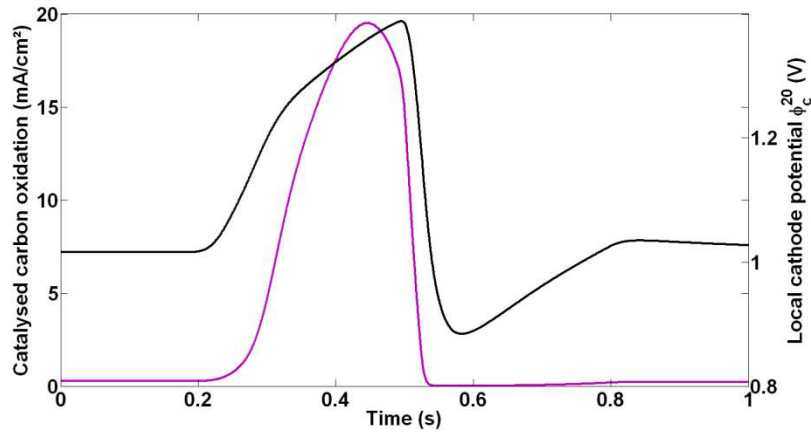


Figure 4-31. Catalysed carbon oxidation in segment 10 of the cathode during a start-up by injection of hydrogen in air. Hydrogen front velocity set to 0.5 m/s.

3. As soon as hydrogen starts to oxidize in the anode compartment, the net faradic current $j_f^{c,10}$ increases. In the cathode, the local cathode potential ϕ_c^{10} drops, which slows down platinum oxidations and even induces some PtO^s reduction. For a short time, $\theta_{\text{PtO}^b}^{c,10}$ continues to increase while $\theta_{\text{PtO}^s}^{c,10}$ decreases (which leads to an increase of $\theta_{\text{PtOH}^s}^{c,10}$). During step 3, oxygen starts also to reduce. Some hydrogen permeates through the membrane and oxidize in the cathode. However, this oxidation represents only a few mA/cm², which is completely negligible.
4. When oxygen and PtO^s reduction compensate platinum oxidation in the bulk (i.e: the formation of PtO^b), the net faradic current becomes null (Figure 4-32). Although the anode and cathode internal currents become necessarily null simultaneously, the anode and cathode net faradic currents become null at different times (Figure 4-26 and Figure 4-33).

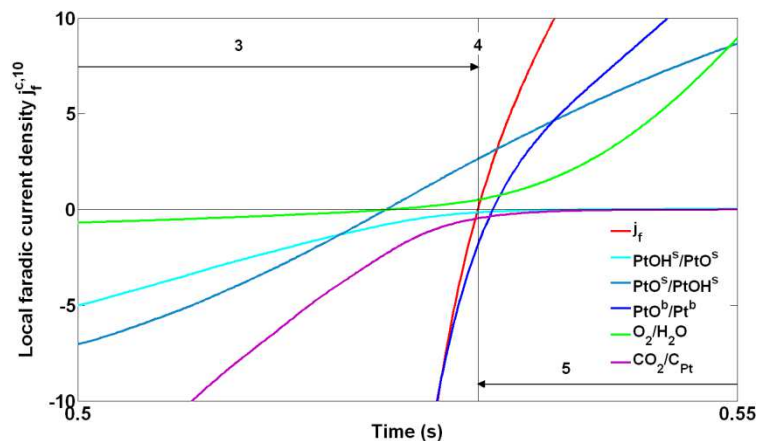


Figure 4-32. Faradic currents during step 4 (when the net faradic current $j_f^{c,10}$ becomes null) in the cathode of segment 10. Hydrogen front velocity set to 0.5 m/s.

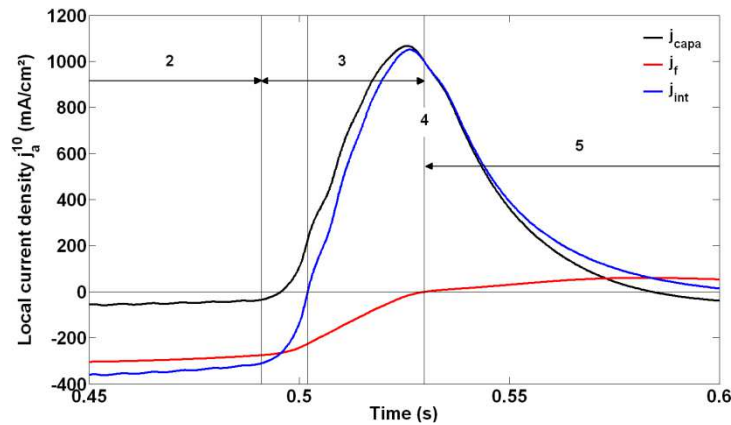


Figure 4-33. Capacitive, faradic and internal current densities between step 2 and 5 (i.e: when they change successively from negative to positive) in the cathode of segment 10. Hydrogen front velocity set to 0.5 m/s.

5. The net faradic current becomes positive. Hydrogen flowing in the anode compartment induces a local drop of the cathode potential, which is sufficient to start reducing PtO^b . The contribution of this reaction to the net faradic current is one of the most important with oxygen reduction. $\theta_{\text{PtO}^b}^{c,10}$ and $\theta_{\text{PtO}^s}^{c,10}$ decrease while $\theta_{\text{PtOH}^s}^{c,10}$ increases. Because of the reduction of oxygen and platinum oxides, the water vapour concentration increases.
6. During start-up, platinum oxides gradients appear between the hydrogen inlet and outlet: an excess of platinum oxides is formed in the segments which remain passive the longest time (Figure 4-34). At the end of the start-up procedure, the amount of platinum oxides homogenizes along the cell (i.e: platinum oxides gradients decrease). This results in very low and positive currents in segment 10. However, the sign of the homogenisation currents depends actually on the location of the segments. Platinum oxides in segments close to the hydrogen outlet need to be reduced since they are in excess compared to the local average amount of platinum oxides in the cathode segments. This results in positive currents (Figure 4-35). On the contrary, the platinum oxides in the segments close to the hydrogen inlet oxidize, which creates negative currents (Figure 4-36). In Figure 4-34, one can also observe that the PtOH^s and PtO^s gradients are reduced much faster than the PtO^b gradient.

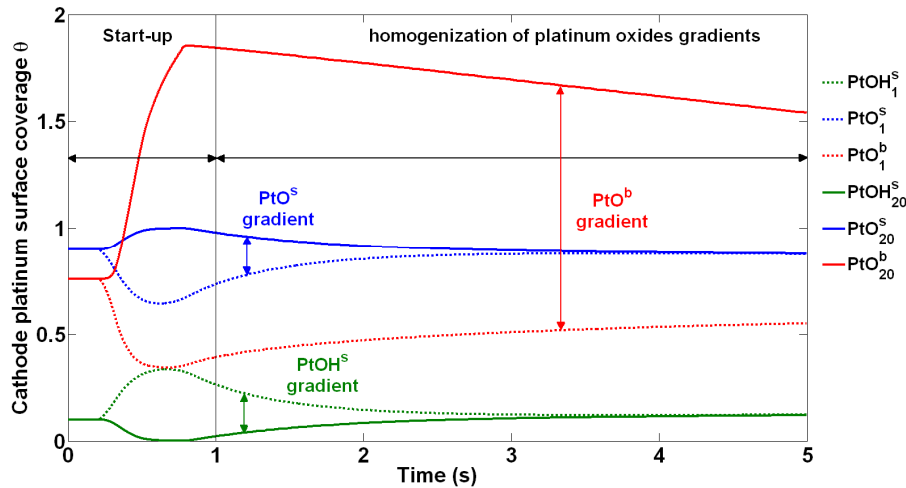


Figure 4-34. Time evolution of the cathode platinum surface coverages $\theta_{PtOH^s}^c$, $\theta_{PtO^s}^c$ and $\theta_{PtO^b}^c$ in segment 1 and 20 during a start-up by injection of hydrogen in air. Hydrogen front velocity set to 0.5 m/s.

Although the evolution of the faradic currents in most of the segments is similar to that described above (segment 10), some differences can emerge:

- Before the end of step 2 and close to the hydrogen outlet, once platinum on the surface of the particles completely oxidized into PtO^s , further oxidation can then only take place in the bulk (Figure 4-35).

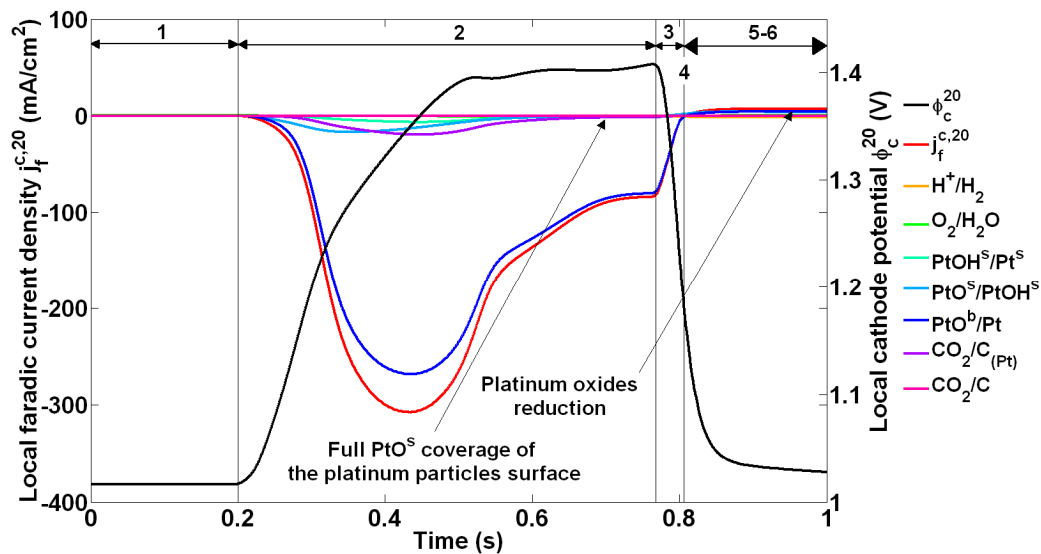


Figure 4-35. Cathode faradic currents in segment 20 during a start-up by injection of hydrogen in air. Hydrogen front velocity set to 0.5 m/s. Forward currents are counted positively.

- Step 2 to 4 can be negligible due to the rapid progression of the hydrogen front in the anode. This happens in the closest segments from the hydrogen inlet, which become immediately active once hydrogen is introduced in the anode compartment: oxygen and platinum oxides reduce at once as in step 5 (Figure 4-36).

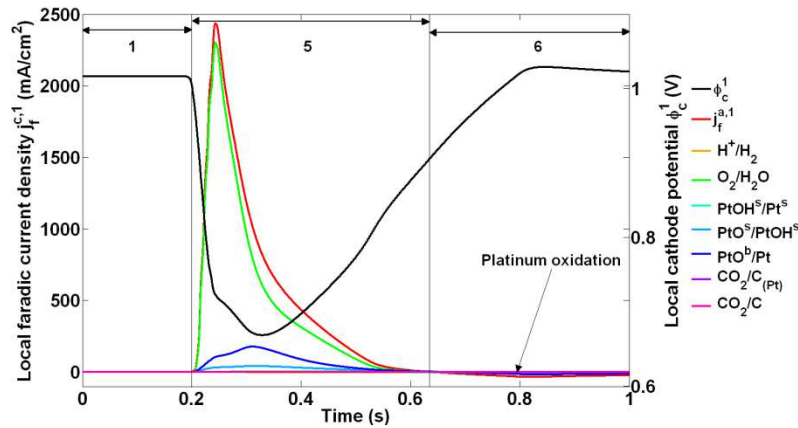


Figure 4-36. Cathode faradic currents in segment 1 during a start-up by injection of hydrogen in air. Hydrogen front velocity set to 0.5 m/s. Forward currents are counted positively.

- The amount of carbon which oxidizes through non-catalysed (4-17) and catalysed (4-18) reactions depends on the location of the segments. Figure 4-37 and Figure 4-38 show that more carbon oxidizes in those which remain passive the longest time. This result is in good agreement with the measurements realised by Kreitmeier et al. [109] presented in Figure 4-39. During all the simulation, 3.9×10^{-3} C/cm² or 0.16 $\mu\text{g}/\text{cm}^2$ of carbon is oxidized through the catalysed reaction. This is less than the experimental value (0.22 $\mu\text{g}/\text{cm}^2$) but of the same order of magnitude. One can also see that non-catalysed carbon oxidation is negligible compared to catalysed carbon oxidation. Finally, the model confirms that the currents resulting from these two reactions represent only a very small fraction of the faradic currents involved in the cathode.

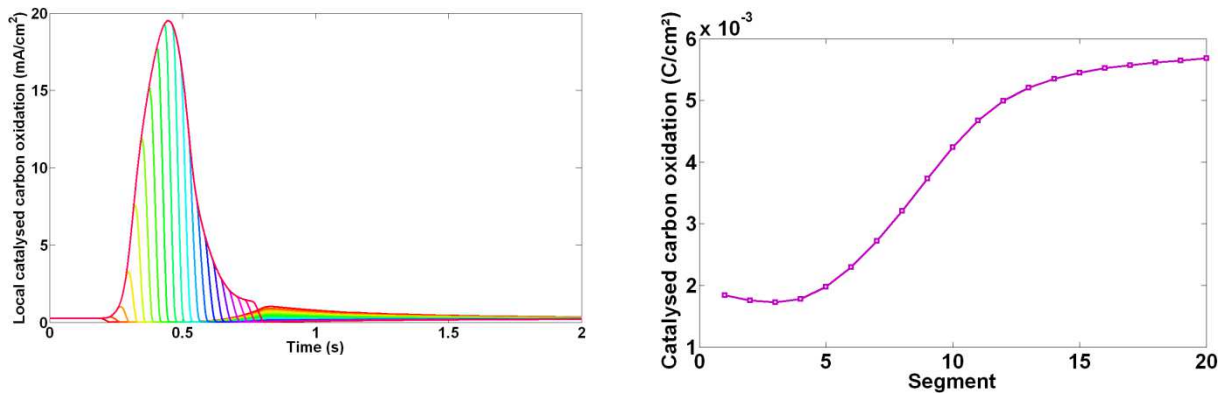


Figure 4-37. Local currents (left) resulting from catalysed carbon oxidation in the cathode during a start-up by injection of hydrogen in air and corresponding charge per segment (right). Hydrogen front velocity set to 0.5 m/s.

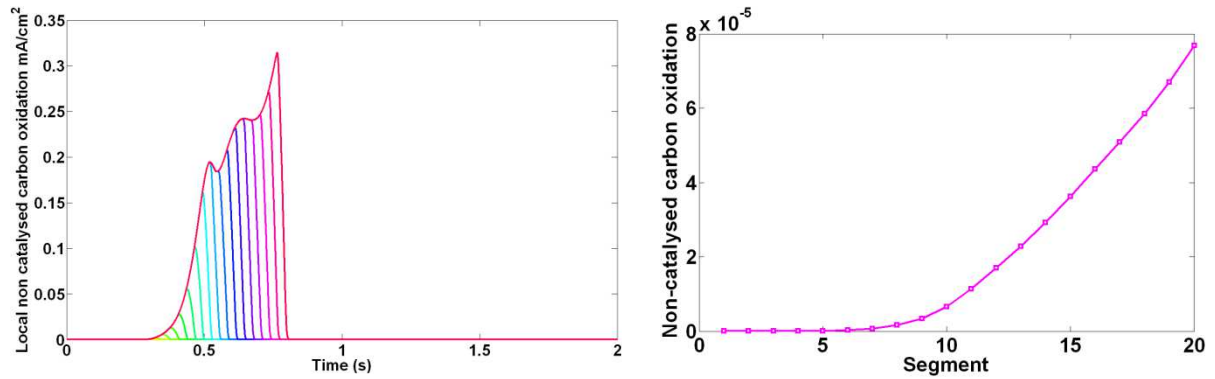


Figure 4-38. Local currents (left) resulting from non-catalysed carbon oxidation in the cathode during a start-up by injection of hydrogen in air and corresponding charge per segment (right). Hydrogen front velocity set to 0.5 m/s.

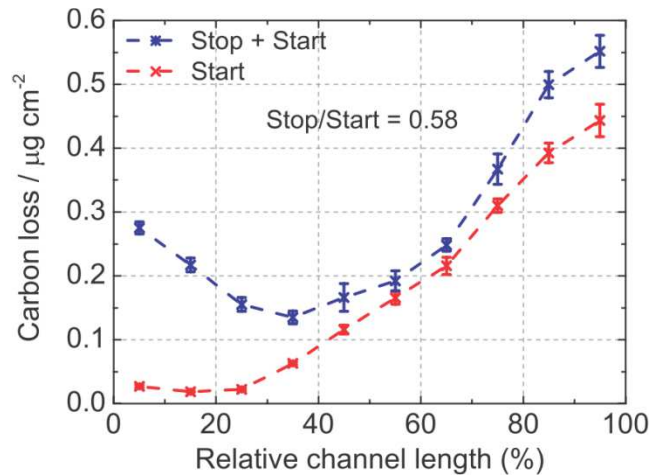


Figure 4-39. Local carbon losses per start/stop determined experimentally at 80°C. Ambient pressure, 70% RH and nominal anode gas velocity of 0.6 m/s [109].

- A PtOH^s gradient develops in the cathode during start-up, between the hydrogen inlet and outlet. At the end of start-up, this heterogeneous amount of platinum oxides along the cathode needs to be homogenized. PtOH^s, in excess in the segments which remained active the longest time (Figure 4-34), reduces according to reaction (4-3) or (4-18), which results in carbon oxidation. In the segments close to the hydrogen outlet, the reduction of PtOHs according to reaction (4-18) is much slower. Therefore, a reaction rate gradient appears for catalysed carbon oxidation (for instance between segment 1 and 20 in Figure 4-40). This gradient remains as long as the PtOH^s surface coverage is not homogeneous along the cathode. The CO₂ emissions which were measured in §2.5 after that start-up finished could be explained by this mechanism.

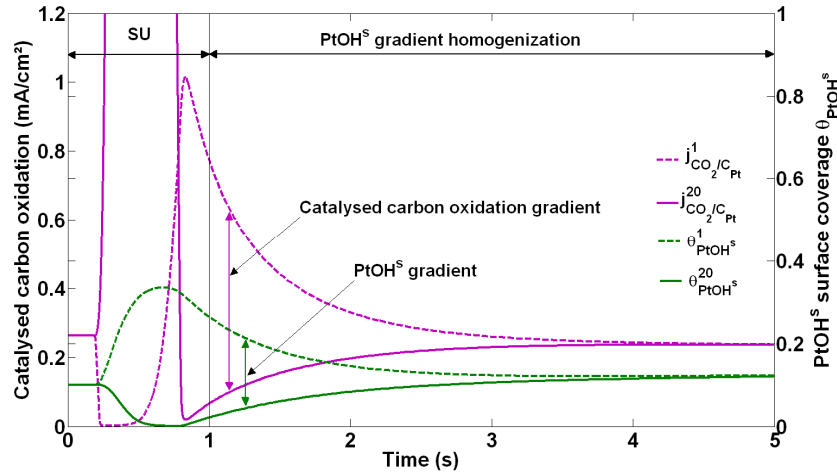


Figure 4-40. Catalysed carbon oxidation and PtOHs surface coverage θ_{PtOH^s} in segment 1 and 20 during a start-up by injection of hydrogen in air. Hydrogen front velocity set to 0.5 m/s.

ii Potential evolution

In this section, local potentials obtained by numerical simulation are compared to those measured experimentally with the cell equipped with local Reference Hydrogen Electrodes (§0). Initially, air is present in both electrodes, which results in $\phi_a^n = \phi_c^n = E_{\text{O}_2/\text{H}_2\text{O}}$. In Figure 4-41, when hydrogen is injected, the experimental and simulated anode potentials of the first segments $\phi_a^{n, x_n \leq x_f}$ (with x_n and x_f the position of the n^{th} segment and that of the front respectively) decrease rapidly due to the presence of hydrogen. The anode potential in the segments located downstream $\phi_a^{n, x_n > x_f}$ decrease also since reduction reactions are initiated by the oxidation reaction in the upstream part of the anode compartment. However the decrease of these potentials is much slower than in the first segments: $\phi_a^{n, x_n \leq x_f} < \phi_a^{n, x_n > x_f}$.

Similarly to the internal currents, the experimental potentials are not so well separated from each other as in the simulation. This could be due to the replacement of air, which must be fast to achieve a satisfying numerical solution. In practice however, this replacement may be more progressive which could results in the simultaneous activation of several segments.

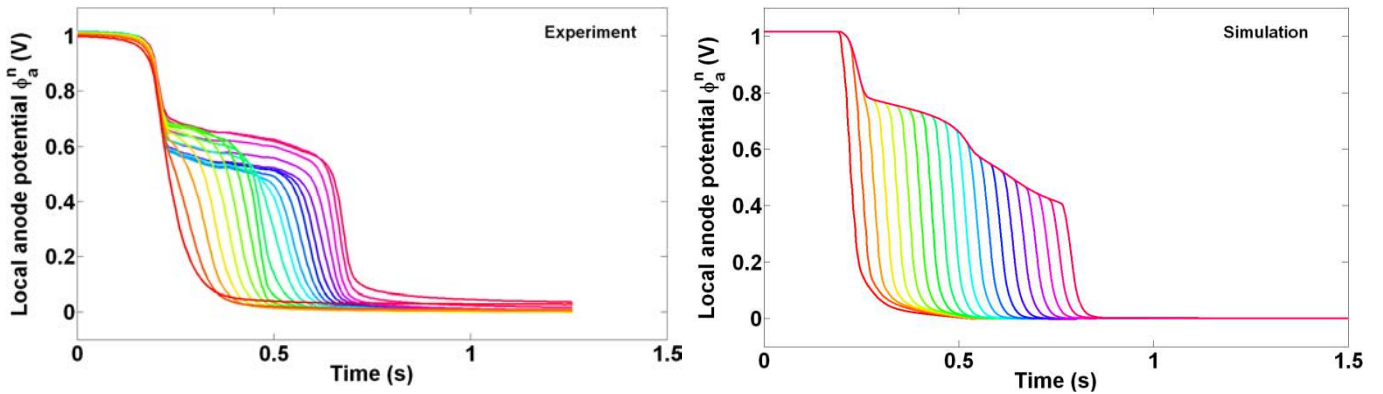


Figure 4-41. Time evolution of the experimental (left) and simulated (right) local anode potentials ϕ_a^n during a start-up by injection of hydrogen in air. Hydrogen front velocity set to 0.5 m/s.

In the cathode, the experimental and numerical potential profiles are close to each other (Figure 4-42). Logically, the potentials evolve differently depending on the location: in the active part ($x_n \leq x_f$), the potential $\phi_c^{n, x_n \leq x_f}$ decreases with time while in the passive part ($x_n > x_f$), $\phi_c^{n, x_n > x_f}$ increases. As a consequence, $\phi_c^{n, x_n \leq x_f} < \phi_c^{n, x_n > x_f}$.

However, the maximal cathode potential value reached in segment 20 was higher in the experiment (about 1.5V) than in the numerical simulation (about 1.4V). According to the model, the conditions are less oxidizing in the passive part of the cell than in the experiment. This leads probably leads to the underestimation of carbon oxidation (Figure 4-37 and Figure 4-38).

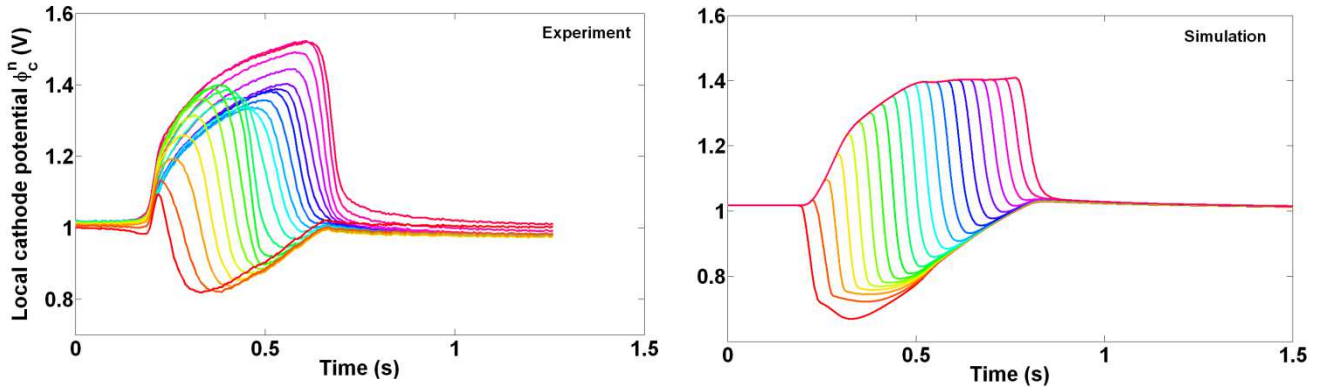


Figure 4-42. Time evolution of the experimental (left) and simulated (right) local cathode potentials ϕ_c^n during a start-up by injection of hydrogen in air. Hydrogen front velocity set to 0.5 m/s.

The time evolution of the anode and cathode potentials are also in good agreement with those observed by Shen et al. [101] (§2.1.2, Figure 2-15 and Figure 2-17). In addition, Shen et al. also represented the electrolyte potential difference between the active and passive parts: $V_e^{up} - V_e^{down}$. Figure 4-43 shows this difference between the first and last segment supplied with hydrogen. Both numerical and experimental (segmented cell equipped with local RHE, §0) results are presented.

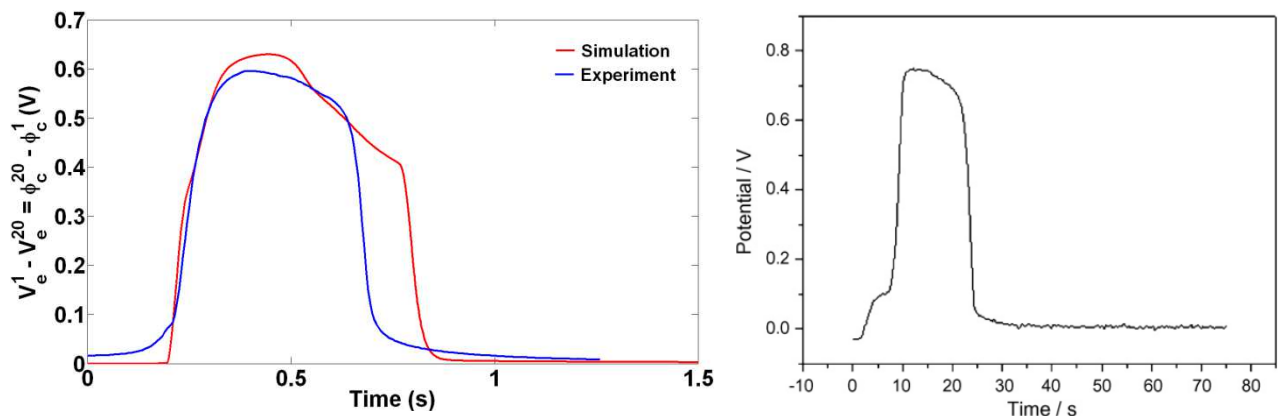


Figure 4-43. Left: Simulation (red) and experimental measurement (blue) of the potential difference between the electrolyte potential in the upstream part V_e^1 and downstream part V_e^{20} parts of a cell during a start-up by injection of hydrogen in air. Hydrogen front velocity set to 0.5 m/s. Right: Electrolyte potentials difference $V_{e,up} - V_{e,down}$ between the upper and lower part of the cell developed by Shen et al. [101] during a start-up in air @ 0.12 slph.

The electrolyte potentials difference presented in Figure 4-43 is a marker of the extent at which internal currents take place during a start-up: the higher and the longer it lasts, the more charges are exchanged between the active and passive parts of the cell. One can see that the experimental and numerical maximum values are close to each other. The maximum value reached in the experiment of Shen et al. is higher than ours but the cell and the conditions (especially the hydrogen front velocity) were also different. However, the evolutions of the potential difference are similar. The simulation does not reproduce perfectly the slow decrease of the potential following the maximum value. The sudden decrease at the end of the start-up occurs also earlier in the experiment than in the numerical simulation. Therefore, the model may overestimate internal currents at the end of the start-up and more specifically during the homogenisation of the platinum oxides through the cathode catalyst layer.

iii Influence of hydrogen flow rate

The numerical simulation enables to distinguish between the contribution of carbon oxidation and other faradic and capacitive contributions to the internal currents during start-ups realised using different hydrogen front velocities.

Figure 4-44 shows that for a hydrogen injection velocity of 0.5 m/s, the faradic reactions represents approximately 5/6th of the total charge exchanged. When the hydrogen injection velocity increases up to 3 m/s, the faradic reactions decrease and they contribute only to half of the total charge exchanged. Oxidation of platinum in the bulk remains the main reaction. PtOH oxidation and catalysed carbon oxidation also participate but to a much smaller extent. Other reactions are negligible. One can also notice that the capacitive contribution to the total charge exchanged increases slightly with the hydrogen injection flow rate.

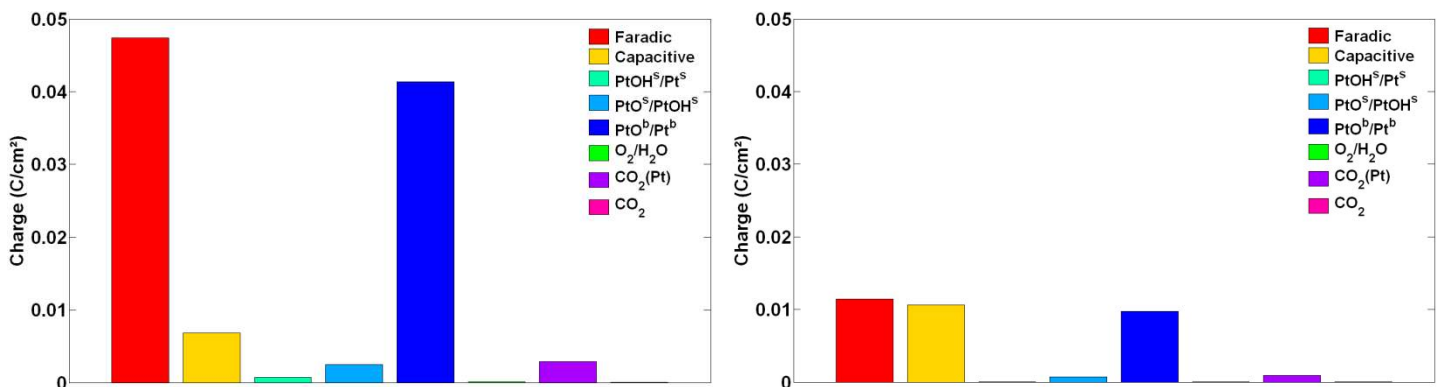


Figure 4-44. Faradic and capacitive contributions to the total charge exchanged in the cathode during a start-up by injection of hydrogen in air at 0.5 m/s (left) and 3 m/s (right).

In chapter 2 (§2.5), carbon dioxide emissions were higher when hydrogen was injected slowly in the anode compartment. In Figure 4-45, the catalysed and non-catalysed carbon oxidation decrease with the hydrogen front velocity. Most of the carbon oxidized is catalysed. The non-catalysed carbon oxidation is negligible except for the lowest hydrogen flow rates and its contribution remains always very low.

While the results of the simulation fit relatively well the experimental values at low hydrogen injection velocities, they underestimate them when the hydrogen flow rate increases. This may be related to the cathode potential, which appears to be lower in the simulation than in the experiment (§4.2.3.a.ii). Moreover, carbon oxidation resulting from possible internal

currents between land and channel is not taken into account in the model. At high hydrogen injection flow rate, this contribution to the carbon dioxide emissions could become more significant (especially in a cell such as our, with straight parallel channels). Indeed, the time needed by hydrogen to diffuse under the channels becomes of the same order of magnitude as the time hydrogen needs to fill the channels from one end to the other.

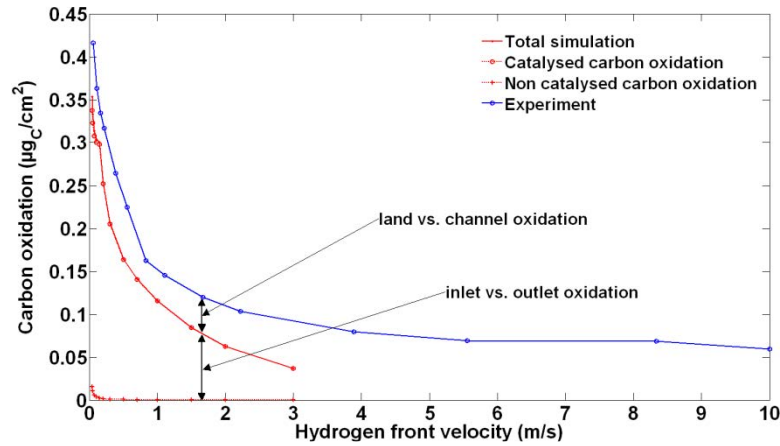


Figure 4-45. Carbon oxidation per start-up depending on the hydrogen front velocity.

b. Simulation of a start-up by injection of hydrogen in nitrogen

When nitrogen is used to flush the anode compartment, one observes that the cell voltage decreases once hydrogen is completely removed. This evolution results from oxygen permeation through the membrane, from the cathode to the anode. When oxygen reaches the anode, it reacts with platinum to form platinum oxides. This progressive oxidation leads to the increase of the potential of the anode, which approaches that of the cathode (i.e: the cell voltage stabilizes at about 0.1V). Indeed, due to the absence of oxygen in the anode compartment (apart from that which permeates), the mixed equilibrium potentials in both electrodes cannot be equal. At the beginning of the numerical simulation presented hereafter, the platinum oxide surface coverage is complete (this result was obtained by numerical simulation of a cell in open circuit, with both electrodes filled with air). 20% of this coverage is due to PtOH^{s} and 80% is due to PtO^{s} . About 40% of bulk platinum is also oxidized. The simulation consists in starting-up the cell by injecting hydrogen in nitrogen. The hydrogen injection velocity is set to 0.5 m/s, similarly to the protocol used for the numerical simulation of a start-up in air.

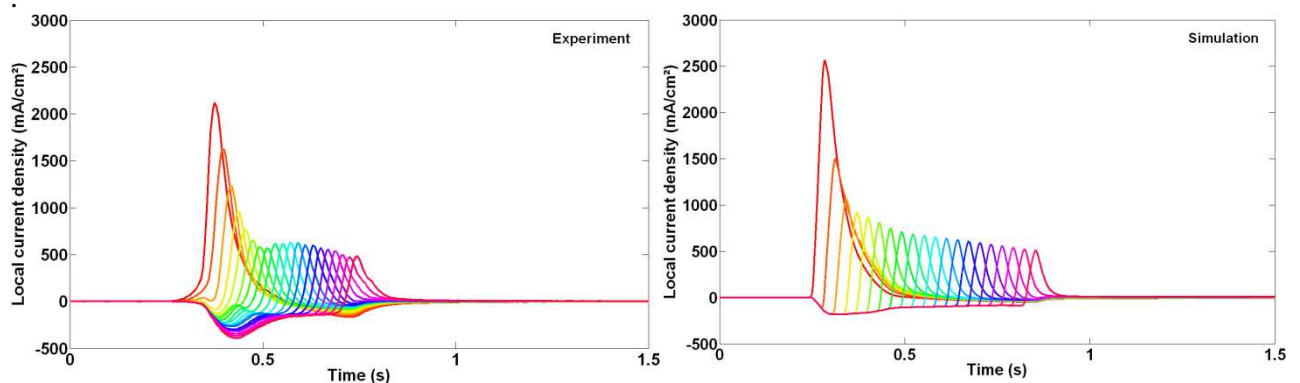


Figure 4-46. Experimental (left) and simulated (right) internal currents during a start-up by injection of hydrogen in nitrogen. Hydrogen front velocity set to 0.5 m/s.

Some improvements are still required to model the reverse currents, which appear significantly lower than the experimental values (Figure 4-46). Values of the kinetic parameters may not be optimal or some reaction mechanisms may have been forgotten. Figure 4-46 also shows that the experimental start-up characteristic time appears slightly shorter than in the numerical simulation. This tends to accentuate the intensity of the experimental reverse currents (and therefore to reduce the difference between numerical and experimental results).

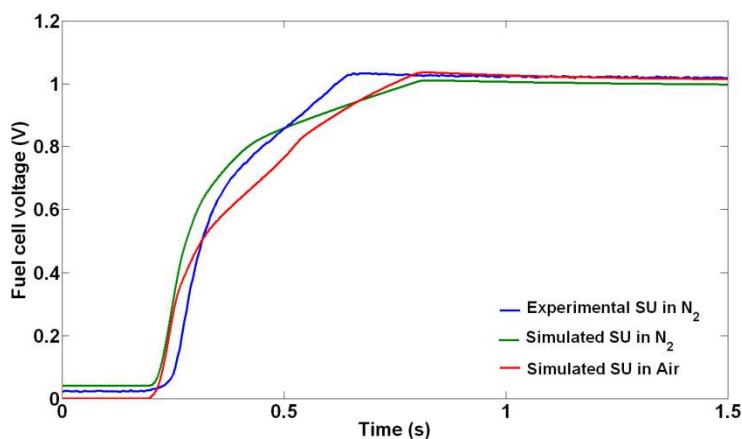


Figure 4-47. Numerical simulation of fuel cell voltage during a start-up by injection of hydrogen in air (red) and in nitrogen (green). In blue: experimental fuel cell voltage during a start-up by injection of hydrogen in nitrogen. Hydrogen front velocity set to 0.5 m/s.

The detail of the different faradic contributions in the anode of segment 10 during a start-up by injection of hydrogen in nitrogen (Figure 4-48) allows the identification of the same steps as during a start-up in air (Figure 4-24). However, the current densities involved are much lower. For instance, hydrogen oxydation is only of about 1.2 A/cm² with nitrogen while it exceeds 2 A/cm² with air. The main explanation for this evolution is the absence of oxygen reduction in the anode compartment during step 2, when the segment is passive. The only reduction reaction is that of platinum oxides.

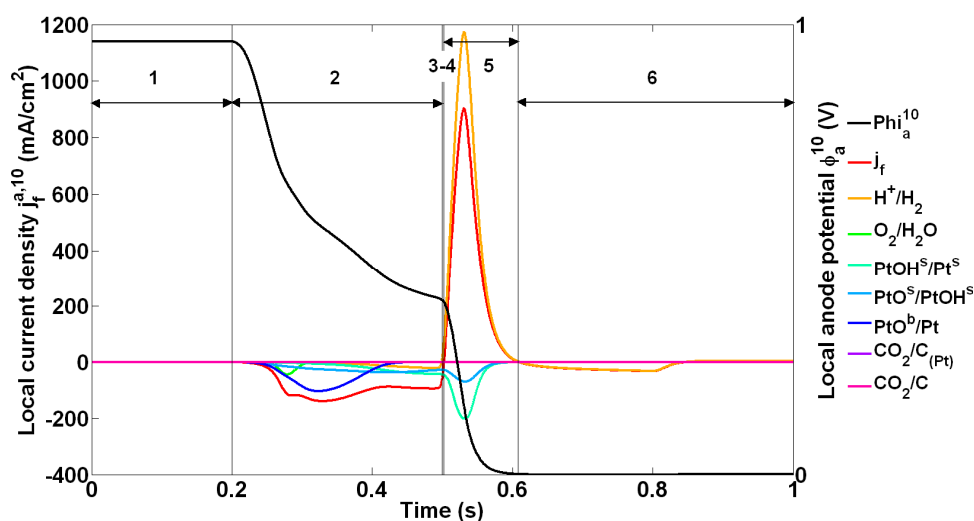


Figure 4-48. Anode faradic currents in segment 10 during a start-up by injection of hydrogen in nitrogen. Hydrogen front velocity set to 0.5 m/s. Forward currents are counted positively.

The same steps as those observed during a start-up in air can be observed in the cathode of segment 10 (Figure 4-49). Contrary to the anode side, all the reactions taking place during a start-up in air also occur during a start-up in nitrogen. However, the current densities, governed by the reduction reactions in the anode side are much lower. For example, the PtO^b oxidation is approximately two times lower with nitrogen than with air during step 2 (Figure 4-29).

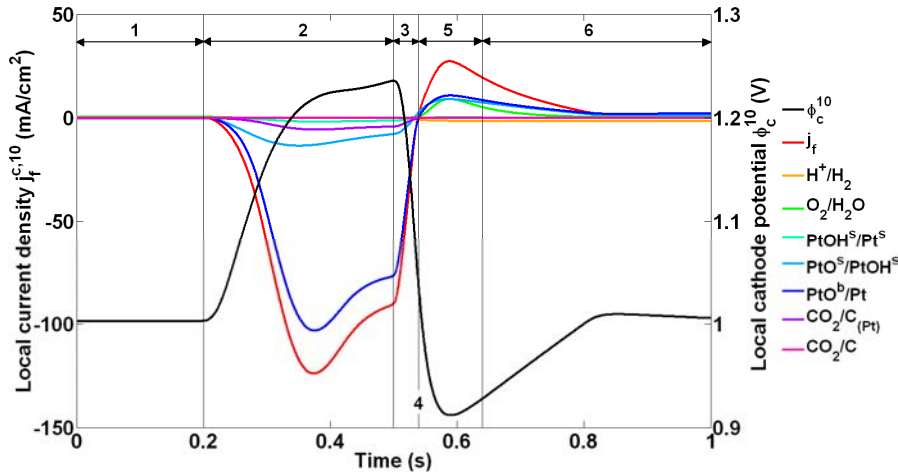


Figure 4-49. Cathode faradic currents in segment 10 during a start-up by injection of hydrogen in nitrogen. Hydrogen front velocity set to 0.5 m/s. Forward currents are counted positively.

Similarly, the currents induced by the catalysed carbon oxidation are much more limited with nitrogen than with air (Figure 4-50). The difference is obvious in the segments close to the hydrogen outlet while there is no significant impact close to the hydrogen inlet (where carbon oxidation is much lower). This explains the small impact of start-ups in nitrogen on the degradation rate of the electrode carbon support observed in §2.5.

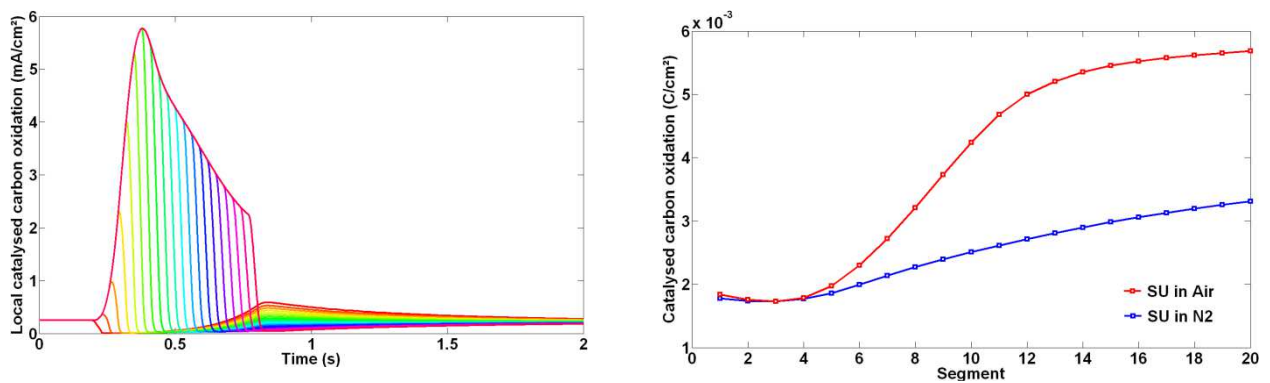


Figure 4-50. Local currents (left) resulting from the catalysed carbon oxidation in the cathode during a start-up by injection of hydrogen in nitrogen and corresponding charge per segment (right).

This lower carbon oxidation could also be explained by the local cathode potentials. Indeed, they remain below 1.3V, which is lower than the values reached during a start-up in air: in Figure 4-42, the cathode potentials of the segment near the hydrogen outlet were above 1.4V. Compared to start-ups in air, the anode potentials of the segments close to the hydrogen outlet decrease faster because no oxygen is present to maintain the potential high (Figure 4-51).

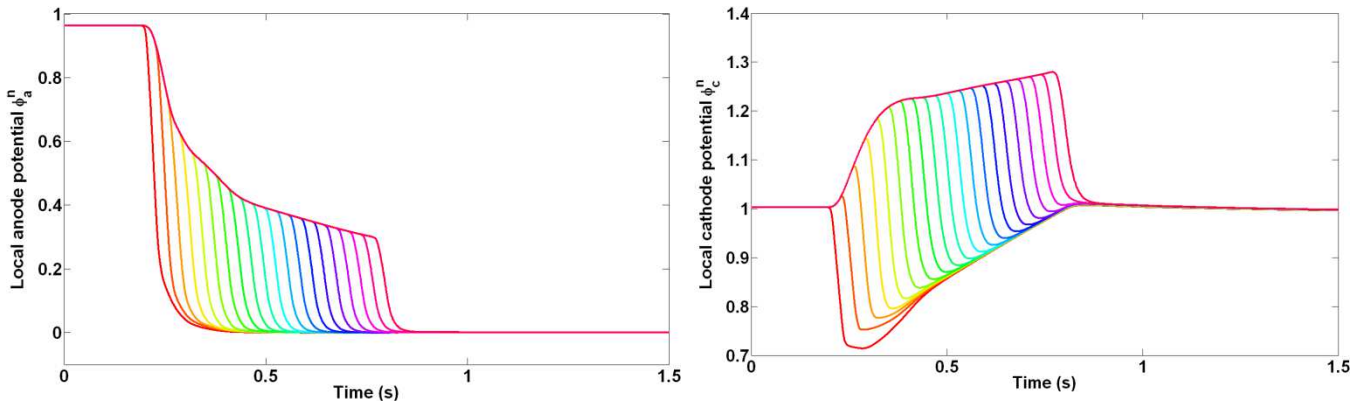


Figure 4-51. Local anode ϕ_a^n (left) and cathode ϕ_c^n (right) potentials during a start-up by injection of hydrogen in nitrogen. Hydrogen front velocity set to 0.5 m/s.

The difference between the electrolyte potential in the upstream and downstream parts of the cell is significantly lower when start-ups are performed in nitrogen than in air (Figure 4-52). This result is consistent with the difference in charge exchanged.

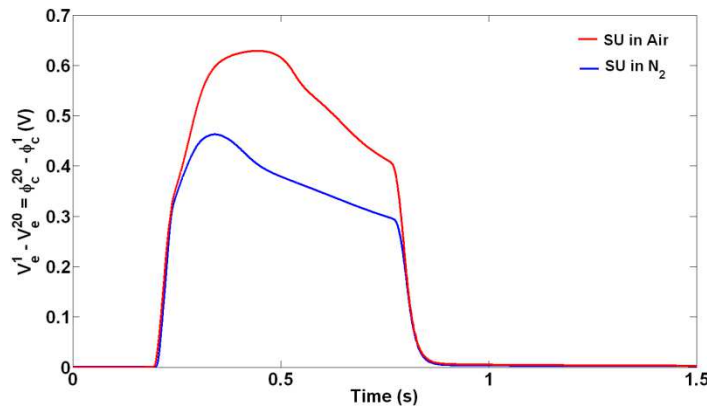


Figure 4-52. Potential difference between the electrolyte potential in the upstream V_e^1 and downstream V_e^{20} parts of a cell during a start-up by injection of hydrogen in nitrogen (blue) and in air (red). Hydrogen front velocity set to 0.5 m/s.

4.3. Conclusion

A high number of phenomena take place simultaneously during start-ups. A part of them consists in electrochemical reactions which are relatively simple to assess while others are more complex. In the active region, the forward currents are mainly produced by hydrogen oxidation in the anode and oxygen reduction in the cathode, as during regular operation. However, one cannot exclude a priori that other redox reactions also occur. In the passive region, the origin of most of the reverse currents remains unidentified, as shown in chapter 2: carbon oxidation was evidenced in the cathode but it was also demonstrated that its contribution is responsible for 10% at best of the reverse currents. Similarly, oxygen reduction is probably not the only contribution to the reverse currents in the anode, especially when start-ups are performed in nitrogen.

The main objective of this chapter was to identify the different contributions to the internal currents, including those which could not be assessed experimentally (in the previous chapters). Therefore, numerical simulations of start-ups were performed. The model considers several electrochemical reactions and takes the capacitive effects as well as the mass transport losses (in the direction perpendicular to the MEA) into account. The kinetic parameters of the electrochemical reactions were estimated starting from polarization curves and cyclic voltammetry.

With the chosen values of the parameters, the simulation of start-ups by injection of hydrogen in air showed that redox reactions involving platinum could explain most of the charge exchanged at the cathode. Platinum oxidation in the bulk represented the main contribution but catalysed carbon oxidation was also significant. The simulations also indicated that a platinum oxide gradient was created in the cathode between the hydrogen inlet and outlet. At the end of the start-up sequence, this gradient homogenizes, which involves carbon oxidation, possibly with additional damages.

The faradic contribution to the charge exchanged appeared to be sensitive to the hydrogen injection flow rate. The higher the hydrogen injection flow rate, the more the capacitive contribution prevailed over the faradic one. This explains why lower damages were observed in chapter 3 when the hydrogen was injected at high velocity to start the cell.

Simulation of start-ups by injection of hydrogen in nitrogen showed that the charge exchanged in the anode results almost entirely from platinum oxide reduction: in this case, the internal currents depend mainly on the anode platinum loading. In addition to platinum oxide reductions, oxygen could also reduce when start-ups were simulated by injecting hydrogen in air. The internal currents were then less limited. Like for start-ups by injection of hydrogen in nitrogen, the reactions in the passive part of the anode can therefore determine the extent of the internal currents.

Further simulations remain still to perform. A sensitivity analysis should determine the influence of each of the parameters on the internal currents. For instance, this can be used to confirm the results obtained with the different Ion Power MEA and to help tuning a MEA to mitigate degradations induced by start-ups. Simulations of shut-downs should also be realised to check whether they damage effectively less the cell than start-ups.

Finally, the model used in this chapter can be improved. Platinum dissolution was not considered since its kinetic could not be assessed. In addition, the reactions considered were taken from the literature. Others may not have been identified yet, like the oxidation of oxygen surface groups on carbon. Finally, the mass transport losses were simplified to make easier the resolution. Refinements are possible but at the expense of the calculation time.

5 Conclusions and Perspectives

Durability remains one of the main issues for commercial release of PEMFC. The objective of this Ph.D thesis was to contribute to a better understanding of the mechanisms leading to the degradations occurring during fuel cell start-up and shut-down. These degradations are responsible for important performance decay and they limit strongly the lifetime of the cell.

Start-up consists in injecting hydrogen in the anode compartment initially filled with air or nitrogen. This operation is usually realised while the cell is in open circuit. Conversely, shut-downs were performed by flushing the anode compartment with air or nitrogen. During these events, it was evidenced that internal currents appeared within the cell. These currents could be measured using a specific cell with one of its current collectors segmented. We showed that there is no need to segment collectors on both sides since internal currents in anode and cathode were identical.

The study of single start-ups (and shut-downs) enabled to put forward three successive stages following the injection of hydrogen in the anode compartment (filled initially with air or nitrogen), with the occurrence of reverse, forward and balancing currents. Reiser et al. [98] associated the reverse currents appearing in the passive part of the cell (the part not yet in the presence of hydrogen at start-up, or already in contact with oxygen at shut-down) to degradations linked to carbon oxidation in the cathode catalyst layer. This interpretation was confirmed by measuring the local potentials along the gas channels using a segmented cell equipped with local Reference Hydrogen Electrodes. The local cathode potentials in the passive part of the cell reached values much higher than the open circuit voltage. These conditions are known to accelerate carbon corrosion and to contribute to other phenomena like long range or short range Ostwald ripening.

This segmented cell equipped with local Reference Hydrogen Electrodes opens up new possibilities. For instance, local anode and cathode diagnosis (EIS, polarization curves) can be performed separately during aging protocols. It will be used more systematically for future works and durability studies of a fuel cell operated in dead-end mode are under way.

Single start-ups and shut-downs were performed in various conditions. Carbon dioxide emissions in the cathode exhaust gases and charge exchanged (the integral over time of the reverse currents) showed similar evolutions. At the global scale, they increased with the residence time of hydrogen and air (or nitrogen) in the anode compartment. At the local scale, the charge exchanged was a function of the time a segment remained in the passive region. The comparison of our results with those of Kreitmeier et al. showed that the distribution of carbon dioxide emissions within the cathode (which they measured recently [109]) was close to that of the charge exchanged. Thus the charge exchanged can be considered as a local marker of the degradations resulting from start-ups or shut-downs.

Charge exchanged and CO₂ emissions resulting from start-ups performed by injection of hydrogen in nitrogen were lower than by injecting hydrogen in an air-filled anode compartment (at equivalent hydrogen injection velocity): when nitrogen fills initially the anode compartment, reduction reactions in the passive part of the anode are limited because of the absence of oxygen (except under the form of platinum oxides or due to crossover through the membrane).

CO₂ emissions and charge exchanged were also much lower during shut-downs than during start-ups. This was probably due to platinum in reduced form in the anode, which oxidized once air was injected.

In the framework of a partnership between the LEMTA and the LANL, we studied the influence of the MEA characteristics on their durability. The increase of the anode or cathode platinum loading resulted in higher charge exchanged; on the contrary, increasing the carbon specific surface of the cathode had no significant effect. However, regarding the impact of a change in the MEA characteristics, the charge exchanged cannot be considered as a marker of carbon oxidation: CO₂ emissions decreased for instance when the cathode platinum loading was higher, which suggests that platinum oxidation prevents carbon corrosion. On the contrary, higher CO₂ emissions were measured when the anode platinum loading and the cathode carbon specific surface were increased.

Aging protocols were also performed to assess the impact in the long term of the repeated start-ups and shut-downs. Monitoring of the cell voltage, local ECSA and current density confirmed the conclusions of the second chapter: the higher the charge exchanged (i.e. the longer oxygen remained in the anode compartment partially filled with hydrogen), the faster the performance decay. Nevertheless, modifications of the MEA characteristics leading to an increase of the charge exchanged did not always implied a lower durability: the lifetime of the MEA with a higher cathode platinum loading was the best although this MEA showed also the highest charge exchanged. This result confirmed that (reversible) platinum oxidation prevents carbon oxidation and -paradoxically- improves the fuel cell durability.

The results obtained in the second and third chapters show that the degradations can be mitigated by adjusting the operating conditions: increasing the gas injection flow rate, using nitrogen instead of air to flush the anode compartment. Another strategy consists in tuning the MEA characteristics by using lower anode platinum loading, lower carbon specific surface at the cathode, or higher cathode platinum loading. Nevertheless, further work is required to assess precisely the influence of the MEA characteristics on the degradations. New experiments are underway regarding the effect of the graphitization of the electrode carbon support, of the MPL or of the GDL thickness. Then, it should be possible to optimize the fuel cell lifetime by adjusting simultaneously all the MEA characteristics. Of course, this optimization work must consider cost issues as well as durability.

Post-mortem analyses of Paxitech MEA confirmed the non-uniform degradation between hydrogen inlet and outlet observed in-situ during the start-up aging protocols. The cathode catalyst layer underwent strong carbon oxidation and short and long Ostwald ripening. Interestingly, degradations were more pronounced under a land than under a channel. This result could be expected regarding the reverse currents measured under a land during start-ups by Schneider et al. [108]. Nevertheless, these channel/land heterogeneities were not systematically observed and their occurrence in the case of other and more common geometries (serpentine flow fields for instance) is still to be confirmed.

Finally, we showed in the second chapter that CO₂ emissions stood for 10% at most of the charge exchanged. A numerical model was thus developed with the objective to identify the other contributions and it seems that redox reactions involving platinum could be responsible for most of them. In addition, the numerical simulation enabled to detect the development of a platinum oxide gradients in the cathode catalyst layer, which homogenize at the end of the start-up. This homogenization process led (probably) to further degradations since it involves carbon oxidation. Eventually, this model will be used to test and to understand the effects of

mitigations techniques such as the connection of a dummy load or a supercapacitor to the cell during start-up. Such load connections were already realised experimentally by Didierjean et al. [130] and significant reductions of the reverse currents have been observed.

References

- [1] N. Garland, T. Benjamin, et J. Kopasz, « DOE Fuel Cell Program: Durability Technical Targets and Testing Protocols », *ECS Transactions*, vol. 11, p. 923–931, 2007.
- [2] R. O’Hayre, D. M. Barnett, et F. B. Prinz, « The Triple Phase Boundary », *Journal of The Electrochemical Society*, vol. 152, n° 2, p. A439, 2005.
- [3] K. More, R. Borup, et K. Reeves, « Identifying Contributing Degradation Phenomena in PEM Fuel Cell Membrane Electride Assemblies Via Electron Microscopy », *ECS Transactions*, vol. 3, p. 717–733, 2006.
- [4] S. D. Thompson, L. R. Jordan, et M. Forsyth, « Platinum electrodeposition for polymer electrolyte membrane fuel cells », *Electrochimica acta*, vol. 46, n° 10-11, p. 1657–1663, 2001.
- [5] R. M. Q. Mello et E. A. Ticianelli, « Kinetic study of the hydrogen oxidation reaction on platinum and Nafion® covered platinum electrodes », *Electrochimica acta*, vol. 42, n° 6, p. 1031–1039, 1997.
- [6] S. Chen et A. Kucernak, « Electrocatalysis under Conditions of High Mass Transport: Investigation of Hydrogen Oxidation on Single Submicron Pt Particles Supported on Carbon », *The Journal of Physical Chemistry B*, vol. 108, n° 37, p. 13984–13994, sept. 2004.
- [7] J. Barber, S. Morin, et B. E. Conway, « Specificity of the kinetics of H₂ evolution to the structure of single-crystal Pt surfaces, and the relation between opd and upd H », *Journal of Electroanalytical Chemistry*, vol. 446, n° 1-2, p. 125–138, avr. 1998.
- [8] J. X. Wang, T. E. Springer, et R. R. Adzic, « Dual-Pathway Kinetic Equation for the Hydrogen Oxidation Reaction on Pt Electrodes », *Journal of The Electrochemical Society*, vol. 153, n° 9, p. A1732, 2006.
- [9] P. Quaino, J. Fernandez, M. Gennero de Chialvo, et A. Chialvo, « Hydrogen oxidation reaction on microelectrodes: Analysis of the contribution of the kinetic routes », *Journal of Molecular Catalysis A: Chemical*, vol. 252, n° 1-2, p. 156–162, 2006.
- [10] S. A. Vilekar, I. Fishtik, et R. Datta, « Kinetics of the Hydrogen Electrode Reaction », *Journal of The Electrochemical Society*, vol. 157, n° 7, p. B1040, 2010.
- [11] E. Skulason, G. S. Karlberg, J. Rossmeisl, T. Bligaard, J. Greeley, H. Jonsson, et J. K. Nørskov, « Density functional theory calculations for the hydrogen evolution reaction in an electrochemical double layer on the Pt(111) electrode », *Physical Chemistry Chemical Physics*, vol. 9, n° 25, p. 3241, 2007.

- [12] O. Antoine et R. Durand, « RRDE study of oxygen reduction on Pt nanoparticles inside Nafion: H₂O₂ production in PEMFC cathode conditions », *Journal of Applied Electrochemistry*, vol. 30, n° 7, p. 839-844, 2000.
- [13] N. Markovic, T. Schmidt, V. Stamenkovic, et P. Ross, « Oxygen reduction reaction on Pt and Pt bimetallic surfaces: a selective review », *FUEL CELLS-WEINHEIM-*, vol. 1, n° 2, p. 105–116, 2001.
- [14] K. C. Neyerlin, W. Gu, J. Jorne, et H. A. Gasteiger, « Determination of Catalyst Unique Parameters for the Oxygen Reduction Reaction in a PEMFC », *Journal of The Electrochemical Society*, vol. 153, n° 10, p. A1955, 2006.
- [15] K. C. Neyerlin, W. Gu, J. Jorne, et H. A. Gasteiger, « Study of the Exchange Current Density for the Hydrogen Oxidation and Evolution Reactions », *Journal of The Electrochemical Society*, vol. 154, n° 7, p. B631, 2007.
- [16] I. A. Schneider, D. Kramer, A. Wokaun, et G. G. Scherer, « Effect of inert gas flow on hydrogen underpotential deposition measurements in polymer electrolyte fuel cells », *Electrochemistry Communications*, vol. 9, n° 7, p. 1607-1612, juill. 2007.
- [17] G. Jerkiewicz, « Hydrogen sorption at/in electrodes », *Progress in Surface Science*, vol. 57, n° 2, p. 137–186, 1998.
- [18] N. Marković et P. N. Ross, « Surface science studies of model fuel cell electrocatalysts », *Surface Science Reports*, vol. 45, n° 4, p. 117–229, 2002.
- [19] B. Conway et B. Tilak, « Interfacial processes involving electrocatalytic evolution and oxidation of H₂, and the role of chemisorbed H », *Electrochimica acta*, vol. 47, n° 22-23, p. 3571–3594, 2002.
- [20] J. Solla-Gullon, V. Montiel, A. Aldaz, et J. Clavilier, « Electrochemical characterisation of platinum nanoparticles prepared by microemulsion: how to clean them without loss of crystalline surface structure », *Journal of Electroanalytical Chemistry*, vol. 491, n° 1, p. 69–77, 2000.
- [21] B. Conway, « Relation of energies and coverages of underpotential and overpotential deposited H at Pt and other metals to the 'volcano curve' for cathodic H₂ evolution kinetics », *Electrochimica Acta*, vol. 45, n° 25-26, p. 4075-4083, août 2000.
- [22] N. M. Markovic, H. A. Gasteiger, et P. N. Ross Jr, « Oxygen reduction on platinum low-index single-crystal surfaces in sulfuric acid solution: rotating ring-Pt (hkl) disk studies », *The Journal of Physical Chemistry*, vol. 99, n° 11, p. 3411–3415, 1995.
- [23] A. Pozio, M. De Francesco, A. Cemmi, F. Cardellini, et L. Giorgi, « Comparison of high surface Pt/C catalysts by cyclic voltammetry », *Journal of power sources*, vol. 105, n° 1, p. 13–19, 2002.

- [24] K. J. J. Mayrhofer, B. B. Blizanac, M. Arenz, V. R. Stamenkovic, P. N. Ross, et N. M. Markovic, «The Impact of Geometric and Surface Electronic Properties of Pt-Catalysts on the Particle Size Effect in Electrocatalysis », *The Journal of Physical Chemistry B*, vol. 109, n° 30, p. 14433-14440, août 2005.
- [25] R. W. Lindström, K. Kortsdottir, M. Wesselmark, A. Oyarce, C. Lagergren, et G. Lindbergh, « Active Area Determination of Porous Pt Electrodes Used in Polymer Electrolyte Fuel Cells: Temperature and Humidity Effects », *J. Electrochem. Soc.*, vol. 157, n° 12, p. B1795, 2010.
- [26] N. Linse, L. Gubler, G. G. Scherer, et A. Wokaun, « The effect of platinum on carbon corrosion behavior in polymer electrolyte fuel cells », *Electrochimica Acta*, vol. 56, n° 22, p. 7541-7549, sept. 2011.
- [27] J. Mainka, G. Maranzana, A. Thomas, J. Dillet, S. Didierjean, et O. Lottin, « One-dimensional Model of Oxygen Transport Impedance Accounting for Convection Perpendicular to the Electrode », *Fuel Cells*, vol. 12, n° 5, p. 848-861, oct. 2012.
- [28] G. Maranzana, J. Mainka, O. Lottin, J. Dillet, A. Lamibrac, A. Thomas, et S. Didierjean, « A proton exchange membrane fuel cell impedance model taking into account convection along the air channel: On the bias between the low frequency limit of the impedance and the slope of the polarization curve », *Electrochimica Acta*, vol. 83, p. 13-27, nov. 2012.
- [29] R. K. Ahluwalia et X. Wang, « Fuel cell systems for transportation: Status and trends », *Journal of Power Sources*, vol. 177, n° 1, p. 167-176, févr. 2008.
- [30] N. Garland, J. Milliken, S. Satyapal, J. Munetz, et K. McMurphy, « Recent Advances in Hydrogen and Fuel Cell Technology », *ECS Transactions*, p. 223-232, 2009.
- [31] R. Borup, J. Meyers, B. Pivovar, Y. S. Kim, R. Mukundan, N. Garland, D. Myers, M. Wilson, F. Garzon, D. Wood, P. Zelenay, K. More, K. Stroh, T. Zawodzinski, J. Boncella, J. E. McGrath, M. Inaba, K. Miyatake, M. Hori, K. Ota, Z. Ogumi, S. Miyata, A. Nishikata, Z. Siroma, Y. Uchimoto, K. Yasuda, K. Kimijima, et N. Iwashita, « Scientific Aspects of Polymer Electrolyte Fuel Cell Durability and Degradation », *Chem. Rev.*, vol. 107, n° 10, p. 3904-3951, oct. 2007.
- [32] F. A. de Bruijn, V. A. T. Dam, et G. J. M. Janssen, « Review: Durability and Degradation Issues of PEM Fuel Cell Components », *Fuel Cells*, vol. 8, n° 1, p. 3-22, févr. 2008.
- [33] W. Schmittinger et A. Vahidi, « A review of the main parameters influencing long-term performance and durability of PEM fuel cells », *Journal of Power Sources*, vol. 180, n° 1, p. 1-14, mai 2008.
- [34] J. Wu, X. Z. Yuan, J. J. Martin, H. Wang, J. Zhang, J. Shen, S. Wu, et W. Merida, « A review of PEM fuel cell durability: Degradation mechanisms and mitigation strategies », *Journal of Power Sources*, vol. 184, n° 1, p. 104-119, 2008.

- [35] Y. Wang, K. S. Chen, J. Mishler, S. C. Cho, et X. C. Adroher, « A review of polymer electrolyte membrane fuel cells: Technology, applications, and needs on fundamental research », *Applied Energy*, oct. 2010.
- [36] A. Hermann, T. Chaudhuri, et P. Spagnol, « Bipolar plates for PEM fuel cells: A review », *International Journal of Hydrogen Energy*, vol. 30, n° 12, p. 1297–1302, 2005.
- [37] R. A. Antunes, M. C. . Oliveira, G. Ett, et V. Ett, « Corrosion of metal bipolar plates for PEM fuel cells: A review », *International Journal of Hydrogen Energy*, vol. 35, n° 8, p. 3632–3647, 2010.
- [38] A. A. Hermas et M. S. Morad, « A comparative study on the corrosion behaviour of 304 austenitic stainless steel in sulfamic and sulfuric acid solutions », *Corrosion Science*, vol. 50, n° 9, p. 2710-2717, sept. 2008.
- [39] J. Wind, R. Späh, W. Kaiser, et G. Böhm, « Metallic bipolar plates for PEM fuel cells », *Journal of Power Sources*, vol. 105, n° 2, p. 256–260, 2002.
- [40] R. F. Silva, D. Franchi, A. Leone, L. Pilloni, A. Masci, et A. Pozio, « Surface conductivity and stability of metallic bipolar plate materials for polymer electrolyte fuel cells », *Electrochimica acta*, vol. 51, n° 17, p. 3592–3598, 2006.
- [41] S. Gamboa, J. Gonzalezrodriguez, E. Valenzuela, B. Campillo, P. Sebastian, et A. Reyesrojas, « Evaluation of the corrosion resistance of Ni–Co–B coatings in simulated PEMFC environment », *Electrochimica Acta*, vol. 51, n° 19, p. 4045-4051, mai 2006.
- [42] E. A. Cho, U. S. Jeon, H. Y. Ha, S. A. Hong, et I. H. Oh, « Characteristics of composite bipolar plates for polymer electrolyte membrane fuel cells », *Journal of power sources*, vol. 125, n° 2, p. 178–182, 2004.
- [43] J. Frisk, M. Hicks, R. Atanasoski, W. Boand, A. Schmoeckel, et M. Kurkowski, « MEA Component Durability », *Fuel Cell Seminar (San Antonio)*, nov. 2004.
- [44] M. Schulze, N. Wagner, T. Kaz, et K. A. Friedrich, « Combined electrochemical and surface analysis investigation of degradation processes in polymer electrolyte membrane fuel cells », *Electrochimica Acta*, vol. 52, n° 6, p. 2328–2336, 2007.
- [45] M. Schulze et C. Christenn, « XPS investigation of the PTFE induced hydrophobic properties of electrodes for low temperature fuel cells », *Applied surface science*, vol. 252, n° 1, p. 148–153, 2005.
- [46] J. P. Meyers et R. M. Darling, « Model of Carbon Corrosion in PEM Fuel Cells », *J. Electrochem. Soc.*, vol. 153, n° 8, p. A1432, 2006.
- [47] N. Takeuchi et T. F. Fuller, « Modeling and Investigation of Design Factors and Their Impact on Carbon Corrosion of PEMFC Electrodes », *J. Electrochem. Soc.*, vol. 155, n° 7, p. B770, 2008.

- [48] A. A. Kulikovsky, « A Simple Model for Carbon Corrosion in PEM Fuel Cell », *J. Electrochem. Soc.*, vol. 158, n° 8, p. B957, 2011.
- [49] S. Maass, F. Finsterwalder, G. Frank, R. Hartmann, et C. Merten, « Carbon support oxidation in PEM fuel cell cathodes », *Journal of Power Sources*, vol. 176, n° 2, p. 444–451, 2008.
- [50] P. L. Antonucci, G. Pinna, L. Pino, et N. Giordano, « A comparative analysis of structural and surface effects in the electrochemical corrosion of carbons.pdf », *Materials Chemistry and Physics*, vol. 21, p. 495-506, 1989.
- [51] E. Antolini, « Formation, microstructural characteristics and stability of carbon supported platinum catalysts for low temperature fuel cells », *Journal of materials science*, vol. 38, n° 14, p. 2995–3005, 2003.
- [52] F. Rodriguez-Reinoso, « The role of carbon materials in heterogeneous catalysis », *Carbon*, vol. 36, n° 3, p. 159–175, 1998.
- [53] N. Giordano, P. L. Antonucci, E. Passalacqua, L. Pino, A. S. Arico, et K. Kinoshita, « Relationship between physicochemical properties and electrooxidation behaviour of carbon materials.pdf », *Electrochimica Acta*, vol. 36, n° 13, p. 1931-1935, 1991.
- [54] M. Murthy, M. Esayan, W. Lee, et J. W. Van Zee, « The Effect of Temperature and Pressure on the Performance of a PEMFC Exposed to Transient CO Concentrations », *Journal of The Electrochemical Society*, vol. 150, n° 1, p. A29, 2003.
- [55] H.-F. Oetjen, « Performance Data of a Proton Exchange Membrane Fuel Cell Using H₂/CO as Fuel Gas », *Journal of The Electrochemical Society*, vol. 143, n° 12, p. 3838, 1996.
- [56] F. Maillard, E. R. Savinova, et U. Stimming, « CO monolayer oxidation on Pt nanoparticles: Further insights into the particle size effects », *Journal of Electroanalytical Chemistry*, vol. 599, n° 2, p. 221–232, 2007.
- [57] M. Arenz, K. J. . Mayrhofer, V. Stamenkovic, B. B. Blizanac, T. Tomoyuki, P. N. Ross, et N. M. Markovic, « The effect of the particle size on the kinetics of CO electrooxidation on high surface area Pt catalysts », *Journal of the American Chemical Society*, vol. 127, n° 18, p. 6819–6829, 2005.
- [58] D. C. Papageorgopoulos et F. A. de Bruijn, « Examining a Potential Fuel Cell Poison », *Journal of The Electrochemical Society*, vol. 149, n° 2, p. A140, 2002.
- [59] M. S. Wilson, F. H. Garzon, K. E. Sickafus, et S. Gottesfeld, « Surface area loss of supported platinum in polymer electrolyte fuel cells », *Journal of the Electrochemical Society*, vol. 140, p. 2872, 1993.
- [60] X. Wang, R. Kumar, et D. J. Myers, « Effect of Voltage on Platinum Dissolution », *Electrochemical and Solid-State Letters*, vol. 9, n° 5, p. A225, 2006.

- [61] P. J. Ferreira, G. J. la O', Y. Shao-Horn, D. Morgan, R. Makharia, S. Kocha, et H. A. Gasteiger, « Instability of Pt/C Electrocatalysts in Proton Exchange Membrane Fuel Cells », *J. Electrochem. Soc.*, vol. 152, n° 11, p. A2256, 2005.
- [62] W. Bi, G. E. Gray, et T. F. Fuller, « PEM Fuel Cell Pt/C Dissolution and Deposition in Nafion Electrolyte », *Electrochemical and Solid-State Letters*, vol. 10, n° 5, p. B101, 2007.
- [63] A. Ohma, S. Suga, S. Yamamoto, et K. Shinohara, « Membrane Degradation Behavior during Open-Circuit Voltage Hold Test », *J. Electrochem. Soc.*, vol. 154, n° 8, p. B757, 2007.
- [64] S. Kundu, M. Cimenti, S. Lee, et D. Bessarabov, « Fingerprint of automotive fuel cell cathode catalyst degradation: Pt band in PEMs », *Membrane Technology*, vol. 2009, n° 10, p. 7–10, 2009.
- [65] E. Antolini et E. R. Gonzalez, « Ceramic materials as supports for low-temperature fuel cell catalysts », *Solid State Ionics*, vol. 180, n° 9-10, p. 746-763, mai 2009.
- [66] P. V. Shanahan, L. Xu, C. Liang, M. Waje, S. Dai, et Y. S. Yan, « Graphitic mesoporous carbon as a durable fuel cell catalyst support », *Journal of Power Sources*, vol. 185, n° 1, p. 423–427, 2008.
- [67] N. Rajalakshmi, H. Ryu, M. M. Shaijumon, et S. Ramaprabhu, « Performance of polymer electrolyte membrane fuel cells with carbon nanotubes as oxygen reduction catalyst support material », *Journal of power sources*, vol. 140, n° 2, p. 250–257, 2005.
- [68] M. Carmo, V. A. Paganin, J. M. Rosolen, et E. R. Gonzalez, « Alternative supports for the preparation of catalysts for low-temperature fuel cells: the use of carbon nanotubes », *Journal of power sources*, vol. 142, n° 1, p. 169–176, 2005.
- [69] H. Chhina, S. Campbell, et O. Kesler, « High surface area synthesis, electrochemical activity, and stability of tungsten carbide supported Pt during oxygen reduction in proton exchange membrane fuel cells », *Journal of Power Sources*, vol. 179, n° 1, p. 50–59, 2008.
- [70] H. R. Colón-Mercado et B. N. Popov, « Stability of platinum based alloy cathode catalysts in PEM fuel cells », *Journal of power sources*, vol. 155, n° 2, p. 253–263, 2006.
- [71] L. Dubau, J. Durst, F. Maillard, M. Chatenet, J. André, et E. Rossinot, « Heterogeneities of Aging within a PEMFC MEA », *Fuel Cells*, vol. 12, n° 2, p. 188–198, avr. 2012.
- [72] D. Cameron, R. Holliday, et D. Thompson, « Gold's future role in fuel cell systems », *Journal of Power Sources*, vol. 118, n° 1-2, p. 298–303, 2003.

- [73] J. Moreira, « Synthesis, characterization and application of a Pd/Vulcan and Pd/C catalyst in a PEM fuel cell », *International Journal of Hydrogen Energy*, vol. 29, n° 9, p. 915-920, août 2004.
- [74] E. Antolini, « Palladium in fuel cell catalysis », *Energy & Environmental Science*, vol. 2, n° 9, p. 915, 2009.
- [75] B. Wang, « Recent development of non-platinum catalysts for oxygen reduction reaction », *Journal of Power Sources*, vol. 152, p. 1–15, 2005.
- [76] Y. Shi, R. Yang, et P. K. Yuet, « Easy decoration of carbon nanotubes with well dispersed gold nanoparticles and the use of the material as an electrocatalyst », *Carbon*, vol. 47, n° 4, p. 1146-1151, avr. 2009.
- [77] B. Smitha, S. Sridhar, et A. A. Khan, « Solid polymer electrolyte membranes for fuel cell applications—a review », *Journal of membrane science*, vol. 259, n° 1, p. 10–26, 2005.
- [78] M. Rikukawa et K. Sanui, « Proton-conducting polymer electrolyte membranes based on hydrocarbon polymers », *Progress in Polymer Science*, vol. 25, n° 10, p. 1463-1502, déc. 2000.
- [79] A. B. LaConti, M. Hamdan, et R. C. McDonald, « Mechanisms of membrane degradation », in *Handbook of Fuel Cells*, W. Vielstich, A. Lamm, H. A. Gasteiger, et H. Yokokawa, Éd. Chichester, UK: John Wiley & Sons, Ltd, 2010.
- [80] A. Pozio, « Nafion degradation in PEFCs from end plate iron contamination », *Electrochimica Acta*, vol. 48, n° 11, p. 1543-1549, mai 2003.
- [81] A. Ohma, S. Suga, S. Yamamoto, et K. Shinohara, « Phenomenon Analysis of PEFC for Automotive Use(1) Membrane Degradation Behavior During OCV Hold Test », in *ECS Transactions*, Cancun, Mexico, 2006, p. 519-529.
- [82] J. Zhang, B. A. Litteer, W. Gu, H. Liu, et H. A. Gasteiger, « Effect of hydrogen and oxygen partial pressure on Pt precipitation within the membrane of PEMFCs », *Journal of the electrochemical society*, vol. 154, n° 10, p. B1006–B1011, 2007.
- [83] D. E. Curtin, R. D. Lousenberg, T. J. Henry, P. C. Tangeman, et M. E. Tisack, « Advanced materials for improved PEMFC performance and life », *Journal of Power Sources*, vol. 131, n° 1-2, p. 41–48, 2004.
- [84] A. Alentiev, J. Kostina, et G. Bondarenko, « Chemical aging of Nafion: FTIR study », *Desalination*, vol. 200, n° 1-3, p. 32–33, 2006.
- [85] C. Chen et T. F. Fuller, « The effect of humidity on the degradation of Nafion® membrane », *Polymer Degradation and Stability*, vol. 94, n° 9, p. 1436-1447, sept. 2009.

- [86] K. Teranishi, K. Kawata, S. Tsushima, et S. Hirai, « Degradation Mechanism of PEMFC under Open Circuit Operation », *Electrochem. Solid-State Lett.*, vol. 9, n° 10, p. A475, 2006.
- [87] M. Inaba, T. Kinumoto, M. Kiriake, R. Umebayashi, A. Tasaka, et Z. Ogumi, « Gas crossover and membrane degradation in polymer electrolyte fuel cells », *Electrochimica Acta*, vol. 51, n° 26, p. 5746–5753, 2006.
- [88] V. A. Sethuraman, J. W. Weidner, A. T. Haug, et L. V. Protsailo, « Durability of Perfluorosulfonic Acid and Hydrocarbon Membranes: Effect of Humidity and Temperature », *Journal of The Electrochemical Society*, vol. 155, n° 2, p. B119, 2008.
- [89] J. Yu, T. Matsuura, Y. Yoshikawa, M. N. Islam, et M. Hori, « In Situ Analysis of Performance Degradation of a PEMFC under Nonsaturated Humidification », *Electrochemical and Solid-State Letters*, vol. 8, n° 3, p. A156, 2005.
- [90] B. Kienitz, B. Pivovar, T. Zawodzinski, et F. H. Garzon, « Cationic Contamination Effects on Polymer Electrolyte Membrane Fuel Cell Performance », *Journal of the Electrochemical Society*, vol. 158, p. B1175, 2011.
- [91] X. Huang, R. Solasi, Y. Zou, M. Feshler, K. Reifsnider, D. Condit, S. Burlatsky, et T. Madden, « Mechanical endurance of polymer electrolyte membrane and PEM fuel cell durability », *Journal of Polymer Science Part B: Polymer Physics*, vol. 44, n° 16, p. 2346-2357, août 2006.
- [92] R. Solasi, Y. Zou, X. Huang, K. Reifsnider, et D. Condit, « On mechanical behavior and in-plane modeling of constrained PEM fuel cell membranes subjected to hydration and temperature cycles », *Journal of Power Sources*, vol. 167, n° 2, p. 366-377, mai 2007.
- [93] J. A. Kerres, « Development of ionomer membranes for fuel cells », *Journal of Membrane Science*, vol. 185, n° 1, p. 3–27, 2001.
- [94] M. Reum, A. Wokaun, et F. N. Büchi, « Measuring the Current Distribution with Submillimeter Resolution in PEFCs », *J. Electrochem. Soc.*, vol. 156, n° 10, p. B1225, 2009.
- [95] M. Reum, S. A. Freunberger, A. Wokaun, et F. N. Büchi, « Measuring the Current Distribution with Sub-Millimeter Resolution in PEFCs », *J. Electrochem. Soc.*, vol. 156, n° 3, p. B301, 2009.
- [96] L. C. Pérez, L. Brandão, J. M. Sousa, et A. Mendes, « Segmented polymer electrolyte membrane fuel cells—A review », *Renewable and Sustainable Energy Reviews*, vol. 15, n° 1, p. 169-185, janv. 2011.
- [97] D. Spornjak, J. D. Fairweather, T. Rockward, R. Mukundan, et R. Borup, « Characterization of Carbon Corrosion in a Segmented PEM Fuel Cell », 2011, p. 741-750.

- [98] C. A. Reiser, L. Bregoli, T. W. Patterson, J. S. Yi, J. D. Yang, M. L. Perry, et T. D. Jarvi, « A Reverse-Current Decay Mechanism for Fuel Cells », *Electrochem. Solid-State Lett.*, vol. 8, n° 6, p. A273, 2005.
- [99] Z. Siroma, N. Fujiwara, T. Ioroi, S. Yamazaki, H. Senoh, K. Yasuda, et K. Tanimoto, « Transient phenomena in a PEMFC during the start-up of gas feeding observed with a 97-fold segmented cell », *Journal of Power Sources*, vol. 172, n° 1, p. 155–162, 2007.
- [100] G. Maranzana, O. Lottin, T. Colinart, S. Chupin, et S. Didierjean, « A multi-instrumented polymer exchange membrane fuel cell: Observation of the in-plane non-homogeneities », *Journal of Power Sources*, vol. 180, n° 2, p. 748-754, juin 2008.
- [101] Q. Shen, M. Hou, D. Liang, Z. Zhou, X. Li, Z. Shao, et B. Yi, « Study on the processes of start-up and shutdown in proton exchange membrane fuel cells », *Journal of Power Sources*, vol. 189, n° 2, p. 1114–1119, 2009.
- [102] J. Kim, J. Lee, et Y. Tak, « Relationship between carbon corrosion and positive electrode potential in a proton-exchange membrane fuel cell during start/stop operation », *Journal of Power Sources*, vol. 192, n° 2, p. 674–678, 2009.
- [103] W. Gu, R. N. Carter, P. T. Yu, et H. A. Gasteiger, « Start/Stop and Local H₂ Starvation Mechanisms of Carbon Corrosion: Model vs. Experiment », in *ECS Transactions*, Washington, DC, 2007, p. 963-973.
- [104] Chizawa, Ogami, Naka, Matsunaga, Aoki, Aoki, « Study of Accelerated Test Protocol for PEFC Focusing on Carbon Corrosion », *ECS Transactions*, vol. 3 (1), p. 645-655, 2006.
- [105] A. Ofstad, J. Davey, S. Sunde, et R. L. Borup, « Carbon Corrosion of a PEMFC During Shut-down/Start-up when Using an Air Purge Procedure », in *ECS Transactions*, Honolulu, HI, 2008, p. 1301-1311.
- [106] H. Tang, Z. Qi, M. Ramani, et J. F. Elter, « PEM fuel cell cathode carbon corrosion due to the formation of air/fuel boundary at the anode », *Journal of Power Sources*, vol. 158, n° 2, p. 1306–1312, 2006.
- [107] G. Maranzana, C. Moyne, J. Dillet, S. Didierjean, et O. Lottin, « About internal currents during start-up in proton exchange membrane fuel cell », *Journal of Power Sources*, vol. 195, n° 18, p. 5990–5995, 2010.
- [108] I. A. Schneider et S. von Dahlen, « Start-Stop Phenomena in Channel and Land Areas of a Polymer Electrolyte Fuel Cell », *Electrochemical and Solid-State Letters*, vol. 14, n° 2, p. B30, 2011.
- [109] S. Kreitmeier, A. Wokaun, et F. N. Büchi, « Local Catalyst Support Degradation during Polymer Electrolyte Fuel Cell Start-Up and Shutdown », *Journal of The Electrochemical Society*, vol. 159, n° 11, p. F787–F793, 2012.

- [110] Y. Shao, G. Yin, et Y. Gao, « Understanding and approaches for the durability issues of Pt-based catalysts for PEM fuel cell », *Journal of Power Sources*, vol. 171, n° 2, p. 558–566, 2007.
- [111] E. Antolini, « Carbon supports for low-temperature fuel cell catalysts », *Applied Catalysis B: Environmental*, vol. 88, n° 1-2, p. 1–24, 2009.
- [112] S. D. Knights, K. M. Colbow, J. St-Pierre, et D. P. Wilkinson, « Aging mechanisms and lifetime of PEFC and DMFC », *Journal of Power Sources*, vol. 127, n° 1-2, p. 127–134, 2004.
- [113] A. P. Young, J. Stumper, et E. Gyenge, « Characterizing the Structural Degradation in a PEMFC Cathode Catalyst Layer: Carbon Corrosion », *J. Electrochem. Soc.*, vol. 156, n° 8, p. B913, 2009.
- [114] K. Yasuda, A. Taniguchi, T. Akita, T. Ioroi, et Z. Siroma, « Platinum dissolution and deposition in the polymer electrolyte membrane of a PEM fuel cell as studied by potential cycling », *Physical Chemistry Chemical Physics*, vol. 8, n° 6, p. 746, 2006.
- [115] S. F. Burlatsky, M. Gummalla, V. V. Atrazhev, D. V. Dmitriev, N. Y. Kuzminyh, et N. S. Erikhman, « The Dynamics of Platinum Precipitation in an Ion Exchange Membrane », *Journal of The Electrochemical Society*, vol. 158, n° 3, p. B322, 2011.
- [116] R. L. Borup, J. R. Davey, F. H. Garzon, D. L. Wood, et M. A. Inbody, « PEM fuel cell electrocatalyst durability measurements », *Journal of Power Sources*, vol. 163, n° 1, p. 76–81, 2006.
- [117] Y. Shao-Horn, P. Ferreira, G. J. la O', D. Morgan, H. A. Gasteiger, et R. Makharia, « Coarsening of Pt Nanoparticles in Proton Exchange Membrane Fuel Cells upon Potential Cycling », *ECS Transactions*, vol. 1, p. 185-195, 2006.
- [118] F. B. Weng, C. Y. Hsu, et C. W. Li, « Experimental investigation of PEM fuel cell aging under current cycling using segmented fuel cell », *International Journal of Hydrogen Energy*, vol. 35, n° 8, p. 3664–3675, 2010.
- [119] D. Stolten, « Hydrogen and fuel cells: fundamentals, technologies and applications », 2010, p. 13.
- [120] R. N. Carter, W. B. Gu, B. Brady, P. T. Yu, K. Subramanian, H. A. Gasteiger, W. Vielstich, et H. Yokokawa, « Electrode degradation mechanisms studies by current distribution measurements Carter », *Handbook of Fuel Cells: Fundamentals, Technology and Applications*, vol. 6, p. 829, 2009.
- [121] K. L. More, K. Perry, M. Chi, et S. Reeves, « Carbon Support Structural Degradation Observed in Aged PEM Fuel Cells », in *Meeting Abstracts*, 2010, p. 611–611.
- [122] L. Dubau, L. Castanheira, M. Lopez-Haro, P. Bayle-Guillemaud, et F. Maillard, « Electrochemical oxidation of carbon in low temperature fuel cells: influence of the gas atmosphere », *223rd ECS Meeting*.

- [123] B. E. Conway, « Electrochemical oxide film formation at noble metals as a surface-chemical process », *Progress in surface science*, vol. 49, n° 4, p. 331–452, 1995.
- [124] G. Jerkiewicz, « Surface-oxide growth at platinum electrodes in aqueous H₂SO₄*1Reexamination of its mechanism through combined cyclic-voltammetry, electrochemical quartz-crystal nanobalance, and Auger electron spectroscopy measurements », *Electrochimica Acta*, vol. 49, n° 9-10, p. 1451-1459, avr. 2004.
- [125] R. M. Darling et J. P. Meyers, « Kinetic Model of Platinum Dissolution in PEMFCs », *J. Electrochem. Soc.*, vol. 150, n° 11, p. A1523, 2003.
- [126] S. Mitsushima, S. Kawahara, K. Ota, et N. Kamiya, « Consumption Rate of Pt under Potential Cycling », *Journal of The Electrochemical Society*, vol. 154, n° 2, p. B153, 2007.
- [127] S. G. Rinaldo, J. Stumper, et M. Eikerling, « Physical Theory of Platinum Nanoparticle Dissolution in Polymer Electrolyte Fuel Cells », *The Journal of Physical Chemistry C*, vol. 114, n° 13, p. 5773-5785, avr. 2010.
- [128] B. E. Conway, B. Barnett, H. Angerstein-Kozłowska, et B. V. Tilak, « A surface-electrochemical basis for the direct logarithmic growth law for initial stages of extension of anodic oxide films formed at noble metals », *The Journal of Chemical Physics*, vol. 93, n° 11, p. 8361, 1990.
- [129] J. Mainka, « Ph.D Thesis », *Université Henri Poincaré-Nancy*.
- [130] S. Didierjean, A. Lamibrac, T. Geneston, A. Rakotondrainibe, G. Maranzana, E. Rozier, F. Beille, et O. Lottin, « Internal currents in response to a load change during fuel cell start-up », *International Journal of Hydrogen Energy*, févr. 2012.

Annex

Manufacturer	Johnson Matthey	Paxitech	Ion Power			
PEM	PFSA 3 layers 30 μm	Nafion XL 212 25 μm	Nafion XL 50 μm			
Anodic electrode reference			10V20E			
Anodic electrode Pt charge (mg/cm ²) Webloading / XRF *	0.2	0.2	0.08/0.09	0.08/0.03	0.08/0.05	0.15/0.18
Anodic electrode % Pt/C		50				
Cathodic Electrode reference			10V40E	10V40E	10V20E	10V40E
Carbon @ cathodic electrode		XC72	XC72 240 m ² /g	XC72 240 m ² /g	Tanaka 800 m ² /g	XC72 240 m ² /g
Cathodic electrode Pt charge (mg/cm ²)/XRF	0.6	0.4	0.44/0.61	0.2/0.27	0.18/0.17	0.23/0.31
Cathodic electrode % Pt/C		50				
Active Area (cm ²)	30	30	31			
Anodic GDL	10BB		SGL24BC	SGL24BC	SGL24BC	SGL24BC
Anodic Gasket thickness (μm)	290	170	210	210	210	210
Cathodic GDL	10BB		SGL24BC	SGL24BC	SGL24BC	SGL24BC
Cathodic Gasket thickness (μm)	420	170	210	210	210	210
Reference	JM MEA	Paxitech MEA	High Pt Cathode	Ref	High Carbon Surface	High Pt Anode

Annex 1. MEAs characteristics.

* For the Ion power, the platinum loading given by the manufacturer was controlled by X-Ray Fluorescence (XRF) spectroscopy.

Global		Initial ECSA (m ² _{Pt} /g _{Pt})	Maximal ECSA (m ² _{Pt} /g _{Pt})	Final ECSA (m ² _{Pt} /g _{Pt})	ECSA loss (m ² _{Pt} /g _{Pt}) ⁽¹⁾	Relative ECSA loss (%) ⁽¹⁾	ECSA loss/cycle (cm ² _{Pt} /g _{Pt})	
Protocol	1	OCV - 0.5 A/cm ²	62.7	64.7	56.9	7.8	12.0	285.1
	2	OCV - 1 A/cm ²	70.2	70.2	60.1	10.1	14.3	369.8
	3	2 slph H ₂ in N ₂	64.5	65.7	47.3	18.4	27.9	674.7
	4	10 slph H ₂ in N ₂	63.9	65.8	52.5	13.3	20.3	560.6
	5	2 slph H ₂ in Air	55.1	58.1	12.0	46.1	79.3	1693.3
	6	10 slph H ₂ in Air	60.7	60.7	29.3	31.4	51.8	1155.2

Annex 2. Global ECSA evolution during the different agings described in §3.4. (1) with reference to the maximum ECSA.

1 st segment		Initial ECSA (m ² _{Pt} /g _{Pt})	Final ECSA (m ² _{Pt} /g _{Pt})	ECSA loss (m ² _{Pt} /g _{Pt}) ⁽¹⁾	Relative ECSA loss (%) ⁽¹⁾	ECSA loss/cycle (cm ² _{Pt} /g _{Pt})	
Protocol	1	OCV - 0.5 A/cm ²	55.8	50.1	5.7	10.3	210.9
	2	OCV - 1 A/cm ²	60.8	51.3	9.5	15.6	347.6
	3	2 slph H ₂ in N ₂	74.1	67.7	6.4	8.7	235.8
	4	10 slph H ₂ in N ₂	57.5	49.5	8.0	13.9	335.2
	5	2 slph H ₂ in Air	55.8	37.1	18.8	33.6	689.4
	6	10 slph H ₂ in Air	64.4	47.9	16.6	25.7	609.7

Annex 3. Local ECSA evolution of the 1st segment during the different agings described in §3.4. (1) with reference to the maximum ECSA.

20 th segment		Initial ECSA (m ² _{Pt} /g _{Pt})	Final ECSA (m ² _{Pt} /g _{Pt})	ECSA loss (m ² _{Pt} /g _{Pt}) ⁽¹⁾	Relative ECSA loss (%) ⁽¹⁾	ECSA loss/cycle (cm ² _{Pt} /g _{Pt})	
Protocol	1	OCV - 0.5 A/cm ²	62.8	59.1	3.7	6.0	137.5
	2	OCV - 1 A/cm ²	68.7	60.5	8.2	11.9	300.3
	3	2 slph H ₂ in N ₂	48.6	31.4	17.1	35.3	630.3
	4	10 slph H ₂ in N ₂	63.7	51.0	12.8	20.0	536.2
	5	2 slph H ₂ in Air	48.4	5.0	43.4	89.7	1596.1
	6	10 slph H ₂ in Air	51.0	9.9	41.1	80.6	1511.5

Annex 4. Local ECSA evolution of the 20th segment during the different agings described in §3.4. (1) with reference to the maximum ECSA.

Annex 5. System of equations and method used for the simulations

In the 2D model used for the numerical simulation of start-up, the cell is divided into N segments. The 1D model simulates polarization curve or cyclic voltametry, which does not require spatial resolution along the channel. Therefore, N=1 in this case. *m* stands for the number of possible reactions in one segment of an electrode.

System of equations

The system gathers several equations:

- Kirschhoff's current law:

At the anode:

$$C_{tot}^a \frac{d\phi_a^n}{dt} = -j_c^n - \sum_{i=1}^m j_{f,n}^{a,i} \quad n \leq N \quad (1)$$

At the cathode:

$$C_{tot}^c \frac{d\phi_c^n}{dt} = j_c^n - \sum_{i=1}^m j_{f,n}^{c,i} \quad n \leq N \quad (2)$$

As a reminder, the equilibrium potentials are functions of the gaseous species concentration and of the electrode potentials (§4.2.1.a).

At the scale of the cell:

$$-\frac{1}{N} \sum_{n=1}^N j_a^n = \frac{1}{N} \sum_{n=1}^N j_c^n = j_{cell} \quad n \leq N \quad (3)$$

- Kirschhoff's voltage law:

At the scale of the cell:

$$U_{cell} = \phi_c^n - \phi_a^n + R_{\infty} j_c^n \quad n \leq N \quad (4)$$

- Mass transport equations:

$$\frac{d\Gamma^n}{dt} = \Phi_n(\Gamma^n, \phi_c^n, \phi_a^n) \quad n \leq N \quad (5)$$

Where Γ^n is a vector gathering the concentrations and the different platinum surface coverages:

$$\Gamma^n = \left[c_{O_2}^{a,n} \quad c_{H_2}^{a,n} \quad c_{H_2O}^{a,n} \quad \theta_{PtOH}^{s,a,n} \quad \theta_{PtO}^{s,a,n} \quad \theta_{PtO}^{b,a,n} \quad c_{O_2}^{c,n} \quad c_{H_2}^{c,n} \quad c_{H_2O}^{c,n} \quad \theta_{PtOH}^{s,c,n} \quad \theta_{PtO}^{s,c,n} \quad \theta_{PtO}^{b,c,n} \right]^t \quad n \leq N \quad (6)$$

The equation (5) corresponds actually to the mass transport equations described in §4.2.1.c.

Resolution

The system can be solved in galvanostatic or in potentiostatic mode.

○ Potentiostatic mode:

The fuel cell voltage U_{cell} is controlled. Equation (4) can be rewritten to express I_c^n as a function of U_{cell} :

$$j_c^n = \frac{U_{cell} - \phi_c^n + \phi_a^n}{R_\infty} \quad n \leq N \quad (7)$$

The new expression of I_c^n can then be reintroduced in equations (1) and (2):

$$C_{tot}^c \frac{d\phi_c^n}{dt} = \frac{U_{cell} - \phi_c^n + \phi_a^n}{R_\infty} - \sum_{i=1}^m j_{f,n}^{c,i} \quad n \leq N \quad (8)$$

$$C_{tot}^a \frac{d\phi_a^n}{dt} = -\frac{U_{cell} - \phi_c^n + \phi_a^n}{R_\infty} - \sum_{i=1}^m j_{f,n}^{a,i} \quad n \leq N \quad (9)$$

The system can be summarized in one single equation:

$$\frac{d}{dt} \begin{pmatrix} \phi_a \\ \phi_c \\ \Gamma \end{pmatrix} = \Phi \left(\begin{pmatrix} \phi_a \\ \phi_c \\ \Gamma \end{pmatrix}, U_{cell} \right) \quad (10)$$

Finally, the current density provided by the cell is obtained by replacing I_c^n in equation (3):

$$j_{cell} = \frac{1}{R_\infty} \left[U_{cell} - \frac{1}{N} \sum_{n=1}^N (\phi_c^n - \phi_a^n) \right] \quad n \leq N \quad (11)$$

○ Galvanostatic mode:

The current density provided by the cell I_{cell} is imposed in equation (3). The expression of U_{cell} in equation (8) and (9) can be replaced by that in equation (11):

$$R_\infty C_{tot}^c \frac{d\phi_c^n}{dt} = R_\infty I_{cell} + \left(\frac{1}{N} \sum_{k=1}^N \phi_c^k - \phi_c^n \right) - \left(\frac{1}{N} \sum_{k=1}^N \phi_a^k - \phi_a^n \right) - R_\infty \sum_{i=1}^m j_{f,n}^{c,i} \quad n \leq N \quad (12)$$

$$R_\infty C_{tot}^a \frac{d\phi_a^n}{dt} = R_\infty j_{cell} + \left(\frac{1}{N} \sum_{k=1}^N \phi_a^k - \phi_a^n \right) - \left(\frac{1}{N} \sum_{k=1}^N \phi_c^k - \phi_c^n \right) - R_\infty \sum_{i=1}^m I_{f,n}^{a,i} \quad n \leq N \quad (13)$$

The system to solve can be summarized in one single matrix equation:

$$\frac{d}{dt} \begin{pmatrix} \phi_a \\ \phi_c \\ \Gamma \end{pmatrix} = \Phi \left(\begin{pmatrix} \phi_a \\ \phi_c \\ \Gamma \end{pmatrix}, j_{cell} \right) \quad (14)$$

Where $\phi_a = [\phi_a^1 \dots \phi_a^N]^t$, $\phi_c = [\phi_c^1 \dots \phi_c^N]^t$ and $\Gamma = [(\Gamma^1)^t \dots (\Gamma^N)^t]^t$.

Finally the fuel cell voltage is obtained with equation (11).

Application

- Polarization curve:

Condition: steady state

Resolution mode: Potentiostatic

Controlled parameter: fuel cell voltage

Number of segments: N = 1

Numerical method: Levenberg-Marquardt

Objective: estimation of parameters in §4.2.2.

- Cyclic voltammetry:

Condition: transient state

Resolution mode: Potentiostatic

Controlled parameter:

- Potential scan rate: 50 mV/s

- Potential range (fuel cell voltage): from 0.1V to 1.2V (and reverse)

Number of segments: N = 1

Numerical method: Runge-Kutta

Objective: estimation of parameters in §4.2.2.

- Start-up:

Condition: transient state

Resolution mode: galvanostatic

Controlled parameter: $I_{cell} = 0A / cm^2$ (cell in open circuit)

Number of segments: N = 100

Numerical method: Runge-Kutta

Objective: simulation of start-up for comparison with §2.4.

In this case, the fuel cell voltage is substituted in equation (8) and (9) by its expression in equation (11):

$$R_{\infty}^n C_{total}^c \frac{d\phi_c^n}{dt} = \left(\frac{1}{N} \sum_{k=1}^N \phi_c^k - \phi_c^n \right) - \left(\frac{1}{N} \sum_{k=1}^N \phi_a^k - \phi_a^n \right) - R_{\infty}^n \sum_{i=1}^m j_{f,n}^{c,i} \quad (15)$$

$$R_{\infty}^n C_{total}^a \frac{d\phi_a^n}{dt} = \left(\frac{1}{N} \sum_{k=1}^N \phi_a^k - \phi_a^n \right) - \left(\frac{1}{N} \sum_{k=1}^N \phi_c^k - \phi_c^n \right) - R_{\infty}^n \sum_{i=1}^m j_{f,n}^{a,i} \quad (16)$$

The system can be written as:

$$\frac{d}{dt} \begin{pmatrix} \phi_a \\ \phi_c \\ \Gamma \end{pmatrix} = M \begin{pmatrix} \phi_a \\ \phi_c \\ \Gamma \end{pmatrix} + K \quad (17)$$

Where M is a 14Nx14N matrix and K a 14xN vector. This system is solved using a Runge-Kutta method.

Annex 6. Estimation of the average diameter of the platinum particles

The total amount of platinum in one electrode is given by:

$$N_{Pt}^{tot} = n_{Pt}^{tot} N_A \quad (18)$$

Which corresponds to a volume:

$$V_{Pt}^{tot} = N_{Pt}^{tot} \frac{4}{3} \pi R_{Atom}^3 \quad (19)$$

With $R_{Atom} = 139.10^{-12} m$ the average radius of the platinum particles.

The average volume of the platinum particles can be expressed as:

$$V_{Part} = \frac{4}{3} \pi R_{Part}^3 \quad (20)$$

With R_{Part} the average radius of the platinum particles.

One can define the amount of platinum particles by:

$$N_{Part} = \frac{V_{Pt}^{tot}}{V_{Part}} = N_{Pt}^{tot} \left(\frac{R_{Atom}}{R_{Part}} \right)^3 \quad (21)$$

The average surface of the platinum particles being:

$$S_{Part} = 4\pi R_{Part}^2 \quad (22)$$

And that of the atom projected on a flat surface being:

$$S_{Atom} = \pi R_{Atom}^2 \quad (23)$$

One can determine the number of atoms per surface of platinum particle:

$$N_{Atom/S_{Part}} = 4 \frac{R_{Part}^2}{R_{Atom}^2} \quad (24)$$

According to Jerkiewicz et al. [124], only a fraction χ of platinum atoms located on the surface of the particles can oxidize (then oxidation takes place only in the bulk):

$$N_{Pt}^s = \chi N_{Atom/S_{part}} N_{part} \quad (25)$$

It is assumed that $1/8^{\text{th}}$ of the total number of platinum atoms corresponds to atoms which are located on the surface and which can oxidize:

$$N_{Pt}^s = \frac{1}{8} N_{Pt}^{tot} \quad (26)$$

Equation (25) can be integrated in the left hand side of equation (26):

$$\chi N_{Atom/S_{part}} N_{part} = \frac{1}{8} N_{Pt}^{tot} \quad (27)$$

Similarly, equations (21) and (24) can be integrated in the left hand side of equation (27):

$$4\chi \frac{R_{Atom}}{R_{part}} N_{Pt}^{tot} = \frac{1}{8} N_{Pt}^{tot} \quad (28)$$

Which can be rewritten to express the average radius of platinum particles:

$$R_{part} = 32\chi R_{Atom} \quad (29)$$

According to Jerkiewicz et al. [124], the oxidation in the bulk starts when half of the platinum particle surface is covered by oxides: $\chi=0.5$.

In the cathode, the assumption concerning the atoms which are located on the surface and which can oxidize is therefore equivalent to consider platinum particles with an average diameter of 4.5 nm.

Résumé

Cette thèse contribue à l'identification des mécanismes de dégradation qui ont lieu durant les phases de démarrage et d'arrêt des Piles à Combustible à Membrane Echangeuse de Proton. Dans un premier temps, des démarrages et arrêts individuels sont étudiés au moyen d'une cellule équipée de collecteurs de courants segmentés. Les courants internes qui sont produits durant ces opérations peuvent ainsi être mesurés. La mesure du dioxyde de carbone dans les gaz d'échappement de la cathode révèle qu'une partie des courants internes correspond à de l'oxydation du carbone. Une autre part provient des réactions (réversibles ou non) d'oxidoréduction impliquant du platine. L'hétérogénéité des dégradations subies par la pile entre l'entrée et la sortie de la cathode est mise en évidence lors de protocoles de vieillissement répétant des démarrages et arrêts. Des analyses post-mortem révèlent un autre niveau d'hétérogénéité, qui concerne également le carbone, entre les dents et les canaux. De ces expériences, il ressort également que les dégradations sont plus importantes lorsque les gaz sont injectés à faible vitesse dans le compartiment anodique mais aussi quand de l'air est utilisé à la place de l'azote pour arrêter la pile.

L'influence des caractéristiques de la MEA sur l'intensité des dégradations est aussi étudié. Un chargement en platine élevé à l'anode ou des électrodes avec des surfaces de carbone actif élevées accélèrent la chute des performances électriques. Au contraire accroître le chargement en platine à la cathode limite ces pertes. Enfin, des simulations numériques des phases de démarrage complètent les résultats expérimentaux. L'oxydation réversible du platine est notamment identifiée comme étant responsable d'une part importante des courants internes.

Mots-clés : Pile à Combustible à Membrane Echangeuse de Protons, dégradations, démarrages et arrêts, pile segmentée, Simulation numérique

Abstract

This work contributes to the identification of the various degradation mechanisms in Polymer Electrolyte Membrane Fuel Cell during start-up and shut-down operations. Single start-ups and shut-downs are first analysed using a cell with segmented cathode current collectors. Thus, internal currents which occur during these operations can be measured. Carbon dioxide measured in the cathode exhaust gas reveals that they result partially from carbon oxidation. Another contribution is the reversible or non reversible redox reactions involving platinum. The heterogeneity of the non reversible platinum oxidation between the inlet and outlet of the cathode is evidenced by the in-situ monitoring of the Electrochemical Surface Area during long-term start-up and shut-down aging protocols. Post-mortem analysis reveals another level of heterogeneity, which concerns also carbon oxidation, between land and channel. From these experiments, it appears also that degradations are more important when gases are injected with a low velocity in the anode compartment and when air is used instead of nitrogen to flush the anode compartment during shut-down.

The influence of the MEA characteristics on the extent of the degradation observed during these aging protocols is also analyzed. High platinum loading in the anode and high surface carbon electrodes accelerate the drop of the electrical performances, while increasing the cathode platinum loading limits their decay. Finally, numerical simulations of start-ups complete the experimental results. Reversible platinum oxidation was found to be one of the main contribution to the internal currents.

Keywords: PEM Fuel Cell, degradations, start-up and shut-down, segmented cell, numerical simulation